DISSERTATION

NONLINEAR SPIN WAVE INSTABILITY PROCESSES IN MANGANESE SUBSTITUTED ZINC Y-TYPE HEXAGONAL FERRITES

Submitted by

Richard G. Cox

Department of Physics

In partial fulfillment of the requirements

for the Degree of Doctor of Philosophy

Colorado State University

Fort Collins, Colorado

Summer 2010

COLORADO STATE UNIVERSITY

February 3, 2010

WE HEREBY RECOMMEND THAT THE DISSERTATION PREPARED UNDER OUR SUPERVISION BY RICHARD GARNER COX ENTITLED NONLINEAR SPIN WAVE INSTABILITY PROCESSES IN MANGANESE SUBSTITUTED ZINC Y-TYPE HEXAGONAL FERRITES BE ACCEPTED AS FULFILLING IN PART REQUIREMENTS FOR THE DEGREE OF DOCTOR OF PHILOSOPHY.

Committee on Graduate Work

_____Richard E. Eykholt

_____Pavel Kabos

_____Robert G. Leisure

_____Carmen S. Menoni

_____Raymond S. Robinson

_____Carl E. Patton
Advisor

_____Hans D. Hochheimer
Department Head

ABSTRACT OF DISSERTATION

NONLINEAR SPIN WAVE INSTABILITY PROCESSES IN MANGANESE SUBSTITUTED ZINC Y-TYPE HEXAGONAL FERRITES

The large magnetocrystalline anisotropy observed in hexagonal ferrites makes these materials ideally suited for high frequency millimeter-wave applications. However, the large microwave losses observed at low-power levels and the high-power handling capabilities of hexagonal ferrites need to be addressed prior to their wide acceptance in real devices. In order to address the above issues, measurements and analyses of the microwave field amplitude (h_{crit}) required to parametrically excite nonlinear spin wave amplitude growth were performed on single crystal easy plane disks of Mn substituted Zn Y-type hexagonal ferrites at 9 GHz and room temperatures. Plots of the h_{crit} dependence on the static magnetic field, termed "butterfly curves," were obtained and analyzed for the resonance saturation (RA), subsidiary absorption (SA), and parallel pumping (PP) configurations.

In order to obtain the butterfly curve data and perform the analyses: (1) a state-of-the-art computer-controlled high-power microwave spectrometer was constructed, (2) the classical spin wave instability theory, originally developed by Suhl and Schloemann, was extended, and (3) instability measurements were performed on multiple Zn Y-type hexagonal ferrites samples for several pumping configurations and static field settings. The measurements and analyses performed here constitute the first time RS, SA, and PP spin wave instability butterfly curve analysis have all been performed in planar hexagonal ferrite samples. This work also corresponds to the first time that resonance saturation

measurements and analyses were performed for static magnetic fields both at and in the vicinity of the ferromagnetic resonant field in a hexagonal ferrite.

The data obtained as part of this work show that the microwave field amplitude required to parametrically excite nonlinear spin wave amplitude growth in hexagonal ferrites is similar to polycrystalline cubic ferrites, which are currently in use in microwave devices. Follow-up measurements, motivated by this work, revealed that h_{crit} can be varied by manipulating the sample dimensions. The analyses performed here indicate that two-magnon scattering is likely not the dominant source of the large low-power microwave losses observed in these hexagonal ferrites; rather that these losses may be an intrinsic property of the material. The theoretical work performed here identified a sign problem with the anti-Larmor uniform mode complex damping terms in several past publications and provides an improved methodology of treating the uniform mode anti-Larmor complex frequency damping.

Richard G. Cox
Department of Physics
Colorado State University
Fort Collins, CO 80523
Summer 2010

ACKNOWLEDGEMENTS

I am greatly indebted and would like to express my gratitude to the following individuals for their part in completion of this Ph.D. dissertation.

First, I acknowledge and thank my thesis advisor, Professor Carl E. Patton, who suggested this research topic and offered guidance for this investigation. I also thank Dr. Pavel Kabos (now at NIST in Boulder) and Professor Richard E. Eykholt who spent many hours mentoring me and answering my numerous questions.

I am grateful to the Magnetic Materials Association for their generous scholarships that provided key financial assistance to my family and me. Further support was given in part by the Office of Naval Research, Grant No. N00014-06-0889.

My sincere appreciation is also due to my high school mathematics teacher, Mrs. Kandice Davis of Gloucester, NC, who provided me with a foundation and rigor in mathematics that was essential to my studies in physics. I am also grateful to Randy and Rhea Toedter whose support during my undergraduate studies was a blessing. Additionally, I thank my former manager at Seagate Technology, Dr. Daniel J. Dummer (now with Medtronic in Minneapolis) whose encouragement regarding the long editing and rewriting phase of this dissertation will always be appreciated.

My deepest gratitude is saved for my family. The depth of my gratitude to my wife, Vanessa, whose love and patience was essential in earning this Ph.D., cannot be put into words. I love you so much. My daughter, Kristen Samantha, and son, Charles Garner, have been troopers over this long process. To my parents, thank you for teaching me the importance of hard work, respect of others, and integrity.

Finally, I praise my Lord and Savior, Jesus Christ, who has provided and continues to provide me comfort, strength, perseverance, and hope.

TABLE OF CONTENTS

CHAPTER 1

INTRODUCTION

An introduction to this study of nonlinear spin wave instability processes in Mn substituted Zn Y-type hexagonal ferrites is presented here. The chapter addresses the motivation, objectives, scope, and organization of this thesis.

1.1 MOTIVATION

There is a critical need to extend the operational frequency of conventional ferrite based microwave devices to the millimeter wave frequency regime. However, to operate these devices at millimeter wave frequencies requires such large external magnetic biasing fields that the devices become impractical. The large magnetocrystalline anisotropy associated with hexagonal ferrites offers a potential solution to the large external magnetic field requirements for high frequency operation (Patton [1988]; Vittoria [1980]; Rodrigue [1963]). However, the large microwave losses observed at low-power levels and the high-power handling capabilities of hexagonal ferrites need to be addressed prior to a wide acceptance of these materials in real devices.

The low-power microwave losses exhibited by hexagonal ferrites are typically about ten to twenty times larger than those observed in conventional cubic ferrites (Hurben *et al*. [1997]). The majority of the work performed to date on hexagonal ferrites has focused on the determination of whether the large low-power losses are due to extrinsic or intrinsic processes. Extrinsic loss processes involve microstructural defects and

inhomogeneities, which can be either minimized or eliminated. Intrinsic loss processes are fundamental to the material and cannot be further reduced (Sparks [1964]; Patton [1975]). The two most common experimental methods used to characterize the low-power microwave losses in hexagonal ferrite have been ferromagnetic resonance (FMR) and effective linewidth (ELW) analysis. The FMR analysis has indicated that there are appreciable microstructural defects present in hexagonal ferrites (Hurben *et al*. [1997]), while the ELW analysis suggest that a significant portion of the losses are due to intrinsic processes (McKinstry [1991]; Truedson *et al*. [1994]).

The high-power microwave handling capabilities of hexagonal ferrites has received relatively little attention. As the microwave power is increased in a microwave device an onset of nonlinear effects, which significantly degrade the device's performance, are often observed. The onset of these nonlinear effects typically occur at a specific power level and usually corresponds to the parametric excitation of specific spin wave modes in the ferrite material (Suhl [1957]; Milano and Schloemann [1961]). The threshold power level required for parametric spin wave mode excitation is directly related to the relaxation rate of the excited spin wave modes. Therefore, by measuring the threshold power, one can determine both the practical power limits and gain insight into the fundamental loss mechanisms of the ferrite material.

The specific spin wave modes that are parametrically excited at high-power levels can be directly affected by the experimental conditions. Therefore, one can influence which spin waves are excited at the nonlinear threshold and in turn study the relaxation processes of those particular spin wave modes. The typical approach is to measure the critical microwave threshold field amplitude (h_{crit}) required to produce the onset of nonlinear spin wave growth as a function of the static magnetic field (H_{ext}) for a fixed microwave frequency and a given microwave, static magnetic field, and ferrite sample orientation. Historically, plots of h_{crit} versus H_{ext} are termed "butterfly curves." Theoretical analyses of the measured butterfly curves are then performed to determine:

(1) which of the available spin wave modes are excited at the threshold field and (2) the relaxation rate of these critical modes. To date, such high-power instability butterfly curve measurements and analyses have yet to be performed in detail on hexagonal ferrites.

1.2 THESIS OBJECTIVES

The focus of this thesis work is the characterization of the nonlinear instability thresholds in hexagonal ferrites in order to determine whether the large low-power losses exhibited by hexagonal ferrites are due to intrinsic or extrinsic damping processes, and in turn obtain the high-power handling capability of the material. In order to achieve the above objectives: (1) a state-of-the-art high-power microwave spectrometer was designed, built, and automated, (2) the classical spin wave instability theory originally developed by Suhl and Schloemann was extended, and (3) spin wave instability measurements and analyses were performed on Zn Y-type hexagonal ferrites for several pumping configurations and frequencies.

1.3 ORGANIZATION AND SCOPE OF STUDY

Chapter 2 provides introductory background information on microwave magnetic ferrite materials. The key concepts of anisotropy, uniform mode precession, spin wave propagation, relaxation, and nonlinear spin wave instability processes are reviewed. This is followed by detailed discussions of the following three most commonly studied spin wave instability processes: (1) resonance saturation, (2) subsidiary absorption, and (3) parallel pumping.

Chapter 3 discusses the classical bulk spin wave instability theory, which was originally developed by Suhl (Suhl [1957]) and Schloemann (Schloemann *et al*. [1960]), and the extensions that were made to it as part of this work. It will be shown that the theory was extended to cover (1) uniaxial anisotropy, (2) a generalized microwave

magnetic pump field orientation, and (3) resonance saturation processes for static magnetic fields not only equal to, but away from the ferromagnetic resonance field. The chapter will also show that several previous publications, which extended Suhl's and Schloemann's theory to include anti-Larmor precessional rotation, contain a sign problem with their uniform mode anti-Larmor complex frequency damping terms. It will be shown that while the sign issue did not have a significant effect on the parallel pumping and the subsidiary absorption analyses given in those papers, it does have a notable effect on resonance saturation threshold field calculations in the limit of large shape and magnetocrystalline anisotropy. This is one of the specific cases of interest for this study. A solution for the above sign issue is also provided in the chapter.

Chapter 4 discusses the high-power microwave spectrometer, which was designed, built, and automated as part of this thesis work. It will be shown that the high-power microwave spectrometer was based upon the systems described by Green, Kohane, and Patton, but built with modern electronics and computer automation (Green and Kohane [1964]; Patton and Green [1971]). The earlier systems had limited frequency and pulse width capabilities and were operated in a highly manual fashion. The spectrometer built as part of this study is capable of generating high-power microwave pulses over a wide range of frequencies, with long pulse widths, is automated and highly versatile. The system can be used to perform not only high-power microwave measurements, such as parallel pumping, subsidiary absorption, and resonance saturation instability measurements, but can also be utilized to characterize low-power ferromagnetic resonance, effective linewidth, and dielectric loss measurements.

Chapter 5 discusses the measurement and analysis results. First an overview is given of the Zn Y-type hexagonal ferrite disc shaped samples used for this work and then the parallel pumping, subsidiary absorption, and resonance saturation instability measurements and analyses are reviewed. The chapter shows that the calculated parallel pumping and subsidiary absorption spin wave linewidths were significantly higher than

expected, and that these results led to further work performed primarily by Alex Nazarov who was able to determine that the large first order spin wave linewidths obtained as part of this thesis work were related to sample size effects (Nazarov *et al.* [2002]). This important finding may be useful in controlling the maximum power handling capability of real devices.

Chapter 6 summarizes the thesis research and discusses its significance. It is argued that the results obtained here indicate that the large microwave losses exhibited by single crystal hexagonal ferrites are likely an intrinsic property of the material. It is hypothesized that the strong spin-lattice coupling that occurs in these materials is the source of the losses. In other words, it will be suggested that the strong spin-orbit coupling, which is the source of the large magnetic crystalline anisotropy fields in hexagonal ferrites that makes these materials so attractive for high-frequency applications, may also be the source of the large low-power microwave losses that inhibits their full utilization in real devices. The chapter also provides suggestions for future work.

Appendix A reviews the passive waveguide components that are utilized in the high-power microwave spectrometer discussed in Chapter 4. Here the basics of (i) rectangular waveguides, (ii) directional couplers, and (iii) microwave cavities are addressed. Derivations of equations that describe the microwave field amplitude inside rectangular and cylindrical reflection type microwave cavities are also provided.

Appendix B reviews the LabVIEW control programs that were developed to calibrate and operate the high-power microwave spectrometer. First, the calibration programs are reviewed and then the measurement programs, which were developed to obtain the spin wave instability butterfly curve data, are discussed.

CHAPTER 2

OVERVIEW OF MICROWAVE FERRITES

This chapter provides background information on the static, linear, and nonlinear dynamic magnetic properties of microwave ferrites. The emphasis is primarily on physical concepts. Details that are given in later chapters or are covered in the suggested references are intentionally omitted. The chapter is divided into the following three sections:

1. The first section provides a brief review of the basic classifications, composition, and static magnetic properties of microwave ferrites, and includes a discussion on anisotropy.
2. The second section reviews the linear dynamic magnetic processes, which occur in microwave ferrites. Here ferromagnetic resonance (FMR), uniform mode precession, spin waves, and relaxation are addressed.
3. The final section reviews the resonance saturation, subsidiary absorption, and parallel pumping nonlinear instability processes, which occur in ferrites at high microwave power levels. A brief review of previous spin wave instability work is also given.

2.1 STATIC PROPERTIES

This section provides a brief review of the basic composition, classifications, and static magnetic properties of microwave ferrites. It also includes a discussion of anisotropy.

The next section then provides a brief review of the linear dynamic properties of ferrite materials.

2.1.1 Composition and Classification

Microwave ferrites are iron oxide magnetic insulators, which fall into the ferrimagnetic classification of magnetic materials. They are ideally suited for microwave applications because their relatively high resistivity leads to minimal eddy current losses. Ferrites are typically categorized by crystal structure into the following three groups: (1) spinel, (2) garnet, and (3) hexagonal (von Aulock [1965]). The spinels and garnets have complicated cubic structures and a general chemical formula of $MeFe_2O_4$ and $Me_3Fe_5O_{12}$, respectively, where *Me* is a 3D or 4F transitional metal. The hexagonal ferrites have a hexagonal crystal structure and are typically designated by different capital letters (M, W, Y, etc.) depending upon the relative amounts of Fe, Ba, and *Me* that are present (von Aulock [1965]). The most commonly studied cubic ferrite is yttrium iron garnet (Sparks [1964]). It has a composition of $Y_3Fe_5O_{12}$ and will be referred to here as YIG. The two most frequently studied hexagonal ferrites are zinc Y-type ($Ba_2Zn_2Fe_{12}O_{22}$) and barium M-type ($BaFe_{12}O_{19}$), which have planar and uniaxial anisotropy, respectively. The theoretical work performed here is applicable to both uniaxial and planar type hexagonal ferrites, while the experimental work is focused on the Zn Y-type ferrites, with easy-plane anisotropy. For more details on the structure and composition of the various ferrite types see Smit and Wijn [1959] and von Aulock [1965].

Strong bonds occur between the composite metal cations and oxygen anions in ferrites. The metal cations and oxygen anions are formed when each oxygen atom acquires two metal valence electrons to fill their 2p shells. The main source of the magnetic moments in ferrites is usually the unpaired spin of the 3d shell electrons in

Fe3+ ions. These iron ions are usually centered in neighboring tetrahedral and octahedral formations of the oxygen atoms. In spinels and garnets, the iron moments at the tetrahedral and octahedral sites are coupled anti-parallel via the oxygen atoms, whereas in hexagonal ferrites both parallel and anti-parallel coupling occurs between the two sites (Wittenauer [2005]). This coupling via oxygen atoms is commonly referred to as super-exchange coupling (Smit and Wijn [1959]). Even though the spins are coupled in an anti-parallel fashion, an imbalance in the net spins at the tetrahedral and octahedral lattice sites results in ferrites having a net saturation magnetization $4\pi M_s$, which is in the 1-to-5 kGauss range. This value is significantly lower than the saturation magnetization values of 10-to-25 kGauss which are observed in standard ferromagnets that have purely parallel spin coupling.

Figure 2.1 summarizes the various magnetic classifications of materials and the electron spin interaction/coupling that leads to these classifications. Electron spin and lattice coupling, which leads to crystalline anisotropy, is not shown in the figure. For ferromagnets and anti-ferromagnets the exchange coupling causes neighboring spins to be aligned parallel and anti-parallel, respectively. Anti-ferromagnets can be considered a special case of ferrimagnets in which the oppositely aligned magnetic moments are of equal magnitude. Ferrites are in the ferrimagnetic classification of magnetic materials. For most cases and in this study in particular, ferrimagnets are regarded as ferromagnetic dielectrics. There is a special case, however, known as exchange resonance in which the dynamic response of ferrimagnets differs from that of ferromagnets, which is not considered here; see von Aulock [1965] for more details.

2.1.2 Magnetic Anisotropy

The last static magnetic property of ferrites to be discussed here is anisotropy. Because of the important role that anisotropy plays in both the linear and nonlinear dynamic

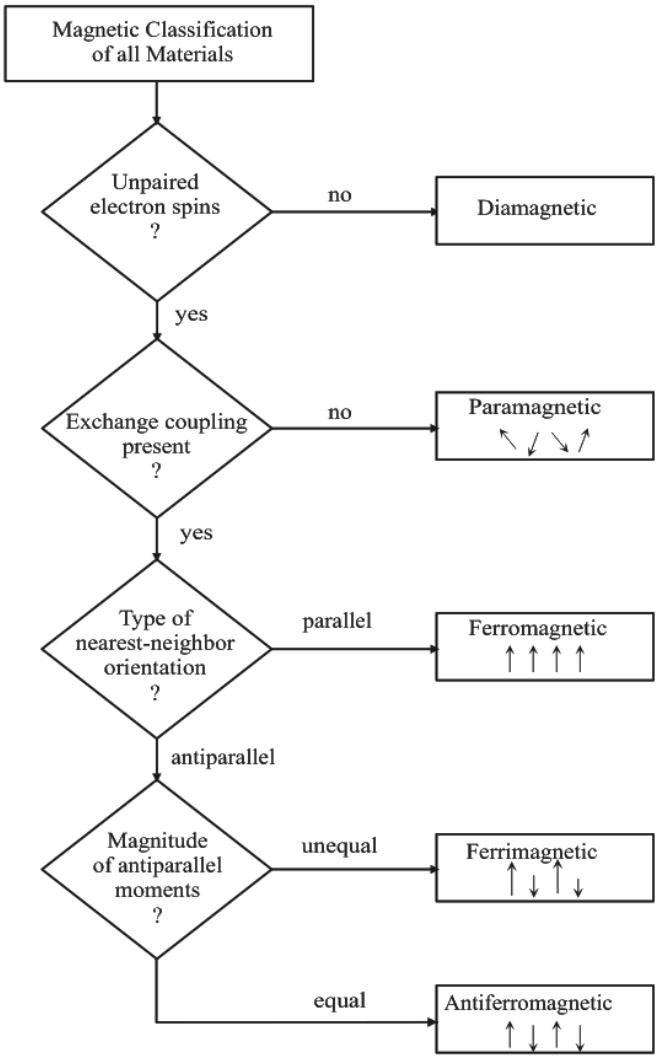

Figure 2.1. Flowchart of the magnetic classifications of materials, after Stancil [1993].

processes within ferrites it will be discussed in some detail here and then more extensively in Chapter 3.

Magnetic anisotropy corresponds to there being a preferential magnetization direction within a given sample and is typically separated into the following two categories: (1) shape anisotropy and (2) crystalline anisotropy. Shape anisotropy is due to the dipole fields that arise between the bounding surfaces of a magnetized sample. These dipole fields, which are commonly referred to as demagnetizing fields, depend on sample geometry and the magnitude and orientation of the magnetization vector.

Different shaped samples of the same exact ferromagnetic material can have different demagnetizing fields. For example, a uniformly magnetized spherical sample has a demagnetizing field of $-4\pi\mathbf{M}_s/3$, where M_s is the saturation magnetization of the sample. Whereas when the same material is fashioned into a thin film, the corresponding demagnetizing field is $-4\pi\mathbf{M}_\mathbf{n}$, where $\mathbf{M}_\mathbf{n}$ is the component of the magnetization oriented normal to the disc plane. Therefore, if the saturation magnetization is aligned into the film plane the demagnetizing field is zero, and if saturation magnetization is aligned out of the plane the demagnetizing field has a magnitude of $-4\pi M_s$ and points in the opposite direction of the saturation magnetization direction. Exact expressions for the demagnetizing fields can be calculated using Maxwell's equations (Jackson [1975]) for a general shaped sample or more simply from Osborn's tensor equations for ellipsoidal shaped samples (Osborn [1945]). The Osborn equations will be discussed in detail in Chapter 3.

Crystalline anisotropy is primarily due to electron spin-orbit-lattice coupling and is usually characterized by a free energy expression that corresponds to the amount of energy required to overcome the spin orbit coupling (Chikazumi [1994]; (Cullity [1972]). First principle calculations of the free energy expression are very difficult if not impossible to perform, so phenomenological equations based upon crystalline symmetries are typically utilized. The energy expression is typically quantified by relating it to an effective magnetic anisotropy field ($\mathbf{H}_\mathbf{A}$). To do this: (1) the Zeeman energy relation ($U_A = -\mathbf{M}\cdot\mathbf{H}_\mathbf{A}$) is rewritten as $\mathbf{H}_\mathbf{A} = -\nabla_\mathbf{M} U_A$, where $\nabla_\mathbf{M}$ is the gradient with respect to the magnetization components, and (2) the magnitude of $\mathbf{H}_\mathbf{A}$ is then determined via magnetic hysteresis measurements (Cullity [1972]). The remainder of this section will show how the above approach is used to model uniaxial and planar anisotropy in hexagonal ferrites.

The preferential magnetization direction of uniaxial and planar hexagonal ferrites is parallel to and perpendicular to the hexagonal crystal c-axis, respectively (Smit and Wijn

[1959]); (von Aulock [1965]). These preferential directions may be modeled with the following free energy per unit volume expression

$$U_A = K_0 - K_1\left(\frac{\mathbf{M}\cdot\hat{\mathbf{u}}_\mathbf{A}}{M_s}\right)^2 . \tag{2.1}$$

Here the K_0 and K_1 are constants for a particular material expressed in ergs/cm^3 and $\hat{\mathbf{u}}_\mathbf{A}$ is the unit vector in the crystalline c-axis direction (Cullity [1972]). The K_0 term in Eq. (2.1) is usually ignored since we are mostly interested in the change of the energy as M rotates from the c-axis. The sign of the second term (K_1) determines whether Eq. (2.1) describes uniaxial or planar anisotropy. A positive K_1 corresponds to the energy being minimized when the magnetization vector is parallel to the c-axis, i.e., uniaxial anisotropy, and a negative K_1 corresponds to the energy being minimized when the magnetization vector is in the *x-y* plane, i.e., planar anisotropy.

As discussed above, the explicit magnetic field anisotropy expression is obtained by performing the following gradient operation on the free energy expression ($\mathbf{H}_\mathbf{A} = -\nabla_\mathbf{M} U_A$). Applying this gradient operation on Eq. (2.1) yields

$$\mathbf{H}_\mathbf{A} = H_A\left(\frac{\mathbf{M}\cdot\hat{\mathbf{u}}_\mathbf{A}}{M_s}\right)\hat{\mathbf{u}}_\mathbf{A}, \tag{2.2}$$

where $H_A = 2K_1/M_s$. The magnitude of both the shape and the crystalline anisotropy (H_A) can be obtained from vibrating sample magnetometery (VSM) measurements.

Figure 2.2 shows VSM hysteresis data which were obtained on a Zn Y-type hexagonal ferrite sample as part of this study. The sample was thin disc shaped with the crystalline easy anisotropy plane in the disc plane. The vertical axis of the plot corresponds to the magnitude of the component of the magnetization, which is aligned

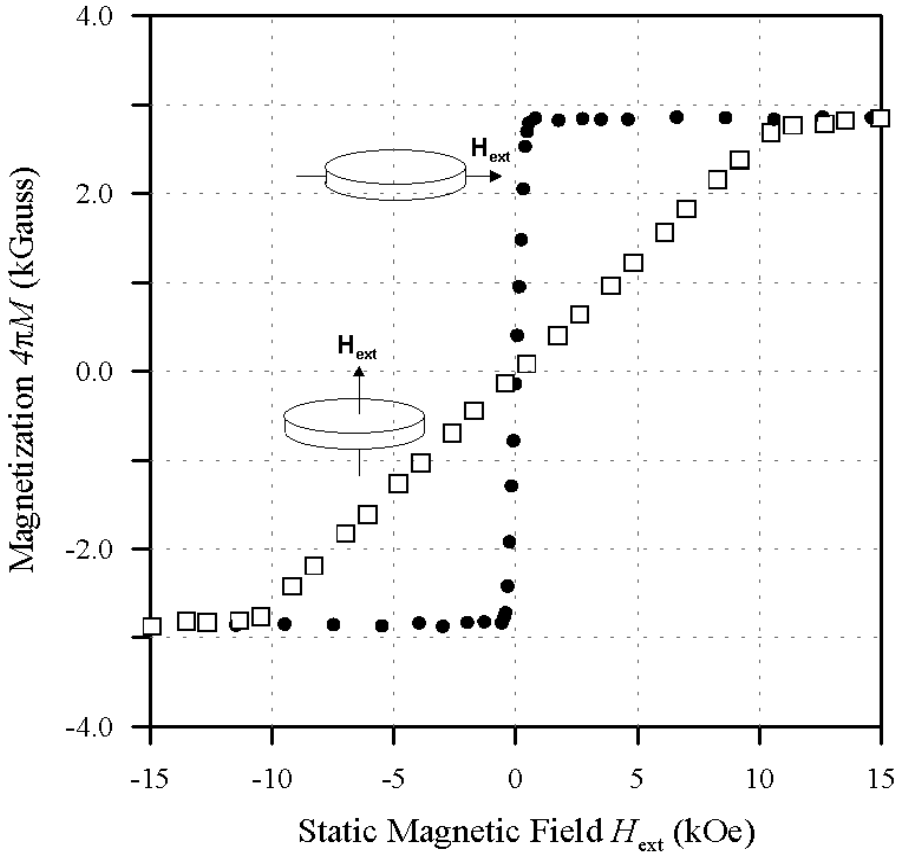

Figure. 2.2. Plots of magnetic hysteresis data that were obtained on a Zn Y-type hexagonal ferrite thin disc with planar anisotropy. The disc and the crystalline anisotropy planes are coplanar. The solid circles and open squares correspond to the data obtained with the external magnetic field applied in and out of the disc plane, respectively.

parallel to the applied magnetic field direction, and the horizontal axis corresponds to the magnitude of the applied field. The solid circles and open squares correspond to the magnetization data that were obtained with the external magnetic field applied parallel and normal to the disc plane, respectively. As can be seen in the figure, a significantly larger external magnetic field was required to saturate the magnetization out of the disc plane than in-plane. The difference of approximately 10 kGauss in the field requirements to saturate the magnetization for the two different orientations is due to both shape and crystalline anisotropy.

The expressions for the static magnetic fields required to saturate the magnetization in the in-plane (H_{sat}^{in}) and out-of-plane (H_{sat}^{out}) directions for the sample shown in Fig. 2.2 may be written as

$$H_{sat}^{in} = 4\pi M_s N_{in}$$
$$H_{sat}^{out} = 4\pi M_s N_{out} + \left|H_A\right|, \tag{2.3}$$

where N_{out} and N_{in} are the Osborn demagnetization coefficients for the out-of-plane and in-plane directions, respectively. These coefficients are calculated based upon the sample dimensions (assuming ellipsoidal in shape) and will be discussed in more detail in the following chapter. For the sample shown in Figure 2.2, N_{in} and N_{out} equaled 0.15 and 0.70, respectively, and as can be seen in Fig. 2.2, $4\pi M_s = 2.9$ kG and $H_{sat}^{out} = 10.1$ kOe. Substituting these parameters into Eq. (2.3) yields $\left|H_A\right| \approx 9$ kOe. As discussed previously, the sign of H_A depends on whether one is addressing uniaxial or planar type crystalline anisotropy and the manner in which the free energy expression is defined. For the Zn Y-type sample shown here which had planar anisotropy, and the free energy expression given in Eq. (2.1), a negative sign is used in the calculations.

Figure 2.3 summarizes typical anisotropy and saturation magnetization values of YIG, Ba M-type, and Zn Y-type hexagonal ferrites. As is seen in the figure, the garnets have an effective cubic anisotropy field that is quite small, on the order of 50 Oe or so. For materials with cubic lattice structure, direction cosines relative to the principal axies are typically used to describe the free energy expression. See Cullity [1972] for more details. For hexagonal ferrites, the expression given in Eq. (2.1) is often used. The effective uniaxial and planar anisotropy fields of Ba M-type and Zn Y-type hexagonal ferrites are approximately 20 kOe and 10 kOe, respectively. As was mentioned

previously these large anisotropy fields are what make the hexagonal ferrites so attractive for high frequency microwave applications.

It is important to realize that the anisotropy field expressions discussed above are not actual Maxwellian fields, rather they are effective field equations based upon phenomenological free energy expressions. While these expressions vary from paper to paper, as long as the approach used to calculate the fields are self-consistent with the specific free energy expression used, then the FMR resonance frequency and other

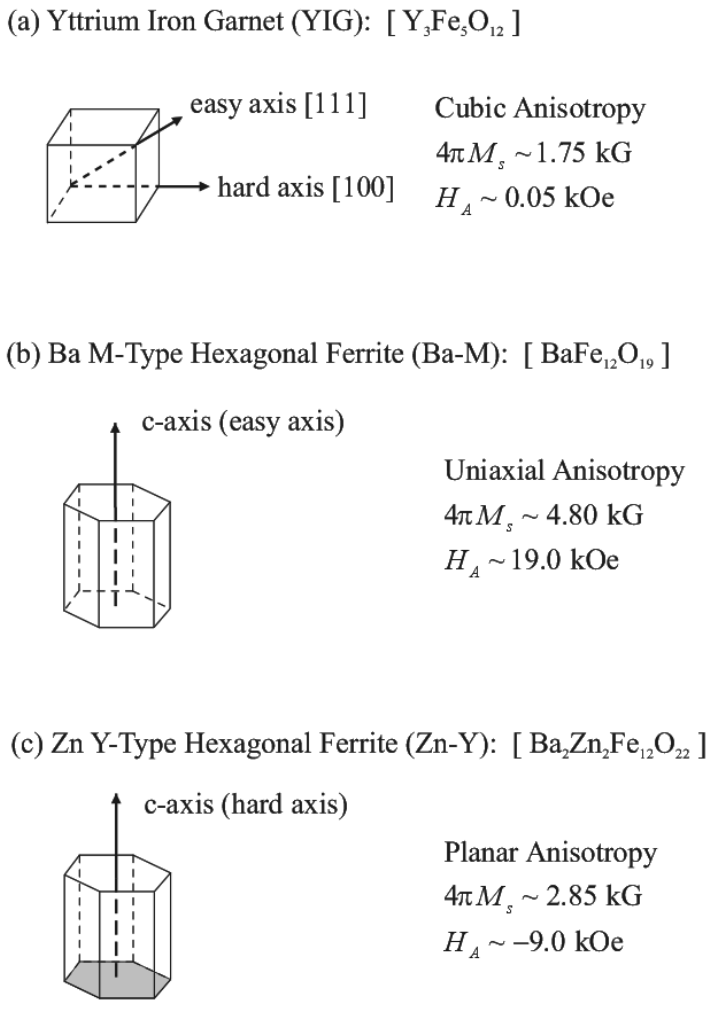

Figure. 2.3. Composition, saturation magnetization ($4\pi M_s$), and effective magnetic anisotropy field (H_A) of (a) YIG, (b) Ba M-type, and (c) Zn Y-type hexagonal ferrites.

physically measurable quantities predicted by the theory are independent of the form of free energy used (Hurben [1996]).

2.2 LINEAR SPIN WAVE PROCESSES

The previous section focused primarily on the static magnetic properties of ferrite materials. This section addresses their linear dynamic magnetic properties. Here ferromagnetic resonance (FMR), uniform mode, spin waves, and relaxation are addressed. In order to introduce these concepts, the physics of a single dipole moment in the presence of a homogenous static magnetic field is first discussed.

2.2.1 Free Precession

When a magnetic dipole moment ($\boldsymbol{\mu}$) that is in a uniform static magnetic field ($\mathbf{H}_{\mathbf{ext}}$) region is misaligned with $\mathbf{H}_{\mathbf{ext}}$, a net torque ($\boldsymbol{\tau}$) given as

$$\boldsymbol{\tau} = \boldsymbol{\mu} \times \mathbf{H}_{\mathbf{ext}} \tag{2.4}$$

is exerted on $\boldsymbol{\mu}$. The time dependent response of the magnetic moment to this torque depends upon the particle's angular momentum and the relaxation rate of the precessional response. The relationship between a particles dipole moment and its angular moment is often expressed as

$$\boldsymbol{\mu} = \gamma \mathbf{J}\,, \tag{2.5}$$

where γ, which is referred to as the gyromagnetic ratio, is given by

$$\gamma = g\frac{q}{2m}. \tag{2.6}$$

Here m is the mass, q is the charge of the particle, and g is the so-called Lende splitting factor. The exact value of the splitting factor depends upon the type of particle of interest and on the form of the angular momentum that is present. For electrons with purely orbital angular momentum $g=1$, purely spin angular momentum $g=2$, and when electrons have both orbital and spin angular momentum g is typically greater than 2 (Chikazumi [1994]).

For most ferrites, the constituent electrons have purely spin angular momentum $g=2$ and the resulting gyromagnetic ratio corresponds to $\gamma/2\pi=-2.8\,(\mathrm{GHz/kOe})$. This value of γ is fundamental to the applicability of ferrite materials at microwave frequencies. Protons have much larger mass than electrons and therefore a significantly smaller gyromagnetic ratio (few kHz/kOe), and in turn are more suited for studies in the kHz frequency range. The sign of the gyromagnetic ratio depends on the sign of the charged particle; for protons it is positive and for electrons it is negative.

The governing equation of motion which describes the precessional motion of the dipole moment about the uniform field can be obtained by (1) applying the fact that the net torque is equal to the time rate of change of the angular momentum ($\boldsymbol{\tau}=\partial\mathbf{J}/\partial t$) and (2) substituting the equations for $\boldsymbol{\tau}$ and $\mathbf{J}$, given in Eq. (2.4) and Eq. (2.5), respectively, into the $\boldsymbol{\tau}=\partial\mathbf{J}/\partial t$ relationship. Upon doing so, one obtains the so-called "torque equation of motion" which may be written as

$$\frac{\partial\boldsymbol{\mu}}{\partial t}=\gamma\left(\boldsymbol{\mu}\times\mathbf{H}_{\mathbf{ext}}\right). \tag{2.7}$$

This equation describes the dynamic response of a magnetic moment in the presence of a uniform magnetic field and in the absence of damping. It will be shown below that the anisotropy fields (both shape and crystalline), which occur in a bulk ferromagnetic sample, lead to modifications of Eq. (2.7).

The frequency of the precession, which can be readily obtained from Eq. (2.7), can be written as

$$\omega = |\gamma| H_{ext} \,. \tag{2.8}$$

As was mentioned previously, the value of 2.8 GHz/kOe for the electron's gyromagnetic ratio makes the electron precessional response ideally suited for studies and applications in the microwave frequency range. Also note that the natural frequency of the precessional motion is linearly dependent upon the external magnetic field strength. This is the reason behind the large static field requirements for high frequency operation of conventional ferrite devices.

Figure 2.4 shows the precessional response of an electron in a uniform static field ($\mathbf{H_{ext}}$). As is shown in the figure, the electron's magnetic moment is aligned in the opposite direction of its angular momentum (**J**). This results in the rotational motion of the magnetic moment being in the counter clockwise direction (as viewed from the positive z-axis) about the static magnetic field. An analogous classical system to the single magnetic moment in region of uniform magnetic field is a spinning top in a gravitational field. If the top is slightly perturbed from the vertical direction, it precesses about the vertical direction and then over a period of time frictional forces eventually damp out the precession. As with the spinning top, an electron's magnetic moment experience damping, which decreases its precessional angle and eventually cause the moment to align with the static field. The mechanisms that are responsible for such damping in ferrite materials will be discussed in section 2.2.4.

2.2.2 Ferromagnetic Resonance

The experimental analysis of magnetic dipole moments precessing about an externally applied static magnetic field typically fall into one of the following three categories:

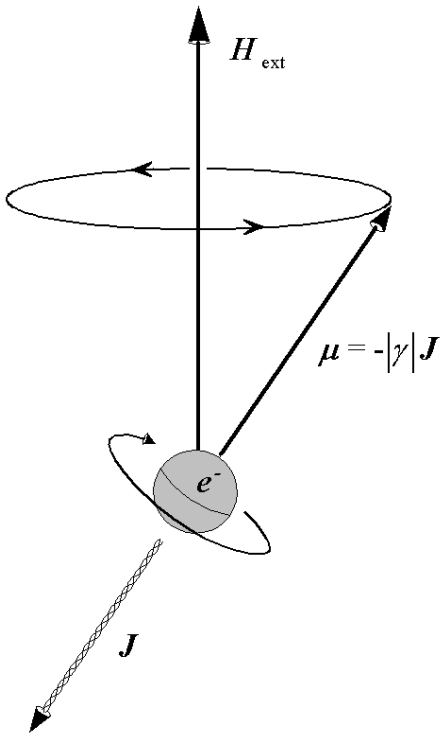

Figure. 2.4. Sketch of an electron's magnetic moment ($\boldsymbol{\mu}$) precessing about an externally applied static magnetic field ($\mathbf{H_{ext}}$).

(1) nuclear magnetic resonance (NMR), (2) electron paramagnetic resonance (EPR), and (3) ferromagnetic resonance (FMR). Nuclear magnetic resonance measurements are performed on the nuclear magnetic moments of diamagnetic materials, which have significantly smaller gyromagnetic ratios than electrons, and therefore usually involve radio frequencies in the kHz range. When these nuclear magnetic resonance measurements are used for medical diagnostics they are euphemistically referred to as Magnetic Resonance Imaging (MRI). EPR measurements are performed on the electron magnetic moments of paramagnetic materials and are frequently used for chemical composition analysis. As with EPR, FMR measurements are also performed on electron magnetic moments but in ferri/ferromagnetic samples in which exchange coupling between the magnetic moments is present. The exchange coupling leads to the samples achieving a net spin alignment at considerably smaller static fields than in EPR

experiments, and the resultant static dipole fields make the FMR resonance equations more complicated than for EPR. The exchange coupling also leads to the rich phenomena of spin waves. This section reviews FMR experiments and the next section addresses spin waves.

In a typical FMR measurement, a large static magnetic field ($\mathbf{H_{ext}}$) and a small amplitude linearly polarized microwave magnetic pump field ($\mathbf{h_p}$) are applied to a ferromagnetic sample of interest. The $\mathbf{H_{ext}}$ field is usually of significant strength to saturate all the domains in the material and along with the internal anisotropy fields set the static equilibrium direction of the magnetic moments. The microwave field, which is typically applied orthogonally to $\mathbf{H_{ext}}$, drives the precession of the magnetic moments about the static field at the frequency f_p. The measurement of the FMR response is usually performed in one of two ways: either (1) the magnitude of the static field H_{ext} is kept constant and the sample absorption is measured as a function of microwave pump frequency f_p, or (2) f_p is kept fixed and the sample absorption is measured as a function of H_{ext}. The second method, which will be referred to here as the field swept method, is typically used in order to avoid frequency dependent transmission line effects that complicate the analysis.

Figure 2.5 shows the relative orientation of the magnetization vector ($\mathbf{M}$), the total static effective magnetic field ($\mathbf{H_{eff}}$), and the microwave magnetic field ($\mathbf{h_p}$) for a typical FMR experiment. It also shows a sketch of a typical field swept FMR resonance profile of normalized absorbed microwave power versus static magnetic field strength. Here instead of a single magnetic moment and an external applied field as shown in Fig. 2.4, we have a net magnetization $\mathbf{M}$ vector that precesses about an effective static magnetic field. The net magnetization is the sum of individual magnetic moments $\boldsymbol{\mu}_i$ in the sample divided by the sample volume V, and may be written $\mathbf{M} = \sum_i \boldsymbol{\mu}_i / V$. The total effective field is the net internal static magnetic field acting on the magnetization

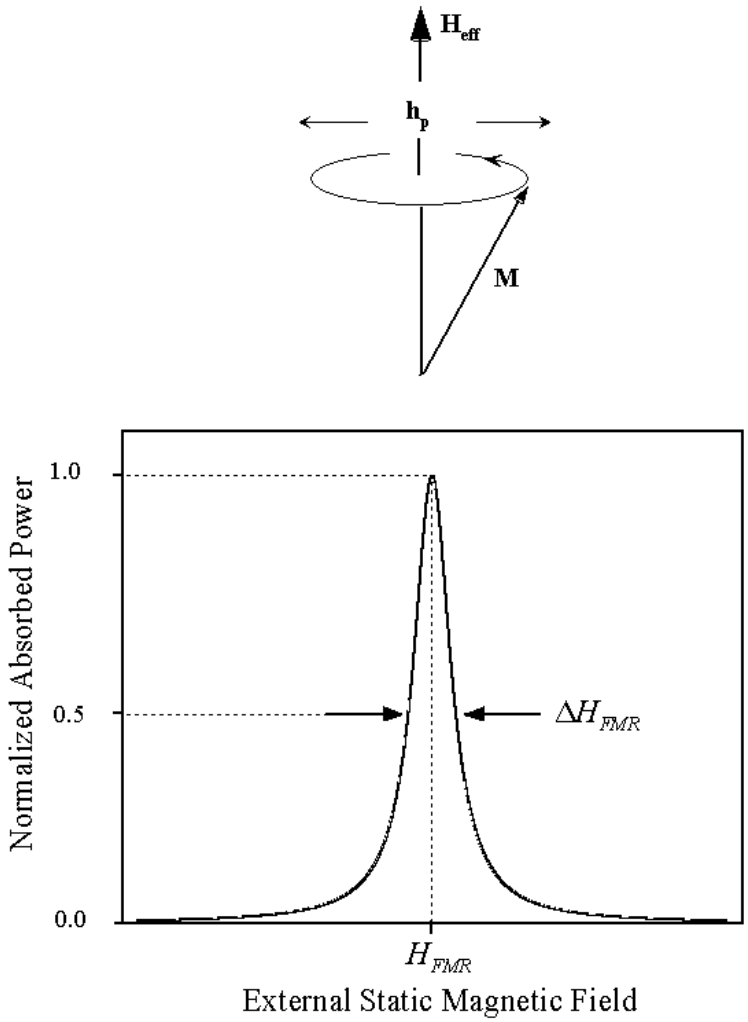

Figure. 2.5. Upper sketch shows the typical orientation of the effective static ($\mathbf{H_{eff}}$) and microwave magnetic ($\mathbf{h_p}$) fields used in an FMR experiment. Lower sketch shows a ferromagnetic resonance profile, of absorbed power versus applied external magnetic field.

vector, and is comprised of the external applied static magnetic field, and the internal demagnetizing and effective crystalline anisotropy magnetic fields.

The two key parameters that are obtained from a FMR resonance profile are the FMR resonance field (H_{FMR}) and linewidth (ΔH_{FMR}). The H_{FMR} field is the external field required to achieve maximum absorption and corresponds to the static field at which the natural resonance frequency of the precessing magnetization equals the applied

microwave field frequency. The ΔH_{FMR} parameter is the width of the resonance profile at half peak height and is directly related to the relaxation rate of the precessing magnetization vector. This linewidth not only has practical importance for device applications, it is also of fundamental importance as it depends upon the relaxation mechanisms that are present in the ferromagnetic material.

The FMR resonance field and linewidth depend on the microwave frequency used. For an operating frequency of 60 GHz, H_{FMR} and ΔH_{FMR} for highly polished single-crystal YIG samples and Ba M-type hexagonal ferrite samples are as follows. YIG has a FMR resonance field of about 20 kOe and has a FMR linewidth of about 0.5 Oe, whereas for Ba-M, $H_{FMR} \approx 2$ kOe and $\Delta H_{FMR} \approx 30$ Oe (Hurben [1996]; Wittenauer *et al*. [1993]). The large reduction in the resonance field for Ba-M compared to YIG is due to crystalline anisotropy and is the reason why hexagonal ferrites are so potentially useful for high frequency applications. The increased linewidth observed in Ba-M compared to YIG is what hinders the full device utilization of the material. As was mentioned previously, the determination of whether these large losses are due to extrinsic or intrinsic relaxation processes is a key goal of this work.

2.2.3 Uniform Mode and Spin Waves

The first FMR measurements were originally performed by Griffiths in the late 1940's (Griffiths [1946]). About two years later, an accepted theory that explained the measured FMR resonance fields and linewidths was developed by Kittel and Herring (Kittel [1947]; Herring and Kittel [1951]). Initially H_{FMR} was modeled with Eq. (2.8) by treating the splitting factor (g) as a fitting term. However, this methodology was quickly abandoned after it was shown that different g values were required to fit the different FMR resonance fields measured on different shaped samples made of the same material (Kittel [1947]).

In order to properly model the resonance field, Kittel along with Herring made the following two modifications to Eq. (2.7): (1) they included a more sophisticated form of the magnetic moment vector, in which $\boldsymbol{\mu}$ was replaced with the total magnetization vector $\mathbf{M}$, and (2) they replaced $\mathbf{H}_{ext}$ with an effective internal field $\mathbf{H}_{eff}$ which included the dipole-dipole and the exchange fields. They then proceeded to explain the measured FMR resonance linewidths via the so-called uniform mode spin wave scattering theory. They argued that in an FMR experiment certain modes, termed uniform modes, are excited by the microwave field and that the scattering of these uniform modes into other so-called spin wave modes was the key source of the observed FMR linewidths.

Kittel's spin wave theory, typically referred to as the "bulk spin wave theory," was based upon a modified view of Bloch's earlier work on spin waves (Kittel [1947]; Herring and Kittel [1951]). In Bloch's work, spin waves were treated quantum mechanically as a progressive variation of the relative phase of precessing dipoles in which the exchange energy is minimized (Bloch [1946]). In Kittel's work, spin waves were treated classically as spatial disturbances of *continuous magnetization* rather than as the discrete spin moments in the lattice. The classical theory assumes that the wave number of the spin waves is much larger than both the wave number of light at the same frequency and the reciprocal of the sample dimensions. Therefore, both electromagnetic and sample boundary effects were ignored.

Figure 2.6 shows illustrations of the uniform and spin wave modes. The uniform mode, which may be considered a spin wave with infinite wavelength, corresponds to all the spins throughout the sample precessing in phase. The two traveling waves shown in the figure correspond to spin waves traveling parallel and perpendicular to the static magnetic field direction. The direction of travel corresponds to the direction in which phase variation of the precessing dipole moments occurs.

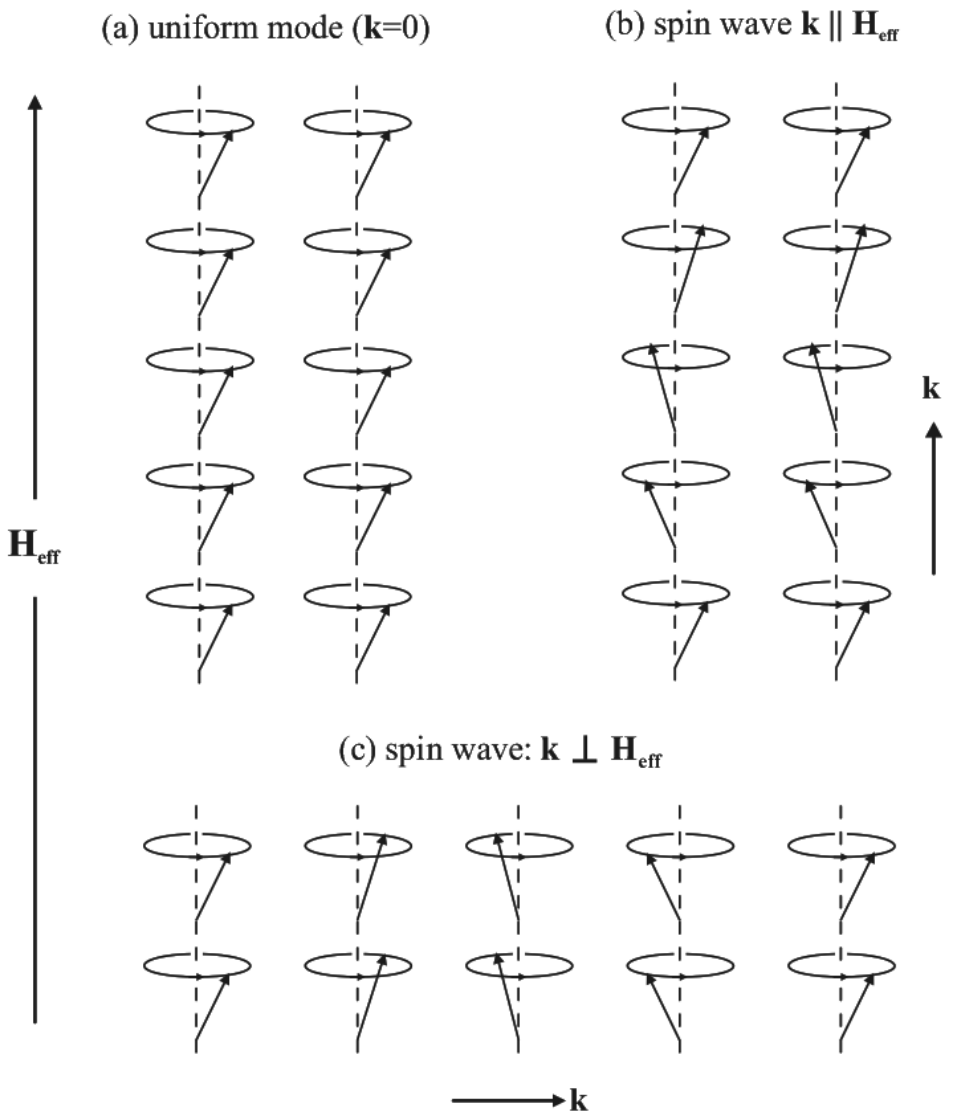

Figure. 2.6. Schematic illustrations of (a) the uniform mode, and spin waves propagating (b) parallel and (c) perpendicular to the effective static magnetic field direction after [Patton, 1975].

In Kittel's and Herring's theory, the total magnetization vector ($\mathbf{M}(\mathbf{r},t)$) is written in terms of a large static component, equal to the saturation magnetization (M_s) of the material, and a small dynamic component ($\mathbf{m}(\mathbf{r},t)$) as

$$\mathbf{M}(\mathbf{r},t) = M_s\,\hat{\mathbf{z}} + \mathbf{m}(\mathbf{r},t)\,. \tag{2.9}$$

Here $\hat{\mathbf{z}}$ is the unit vector in the z-direction which corresponds to the static equilibrium direction of the magnetization vector. The small dynamic magnetization term is then written as a Fourier series,

$$\mathbf{m}(\mathbf{r},t) = \mathbf{m}_{\mathbf{o}}(t) + \sum_{k\neq 0} \mathbf{m}_{\mathbf{k}}(t)\, e^{-i\mathbf{k}\cdot\mathbf{r}}, \tag{2.10}$$

where $\mathbf{m}_{\mathbf{o}}(t)$ and $\mathbf{m}_{\mathbf{k}}(t)$ are the harmonic time dependent amplitudes of the uniform mode and spin wave modes with a wave vector of 0 and $\mathbf{k}$ respectively. The $\mathbf{m}_{\mathbf{o}}(t)$ term, which describes the in-phase spatially uniform component of the dynamic response, is the main mode excited by the microwave field in an FMR experiment. The $\mathbf{m}_{\mathbf{k}}(t)$ modes, in contrast, describe the time dependent spatially distributed spin wave modes. As was mentioned previously, the scattering of the uniform mode into spin waves is one of the key relaxation mechanisms of the uniform mode and will be discussed in more detail in the next subsection.

The torque equation of motion used by Kittel to describe the dynamic response of the magnetic moments is typically written as

$$\frac{\partial \mathbf{M}(\mathbf{r},t)}{\partial t} = -\left|\gamma\right| \mathbf{M}(\mathbf{r},t) \times \mathbf{H}_{\mathbf{eff}}(\mathbf{r},t). \tag{2.11}$$

where

$$\mathbf{H}_{\mathbf{eff}} = \mathbf{H}_{\mathbf{ext}} + \mathbf{h}_{\mathbf{p}} + \mathbf{H}_{\mathbf{demag}} + \mathbf{H}_{\mathbf{dipole}} + \mathbf{H}_{\mathbf{A}}. \tag{2.12}$$

Here, the $\mathbf{H}_{\mathbf{ext}}$ and $h_p(t)$ terms are the externally applied static and microwave magnetic fields, respectively, and the H_{demag}, $\mathbf{H}_{\mathbf{dipole}}$, and H_A terms are the internal demagnetizing, dipole, and crystalline anisotropy magnetic fields (not included in

Kittel's initial theory), respectively. The analytic expressions of these fields will be given in the next chapter. Note that the internal fields depend upon $\mathbf{M}(\mathbf{r},t)$ and in turn lead to the torque equation being nonlinear in $m_o(t)$, $m_k(\mathbf{r},t)$, and $h_p(t)$. In Kittel's theory all nonlinear terms are discarded.

Equation (2.11) does not include any relaxation terms, and damping was initially treated in the linear theory by forcing the FMR and spin wave frequency terms to be complex. Thereafter, Kittel, Bloch, Bloombergen, Landau and Lifshitz, Gilbert, and others added different phenomenological damping terms to Eq. (2.11) in order to model different relaxation mechanisms. Some of these relaxation mechanisms will be discussed in the next section, and the various phenomenological damping expressions will be discussed in more detail in the following chapter.

Once the nonlinear terms in Eq. (2.11) are discarded, the equation is then separated into two linear first order differential equations, one in terms of $\mathbf{m_o}(t)$ and the other in terms of $\mathbf{m_k}(t)$. These equations are then solved separately for the uniform mode resonance frequency (ω_{FMR}) and spin wave dispersion relation $\omega_k(\mathbf{k})$. These expressions may be written for an isotropic thin film sample magnetized in-plane as

$$\omega_{FMR} = |\gamma| \sqrt{(H_{ext})(H_{ext} + 4\pi M_s)}, \tag{2.13}$$

and

$$\omega_k = |\gamma| \sqrt{\left(H_{ext} + Dk^2\right)\left(H_{ext} + Dk^2 + 4\pi M_s \sin^2\theta_k\right)}, \tag{2.14}$$

where D is the so-called exchange constant, which for YIG is equal to $5.4 \cdot 10^{-9}\,\mathrm{Oe}\cdot\mathrm{cm}^2/\mathrm{rad}^2$ (Kittel [1947]; Herring and Kittel [1951]), and θ_k is the polar angle, which describes the angle between the spin wave propagation direction and the z-

axis. See Fig. 2.7 for more details. The differences between the FMR resonance frequency expression given in Eq. (2.13) and the one given in Eq. (2.8) is due to the demagnetizing field which arises from the dipole field of bounded media. The remainder of this section will review the ω_{FMR} and $\omega_k(\mathbf{k})$ expressions in a qualitative manner. Detailed calculations are provided in Chapter 3 and can be found in several comprehensive books (Lax and Button [1962]; Sparks [1964]).

Figure 2.7 shows a sketch of the spin wave dispersion curves for an isotropic bulk sample. The upper and lower curves correspond to the spin wave dispersion curves for spin waves with spin wave polar propagation angles θ_k of 0° and 90°, respectively. The spin wave band, also referred to as the spin wave manifold, consists of the region between these curves. The circle shown on the frequency axis corresponds to the uniform mode resonant frequency. The relative positioning of ω_{FMR} within the band is dependent upon the static field orientation and sample geometry. For an isotropic thin film sample magnetized in-plane, ω_{FMR} lies at the top of the manifold. For a thin film magnetized out-of the film plane, ω_{FMR} lies at the bottom of the manifold, and for an isotropic spherically shaped sample, ω_{FMR} usually lies in between the lower and upper branches of the manifold. This relative positioning of the FMR resonance frequency within the spin wave manifold plays an important role in the scattering of the uniform mode into spin waves, and will be discussed in more detail in next section.

The basic features of the spin wave manifold shown in Fig. 2.7 can be qualitatively explained by energy considerations. The net energy of the magnetic moments is comprised of the Zeeman energies from the interaction of the (1) static magnetic field and the saturation magnetization, (2) dipole-dipole fields, (3) localized exchange, and (4) anisotropy fields. The static Zeeman energy ($\mathbf{M}\cdot\mathbf{H}_{\mathbf{ext}}$) causes the relative frequency position of the whole manifold to be dependent upon the applied static field. An increased static field shifts the whole spin wave manifold up in frequency.

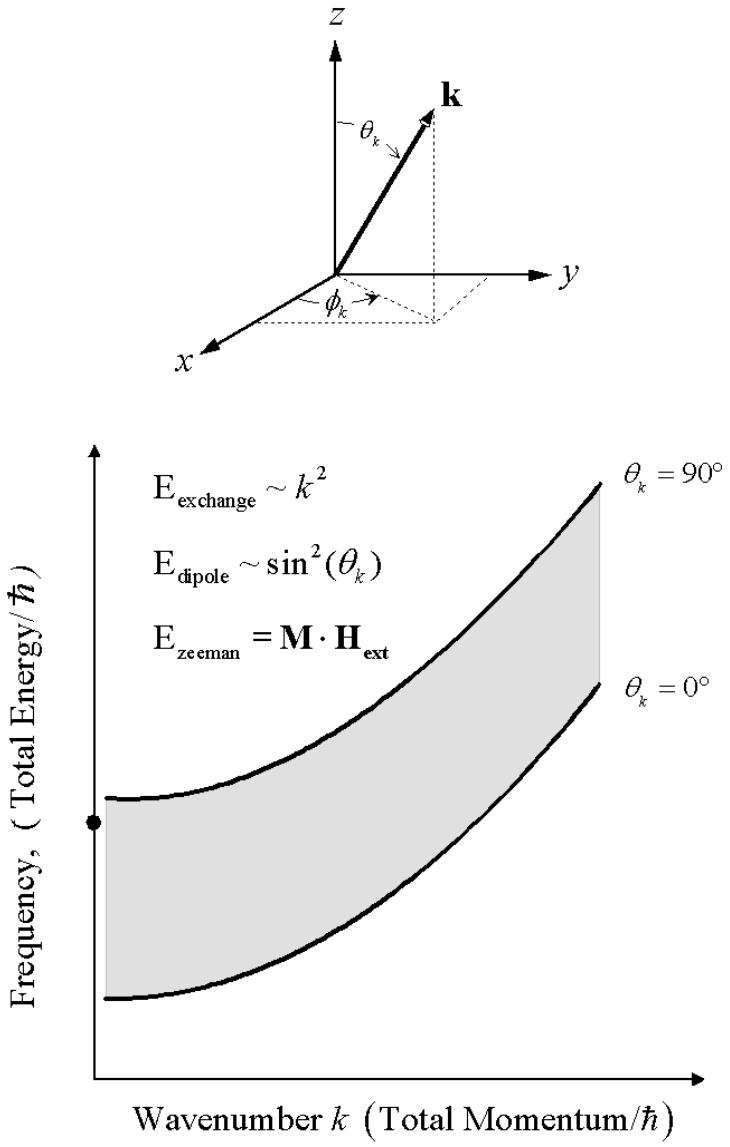

Figure. 2.7. Sketches of the spin wave polar coordinate system and isotropic dispersion manifold. The spin wave manifold is comprised of the region between the upper (θ_k = 90°) and lower (θ_k = 0°) bands. The solid circle corresponds to the uniform mode resonance frequency (ω_{FMR}). The diagram also depicts the energy contributions of the exchange, dipole-dipole, and Zeeman energies to the dispersion manifold.

The dipole-dipole interactions are the source of the spin wave energy dependence on the propagation direction of the spin waves. Spin waves that propagate parallel to the effective static field have no net dipole field and therefore have lower energy, whereas

the that propagate perpendicular to the effective static field experience a maximum "self" dipole field and have the highest energy. The exchange energy causes the spin wave frequency to be dependent upon the wave number. This energy is related to the cosine of the angular (δ) deviation of neighboring spins. The small angle approximation $\cos(\delta) \approx 1 - \frac{1}{2}\delta^2$ combined with the fact that the angular deviation of the neighboring spins is inversely proportional to the wavelength of the spin waves leads to the frequency dependence upon the square of the wave number.

It is important to keep in mind that the Kittel's theory ignores all spin wave interactions with the sample boundaries. The validity of this approximation depends on the sample size, the wavelength, and the relaxation rate of the spin waves. If one is considering a "large" sample, small wavelengths, and or "large" damping rates, then the spin wave interaction with sample boundaries can be ignored and the above theory is applicable. When these conditions are not satisfied, a spin wave theory, which takes the sample surfaces into account, must be used. For "long" wavelength spin wave modes in thin film ferromagnetic samples, the magnetostatic mode theory originally developed by Damon and Eshbach (Damon and Eshbach [1961]) is applicable. In this theory, the spin wave wavelength is considered long enough so that exchange interactions are ignored. For a discussion regarding extensions of this theory, in which exchange interactions are included see Kalinikos [1980]. Patton [1988]; and Hurben and Patton [1996]) also provide an excellent review of these theories. The single crystal Zn Y-type hexagonal ferrite samples used for this study were of large enough size and had significantly large enough relaxation rates that the bulk spin wave theory was considered applicable.

2.2.4 Relaxation

The microwave energy that is coupled to the uniform mode in a FMR experiment ultimately ends up in the lattice, and results in a net temperature rise of the sample (Sparks [1964]).

Figure 2.8 summarizes the transfer of energy from the uniform mode to the lattice. As in seen in the figure, this can occur via multiple relaxation processes that may or may not involve degenerate spin waves. These relaxation processes are typically categorized as either intrinsic or extrinsic processes (Sparks [1964]). The intrinsic relaxation processes are considered fundamental to the material and cannot be eliminated. The non-intrinsic processes are due to surface defects, impurities, and inhomogeneties, all of which usually involve degenerate spin wave modes, and in some instances may be significantly reduced by process changes such as improved sample polishing techniques, purer starting materials, better thermal annealing, etc.

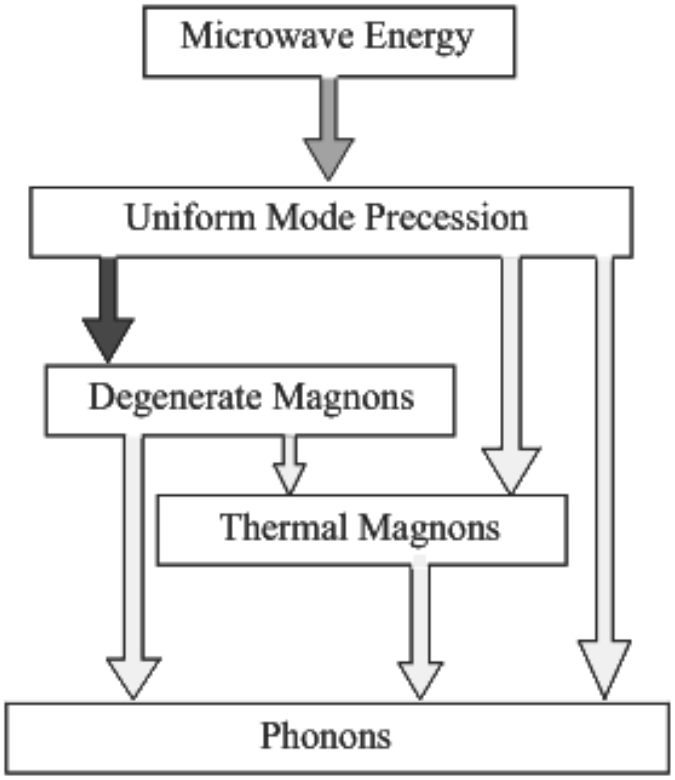

Figure. 2.8. Block diagram that depicts the possible ferromagnetic relaxation paths that are present in a ferrite material, after Sparks [1964]. The solid black arrow indicates the 2-magnon extrinsic relaxation.

Yttrium Iron Garnet (YIG), which in single crystal form has the lowest losses of all the ferrites, has been instrumental to the understanding of relaxation processes in ferrite materials. Many experiments have been performed in which various relaxation mechanisms have been selectively introduced to pure YIG. These experiments on YIG have been so useful in providing both physical understanding and experimental signatures of the various loss mechanisms that Kittel is known to have said that YIG is to ferromagnetic resonance research as what the fruit fly is to genetics research (Sparks [1964]). See Patton [1975]; Patton [1984]; Sparks [1964]; and Lax and Button [1962] for comprehensive reviews of the various relaxation mechanisms and experiments that have been studied in YIG and other ferrites.

One intrinsic loss mechanism that is pertinent to hexagonal ferrites is valence-exchange or charge transfer relaxation mechanism (Sparks [1964]). This process which corresponds to electron hopping between Fe^{2+} (ferrous) and Fe^{3+} (ferric) ions on equivalent crystal lattice sites can yield a significant contribution to the overall conductivity of the material. This electron hopping is typically eliminated by the substitution of Mn (Smit and Wijn [1959]); (Savage *et al*. [1965]). It should be noted that the material used in this study had such Mn substitution and, therefore, valence-exchange losses are not considered to be the major source of the large losses exhibited by the material.

One of the most significant non-intrinsic loss mechanisms is the so-called two-magnon scattering process. This relaxation process corresponds to a single uniform mode magnon ($\mathbf{k} = 0$) being scattered into a *single* ($\mathbf{k} \neq 0$) spin wave magnon of equivalent energy. Note that such a scattering process cannot conserve the wave vector (momentum). Therefore, there must be a "third" party that conserves the momentum. This "third" party is a sample defect (pit, grain boundary, etc.). The first experimental studies of the two-magnon scattering were performed on YIG samples with varying amounts of surface roughness in which it was clearly shown that the FMR linewidth

tracked the amount of surface polishing. As the quality of the surfaces increased, the linewidths decreased accordingly (LeCraw *et al*. [1958]). Such two-magnon losses are a major contributor to the overall losses in polycrystalline samples.

Relaxation is typically addressed in the classical linear uniform mode and spin wave theories by adding a phenomenological damping term to Eq. (2.11). The two most commonly used phenomenological damping terms are the Landau-Lifshitz (LL) (Landau and Lifshitz [1935]) and the Block-Bloembergen (BB) (Bloch [1946]; Bloembergen [1956]) damping terms. The LL form of the equation of motion conserves the magnetization vector and is often used to describe intrinsic relaxation processes (Hurben [1996]). The BB equation of motion does not conserve the magnetization vector (**M** decreases as it relaxes to static equilibrium position) and has been successful in describing 2-magnon (non-intrinsic) processes. In contrast, for the nonlinear spin wave instability analysis relaxation is typically modeled by forcing the FMR and spin wave frequencies to be complex. All three approaches will be discussed in detail in Chapter 3.

The majority of the previous experimental and theoretical research performed at the Colorado State University Magnetics Laboratory regarding the relaxation processes in hexagonal ferrites has involved angle dependent two-magnon (Hurben [1996]) and effective linewidth (McKinstry [1991]) loss analysis. Hurben's analysis suggests that two-magnon damping processes are present in hexagonal ferrites. The effective linewidth analyses show that there are also a significant amount of intrinsic losses present in these materials. One of the goals of this work is to perform nonlinear spin wave instability measurements on hexagonal ferrites in order to provide further evidence concerning the nature of these losses. The connection between the non-linear instability thresholds and the relaxation mechanisms that are present in a ferrite material is a key topic of the next section.

2.3 NONLINEAR SPIN WAVE PROCESSES

The previous section discussed linear dynamic magnetic processes, which occur in ferrites at low-microwave power levels. This section addresses nonlinear dynamic processes that occur at high-power levels. First, a high-power FMR response curve is given, and then the nonlinear instability processes that are responsible for the observed high-power FMR response are reviewed. This is followed by discussion of the critical microwave field amplitude (h_{crit}) required to excite nonlinear spin wave amplitude growth, and a typical butterfly curve plot of h_{crit} versus H_{ext} is also given. The section concludes with a brief review of the spin wave instability theory and previous nonlinear instability work. Detailed derivations of the threshold fields are provided in the next chapter.

2.3.1 High-Power FMR Measurements

The first high-power nonlinear FMR resonance measurements were performed by Damon [1953]; Bloembergen and Wang [1954]. Figure 2.9 shows similar high-power FMR data, measured as part of this work, which demonstrates the nonlinear effects. The data were obtained on the Zn Y-type hexagonal ferrite disc-shaped sample addressed previously in Fig. 2.2. The FMR data shown in Fig. 2.9 were obtained with the static and microwave magnetic fields applied orthogonally within the disk plane. The solid and open circles show the FMR response at low and high power levels, as indicated. At high power levels, two new effects are observed. One effect is the broadened and decreased peak height of the FMR resonance profile. This occurs at a much lower power level than what is expected from a nonlinear theory that only includes uniform mode terms, and is typically referred to as either "premature saturation" or "resonance saturation" (Schloemann [1959]). The second high-power effect is the substantial increase in sample absorption over a wide static field region below the FMR resonance

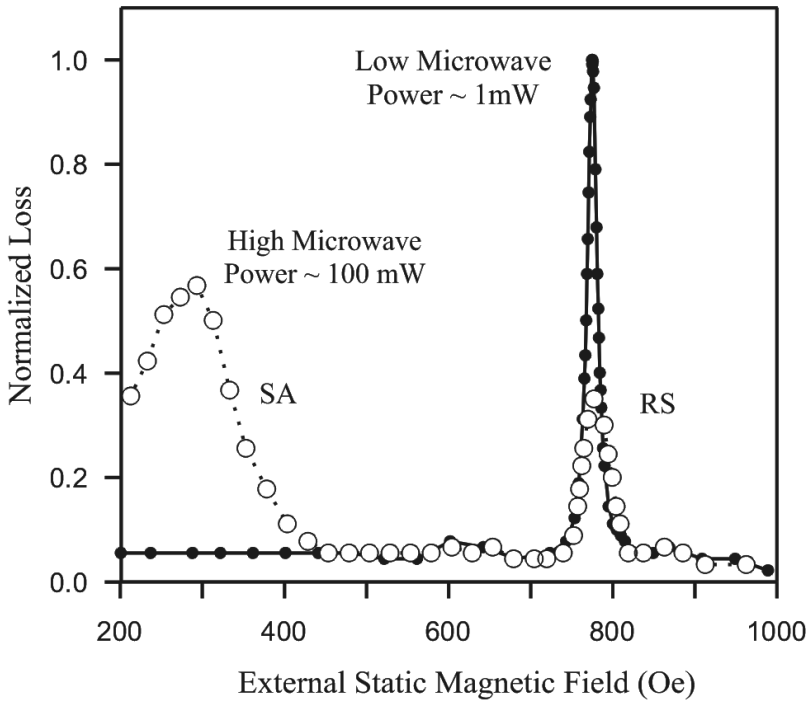

Figure. 2.9. FMR data obtained at low (solid circles) and high (open circles) microwave power levels as indicated. The data were obtained on an in-plane magnetized Mn substituted Zn Y-type easy plane disk at 9 GHz. The high-power effects observed at magnetic fields near the FMR resonance field are termed resonance saturation (RS) effects and those far below the FMR resonance are termed subsidiary absorption (SA).

field. This effect is typically referred to as "subsidiary absorption." A high-power microwave field that is applied orthogonally to the equilibrium saturation magnetization direction drives the above two effects. When a microwave field is applied parallel to the saturation magnetization direction, a third nonlinear effect called parallel pumping also occurs at high-power levels. The parallel pumping effect is similar to subsidiary absorption in that it also corresponds to an increased absorption region over a static field range that is below the FMR resonance field.

In most cases, the above nonlinear effects are detrimental to microwave ferrite device performance. For example, resonance saturation can lead to a significant widening in the frequency range of a bandpass filter, which is based upon a narrow FMR resonance linewidth of a ferrite material. The onset of parallel pumping and subsidiary absorption

nonlinear processes can lead to significant unwanted insertion losses of circulators, phase shifters, and isolators which are operated at static fields in the subsidiary absorption regions. There are a few cases, however, in which nonlinear instability processes can be useful for device operation. Two examples are high-power limiters and parametric amplifiers. A high-power limiter is used to protect down-line devices from excessively high microwave power levels. These devices usually involve ferrites that are biased in the subsidiary absorption regime. At low power levels, the sample losses and corresponding device insertion losses are low. Then once the incident power is increased above a certain threshold power level, the sample losses increase rapidly and in turn provide protection for down-line devices. Parametric amplifiers are based upon the fact that as microwave power is increased slightly above the threshold point, certain critical spin wave modes are excited at half the frequency of the applied pump field. These critical modes will be discussed in more detail in the next section. For more details on ferrite devices see (Adam *et al*. [1991]; Lax and Button [1962]; Schloemann [1959]; and Pucel [1957]).

2.3.2 Butterfly Curve Measurements

The onset of the nonlinear resonance saturation, subsidiary absorption, and parallel pumping processes occurs at specific threshold power levels. That is, for a given static magnetic field, the change from the low to high-power response takes place abruptly at a specific threshold microwave power level. For incident power levels below this threshold, the sample loss scales linearly with the incident power. Above the threshold, the response is highly nonlinear. The change in the sample loss at the threshold point can consist of either a sudden increase or a decrease in the absorbed power, depending upon the external static field setting and which process is being studied.

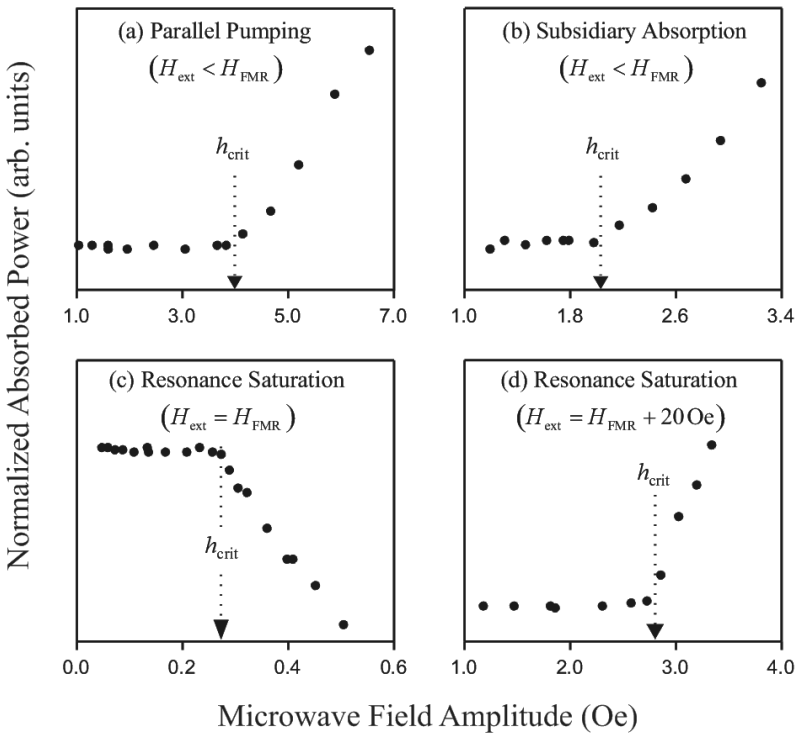

Figure. 2.10. Plots of normalized microwave absorption versus microwave field amplitude. The data were normalized to the microwave power that was incident on the sample and were obtained on an Mn substituted Zn Y-type hexagonal ferrite easy-plane disk at 9 GHz for the RS, SA, and PP pumping configurations. The arrows indicate the microwave threshold field, h_{crit}, required to excite nonlinear spin wave amplitude growth.

Figure 2.10 shows the experimental threshold field signatures of the various instability processes. Graphs (a) and (b) are parallel pumping and subsidiary absorption threshold data, respectively. The data were measured with H_{ext} set to significantly lower values than the FMR resonance field, H_{FMR}. Graphs (c) and (d) illustrate resonance saturation threshold data obtained with $H_{ext} = H_{FMR}$ and $H_{ext} = H_{FMR} + 20\,Oe$, respectively. The low-power FMR resonance linewidth of the sample was about 20 Oe. The estimated critical microwave threshold field amplitude (h_{crit}) is indicated in each graph. Graphs (a) and (b) show that in the subsidiary loss regime, the loss increases abruptly as the microwave field is increased above h_{crit}. Graphs (c) and (d) show that in the FMR regime, the loss can either increase or decrease abruptly as the microwave field

amplitude is increased above h_{crit} , depending on the setting of H_{ext}. Precisely at resonance, a decrease in the absorption is observed. For a static field slightly off resonance on the order of the linewidth or so an increase is observed. The dependence of h_{crit} upon H_{ext} , which is summarized by a so-called butterfly curve plot, is the topic of the next subsection.

The above nonlinear effects are due to the parametric excitation of spin waves. The microwave energy is coupled into the available spin wave modes indirectly either through the uniform mode or through the wobble in the z-component of the magnetization for parallel pumping. At low-power levels, the excited spin waves lose this energy through normal relaxation processes. Then as the microwave power is increased to high enough values, the spin waves suddenly become excited above thermal levels at a specific critical threshold power level. The transition from linear to nonlinear response corresponds to the point at which the amount of power coupled into the spin waves exactly matches the spin wave relaxation rate. The particular mode that is excited at the lowest power level is referred to as the critical mode. In the transverse pumping processes (resonance saturation and subsidiary absorption), the microwave field couples into the critical modes indirectly via the uniform mode, whereas in the parallel pumping process, the coupling occurs via the wobble in the z-component of the magnetization. For the resonance saturation process, the critical spin wave mode frequency (ω_{crit}) equals the microwave pump frequency (ω_p), whereas for the subsidiary absorption and parallel pumping process $\omega_{crit} = \omega_p / 2$.

Figure 2.11 summarizes the coupling methods and critical modes excited in the three instability processes. The wavy line in the figure represents a microwave photon, and the open and solid circles represent uniform mode and spin waves (magnons), respectively. For resonance saturation, two microwave photons excite two uniform mode ($k \approx 0$) magnons at ω_p . These uniform mode magnons then excite two oppositely directed spin wave magnons at $\omega_k = \omega_p$. For the subsidiary absorption and parallel

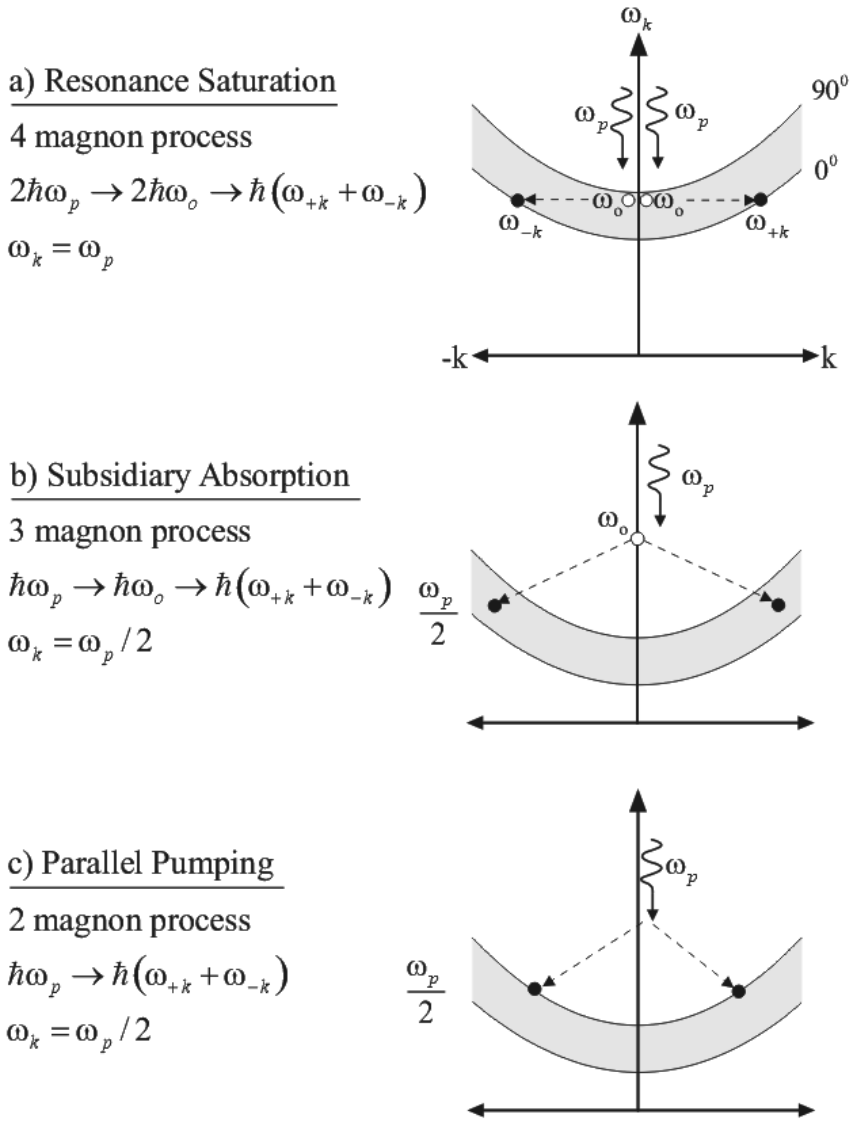

Figure. 2.11. Summary of the photon and magnon interactions which occur in the (a) resonance saturation, (b) subsidiary absorption, and (c) parallel pumping instability processes. The diagrams show schematic spin wave dispersion bands for an isotropic material. The open and solid circles indicate the uniform and spin wave mode magnons, respectively. The wavy arrows indicate the microwave photon.

pumping processes, one microwave photon creates two magnons at $\omega_k = \omega_p / 2$ with opposite k values. This occurs indirectly through a $k \approx 0$ magnon for the subsidiary absorption process and directly for the parallel pumping process. As can be seen in

Fig. 2.11, all three nonlinear instability scattering processes conserve both energy and momentum.

The wave number and propagation direction of the critical modes depends upon several factors such as the pumping configuration, operating frequency, sample geometry, anisotropy, static field setting, and the spin wave relaxation. The critical modes shown in Fig. 2.11 correspond to an isotropic bulk media in which the spin wave relaxation is independent of the wave vector. For this case, the polar propagation angle of the critical modes for resonance saturation, subsidiary absorption, and parallel pumping are $\theta_k = 0°$, $\theta_k \approx 45°$, and $\theta_k = 90°$, respectively. The details of how the critical modes are calculated will be discussed briefly in the next section of this chapter and in detail in Chapter 3.

In most cases the subsidiary absorption region occurs for static fields that are significantly lower than the FMR resonance field. However, under certain circumstances (at low frequencies and for highly anisotropy samples) ω_p and $\omega_p/2$ both lie within the manifold region for the same H_{ext}. When this condition is satisfied, it is referred to as coincidence and corresponds to a significant reduction in the threshold field. See (Suhl [1957]; Schloemann [1959]; and Spencer *et al*. [1958]) for details on coincidence measurements. For this work, the coincidence condition was not satisfied, and the subsidiary absorption and resonance saturation processes were excited in an independent fashion and thereby treated separately.

A butterfly curve summarizes the threshold field dependence on the static field for a fixed microwave frequency. It is determined by acquiring sample loss versus microwave field amplitude data (h_p), similar to the data shown Fig. 2.10, for multiple static fields (H_{ext}). Each loss versus h_p plot obtained at fixed H_{ext} and ω_p, is analyzed for its corresponding microwave threshold field h_{crit} value, and the butterfly curve is then obtained by plotting h_{crit} versus H_{ext}.

Figure 2.12 shows a parallel pumping butterfly curve plot of h_{crit} versus H_{ext}. The data were obtained at 8.93 GHz with the static and microwave field applied parallel to each other in the film plane of a YIG sample. The data were obtained as part of qualifying the high-power microwave spectrometer which was developed as part of this work and is discussed in detail in Chapter 4.

The lower sketches in Fig. 2.12 show the spin wave manifold for three different field settings as indicated in the figure. Note that for $H_{ext} < 940$ Oe the critical modes can have polar angle ranging from 90^{o} to 0^{o}. For $H_{ext} > 940$ Oe, the maximum possible spin wave polar angle decreases with increasing static magnetic field strength. For $H_{ext} = 1440$ Oe, only spin wave with $\theta_{\text{k}} = 0^{\text{o}}$ is available for coupling, and for $H_{ext} > 1440$ Oe, no spin waves are available for nonlinear excitation.

The elegant shape of the threshold field versus static field curve shown in Fig. 2.12 is similar to the shape of butterfly wings, hence the name "butterfly curve" coined by the early researchers to describe such plots. This terminology is now used to describe all h_{crit} versus H_{ext} plots regardless of their shapes. As has been mentioned previously, the butterfly curve delineates the linear from the nonlinear regimes for different static field values and a fixed microwave frequency. For microwave field amplitudes below the butterfly curve line, the sample losses scale linearly with the microwave field amplitude, but above the threshold field the response is highly nonlinear. Such a plot not only provides a direct summary of a given material's high-power handling capabilities, it is also useful for determining which spin wave modes are excited at the threshold field and the relaxation rates of those modes. The methods used to obtain the critical modes and their corresponding relaxation rates from the analysis of butterfly curve data is discussed in the next section.

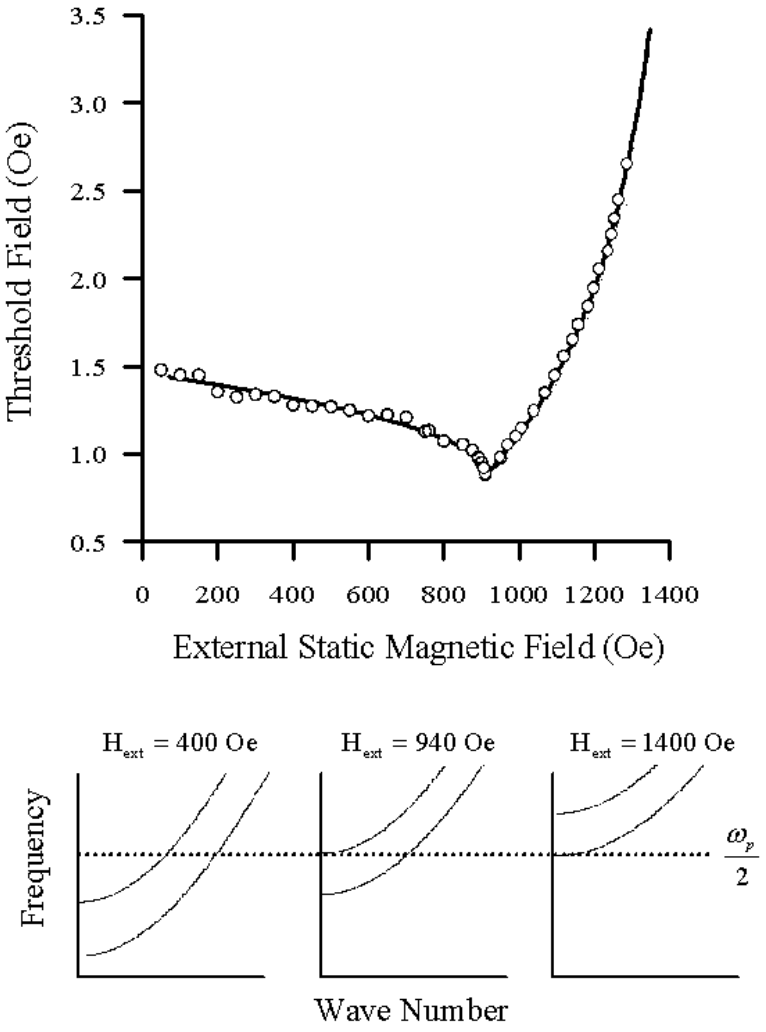

Figure. 2.12. Top plot show parallel pump butterfly curve data and fit, obtained on a YIG thick film at 8.93 GHz. The lower sketches show the relative position of the spin wave manifold for three different static fields as indicated. The horizontal dotted line corresponds to the frequency of the critical modes.

2.3.3 Spin Wave Instability Theory

The first successful theoretical treatment of the resonance saturation and subsidiary absorption instability processes was performed by Suhl [1957]. Approximately three years later Schloemann successfully predicted the parallel pumping instability process (Schloemann *et al*. [1960]). Schloemann along with Bady were also the first researchers to extend Suhl's original theory to include anisotropy (Schloemann *et al*. [1963]). This

section provides a brief introduction to Suhl's and Scloemann's spin wave instability theories. The nonlinear torque equation of motion and the resulting expression for the dynamic spin wave magnetization is discussed. Then the coupling coefficient $G_k(h_p)$ and spin wave linewidth ΔH_k concepts are introduced, and an expression for h_{crit} is given. This is followed by a review of how the h_{crit} and ΔH_k expressions are used to calculate a butterfly curve and in turn determine the critical modes and the relaxation rate of these modes. The focus will primarily be on parallel pumping processes in isotropic media. Detailed derivations are provided in Chapter 3.

As was the case for the linear uniform mode and spin wave theories, the nonlinear spin wave theory is also based upon the torque equation of motion. This equation, which is given in Eq. (2.11), is expanded to various orders of nonlinearity depending upon the instability process that is of interest (parallel pumping, subsidiary absorption, or resonance saturation). After expanding the torque equation to the appropriate order of nonlinear terms, a perturbative approach is used to solve the nonlinear differential equations. First, a solution to the linearized equation of motion is obtained, and then the nonlinear terms are treated as a small perturbation on the linear response. This is a reasonable approach because the theory is only interested in modeling the transition point from the linear to nonlinear and not the response above it.

The details of the methods used to choose the appropriate order of nonlinearity and the analytic approach used to solve the reduced nonlinear equations is given in Chapter 3. The remainder of this section will review the expressions obtained by Schloemann for the parallel pumping instability process in isotropic samples (Schloemann *et al*. [1960]), and provide example butterfly curve analysis.

2.3.4 Parallel Pumping in Isotropic Samples

As was mentioned previously, Schloemann was the first to solve the nonlinear torque equation of motion for the parallel pumping process. Schloemman's expression for the

threshold field required to excite nonlinear spin wave amplitude growth for the parallel pumping instability process may be written as

$$h_{crit} = \left(\frac{\omega_p}{|\gamma| 4\pi M_s \sin^2 \theta_k} \right) \Delta H_k \Big|_{\mathrm{k=k_{crit}}} , \qquad (2.15)$$

where θ_k is the polar angle that describes the spin wave propagation direction and ΔH_k is the so-called spin wave linewidth. It is important to note that ΔH_k is *not* an actual measured resonance linewidth; rather it is the relaxation rate, η_k, of the critical spin wave modes expressed in magnetic field units in order to provide a quick comparison to measured FMR linewidths. For the parallel pumping in an isotropic sphere-shaped sample, $\Delta H_k = 2\eta_k / |\gamma|$. The $\mathrm{k = k_{crit}}$ term at the end of the equation signifies that the critical mode is the spin wave mode that minimizes the h_{crit} expression in Eq. (2.15).

The h_{crit} expression given in Eq. (2.15) is used in combination with the measured butterfly curve and the spin wave dispersion relation to determine the critical modes and the corresponding spin wave linewidths of these modes. The procedure is as follows. The threshold field is calculated by minimizing the h_{crit} expression for a specific H_{ext} field value. The minimization is carried out over all the available spin wave states in which $\omega_k = \omega_p / 2$. The range of such states is defined through the spin wave dispersion relation $\omega_k(\mathrm{k})$, discussed in the previous section, and given in Eq. (2.14). The above procedure is repeated for each of the H_{ext} field values of interest, and the calculated butterfly curve is then matched to the measured data by adjusting ΔH_k. Initially a constant ΔH_k value is used, and then in order to better fit the butterfly curve wave vector dependent terms are incorporated to the ΔH_k expression as needed. These added terms can effect which spin waves are the critical modes, so the minimization procedure is repeated each time ΔH_k is changed. This iterative process is repeated until good agreement is obtained between the calculated and measured butterfly curves.

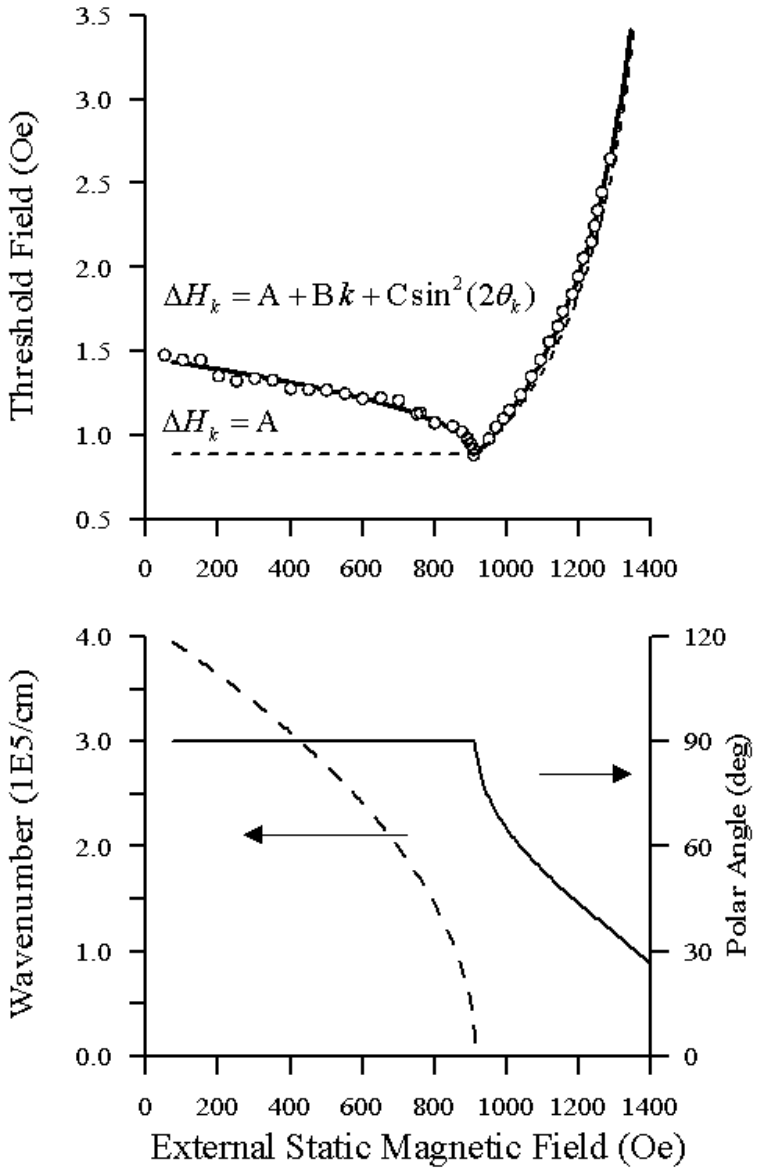

Figure. 2.13. Top plot show parallel pump butterfly curve data and calculated threshold. The data (open circles) were obtained on YIG thick film at 8.93 GHz. The lower plot summarizes the critical mode wave number and polar angle dependence upon static field for both spin wave linewidths.

Figure 2.13 summarizes numerical parallel pumping butterfly curve calculations, which were obtained from Eq. (2.15). The upper plot in Fig. 2.13 shows the calculated h_{crit} versus H_{ext} results along with the measured parallel pumping butterfly curve data that were originally shown in Fig. 2.12. The dashed line was obtained with

$$\Delta H_k = 0.49 \text{ Oe} \tag{2.16}$$

and the solid line was obtained with a spin wave linewidth equal to

$$\Delta H_k = 0.49 \text{ Oe} + 7.7 \text{ x} 10^7 k + 0.03 \sin^2(2\theta_k) . \tag{2.17}$$

The lower plot in Fig. 2.13 shows the critical mode wave number and polar angle dependence upon the static magnetic field. The same exact critical modes were obtained for both spin wave linewidth expressions. For $H_{ext} < 940$ Oe, the polar angle of the critical mode equals 90 degrees, and the wave number decreases with increasing fields. For $H_{ext} > 940$ Oe, spin waves with polar angles of 90 degrees are no longer available and the critical modes correspond to the maximum allowed polar angle that is available at the given field of interest. This corresponds to spin waves with a wave number of zero.

Figure 2.14 shows a sketch of the locations of the parallel pump critical modes within the spin wave manifold. The thick solid line represents the location of the critical modes within the manifold for different static field values. It should be realized that the spin wave manifold shifts up in frequency with increasing static field values as shown in the lower plots of Fig. 2.12, this shift is not shown in the sketch in Fig. 2.14. Such sketches will be shown in both the theory and the results chapters as they provide a quick summary of the critical mode location within the manifold.

The theory is successful in not only fitting the actual butterfly curve data but also in correctly predicting which spin wave modes are excited at the threshold field. The critical mode predictions have been verified with Brillouin Light Scattering (BLS) measurement techniques. For detailed discussion of the BLS measurement technique see Wilber *et al*. [1984]; and Sandercock and Wettling [1979]. Such BLS measurements of critical modes in isotropic materials have been performed for parallel pump instability

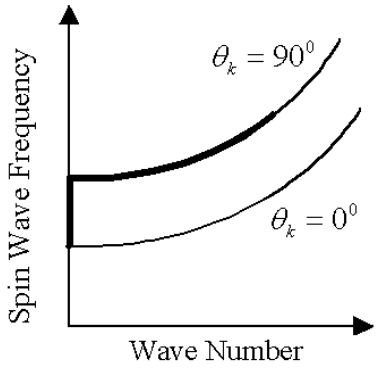

Figure. 2.14. Sketch of the critical mode location within the spin wave manifold for the PP butterfly curve shown in Fig. 2.13. Note that while the manifold is shown as stationary, it actually moves up with increasing static field as shown in Fig. 3.12.

processes (Wilber *et al*. [1984]; Kabos *et al*. [1997]), subsidiary absorption processes (Wiese *et al*. [1995]), and resonance saturation (Kabos *et al*. [1996]). In the majority of the cases, excellent agreement is obtained between the predicted and measured critical modes. Such measurements have yet to be performed in detail on hexagonal ferrites.

2.3.5 Previous Spin Wave Linewidth Analyses

As was discussed above, nonlinear instability measurements and butterfly curve analysis provides a means, albeit indirect, of obtaining the relaxation rate dependence on wave number for certain specific spin wave modes. Therefore, a combined FMR and spin wave instability study can yield a considerable amount of information regarding the fundamental relaxation mechanisms that are present in a given material.

The majority of the previous spin wave linewidth ΔH_k studies have focused on isotropic or weakly anisotropic materials. As may be expected the material of choice has been YIG. The ΔH_k dependences upon surface roughness, sample geometry, operating frequency, temperature, impurity content, weak cubic crystalline anisotropy fields, grain size, porosity, and small static field limits in which the sample is only partially magnetized have all been studied.

For a comprehensive review of the previous spin wave linewidth work see (Patton [1975]; Patton [1988]; Chen and Patton [1994]; Lax and Button [1962]; and Sparks [1964]). Recently, it has been determined that parallel pumping and subsidiary absorption measurements performed above the threshold field in single-crystal YIG are an excellent method of studying chaotic systems. For a good review of these chaos studies see Wigen [1994].

In summary, butterfly curve measurements and analyses have been studied extensively for parallel pumping and subsidiary absorption, but most of this work has been for isotropic polycrystalline ferrites or cubic single crystal materials with low anisotropy. For resonance saturation, the focus has also been on low anisotropy materials and only on the threshold response precisely at the FMR peak. The findings show that the spin wave linewidth is a good indication of the intrinsic relaxation rates of a given sample. Until now, comparatively little work has been performed on hexagonal ferrites.

CHAPTER 3

SPIN WAVE INSTABILITY THEORY

This chapter reviews the classical spin wave instability theory originally developed by Suhl and Schloemann and discusses the extensions that were made to it as part of this work. It will be shown that when the original theory is extended to include shape and crystalline anisotropy, the uniform mode anti-Larmor processional term can no longer be neglected. Also, in several previous publications in which damping was modeled by forcing the uniform mode frequency to be complex, the wrong sign was utilized for the complex anti-Larmor damping term. This chapter will show that while it is appropriate for the complex damping term to be added to the Larmor processional frequency, it should be subtracted from the anti-Larmor processional frequency.

The chapter is organized in the following manner:

1. In the first section, a general overview of the instability theory originally developed by Suhl and Schloemann is given. The key assumptions and basic procedures are reviewed.
2. In the second section, the complex phasor variables, effective magnetic field expressions, and the reduced equation of motion are introduced.
3. In section three, the linear uniform mode solutions to the reduced equation of motion are obtained, and the significance of the sign choice used to model the anti-Larmor damping term is discussed. This section also provides comparative

results obtained from Landau-Lifshitz and Bloch-Bloembergen equations of motion.

4. Section four addresses the linear spin wave theory. The spin wave dispersion relationship and the so-called spin wave manifold are reviewed, and the effects that anisotropy has on them are discussed.
5. Section five addresses the nonlinear spin wave theory. Steady state solutions of the nonlinear equations are obtained and the analytical threshold field equations for parallel pumping, subsidiary absorption, and resonance saturation processes are derived.
6. In the sixth section, example numerical threshold field results for specific limiting cases are given, and the effects of modeling with a negative versus a positive complex anti-Larmor damping term are reviewed. It will be shown that for the majority of the past publications, which focused on first order instability processes, modeling with the incorrect damping sign had a negligible effect. However, the sign of the anti-Larmor damping term does play a significant role for second order instability calculations in the limit of highly anisotropic media. This is a key case of interest for this study.

3.1 GENERAL OVERVIEW

The classical nonlinear spin wave instability theory was originally developed by Suhl [1957] to describe the resonance saturation and subsidiary absorption effects observed by Bloembergen and Wang [1954] and Damon [1951]. Then in the mid 1960's, Schloemann [1960] extended Suhl's initial work to include parallel pumping, and in so doing predicted the parallel pumping spin wave instability process prior to its first experimental observation in ferrites.

Since its inception, the classical nonlinear spin wave instability theory has been highly successful in describing the instability processes in bulk microwave magnetic

materials. According to the theory, the instability effects are the result of two competing processes: damping and parametric excitation. At low microwave power levels, an insignificant amount of power is coupled into spin waves and their amplitudes stay at thermal equilibrium levels. Then as the microwave power is increased, a critical power level is eventually reached at which certain spin waves, termed critical modes, are parametrically excited above their thermal levels. The microwave field parametrically excites these critical modes either via the oscillating z-component of the magnetization vector for parallel pumping, or via the uniform mode for the subsidiary absorption and resonance saturation instability processes. (See Chapter 2 for an overview of the parallel pumping, subsidiary absorption, and resonance saturation instability processes.) The end result of the theoretical calculations are: (1) analytic expressions for the threshold field required to excite nonlinear spin wave amplitude growth, (2) a determination of which spin waves are excited at the threshold point, and (3) the calculated relaxation rate of those spin waves.

In the course of this work, two main extensions were made to the classical spin wave instability theory. A generalized microwave field expression was utilized, and the resonance saturation instability calculations included static magnetic fields not only at the FMR resonance field but off it as well. Past calculations dealing with anisotropic samples utilized a microwave field that was oriented along a single principal axis, and the second order theoretical calculations focused only on the threshold response at the FMR peak (Schloemann *et al*. [1963]). The extensions that were made to the theory will be discussed in more detail shortly.

The remainder of this section will review the coordinate system that is utilized for the analysis presented here. The next sections then summarize the key assumptions that are made in the theory and provide a roadmap of the calculation procedure.

Figure 3.1 shows the Cartesian coordinate system which is used throughout this chapter to describe (a) the magnetization vector and the sample geometry, and (b) the

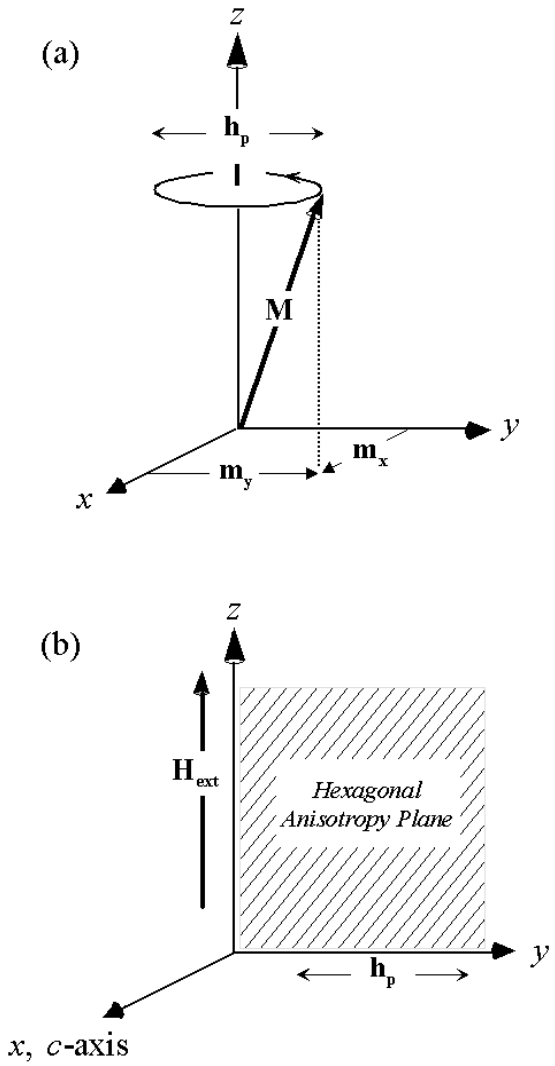

Figure. 3.1. Rectangular coordinate system that describes: (a) the precessional motion of the magnetization vector **M**(**r**,t) about the static equilibrium *z*-direction and (b) the orientation of the external static ($\mathbf{H_{ext}}$) and microwave ($\mathbf{h_p}$) magnetic fields relative to the hexagonal anisotropy plane. In the theoretical treatment given here, the *z*-axis corresponds to the applied $\mathbf{H_{ext}}$ direction, and a generalized microwave field expression is utilized.

relative orientation of the applied magnetic fields and hexagonal *c*-axis. The sample is assumed to be ellipsoidal-shaped with principal axes along the coordinate axes. The *x*-axis corresponds to the crystalline *c*-axis of the hexagonal samples. It is the easy and hard directions for samples with uniaxial and easy-plane anisotropy, respectively.

Therefore, the *y*-*z* plane corresponds to the hard and the easy anisotropy planes for samples with uniaxial and planar anisotropy, respectively. The *y*-axis corresponds to the applied microwave field ($\mathbf{h_p}$) direction for the perpendicular pumping configuration, which is shown in the figure. For the theoretical development performed here, a general microwave magnetic field expression will be utilized. The *z*-axis is the direction of applied static field ($\mathbf{H_{ext}}$) and corresponds to the static equilibrium direction of the magnetization vector ($\mathbf{M}$). The sample and coordinate orientation used here was chosen to provide ease of comparison between the extended theory developed as part of this work and Schloemann's earlier work (Schloemann *et al*. [1963]).

3.1.1 Key Assumptions

There are five key assumptions that are made in the spin wave instability theory. These assumptions, all of which concern the magnetization vector $\mathbf{M}(\mathbf{r},t)$ are as follows:

(1) The static magnetization is assumed to be aligned along the z-axis such that in the absence of microwave driving field $\mathbf{M}(\mathbf{r},t) = M_s\,\hat{\mathbf{z}}$. This is a valid assumption as the exchange coupling in ferrites cause the magnetic moments to be aligned within domains, and the externally applied magnetic fields used here are of sufficient strength to align the domains in a single direction. The field required to obtain alignment is determined theoretically from demagnetizing and anisotropy field calculations (Osborn [1945]) and verified experimentally via vibrating sample magnetometry (VSM) measurements.

(2) The dynamic components of the magnetization vector are assumed to be much smaller than M_s**.** This assumption corresponds to $M_s >> \left| m_{x,y} \right| >> \left| m_z \right|$. In the linear theory, the dynamic $m_x(\mathbf{r},t)$ and $m_y(\mathbf{r},t)$ components are kept to linear order and the dynamic *z*-component is discarded. In the nonlinear theory, the dynamic $m_x(\mathbf{r},t)$ and $m_y(\mathbf{r},t)$ components are kept to second order and $m_z(\mathbf{r},t)$

is written as a truncated Taylor series in terms of the x and y dynamic components. The Taylor series expansion and higher order truncation are appropriate for the instability calculations since the analysis focuses on modeling the initial onset of the nonlinear response. When dealing with highly nonlinear excitations, which occur for microwave field amplitudes above the threshold point, higher order terms that are not considered here should be included.

(3) The sample is assumed to have infinite dimensions. This assumption significantly simplifies the analysis because the dynamic magnetization response at the sample boundaries is ignored. Instead, periodic boundary conditions are utilized, and the dynamic components of $\mathbf{M}(\mathbf{r},t)$ are expanded as a spatial Fourier series. The validity of the infinite sample size assumption depends upon the wavelength (λ_k) of the spin waves, the sample size, and the magnitude of the spin wave damping. The assumption is usually valid for most polycrystalline isotropic and highly anisotropic single-crystal samples because of the large damping rates that are typically present. For samples where edge effects cannot be ignored, either the "magnetostatic mode" or "dipole exchange mode" theories must be used. See Kalinikos [1980], Patton [1988] and Hurben and Patton [1996] for a discussion of these theories.

(**4) The microwave field is assumed to be uniform throughout the sample, directly exciting the uniform mode response and parametrically exciting the spin waves.** This assumption corresponds to the microwave field exciting the uniform mode term at low power. Therefore, $\mathbf{h}_p$ is only associated with the uniform mode equations not those pertaining to the spin wave modes. Then at high-power levels; the microwave field is assumed to indirectly excite certain spin wave modes either through the uniform mode response for resonance saturation and subsidiary absorption processes, or through the variation in the z-component of the spin waves for the parallel pumping process. The uniform microwave field

assumption is valid as long as the sample size is relatively small compared to the wavelength of the microwave field. This is the case for the samples studied here.

(5) Electromagnetic propagation is assumed to be negligible. This final assumption is often referred to as the "magnetostatic approximation" and corresponds to the velocity of spin waves being significantly smaller than the velocity of electromagnetic waves in the medium. This assumption greatly simplifies the analytic calculation of the spin wave magnetic dipole fields derived from Maxwell's equations. The validity of assumption (5) depends upon the conductivity of the material of interest. For non-metallic samples, which is the case of interest for this work, the spin wave group velocity ($\partial\omega_k/\partial k$) is far from the "light line" and the assumption is quite valid. For a discussion of electromagnetic propagation effects see Patton [1976].

The above assumptions and the corresponding mathematical analysis presented in the following sections are validated in part by how well the theoretical butterfly curves match the measured response, and also by the good agreement observed between the theoretical predicted critical modes and the measured spin wave vector and frequencies obtained by Brillion Light Scattering (BLS) measurements. See [Wilber *et. al.*, 1984] for a discussion of these measurements.

3.2 EQUATION OF MOTION

In Suhl's and Schloemann's formalism, the dynamic response of the magnetization vector is modeled with the torque equation. This equation, which was derived in Chapter 2 for a single dipole moment, may be written for a bulk sample as

$$\frac{\partial \mathbf{M}(\mathbf{r},t)}{\partial t} = -|\gamma|\mathbf{M}(\mathbf{r},t)\times\mathbf{H}_{\text{eff}}(\mathbf{r},t)\,. \tag{3.1}$$

Here $\mathbf{M}(\mathbf{r},t)$ is the magnetization vector, and corresponds to the sum of the dipole moments in the sample per unit volume, γ is the gyromagnetic ratio, and $\mathbf{H}_{\text{eff}}(\mathbf{r},t)$ is the total effective magnetic field present in the sample. The magnetization vector may be written as

$$\mathbf{M}(\mathbf{r},t) = M_s \hat{\mathbf{z}} + \mathbf{m}(\mathbf{r},t) \tag{3.2}$$

where M_s is the static saturation magnetization and $\mathbf{m}(\mathbf{r},t)$ is the dynamic response. It is worth noting that the internal magnetic fields depend upon $\mathbf{M}(\mathbf{r},t)$, and thus cause the torque equation to be nonlinear in terms of $\mathbf{m}(\mathbf{r},t)$.

Equation (3.1) can be rewritten in terms of rectangular coordinates as three first order coupled nonlinear differential equations in the following manner

$$\begin{aligned}
\dot{m}_x(\mathbf{r},t) &= -|\gamma|\left[m_y(\mathbf{r},t) H_{\text{eff}}{}^{z}(\mathbf{r},t) - M_z(\mathbf{r},t) H_{\text{eff}}{}^{y}(\mathbf{r},t) \right], \\
\dot{m}_y(\mathbf{r},t) &= -|\gamma|\left[M_z(\mathbf{r},t) H_{eff}{}^{x}(\mathbf{r},t) - m_x(\mathbf{r},t) H_{eff}{}^{z}(\mathbf{r},t) \right], \\
&\text{and} \\
\dot{m}_z(\mathbf{r},t) &= -|\gamma|\left[m_x(\mathbf{r},t) H_{eff}{}^{y}(\mathbf{r},t) - m_y(\mathbf{r},t) H_{eff}{}^{x}(\mathbf{r},t) \right].
\end{aligned} \tag{3.3}$$

Here

$$M_z(\mathbf{r},t) = M_s + m_z(\mathbf{r},t), \tag{3.4}$$

where $m_z(\mathbf{r},t)$ is a very small dynamic component that can be expressed in terms of the dynamic $m_x(\mathbf{r},t)$ and $m_y(\mathbf{r},t)$ components. This is done by requiring that $|\mathbf{M}(\mathbf{r},t)| = M_s$ and solving for $m_z(\mathbf{r},t)$. As was discussed above (assumption #2) this solution is then expressed as a truncated Taylor series, which maybe written as

$$m_z(\mathbf{r},t) \sim -\frac{m_x{}^2(\mathbf{r},t)+m_y{}^2(\mathbf{r},t)}{2M_s} \quad . \tag{3.5}$$

Therefore, the $\dot{m}_z(\mathbf{r},t)$ deferential equation given in Eq. (3.3) is redundant, and the equation of motion can be completely described (to second order) by the first two coupled differential equations for $\dot{m}_x(\mathbf{r},t)$ and $\dot{m}_y(\mathbf{r},t)$, and the $m_z(\mathbf{r},t)$ expression given in Eq. (3.5).

As was stated in assumption #3, periodic boundary conditions are applied to the dynamic magnetization vector $\mathbf{m}(\mathbf{r},t)$ and it can be written as a Fourier series in the following manner

$$\mathbf{m}(\mathbf{r},t) = \mathbf{m}_{\mathrm{o}}(t) + \sum_{k\neq 0} \mathbf{m}_k(t) e^{i\mathbf{k}\cdot\mathbf{r}} \; . \tag{3.6}$$

Here $\mathbf{m}_{\mathrm{o}}(t)$ is the uniform mode response and $\mathbf{m}_k(t)$ is the spin wave mode amplitude with wave vector $\mathbf{k}$. The relative magnitude of the saturation magnetization, uniform mode, and spin wave amplitude is $M_s >> \left|\mathbf{m}_{\mathrm{o}}(t)\right| >> \left|\mathbf{m}_{\mathrm{k}}(\mathbf{r},t)\right|$. Requiring the magnetization vector to be real, i.e., that $\mathbf{M}(\mathbf{r},t) = \mathbf{M}(\mathbf{r},t)^*$, results in the following criteria for the uniform mode and spin wave amplitude terms

$$\begin{aligned} &\mathbf{m}_{\mathrm{o}}(t) = \mathbf{m}_{\mathrm{o}}{}^*(t) \;\text{ and} \\ &\mathbf{m}_k(t) = \mathbf{m}_{-k}{}^*(t) \, . \end{aligned} \tag{3.7}$$

Furthermore, these modes are orthogonal such that

$$\frac{1}{V}\int d^3r \, \mathrm{e}^{[i(\mathbf{k}-\mathbf{k}')\cdot\mathbf{r}]} = \delta_{\mathrm{k,k}'} \tag{3.8}$$

where V is the sample volume, and $\delta_{k,k'}$ is the Kronecker delta function. Equations (3.7) and (3.8) are used to simplify the nonlinear spin wave equation of motion, and will be discussed in more detail shortly.

In order to simplify the math and make the analysis more intuitive, Suhl and Schloemann rewrite the uniform mode and spin wave amplitude in terms of dimensionless complex phasor variables $\alpha_o(t)$ and $\alpha_k(t)$. These phasor variables, are given as

$$\alpha_o(t) = \frac{m_{ox}(t) + \mathrm{i}\, m_{oy}(t)}{M_s}$$

and (3.9)

$$\alpha_k(t) = \frac{m_{kx}(t) + \mathrm{i}\, m_{ky}(t)}{M_s}.$$

The requirement on the dynamic components given in Eq. (3.7) results in a third expression

$$\alpha_{-k}{}^{*}(t) = \frac{m_{kx}(t) - \mathrm{i}\, m_{ky}(t)}{M_s} \quad . \tag{3.10}$$

The utilization of these three expressions allows for the rotational response of the dynamic components to be clearly identified, and the two coupled nonlinear differential equations given in Eq. (3.3) to be expressed as a single differential equation. To do this the $m_x(\mathbf{r},t)$ and $m_y(\mathbf{r},t)$ terms are rewritten in terms of the $\alpha_o(t)$ and $\alpha_k(t)$ in the following manner

$$m_x(\mathbf{r},t) = \frac{M_s}{2}\left[\alpha_o + \alpha_o^* + \sum_{k\neq 0}\left\{\left(\alpha_k + \alpha_{-k}^*\right)e^{i\mathbf{k}\cdot\mathbf{r}}\right\}\right]$$

and (3.11)

$$m_y(\mathbf{r},t) = \frac{M_s}{2\mathrm{i}}\left[\alpha_o - \alpha_o^* + \sum_{k\neq 0}\left\{\left(\alpha_k - \alpha_{-k}^*\right)e^{i\mathbf{k}\cdot\mathbf{r}}\right\}\right].$$

The dynamic z component of the magnetization vector ($m_z(\mathbf{r},t)$) is also expressed in terms of the phasor variables by combining equations (3.5) and (3.11). This results in the following expression

$$m_z(\mathbf{r},t) \approx -\frac{M_s}{2}\left[\alpha_o\alpha_o^* + \sum_{k\neq 0}\left\{\left(\alpha_o\alpha_{-k}^* + \alpha_o^*\alpha_k\right)e^{i\mathbf{k}\cdot\mathbf{r}}\right\}\right] \tag{3.12}$$

Note that in order to make the above expressions less cumbersome, the explicit time dependence of the $\alpha_o(t)$ and $\alpha_k(t)$ terms was not shown, this notation will be used below where appropriate.

After rewriting the torque equation given in Eq. (3.3) in terms of the above uniform mode and spin wave phasor variables, one obtains the following expression for the equation of motion

$$\dot{\alpha}_o + \sum_{k\neq 0}\dot{\alpha}_k e^{i\mathbf{k}\cdot\mathbf{r}} = \mathrm{i}|\gamma|\left[\alpha_o + \sum_{k\neq 0}\alpha_k e^{i\mathbf{k}\cdot\mathbf{r}}\right]H_{eff}^z(\mathbf{r},t) - \mathrm{i}|\gamma|\frac{M_z(\mathbf{r},t)}{M_s}\left[H_{eff}^x(\mathbf{r},t) + iH_{eff}^y(\mathbf{r},t)\right] \tag{3.13}$$

and its adjoint (not shown). The exact expressions for the effective magnetic fields will be given in the next section. In the meantime it is worth noting that this equation does not include damping. Suhl and Schloemann include damping in their models via the introduction of complex frequency terms. This will be discussed in more detail in the linear uniform mode section of this chapter.

3.2.1 Effective Magnetic Field Expressions

The total effective magnetic field expression in Eq. (3.1) may be written as

$$\mathbf{H}_{\text{eff}}(\mathbf{r},t) = \mathbf{H}_{\text{ext}} + \mathbf{h}_{\text{p}}(t) + \mathbf{H}_{\text{dip}}(\mathbf{r},t) + \mathbf{h}_{\text{ex}}(\mathbf{r},t) + \mathbf{h}_{\text{A}}(\mathbf{r},t). \tag{3.14}$$

Here $\mathbf{H}_{\text{ext}}$ and $\mathbf{h}_{\text{p}}(t)$ are the static and microwave magnetic fields, respectively, applied externally to the sample. The $\mathbf{H}_{\text{dip}}(\mathbf{r},t)$, $\mathbf{h}_{\text{ex}}(\mathbf{r},t)$, and $\mathbf{h}_{\text{A}}(\mathbf{r},t)$ terms are the internal magnetic fields, which arise due to dipole-dipole interactions, exchange coupling, and magnetocrystalline anisotropy, respectively. The expressions given in this section for the effective fields will be combined into the working equations for $H_{eff}^{x}(\mathbf{r},t) + iH_{eff}^{y}(\mathbf{r},t)$ and $H_{eff}^{z}(\mathbf{r},t)$, which are required to solve the equation of motion given in Eq. (3.13)Detailed derivations of the individual fields are not shown here, rather references are provided.

In order to keep the size of the equations that are to follow more manageable, the explicit time and spatial functional dependences "(t)" and "$(\mathbf{r},t)$" will not always be shown. Instead, capitalized letters will be used to represent the static terms and lower case letters will be used to denote time dependent terms. This notation will be utilized from here on except for when it is necessary to show the time and spatial dependencies explicitly to eliminate confusion.

The external applied static and microwave fields may be written as

$$\mathbf{H}_{\text{ext}} = H_{ext}\,\hat{\mathbf{z}} \tag{3.15}$$

and

$$\mathbf{h}_{\text{p}}(t) = h_p a_x \cos(\omega_p t + \delta_x)\,\hat{\mathbf{x}} + h_p a_y \cos(\omega_p t + \delta_y)\,\hat{\mathbf{y}} + h_p a_z \cos(\omega_p t)\,\hat{\mathbf{z}} \tag{3.16}$$

respectively. Here the microwave magnetic field is expressed with arbitrary phase and direction. The $a_{x,y,z}$ terms are the relative amplitude of the various components, the δ_x and δ_y terms are the relative phase terms of the *x* and *y* components, respectively. For example, to express a linearly polarized field applied in the ***y*** direction (field orientation used to obtain the subsidiary absorption data shown here) one sets $a_y = 1$ and $a_x, a_z, \delta_x, \delta_y = 0$.

The dipole field expressions are derived from Maxwell's equations, and can be written in terms of spatially uniform and nonuniform components. The spatially uniform dipole fields, which are often referred to as demagnetizing fields, depend upon the sample shape and orientation of the applied magnetic fields. For an ellipsoidal shaped sample, in which the external $\mathbf{h}_{\mathrm{p}}$ and $\mathbf{H}_{\mathrm{ext}}$ magnetic fields are applied along the principal axes, these demagnetizing fields can be written as

$$\begin{aligned} \mathbf{H}_{\mathrm{demag}} &= -4\pi M_s N_z \, \hat{\mathbf{z}} \,, \\ \mathbf{h}_{\mathrm{demag}} &= -4\pi \left(N_x m_{ox} \, \hat{\mathbf{x}} + N_y m_{oy} \, \hat{\mathbf{y}} + N_z m_{oz} \, \hat{\mathbf{z}} \right). \end{aligned} \tag{3.17}$$

Here N_x, N_y, and N_z are the so-called Osborn demagnetizing constants for the principal *x*, *y*, and *z* axes of the sample, respectively, and their sum is unity (Osborn [1945]).

The spatially dependent dipole fields are derived from Maxwell's equations by making the so-called magnetostatic approximation (assumption (5) given above), and may be written as

$$\mathbf{h}_{\mathrm{dip}}(\mathbf{r},t) = -4\pi \sum_{k \neq 0} \left\{ \frac{\mathbf{k} \cdot \mathbf{m}_{\mathrm{k}}(\mathbf{r},t)}{k^2} \mathbf{k} \, e^{i\mathbf{k}\cdot\mathbf{r}} \right\} \,. \tag{3.18}$$

Where **k** is the wave vector of a given spin wave mode. See Appendix A in (Chen and Patton [1994]) for a full derivation. The dipole field expression, given in Eq. (3.18), can be written in terms of the complex uniform mode $\alpha_o(t)$ and the spin wave $\alpha_k(\mathbf{r},t)$ phasor variables as

$$\mathbf{h}_{\text{dip}} = \frac{-4\pi M_s}{2} \sum_{k\neq 0} \left[\frac{\mathbf{k}}{k} \left\{ \left(e^{-i\phi_k} \alpha_k + e^{i\phi_k} \alpha_{-k}{}^* \right) \sin\theta_k - \left(\alpha_o \alpha_{-k}{}^* + \alpha_o{}^* \alpha_k \right) \cos\theta_k \right\} e^{i\mathbf{k}\cdot\mathbf{r}} \right] \quad (3.19)$$

Here the θ_k and ϕ_k terms are the polar and azimuthal angles of the spherical coordinate system, respectively, which describe the spin wave wave-vector **k** propagation direction. See diagram (a) in Fig. 3.7 for a sketch of the spherical coordinate system that is used here.

The next effective magnetic field of interest is the exchange field; this field is quantum mechanical in nature and is typically determined from an exchange energy expression. The expression used in this work was first derived by Herring and Kittel [1951] and is given as

$$\mathbf{h}_{\text{exchange}}(\mathbf{r},t) = -\frac{D}{M_s} \sum_{k\neq 0} \left\{ k^2 \, \mathbf{m}_{\text{k}}(\mathbf{r},t) \, e^{i\mathbf{k}\cdot\mathbf{r}} \right\} \quad . \quad (3.20)$$

Here D is the so-called exchange constant. There is some evidence that the exchange constants for hexagonal ferrites are anisotropic and vary with the spin wave propagation direction (Mita and Shinizu [1973]). These effects, which require D to be a tensor quantity, are not considered here. Rather, D is assumed to be a constant and the yttrium iron garnet value of $5.4\text{x}10^{-9}\,\text{Oe}\,\text{cm}^2$ is used. For a discussion of effect different D values on spin wave dispersion see Nazarov, *et al.* [2003].

The last internal magnetic field to be discussed here is the anisotropy field. As with the exchange field, this field is not a Maxwellian field. As was discussed in detail in

Chapter 2 the anisotropy field can be determined from an empirical free energy expression. For the coordinate system (hexagonal c-axis along the *x*-axis) shown in Fig. 3.1, the free energy U_A can be expressed as

$$U_A = U_o - K_u \left(\frac{\left| m_x(\mathbf{r},t) \right|}{M_s} \right)^2 , \tag{3.21}$$

where the sign of K_u determines whether the anisotropy is uniaxial or planar. A negative K_u corresponds to planar anisotropy with preferential plane in the *y*-*z* plane (since energy is minimized by $\left| m_x(\mathbf{r},t) \right| = 0$), whereas a positive K_u corresponds to a sample with uniaxial anisotropy and easy direction for the magnetization along the *x*-axis.

The above energy equation is converted to a magnetic field expression by rewriting $U_A = -\mathrm{M} \bullet \mathrm{H_A}$ as $\mathrm{H_A} = -\nabla_{\mathrm{M}} U_A$. Applying this gradient operation with respect to the magnetization components on Eq. (3.21) results in the following anisotropy field expression

$$\mathbf{h}_{\mathrm{A}}(\mathbf{r},t) = \frac{H_A}{M_s} m_x(\mathbf{r},t)\, \hat{\mathbf{x}} \tag{3.22}$$

where $H_A = 2K_u / M_s$. This anisotropy field expression models both uniaxial and planar anisotropy depending on the sign of K_u.

In summary, the total effective magnetic field inside an ellipsoidal shaped hexagonal ferrite sample with crystalline c-axis along the *x*-direction, and the external static field applied along the *z*-axis may be written as

$$\begin{aligned} \mathbf{H}_{\text{eff}} = &\left(h_p^x + h_{demag}^x + h_{dip}^x + h_{ex}^x + h_A^x \right) \hat{\mathbf{x}} \; + \; \left(h_p^y + h_{demag}^y + h_{dip}^y + h_{ex}^x \right) \hat{\mathbf{y}} \; + \\ &\left(H_{ext} + H_{demag}^z + h_p^z + h_{demag}^z + h_{ex}^z \right) \hat{\mathbf{z}} . \end{aligned} \tag{3.23}$$

In order to obtain the two desired effective magnetic fields expressions $H_{eff}^{x}(\mathbf{r},t)+iH_{eff}^{y}(\mathbf{r},t)$ and $H_{eff}^{z}(\mathbf{r},t)$, which are required to solve the equation of motion, the *x* and *y* field components in Eq. (3.14) are combined in the appropriate manner, and the dynamic magnetization terms $m_x(\mathbf{r},t)$, $m_y(\mathbf{r},t)$, and $m_z(\mathbf{r},t)$ are rewritten in terms of the complex phasor variables $\alpha_o(t)$ and $\alpha_k(t)$. Upon doing this, the following expression for $H_{eff}^{x}(\mathbf{r},t)+iH_{eff}^{y}(\mathbf{r},t)$ is obtained

$$H_{eff}^{x}+iH_{eff}^{y}=h_c+H_1\alpha_o+H_2\alpha_o^{*}+\sum_{k\neq 0}\left\{\left(H_3\alpha_k+H_4\alpha_{-k}^{*}\right)e^{i\mathbf{k}\cdot\mathbf{r}}\right\} + \sum_{k\neq 0}\left\{H_5\left(\alpha_o^{*}\alpha_k+\alpha_o\alpha_{-k}^{*}\right)e^{i\mathbf{k}\cdot\mathbf{r}}\right\}. \tag{3.24}$$

where

$$h_c=h_p^{x}+ih_p^{y},$$

$$H_1=H_A/2-(4\pi M_s/2)\left(N_x+N_y\right),$$

$$H_2=H_A/2+(4\pi M_s/2)\left(N_y-N_x\right),$$

$$H_3=H_A/2-(4\pi M_s/2)\sin^2(\theta_k)-Dk^2, \tag{3.25}$$

$$H_4=H_A/2-(4\pi M_s/2)\sin^2(\theta_k)e^{2i\phi_k},$$

and

$$H_5=(4\pi M_s/2)\cos\theta_k\sin\theta_k e^{i\phi_k}.$$

The subscript "*c*" in h_c is to remind the reader that this is a complex field expression for the microwave pumping field. The $H_{eff}^{z}(\mathbf{r},t)$ expression maybe written as

$$H_{eff}^{z}=H_{\text{int}}+h_p^{z}+\sum_{k\neq 0}\left\{H_{z1}\alpha_k+H_{z1}^{*}\alpha_{-k}^{*}\right\}e^{i\mathbf{k}\cdot\mathbf{r}}+H_{z2}\alpha_o\alpha_o^{*}+\sum_{k\neq 0}H_{z3}\left\{\alpha_o^{*}\alpha_k+\alpha_o\alpha_{-k}^{*}\right\}e^{i\mathbf{k}\cdot\mathbf{r}}, \tag{3.26}$$

where the static coefficients are given as

$$H_{\text{int}} = H_{ext} - 4\pi M_s N_z \,,$$

$$H_{z1} = -(4\pi M_s/2)\cos\theta_k \sin\theta_k e^{-i\phi_k} \,,$$

$$H_{z2} = (4\pi M_s/2)N_z \,, \tag{3.27}$$

and

$$H_{z3} = (4\pi M_s/2)\cos^2(\theta_k) + (D/2)k^2 \,.$$

3.2.2 Reduced Equation of Motion

As was discussed previously, an analytic solution to the full equation of motion given in Eq. (3.3) which includes all possible orders of nonlinearity in $m_x(\mathbf{r},t)$, $m_y(\mathbf{r},t)$, and $m_z(\mathbf{r},t)$ is not the goal of this work. Rather, we are interested in determining the solution to a reduced form of the equation of motion that includes only the relevant order of nonlinearity.

The reduced equation of motion is obtained by substituting the effective field expressions for $H_{eff}^{x} + iH_{eff}^{y}$ and H_{eff}^{z} given in Eqs. (3.24) and (3.26), respectively, into Eq. (3.13) and then discarding all α_k terms of second and higher order and all α_o, h_p, and $h_p\,\alpha_o$ terms of third and higher order. After a fairly tedious amount of algebraic analysis, one obtains the following reduced equations of motion for the uniform and the spin wave modes

$$\frac{1}{\mathrm{i}}\begin{bmatrix}\dot{\alpha}_{\mathrm{o}}\\ \dot{\alpha}_{\mathrm{o}}^{*}\end{bmatrix} = \begin{bmatrix}A_{\mathrm{o}} & B_{\mathrm{o}}\\ -B_{\mathrm{o}}^{*} & -A_{\mathrm{o}}^{*}\end{bmatrix}\begin{bmatrix}\alpha_{\mathrm{o}}\\ \alpha_{\mathrm{o}}^{*}\end{bmatrix} - |\gamma|\begin{bmatrix}h_{\mathrm{c}}\\ -h_{c}^{*}\end{bmatrix}$$

and (3.28)

$$\frac{1}{\mathrm{i}}\begin{bmatrix}\dot{\alpha}_{k}\\ \dot{\alpha}_{-k}^{*}\end{bmatrix} = \begin{bmatrix}A_k + c_k & B_k + d_k\\ -B_{-k}^{*} - d_{-k}^{*} & -A_{-k}^{*} - c_{-k}^{*}\end{bmatrix}\begin{bmatrix}\alpha_{k}\\ \alpha_{-k}^{*}\end{bmatrix}$$

respectively. The working equations for the various terms in Eq. (3.28) are as follows. The time independent A_o, B_o, A_k, and B_k terms may be written as

$$A_o = |\gamma|(H_{int} - H_1),$$
$$B_o = -|\gamma| H_2,$$
$$A_k = |\gamma|(H_{int} - H_3), \tag{3.29}$$
and
$$B_k = -|\gamma| H_4.$$

The A_o and B_o terms are both real, so the complex conjugation will be dropped in future equations. The time dependent $c_k(t)$ and $d_k(t)$ terms, which cause Eq. (3.28) to be nonlinear, may be written as

$$c_k(t) = |\gamma|\left[h_p^z + C_{11}\alpha_o + C_{12}\alpha_o^* + C_{21}\,\alpha_o\,\alpha_o^* + \frac{H_2}{2}(\alpha_o^*)^2 \right]$$
and (3.30)
$$d_k(t) = |\gamma|\left[D_{11}\alpha_o + D_{21}\alpha_o\,\alpha_o^* + D_{22}\,\alpha_o^{\,2} \right]$$

where

$$C_{11} = H_{z1},$$
$$C_{12} = -H_5,$$
$$C_{21} = H_{z2} + H_{z3} + (H_1 + H_3)/2,$$
and (3.31)
$$D_{11} = H_{z1}^* - H_5,$$
$$D_{21} = (H_2 + H_4)/2,$$
$$D_{22} = H_{z3} + H_1/2\ .$$

A significant portion of the classical micromagnetic spin wave theory can be derived from Eq. (3.28). This equation will be used here to model: (1) the linear uniform mode FMR response, (2) the linear spin wave dispersion relation, and (3) the nonlinear spin wave instability thresholds for parallel pumping, subsidiary absorption, and resonance saturation instability processes. Note that Eq. (3.28) does not include damping. In order to do so, Suhl and Schloemann force the uniform mode and spin wave frequencies to be complex; this will be discussed in more detail in the following sections.

3.3 LINEAR UNIFORM MODE ANALYSIS

This section addresses the linear uniform mode theory. First, the uniform mode resonance frequency is obtained and the so-called stiffness fields, which provide physical insight into the resonance frequency, are introduced. Then the steady state uniform mode solutions are obtained, and several published methods of adding damping to these solutions via complex frequencies are reviewed. The third subsection shows that in several of the past publications the incorrect damping sign was utilized for the anti-Larmor uniform mode complex frequency damping terms. The fourth subsection then provides a direct comparison between the uniform mode solutions obtained using complex frequency damping terms with solutions obtained from the Landau-Lifshitz and Bloch-Bloembergen equations of motion, which contain damping from the onset. The last subsection analyzes the conditions under which using the wrong anti-Larmor complex damping sign have the largest effect on the linear uniform mode amplitude response. The corresponding effects on the instability threshold fields will be discussed in section 3.6 of this chapter.

3.3.1 Resonance Frequency

The linear uniform mode equation of motion in Eq. (3.28), may be written as

$$\frac{\partial}{\partial t}\begin{bmatrix}\alpha_o \\ \alpha_o^*\end{bmatrix} = i\begin{bmatrix}A_o & B_o \\ -B_o & -A_o\end{bmatrix}\begin{bmatrix}\alpha_o \\ \alpha_o^*\end{bmatrix} + i|\gamma|\begin{bmatrix}-h_c \\ h_c^*\end{bmatrix}. \tag{3.32}$$

The two coupled first order differential equations in Eq. (3.32) can be readily combined into a single second order differential equation for $\alpha_o(t)$ that is written as

$$\frac{\partial^2 \alpha_o(t)}{\partial t^2} + \lambda^2 \alpha_o(t) = F(t). \tag{3.33}$$

Equation (3.33) is the governing equation of an undamped driven harmonic oscillator, where λ is the resonance frequency and $F(t)$ is the effective driving term. The working equations for these terms are

$$\lambda^2 = A_o{}^2 - B_o{}^2 ,$$

and (3.34)

$$F(t) = |\gamma|\left[-i\dot{h}_c + A_o h_c(t) - B_o h_c(t)^*\right] \quad .$$

The A_o and B_o terms are obtained from Eq. (3.29) as

$$A_o = |\gamma|\left(H_{\text{int}} - H_A/2 + 4\pi M_s(N_x + N_y)/2\right)$$

and (3.35)

$$B_o = -|\gamma|\left(H_A/2 + 4\pi M_s(N_y - N_x)/2\right).$$

Therefore, the uniform mode resonance frequency (ω_o) expression given by λ in Eq. (3.34) may be written as

$$\omega_o{}^2 = |\gamma|\sqrt{\left[H_{\text{int}} + 4\pi M_s N_x - H_A\right]\left[H_{\text{int}} + 4\pi M_s N_y\right]}. \tag{3.36}$$

This expression corresponds to the FMR resonance frequency ω_{FMR} discussed in Chapter 2. This expression is highly successful at modeling the measured FMR resonance frequencies in hexagonal ferrites. For some examples of this, see Hurben [1996].

In order to provide physical insight into the resonance frequency expression Eq. (3.36) is often rewritten in terms of "stiffness" fields as

$$\omega_{\mathrm{o}} = |\gamma| \sqrt{H_{\mathrm{ox}} H_{\mathrm{oy}}} \,. \tag{3.37}$$

Here the H_{ox} and H_{oy} terms are the net static magnetic fields that exert a torque on the magnetization vector as it is tilted away from the equilibrium *z*-direction into the *z*-*x* and *z*-*y* planes, respectively. See Fig. 3.1 for a diagram of the coordinate system and static equilibrium direction. From an inspection of Eq.(3.36) and Eq. (3.37), one can see that the stiffness fields can be written as

$$H_{\mathrm{ox}} = H_{\mathrm{int}} + 4\pi M_s N_x - H_A \,,$$

and (3.38)

$$H_{oy} = H_{\mathrm{int}} + 4\pi M_s N_y \,.$$

First consider the H_{ox} stiffness field term. As can be seen in Eq. (3.38), there are three different torque sources exerted on the magnetization vector as it is tilted away from the *z*-axis into the *z*-*x* plane: (1) the internal field $H_{\mathrm{int}} = H_{ext} - 4\pi M_s N_z$, which resists the rotation away from the z-axis, (2) the demagnetizing field $4\pi M_s N_x$, which resists the tilt of the magnetization into the *x*-axis direction, and (3) the anisotropy field H_A, which either acts to pull the magnetization vector towards the *x*-axis (for uniaxial case) or resists the tilt into the *x*-axis (for easy-plane case, $H_A < 0$).

Now consider the H_{oy} demagnetizing field. As can be seen in Eq. (3.38), the H_{oy} stiffness field has only two torque sources that correspond to the internal applied static field and the *y*-component of the demagnetizing field. Both torque fields try to keep the magnetization vector aligned along the *z*-axis.

Figure 3.2 summarizes the H_{ox} and H_{oy} stiffness fields for four different configurations: (a) isotropic sphere, (b) isotropic thin film magnetized perpendicular to the film plane, (c) isotropic thin film magnetized parallel to the film plane, and (d) an anisotropic thin film magnetized parallel to the film plane. For the isotropic sphere, there is only a single torque source acting on the uniform mode magnetization vector, the external static magnetic field (H_{ext}), which exerts the same amount of torque on the magnetization whether it is tilted away from the *z*-axis into the z-*x* or z-*y* planes. For this case, $H_{ox} = H_{oy} = |\gamma| H_{ext}$.

For the isotropic thin film, cases (b) and (c) shown in Fig. 3.2, there are two sources of torque: the external magnetic field and the internal demagnetizing field. For a static field applied out of the disc plane, case (b), the demagnetizing field applies the same amount of torque on the magnetization whether it is tilted into the *x* or *y* directions, and as with the isotropic sphere $H_{ox} = H_{oy}$. But for this case, the stiffness fields include the demagnetization field such that $H_{ox} = H_{oy} = H_{ext} - 4\pi M_s$. For the isotropic thin film with in-plane magnetization, case (c), the demagnetizing field only exerts a torque when the magnetization is tilted out of the sample plane into the x-direction, and in turn, $H_{ox} > H_{oy}$.

The above differences in the stiffness fields for cases (a), (b), and (c) have a real measurable effect on the FMR resonance frequency. For the same exact thin isotropic ferrite disk sample a different resonance frequency is observed depending upon whether the sample is magnetized in or out of the disk plane. When the sample is magnetized in the disk plane versus out of the plane, a higher FMR resonance is measured that is equal to $\omega_o = |\gamma| \sqrt{H_{ext}(H_{ext} + 4\pi M_s)}$ versus $\omega_o = |\gamma|(H_{ext} - 4\pi M_s)$, respectively. Furthermore,

(a) Isotropic Sphere

$$\omega_{FMR} = |\gamma| \sqrt{H_{ox} H_{oy}}$$

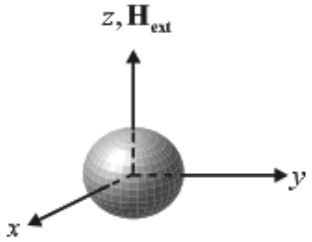

$$N_x = N_y = N_z = 1/3$$
$$H_A = 0$$
$$H_{ox} = H_{ext}$$
$$H_{oy} = H_{ext}$$

(b) Isotropic Thin Film (film plane = x-y plane)

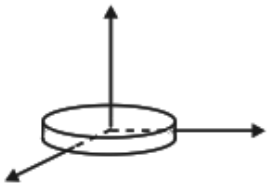

$$N_x = N_y = 0, \quad N_z = 1$$
$$H_A = 0$$
$$H_{ox} = H_{ext} - 4\pi M_s$$
$$H_{oy} = H_{ext} - 4\pi M_s$$

(c) Isotropic Thin Film (film plane = y-z plane)

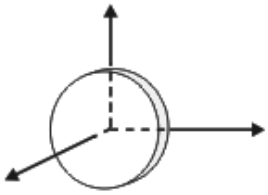

$$N_x = 1, \quad N_y = N_z = 0$$
$$H_A = 0$$
$$H_{ox} = H_{ext} + 4\pi M_s$$
$$H_{oy} = H_{ext}$$

(d) Planar Anisotropic Thin Film (film plane = y-z plane)

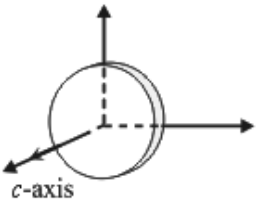

$$N_x = 1, \quad N_y = N_z = 0$$
$$H_A = -|H_A|$$
$$H_{ox} = H_{ext} + 4\pi M_s + |H_A|$$
$$H_{oy} = H_{ext}$$

Figure. 3.2. Uniform mode stiffness field equations for several sample geometries, orientations, and anisotropy types. For each configuration, the z-axis corresponds to the static equilibrium direction of the magnetization vector.

if the same material is shaped as a sphere, we then obtain an FMR resonance frequency ($\omega_o = |\gamma| H_{ext}$) that is between the in plan and out of plane magnetized disk sample.

The addition of anisotropy adds further complications; this is addressed in case (d) in Fig. 3.2. This case corresponds to a thin disk shaped sample with easy-plane anisotropy. The easy-plane is coplanar with the disc plane (sample geometry extensively studied as part of this work). For this configuration, we now have three sources of torque: the external, demagnetizing, and anisotropy fields. All three of these magnetic field sources work together to resist a tilt of the magnetization vector away from the *z*-axis toward the *x*-axis. However, only the external field acts to resist the tilt from the *z*-axis to the *y*-direction. This results in $H_{ox} >> H_{oy}$, and in turn ω_o is significantly larger than what is observed for the isotropic sample, case (c). This is why such samples with high anisotropy values are favorable for high frequency applications. It is important to note that in order to obtain the above benefit of increased resonance frequency, one has to apply the external magnetic field in the appropriate direction relative to the magnetocrystalline anisotropy direction. If the same sample discussed in case (d) is magnetized out of the disc plane, then the torque from the effective anisotropy field would oppose the torque from the externally applied field, resulting in a significant lowering of the resonance frequency.

The stiffness field expressions given in Eq. (3.38) and Fig. 3.2 are only valid if the static field is applied along a principle axis of an ellipsoidal shaped sample with the anisotropy orientation shown in Fig. 3.1. For a more generalized stiffness field analysis, in which the static field is not restricted to being aligned along one of the principle axes, see Hurben and Patton [1988] and McKinstry *et al*. [1985].

In order to simplify the dynamic magnetization expressions that are to follow, it is convenient to rewrite the stiffness fields in frequency units. The resulting stiffness

frequencies are obtained by multiplying each stiffness field by $|\gamma|$, and may be written as

$$\omega_{ox} = |\gamma| H_{ox}$$

and (3.39)

$$\omega_{oy} = |\gamma| H_{oy} .$$

This in turn results in the following uniform mode resonance frequency expression

$$\omega_o = |\gamma| \sqrt{H_{ox} H_{oy}} = \sqrt{\omega_{ox} \omega_{oy}} . \quad (3.40)$$

It can be shown that the stiffness frequencies can be used to determine the ellipticity of the uniform mode precessional cone. The ellipticity of the uniform mode processional cone, which is defined as the magnitude of ratio of the dynamic m_{ox} and m_{oy} components of the magnetization, may be written as

$$ellipticity = \left| \frac{m_{ox}}{m_{oy}} \right| = \sqrt{\frac{\omega_{oy}}{\omega_{ox}}} . \quad (3.41)$$

See Appendix B in Chen and Patton [1994] for a full derivation of the above expression. Based upon Eq. (3.41), if $\omega_{oy} = \omega_{ox}$ then $|m_{ox}| = |m_{oy}|$, and the uniform mode precessional cone is circular. This is the case for the both the isotropic sphere and the out-of-plane magnetized isotropic thin film shown in Figure 3.2. However, for the in-plane magnetized isotropic and anisotropic thin films shown in the bottom of Fig 3.2, there is more torque exerted on m_{ox} than on m_{oy}, causing m_{ox} to be smaller than m_{oy} (especially for the anisotropic case). The important role that ellipticity plays in nonlinear instability processes will be discussed in detail below.

3.3.2 Steady State Solutions

We will now turn our attention to the steady state uniform mode solution of Eq. (3.33) which can be obtained with a trial solution of the form $\alpha_o(t) = A\exp(i\omega_p t) + B\exp(-i\omega_p t)$. Substituting this trial solution into Eq. (3.33) and solving for the A and B constants yields

$$\alpha_o(t) = \frac{|\gamma| h_o}{2}\left[q_L e^{i\omega_p t} + q_{AL} e^{-i\omega_p t} \right], \tag{3.42}$$

where h_o is the magnitude of an externally applied microwave field applied in *x*-*y* plane, and ω_p is the angular frequency of the pumping field. The q_L and q_{AL} terms are referred to as the Larmor and anti-Larmor uniform mode coefficients, respectively. Equation (3.42) separates the time dependent uniform mode response into two circularly polarized components which precess in opposite directions. The $q_L \exp(i\omega_p t)$ term corresponds to the Larmor precession, and the $q_{AL}\exp(-i\omega_p t)$ term corresponds to the anti-Larmor precession.

Figure 3.3 shows a sketch of the Larmor and anti-Larmor precession as viewed from the positive *z*-axis. As can be seen in the figure, the Larmor precession corresponds to a counter clockwise rotation and the anti-Larmor precession corresponds a clockwise rotation of the magnetization. The amplitude of the anti-Larmor response is shown to be smaller than the Larmor response. It will be shown explicitly below that the relative magnitude of the two terms is directly related to the ellipticity of the uniform mode precession; a purely circular uniform mode precession response (zero ellipticity) corresponds to the anti-Larmor response being zero or negligible compared to the Larmor response.

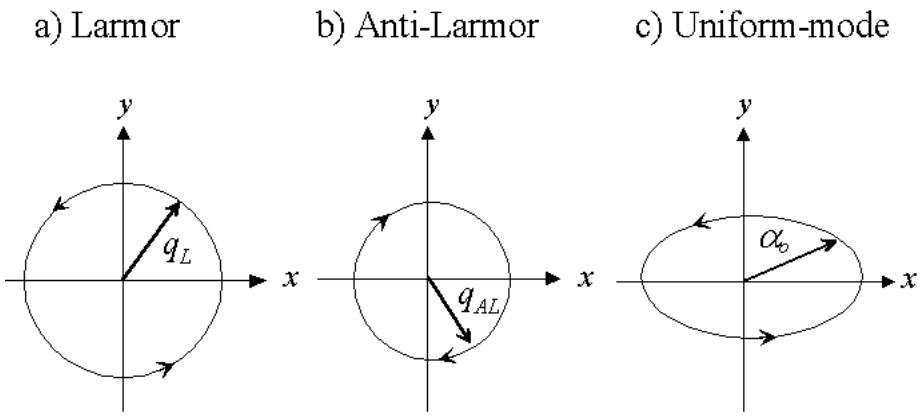

Figure. 3.3. Top view sketch of the precession cones of the Larmor, Anti-Larmor, and resulting uniform mode amplitude response.

Equation (3.42) predicts that the uniform mode amplitude is linearly dependent on the microwave field amplitude. This linear response is only true for low-power microwave levels. As the microwave power is increased, the nonlinear uniform mode terms (not modeled here) eventually become significant. Before this occurs, however, the spin wave instability threshold is reached and the microwave field energy is coupled from the uniform mode into the critical spin wave modes. This will be discussed in detail in the nonlinear section of this chapter.

The q_L and q_{AL} terms in Eq. (3.42) may be written as

$$q_L = \frac{\left(\omega_{oy} + \omega_p\right) a_x e^{i\delta_x} + i\left(\omega_{ox} + \omega_p\right) a_y e^{i\delta_y}}{\omega_o^{\,2} - \omega_p^{\,2}},$$

and (3.43)

$$q_{AL} = \frac{\left(\omega_{oy} - \omega_p\right) a_x e^{-i\delta_x} + i\left(\omega_{ox} - \omega_p\right) a_y e^{-i\delta_y}}{\omega_o^{\,2} - \omega_p^{\,2}} \quad .$$

Here, the ω_{ox} and ω_{oy} terms are the stiffness frequencies, which were defined in the previous section, and the $a_{x,y}$ and $\delta_{x,y}$ terms correspond to the relative phase and orientation of a microwave field applied in the *x*-*y* plane. See Eq. (3.16) for details.

An inspection of Eq. (3.43) reveals that the uniform mode response given in Eq. (3.42) becomes infinite when the resonance condition ($\omega_p = \omega_o$) is satisfied. This non-physical result occurs because damping was not included in the original equation of motion. This is remedied by the addition of phenomenological complex frequency damping terms. The exact method of doing this has varied depending upon the complexity of the uniform mode solution. We will review three different complex frequency techniques that have been utilized by Suhl [1957], Patton [1969], and Schloemann *et al*. [1963]. The reasons for doing this are threefold: (1) to show the complications that arise when $\omega_{ox} \neq \omega_{oy}$ (i.e., elliptical uniform precession), (2) to highlight the different approaches used by Patton and Schloemann to address these complications, and (3) to provide working steady state uniform mode equations that include damping, which will be utilized in later sections.

In the first published theoretical paper regarding spin wave instability processes, Suhl [1957] addressed the simplest microwave field and sample geometry possible: a microwave field with circular polarization in the Larmor direction of the form $h_o \exp(i\omega_p t)$ applied to an isotropic sphere. For this case, $\omega_{ox} = \omega_{oy} = \omega_o$ and the Larmor and anti-Larmor coefficients given in Eq. (3.43) reduce to

$$q_L = \frac{1}{\omega_o - \omega_p}$$

and (3.44)

$$q_{AL} = 0,$$

respectively. Suhl then added damping to the above q_L term by replacing ω_o with a complex frequency term Ω_o, which is given as

$$\Omega_o = \omega_o + i\eta_o\,, \tag{3.45}$$

where η_o is the relaxation rate of the uniform mode response. This term is related to the measured uniform FMR linewidth via the following relationship

$$\eta_o = 1/2 \left|\partial\omega_o/\partial H_{ext}\right|_{FMR} \Delta H_{FMR} \,. \tag{3.46}$$

The uniform mode resonance frequency equation for an isotropic sphere is $\omega_o = |\gamma| H_{ext}$, which results in the following relationship for the relaxation rate

$$\eta_o = |\gamma| \Delta H_{FMR}/2 \,. \tag{3.47}$$

Substituting the above q_L, Ω_o, and η_o expressions into Eq. (3.42) yields Suhl's expression for the steady state uniform mode response which may be written as

$$\alpha_o(t) = \frac{|\gamma| h_o}{2}\left[\frac{1}{\omega_o - \omega_p + i|\gamma|\Delta H_{FMR}/2}\, e^{i\omega_p t}\right]. \tag{3.48}$$

As can be seen from Eq. (3.48), the uniform mode amplitude is now well behaved at the resonance condition $\omega_p = \omega_o$.

Patton extended Suhl's treatment to address a more generalized microwave field and sample geometry (Patton [1969]). He utilized a microwave field expression of the form

$$h_p(t) = h_o\left[a_x \cos(\omega_p t + \delta_x)\,\hat{x} + a_y \cos(\omega_p t + \delta_y)\,\hat{y}\right] \tag{3.49}$$

applied to an isotropic sample of general ellipsoidal shape. For this case, Patton obtained the following Larmor (q_L) and anti-Larmor (q_{AL}) uniform mode coefficients

$$q_L = \frac{\left(\omega_{\text{oy}} + \omega_p\right) a_x e^{i\delta_x} + i\left(\omega_{\text{ox}} + \omega_p\right) a_y e^{i\delta_y}}{\omega_{\text{ox}}\omega_{\text{oy}} - \omega_p{}^2}$$

and (3.50)

$$q_{AL} = \frac{\left(\omega_{\text{oy}} - \omega_p\right) a_x e^{-i\delta_x} + i\left(\omega_{\text{ox}} - \omega_p\right) a_y e^{-i\delta_y}}{\omega_{\text{ox}}\omega_{\text{oy}} - \omega_p{}^2},$$

respectively. This is the same solution as was obtained previously and given in Eq. (3.42) and Eq. (3.43), in which $\omega_{\text{ox}}\omega_{\text{oy}}$ is used explicitly in the denominator instead of $\omega_{\text{o}}{}^2$. See Patton [1969] for the exact equations used for the stiffness frequency terms. Notice that unlike the uniform mode coefficients obtained by Suhl for the isotropic sphere case given in Eq. (3.44), the uniform mode coefficients obtained by Patton for the more general case, which are given in Eq. (3.50) have a nonzero anti-Larmor coefficient and contain stiffness frequency terms in both the numerator and the denominator.

In order to model damping for this more generalized case, Patton replaced both the resonance frequency and its constituent stiffness frequencies with complex terms in the following manner

$$\omega_{\text{o}} \rightarrow \Omega_{\text{o}} = \omega_{\text{o}} + i\eta_o ,$$

$$\omega_{\text{ox}} \rightarrow \Omega_{\text{ox}} = \omega_{\text{ox}} + iq_o , \quad (3.51)$$

and

$$\omega_{\text{oy}} \rightarrow \Omega_{\text{oy}} = \omega_{\text{oy}} + iq_o .$$

As with Suhl, Patton related the uniform mode relaxation rate (η_o) to the measured FMR linewidth via Eq. (3.46). He then obtained a working expression for the stiffness frequency damping term q_o by requiring $\Omega_o = \sqrt{\Omega_{ox}\Omega_{oy}}$. This can be written as

$$\sqrt{\omega_{ox}\omega_{oy}} + i\eta_o = \sqrt{(\omega_{ox} + iq_o)(\omega_{oy} + iq_o)}\,. \tag{3.52}$$

Since $q_o << \omega_{ox}$ and ω_{oy}, the square root on the right side of Eq. (3.52) was then rewritten as a truncated Taylor series as

$$\sqrt{\omega_{ox}\omega_{oy}} + i\eta_o = \sqrt{\omega_{ox}\omega_{oy}}\left[1 + i\frac{q_o}{2}\left(\frac{\omega_{ox} + \omega_{oy}}{\omega_{ox}\omega_{oy}}\right)\right]. \tag{3.53}$$

Solving this for q_o results in

$$q_o = \frac{2\omega_{ox}\omega_{oy}}{\omega_{ox} + \omega_{oy}}\eta_o = \frac{2\omega_o}{\omega_{ox} + \omega_{oy}}\eta_o\,. \tag{3.54}$$

Note that in the limit of a circularly polarized field applied to a spherically shaped sample, the above stiffness frequencies and damping rate reduce to $\omega_{ox} = \omega_{oy} = \omega_o$ and $q_o = \eta_o$, respectively, and Patton's expressions are in exact agreement with Suhl's.

Schloemann extended Suhl's initial analysis to include anisotropy (Schloemann *et al*. [1963]). In his work, he utilized a linearly polarized microwave field of the form $h_o \cos(\omega_p t)\hat{\mathbf{y}}$ applied to a thin film sample with planar anisotropy (same field and sample configuration as shown in Fig. 3.2(d)). For this case, he obtained the following Larmor and anti-Larmor uniform mode coefficients

$$q_L = \frac{\omega_{ox} + \omega_p}{\omega_{ox}\omega_{oy} - \omega_p^{\,2}},$$

and (3.55)

$$q_{AL} = \frac{\omega_{ox} - \omega_p}{\omega_{ox}\omega_{oy} - \omega_p^{\,2}}\,.$$

See Schloemann *et al*. [1963] for the exact stiffness frequency expressions. As with Patton, Schloemann's uniform mode coefficients contain a nonzero anti-Larmor term as well as stiffness frequency terms in the numerator. Instead of making these stiffness frequency terms complex, Schloemann instead transformed the above equation into a different coordinate frame in which the uniform mode was nearly circularly polarized.

The transformation was performed by requiring $\alpha_o(t) = \beta_o(t) + \Lambda\beta_o(t)^*$, and resulted in the following transformed uniform mode equation

$$\beta_o(t) = \frac{|\gamma| h_o}{2(1-\Lambda)}\left[\frac{1}{\omega_o - \omega_p}e^{i\omega_p t} + \frac{1}{\omega_o + \omega_p}e^{-i\omega_p t}\right], \tag{3.56}$$

where $\Lambda = -(\omega_{ox} + \omega_{oy} - 2\omega_o)(\omega_{ox} - \omega_{oy})^{-1}$. Schloemann then added uniform mode damping into the theory by replacing $\omega_o \to \omega_o + i\eta_o$. Thereafter, he rewrote his nonlinear spin wave equation of motion in terms of β_o instead of α_o in order to obtain the desired threshold field equations.

3.3.3 Anti-Larmor CF Sign Problem

This subsection will show that there is a sign issue present in both Patton's [1969] and Schloemann's [1963] methods of adding damping to the anti-Larmor coefficients of the uniform mode expression, which were discussed in the previous section. In order to identify the sign problem, both the transient as well as the steady state response will be analyzed here.

A general uniform mode solution that includes both the transient and the steady state solutions may be written as

$$\alpha_o(t) = A_L e^{i\omega_o t} + A_{AL} e^{-i\omega_o t} + B_L e^{i\omega_p t} + B_{AL} e^{-i\omega_p t}. \tag{3.57}$$

The first two terms in Eq. (3.57) are transient terms and the second two are the steady state terms. It is clear that in order to damp out the transient terms, one can replace the resonant frequency ω_o with a complex term Ω_o. But, note that the sign of the complex component ($\Omega_o = \omega_o \pm i\eta$) depends on the sign of the $i\omega_o t$ term in the exponents of the transient terms. In Patton's and Schloemann's work discussed in the previous section both the positive (Larmor) and negative (anti-Larmor) exponential terms were treated with the same complex frequency sign. This corresponds to an anti-Larmor transient response that grows (not decays) exponentially with time $e^{(-i\omega_o+\eta_o t)}$.

For clarity, the corrected form of the uniform mode solution, which has the proper complex frequency damping signs, and is utilized in this work, can be written as

$$\alpha_o(t) = \frac{|\gamma| h_o}{2}\left[q_L e^{i\omega_p t} + q_{AL} e^{-i\omega_p t} \right]. \tag{3.58}$$

where

$$q_L = \frac{\left(\Omega_{oy} + \omega_p\right) a_x e^{i\delta_x} + i\left(\Omega_{ox} + \omega_p\right) a_y e^{i\delta_y}}{\Omega_o{}^2 - \omega_p{}^2}$$

and (3.59)

$$q_{AL} = \frac{\left(\Omega_{oy}{}^* - \omega_p\right) a_x e^{-i\delta_x} + i\left(\Omega_{ox}{}^* - \omega_p\right) a_y e^{-i\delta_y}}{\left(\Omega_o{}^*\right)^2 - \omega_p{}^2}.$$

The above complex frequencies terms are $\Omega_o = \omega_o + i\eta_o$, $\Omega_{ox} = \omega_{ox} + iq_o$, and $\Omega_{oy} = \omega_{oy} + iq_o$, where the relationship between q_o, η_o, and ΔH_{FMR} are given in Eq. (3.46) and Eq. (3.54), respectively.

3.3.4 Landau-Lifshitz & Bloch-Bloembergen

While it is obvious that the sign of the anti-Larmor complex damping term has a significant effect on the transient response, it is not yet clear how significant the sign of the anti-Larmor term is for the steady state solution. In order to address the significance of the sign, this section will compare the steady state uniform mode solutions obtained from the torque equation of motion using complex frequency (CF) damping terms with those solutions obtained from the Landau-Lifshitz (LL) and Bloch-Bloembergen (BB) uniform mode equations of motion, which contain damping from the onset, and hence do not require complex frequencies. It will be shown that the anti-Larmor uniform mode coefficient (q_{AL}) obtained with the corrected CF technique is in good agreement with those obtained from the LL and the BB equations of motion. It will also be shown that there is a noticeable sign difference in the q_{AL} expression obtained with the original CF technique, which had the sign problem, compared to the LL and BB solutions.

For the comparison performed here, the hexagonal thin film sample geometry and static field orientation shown in Fig. 3.2(d) and a linearly polarized microwave field of the form $\mathrm{h}_p(t) = h_o \cos(\omega_p t)\,\hat{\mathrm{y}}$ are utilized.

The Landau-Lifshitz and Bloch-Bloembergen equations of motion can be written as

$$\frac{\partial \mathbf{M}(\mathbf{r},t)}{\partial t} = -\left|\gamma\right| \mathbf{M}(\mathbf{r},t) \times \mathbf{H}_{\mathbf{eff}}(\mathbf{r},t) - \mathbf{DampingTerm}\,, \tag{3.60}$$

where the (LL) and (BB) phenomenological damping terms and are given as

$$\mathbf{DampingTerm}_{\mathbf{LL}} = \alpha \frac{|\gamma|}{M_s} \mathrm{M} \times \left(\mathbf{M} \times \mathbf{H}_{\mathrm{eff}} \right) \text{ and}$$
$$\mathbf{DampingTerm}_{\mathbf{BB}} = \frac{1}{\mathrm{T}} \left(m_x \hat{\mathbf{x}} + m_y \hat{\mathbf{y}} \right), \tag{3.61}$$

respectively. Here, α is the dimensionless LL damping term, and $1/\mathrm{T}$ is the BB relaxation rate. Upon inspection of the above damping terms, one can see that the LL damping term is used to describe processes that conserve $\left| \mathbf{M}(\mathbf{r},t) \right|$, whereas BB models damping processes that result in a decrease in $\left| \mathbf{M}(\mathbf{r},t) \right|$.

Figure 3.4 shows a sketch of the relaxation paths of the magnetization vector (in the absence of a microwave-pumping field) described by the LL and BB damping models. Upon inspection of Eq. (3.61), one can see that the LL damping equation models damping mechanisms, which scale with the uniform mode processional frequency (since $\mathbf{M} \times \mathbf{H}_{\mathbf{eff}} \sim \dot{\mathbf{M}}$, as shown in Eq. (3.60)). Whereas the BB damping equation models damping processes, which are constant with frequency. For more details on these two damping types see Lax and Button [1962], Patton [1975], and Sparks [1964].

The uniform mode steady state solutions to the LL and BB equations can be obtained with the same procedure as described previously, i.e., (i) a complex uniform mode response term $\alpha_o(t)$ is introduced, (ii) all nonlinear $\alpha_o(t)$ and spin wave terms are neglected, and (iii) the resulting two first order coupled differential equations are combined into a single second order differential equation for $\alpha_o(t)$. Note that care must be taken to not confuse the above LL α damping and the uniform mode $\alpha_o(t)$ terms. After performing the above steps on equations (3.60) and (3.61) one obtains the following governing equation of a damped driven harmonic oscillator

$$\frac{\partial^2 \alpha_o(t)}{\partial t^2} + 2\eta \frac{\partial \alpha_o(t)}{\partial t} + \lambda^2 \alpha_o(t) = F(t), \tag{3.62}$$

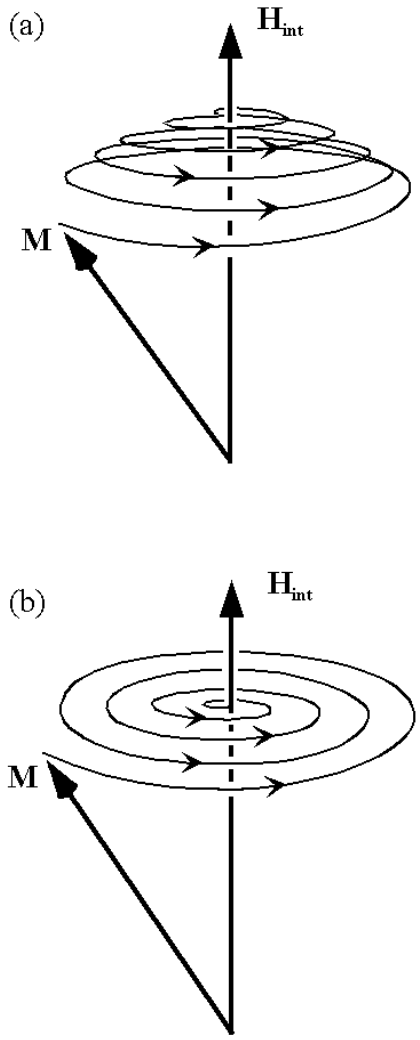

Figure. 3.4. Sketch of the free decay of the magnetization (**M**) vector in the absence of a microwave pump field. The relaxation response is shown for damping processes that (a) conserve (LL) and (b) do not conserve (BB) the length of **M**, after [Hurben, 1996].

where η is the damping rate, λ is the resonance frequency, and $F(t)$ is the effective driving function.

The damping terms for the LL and BB equations of motion are

$$\eta_{\mathrm{LL}} = (\alpha/2)\left(\omega_{\mathrm{ox}} + \omega_{\mathrm{oy}}\right)$$

and (3.63)

$$\eta_{\mathrm{BB}} = 1/\mathrm{T},$$

respectively, and the forcing terms for the two processes are

$$F_{\mathrm{LL}} = |\gamma|\left[(1+i\alpha)\dot{h}_y(t) + i\omega_{\mathrm{ox}} h_y(t)\right]$$

and (3.64)

$$F_{\mathrm{BB}} = |\gamma|\left[\dot{h}_y(t) + (i\omega_{\mathrm{ox}} + 1/\mathrm{T})\, h_y(t)\right].$$

The Larmor (q_L) and anti-Larmor (q_{AL}) uniform mode coefficients for the LL and BB equations of motion can be determined by substituting $\alpha_o = (|\gamma| h_o / 2)(q_L \mathrm{e}^{i\omega_p t} + q_{AL} \mathrm{e}^{-i\omega_p t})$ into Eq.(3.62) and solving for q_L and q_{AL}.

Table 3.1 summarizes the steady state uniform mode coefficients q_L and q_{AL} which are obtained with the four different damping models. The first column describes which type of damping is being analyzed. The CF-1 method corresponds to the complex frequency technique that used the wrong sign for the anti-Larmor complex frequency term, i.e., where $\Omega_o = \omega_{\mathrm{o}} + i\eta_o$ is used for both Larmor and anti-Larmor coefficients. The CF-2 method corresponds to the corrected complex frequency technique where the complex conjugate $\Omega_o^{\,*} = \omega_o - i\eta_o$ is used for q_{AL}. The damping methods labeled LL and BB correspond to solutions obtained with the Landau-Lifshitz and Bloch-Bloembergen equations of motion, respectively. The second and third columns are the q_L and q_{AL} expressions, and the last column is q_{AL} at resonance ($\omega_{\mathrm{o}} = \omega_p$).

An inspection of Table 3.1 reveals the following three key findings: (1) the complex frequency method used by Patton to model uniform mode damping results in very similar uniform mode coefficient equations as the LL and BB equations of motions, (2) the original complex frequency model utilized by Patton leads to a notable sign difference in the steady state anti-Larmor coefficients compared to the LL and BB results, and (3) the modified complex frequency approach, in which the anti-Larmor damping is modeled with the negative damping sign, is in excellent agreement with the

Damping Method	**Larmor Term** (q_L)	**Anti - Larmor Term** (q_{AL})	**Anti - Larmor Term at FMR Resonance** $q_{AL}(\omega_p = \omega_o)$
CF-1	$\dfrac{i(\omega_{ox}+\omega_p)-\dfrac{2\eta\omega_o}{\omega_{ox}+\omega_{oy}}}{(\omega_o^2-\omega_p^2)+i(2\eta\omega_o)}$	$\dfrac{i(\omega_{ox}-\omega_p)-\dfrac{2\eta\omega_o}{\omega_{ox}+\omega_{oy}}}{(\omega_o^2-\omega_p^2)+i(2\eta\omega_o)}$	$+\left(\dfrac{\omega_{ox}-\omega_o}{2\eta\omega_o}\right)+\dfrac{i}{\omega_{ox}+\omega_{oy}}$
CF-2	$\dfrac{i(\omega_{ox}+\omega_p)-\dfrac{2\eta\omega_o}{\omega_{ox}+\omega_{oy}}}{(\omega_o^2-\omega_p^2)+i(2\eta\omega_o)}$	$\dfrac{i(\omega_{ox}-\omega_p)+\dfrac{2\eta\omega_o}{\omega_{ox}+\omega_{oy}}}{(\omega_o^2-\omega_p^2)-i(2\eta\omega_o)}$	$-\left(\dfrac{\omega_{ox}-\omega_o}{2\eta\omega_o}\right)+\dfrac{i}{\omega_{ox}+\omega_{oy}}$
LL	$\dfrac{i(\omega_{ox}+\omega_p)-\dfrac{2\eta_{LL}\omega_p}{\omega_{ox}+\omega_{oy}}}{(\omega_o^2-\omega_p^2)+i(2\eta_{LL}\omega_p)}$	$\dfrac{i(\omega_{ox}-\omega_p)+\dfrac{2\eta_{LL}\omega_p}{\omega_{ox}+\omega_{oy}}}{(\omega_o^2-\omega_p^2)-i(2\eta_{LL}\omega_p)}$	$-\left(\dfrac{\omega_{ox}-\omega_o}{2\eta_{LL}\omega_p}\right)+\dfrac{i}{\omega_{ox}+\omega_{oy}}$
BB	$\dfrac{i(\omega_{ox}+\omega_p)+\eta_{BB}}{(\omega_o^2-\omega_p^2)+i(2\eta_{BB}\omega_p)}$	$\dfrac{i(\omega_{ox}-\omega_p)+\eta_{BB}}{(\omega_o^2-\omega_p^2)-i(2\eta_{BB}\omega_p)}$	$-\left(\dfrac{\omega_{ox}-\omega_o}{2\eta_{BB}\omega_o}\right)+\dfrac{i}{2\omega_o}$

Table 3.1. Summary of the Larmor (q_L) and anti-Larmor (q_{AL}) uniform mode coefficients obtained from the torque equation of motion using the published complex frequency technique (CF-1), corrected complex frequency technique (CF-2), Landau Lifshitz equation of motion (LL), and Bloch Bloembergen equation of motion (BB). Note that for CF-1, the damping term in the numerator of q_{AL} is positive; while for CF-2, LL, and BB it is negative.

LL and BB results. These findings provide considerable credibility to Patton's method of making the stiffness frequencies complex and show that the sign of the damping term used for the anti-Larmor complex frequency effects both the uniform mode transient and steady state solutions.

3.3.5 Impact of the CF Sign Issue

The impact of using with the wrong anti-Larmor complex frequency (CF) sign on the steady state uniform mode response depends upon the relative magnitude of the anti-Larmor $|q_{AL}|$ and Larmor $|q_L|$ coefficients. This section will show that the ratio of $|q_{AL}|/|q_L|$ depends upon: (1) the sample and static magnetic field geometry, (2) the magnitude and orientation of the anisotropy, and (3) the operating frequency.

Figure 3.5 shows plots of the Larmor and anti-Larmor uniform mode coefficients versus the external magnetic field for four different cases: (i) isotropic sphere, (ii) isotropic thin-film, (iii) anisotropic thin film, and (iv) anisotropic sphere. The plots in Fig. 3.5 were calculated with the CF-2 corrected complex frequency expressions given in Table 3.1, using saturation magnetization ($4\pi M_s$) and FMR linewidth (ΔH_{FMR}) of 2850 Gauss and 10 Oe, respectively. An anisotropy field of $|H_A| = 9.5$ kOe was used for the anisotropic samples. The above saturation magnetization, FMR linewidth, and anisotropy values are typical for Mn-doped Zn Y-type hexagonal single crystal samples studied here. The numeric results shown in the upper three plots were calculated with a microwave pump frequency of 10 GHz, and a value of 30 GHz was used for the fourth plot. The units of the vertical axes are 1/GHz. The solid and dotted lines in the plots correspond to $|q_L|$ and $|q_{AL}|$, respectively.

As can be seen in the figure, $|q_{AL}|/|q_L|$ is the largest for the anisotropic sample geometry (c). However, anisotropy alone is not the reason for this, as can be seen in plot (d) which also has anisotropy but $|q_{AL}| = 0$. Rather $|q_{AL}|/|q_L|$ is a maximum when the stiffness fields H_{ox} and H_{oy} are very different, and the uniform mode is highly elliptical. See Fig. 3.2 for a summary of the stiffness fields for the cases (a) through (c) shown in Figure 3.5. The stiffness fields for Fig. 3.5(d) are equal to $H_{ox} = H_{oy} = H_{ext} + |H_A|$. This results in the FMR resonance frequency being the largest of all the other cases shown in the figure. Hence $\omega_p = 30$ GHz was used for plot(d) and $|q_{AL}| = 0$.

The relative magnitude of $|q_{AL}|$ and $|q_L|$ not only depends upon sample geometry, anisotropy, and static field orientation but also upon the operating frequency of the applied microwave field. To show this, we will now focus on the uniform mode coefficients at resonance $(\omega_o = \omega_p)$ for case Fig. 3.5(c) at different operating frequencies.

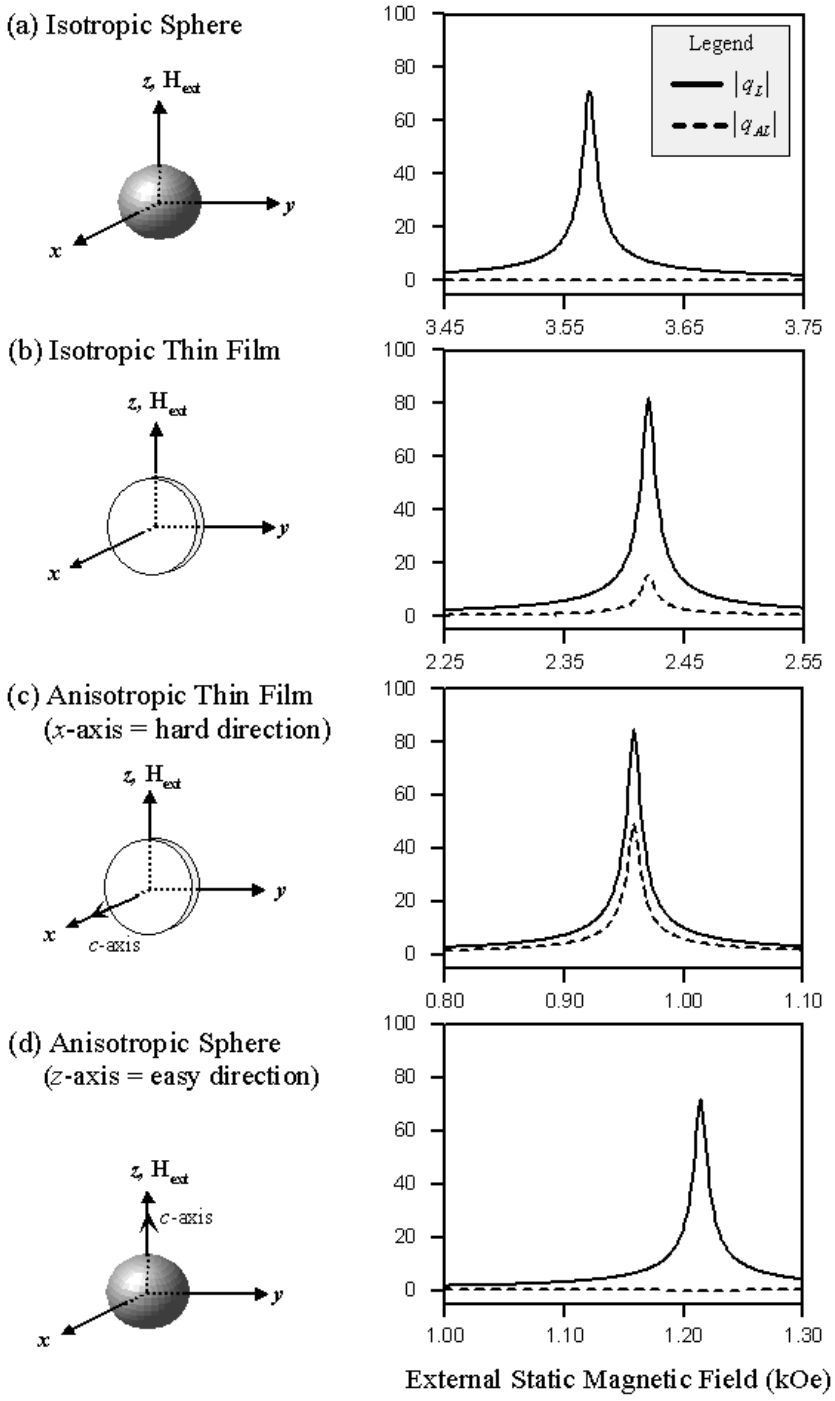

Figure. 3.5. Magnitude plots of Larmor (solid line) and anti-Larmor (dotted line) uniform mode coefficients versus external static magnetic field. Calculations were performed with the CF-2 expressions given in Table 3.1, using sample parameter values of $\Delta H_{FMR} = 10\,\text{Oe}$, $4\pi M_s = 2.85\,\text{kOe}$, $|\gamma| = 2.8\,\text{GHz/kOe}$, and the field and sample geometry as shown. A pump frequency of 10 GHz was used for the plots (a)-(c), and 30 GHz was used for plot (c).

Figure 3.6 shows a plot of the relative magnitude of $|q_{AL}|/|q_{AL}|$ versus the microwave frequency. The calculations were performed with $H_{\text{ext}} = H_{\text{FMR}}$ such that $\omega_{\text{o}} = \omega_p$ for all frequency points. The sample parameters and orientation shown in Fig 3.5 (c) were utilized. One can clearly see that as the frequency is increased, the relative magnitude of the anti-Larmor coefficient decreases significantly compared to the Larmor coefficient. Therefore, the effects of utilizing the wrong sign are the largest at the lower operating frequencies.

In summary, the effects of using the incorrect anti-Larmor complex frequency damping sign on the calculated uniform mode response increase with the ellipticity of the uniform mode precession cone. This ellipticity is the largest for samples with high anisotropy, under the appropriate static field and sample orientation, at low operating frequencies. Such a condition will be addressed in Section 3.6 of this chapter. It will be shown there, that the incorrect anti-Larmor damping sign has a notable effect on the calculated resonance saturation instability threshold fields.

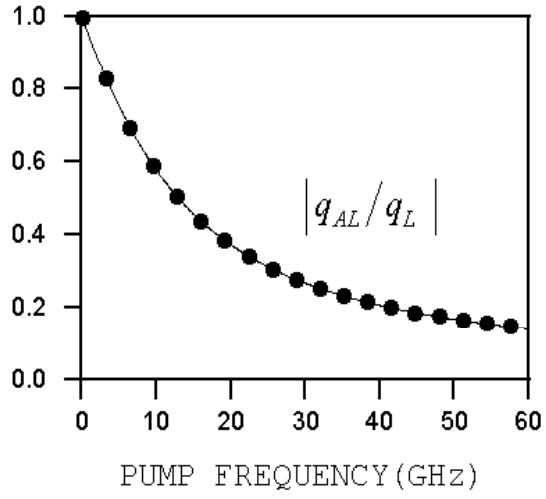

Figure. 3.6. Plot of ratio ($|q_{AL}|/|q_L|$) versus operating frequency. The calculations were performed with the sample parameters, geometry, and field orientation given in Fig.3.5(c). For each frequency point, the ratio was calculated with $H_{ext} = H_{FMR}$.

3.4 LINEAR SPIN WAVE ANALYSIS

In this section, the linear spin wave dispersion relation $\omega_k(\mathbf{k})$ and the spin wave eigen vectors are obtained from a simplified version of the reduced equation of motion. As with the linear uniform mode analysis, stiffness fields will be introduced in order to help with understanding the physics of the dispersion relationship. Then the so-called spin wave manifold, which graphically summarizes the ω_k dependence upon $\mathbf{H}_{\mathbf{ext}}$, $\mathbf{k}$, and $\mathbf{H}_{\mathbf{A}}$ is introduced and the effects of anisotropy upon the manifold are discussed. Lastly, the linear spin wave eigen vectors are used to construct a transformation matrix, which is utilized in the next section to transform the nonlinear spin wave differential equations into a more readily solvable form.

Prior to proceeding with the linear spin wave theory analysis, we will briefly review the physical model of spin waves in bulk ferromagnetic materials. As was discussed in Chapter 2, a ferromagnetic sample can be considered to be a periodic array of individual exchange coupled dipole moments or spins, where the net magnetization is the volume average of these individual moments. A spin wave corresponds to a propagating plane wave of the dynamic magnetization in which all the dipole moments precess with the same frequency throughout the sample but with a different phase from point to point along the propagation direction. In the bulk spin wave theory, which is being addressed here, all spin wave interactions with the sample boundaries are ignored.

Figure 3.7 shows an illustration of the spherical coordinate system which is utilized here to describe the spin wave propagation direction and shows a schematic diagram of the precessing dipole moments for spin waves traveling parallel and perpendicular to the static equilibrium direction.

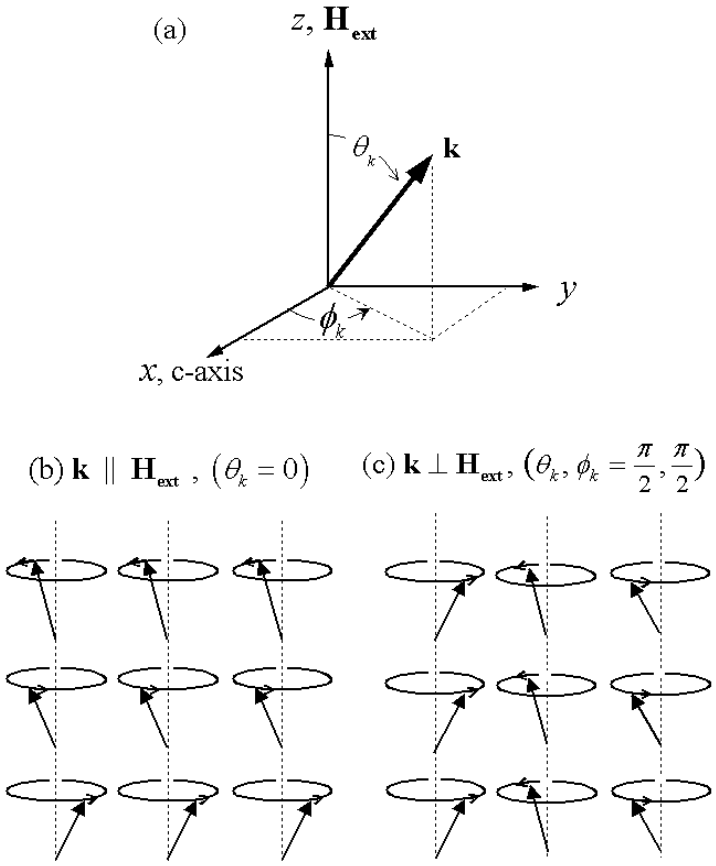

Figure. 3.7. Illustrations of the (a) spherical coordinate system used to describe spin wave propagation direction, and the constituent dipole moments for spin waves traveling (b) parallel and (c) perpendicular to the external static magnetic field direction.

3.4.1 Spin Wave Frequency

The linear spin wave equation of motion is obtained by neglecting the nonlinear terms in the reduced equation of motion given in Eq. (3.25). This results in two linear coupled differential equations for $\alpha_k(t)$ and $\alpha_{-k}^{*}(t)$, which may be written in matrix form as

$$\frac{\partial}{\partial t}\begin{bmatrix} \alpha_k \\ \alpha_{-k}^{*} \end{bmatrix} - i\begin{bmatrix} A_k & B_k \\ -B_k^{*} & -A_k \end{bmatrix}\begin{bmatrix} \alpha_k \\ \alpha_{-k}^{*} \end{bmatrix} = \begin{bmatrix} 0 \\ 0 \end{bmatrix}. \tag{3.65}$$

These equations can be readily uncoupled into the following second order linear differential equation

$$\frac{\partial^2 \alpha_k(t)}{\partial t^2} + \omega_k{}^2 \alpha_k(t) = 0. \tag{3.66}$$

This equation corresponds to the governing equation of an undamped undriven harmonic oscillator, where ω_k is the natural frequency of the oscillator. No driving terms appear in Eq. (3.66) because based upon assumption (4) discussed in Section 4.1 the linear microwave field terms in the reduced equation of motion (Eq. (3.28)) were associated with the linear uniform mode equation. It can be readily shown that when Eq. (3.65) is converted into the form of Eq. (3.66), one obtains the following ω_k equation

$$\omega_k{}^2 = |A_k|^2 - |B_k|^2 . \tag{3.67}$$

The A_k and B_k terms, which were defined previously in Eq. (3.29), can be written as

$$A_k = |\gamma|\left(H_{\text{int}} + \frac{1}{2} 4\pi M_s \sin^2\theta_k + Dk^2 - \frac{1}{2} H_A \right),$$

and (3.68)

$$B_k = |\gamma|\left(\frac{1}{2} 4\pi M_s \sin^2\theta_k \, e^{2i\phi_k} - \frac{1}{2} H_A \right).$$

The H_{int} term in Eq. (3.68) is the internal static field given as $H_{\text{int}} = H_{ext} - 4\pi M_s N_z$, the D term is the exchange constant, and H_A is the anisotropy field.

As with the uniform mode analysis, the spin wave frequency can be rewritten in terms of stiffness fields and provide physical insight into the spin wave dispersion relationship. These stiffness fields are defined with the following relationship:

H_A	θ_k, ϕ_k	H_{kx}	H_{ky}
0	0, NA	$H_{\text{int}} + Dk^2$	$H_{\text{int}} + Dk^2$
0	$\frac{\pi}{2}, 0$	$H_{\text{int}} + Dk^2 + 4\pi M_s$	$H_{\text{int}} + Dk^2$
0	$\frac{\pi}{2}, \frac{\pi}{2}$	$H_{\text{int}} + Dk^2$	$H_{\text{int}} + Dk^2 + 4\pi M_s$
< 0	0, NA	$H_{\text{int}} + Dk^2 + \lvert H_A \rvert$	$H_{\text{int}} + Dk^2$
< 0	$\frac{\pi}{2}, 0$	$H_{\text{int}} + Dk^2 + 4\pi M_s + \lvert H_A \rvert$	$H_{\text{int}} + Dk^2$
< 0	$\frac{\pi}{2}, \frac{\pi}{2}$	$H_{\text{int}} + Dk^2 + \lvert H_A \rvert$	$H_{\text{int}} + Dk^2 + 4\pi M_s$
> 0	0, NA	$H_{\text{int}} + Dk^2 - \lvert H_A \rvert$	$H_{\text{int}} + Dk^2$

Table 3.2. Summary of the spin wave H_{kx} and H_{ky} stiffness fields for different spin wave propagation directions and anisotropies. Anisotropy values of $H_A = 0$, $H_A < 0$, and $H_A = 0$ correspond to isotropic, *y-z* easy-plane anisotropy, and *x-axis* uniaxial anisotropy, respectively.

$$\omega_k^{\,2} = |\gamma|^2 H_{\text{kx}} H_{\text{ky}} , \tag{3.69}$$

where H_{kx} and H_{ky} correspond to static magnetic fields which apply a torque upon the dipole moments as they rotate away from the equilibrium direction (*z*-axis) into the *z-x* and *z-y* planes, respectively. From an inspection of Eqs. (3.67) and (3.69) one can see that the spin wave stiffness fields may be written as

$$H_{\text{kx}} = \left(|A_k| + |B_k| \right) / |\gamma|$$

and (3.70)

$$H_{\text{ky}} = \left(|A_k| - |B_k| \right) / |\gamma| .$$

Table 3.2 summarizes the stiffness fields for spin waves propagating in the principal *x*, *y* and *z* directions in both isotropic and anisotropic samples. The first column, titled H_A, identifies what type of anisotropy is present. Values of $H_A = 0$, $H_A < 0$, and

$H_A > 0$ correspond to a samples that have no anisotropy, planar anisotropy with easy plane in the *y*-*z* plane, and uniaxial anisotropy with easy direction in the *x*-direction, respectively. The second column in Table 3.2 identifies the spin wave propagation direction (θ_k, ϕ_k), and the third and forth columns correspond to the H_{kx} and H_{ky} stiffness fields. The fields were determined from relationships given in Eqs. (3.70) and (3.68) and the sample and field orientation shown in Fig. 3.1 and Fig. 3.7. Unlike for the uniform mode case, the spin wave stiffness fields are not highly dependent on the sample geometry. This is as one would expect because spin wave sample boundary effects are ignored here.

First consider the stiffness fields for the isotropic case $(H_A = 0)$ given in Table 3.2. For spin waves traveling parallel to the static equilibrium direction ($\theta_k = 0$) there are two torque sources, one due to the internal static field H_{int} and the other from the exchange field Dk^2. Both of these magnetic fields work to resist the tilt of the precessing dipole moments from the *z*-axis and result in the same amount of torque being applied to the precessing dipole moments regardless if they are tilted from the z-axis into the *z*-*x* or the *z*-*y* planes. Therefore, $H_{kx} = H_{ky} = H_{\text{int}} + Dk^2$. For spin waves traveling perpendicular to the static equilibrium direction ($\theta_k = \pi / 2$) a third torque source due to the self dipole-dipole interactions of the precessing dipole moments is present. This dipole field applies a torque that is in the opposite to the spin wave propagation direction. The magnitude of the torque field is the same regardless of if the spin waves are propagating in the *x* or the *y* direction, but its association with H_{kx} or H_{ky} depends on whether the spin waves are traveling in the *x* or *y* directions, respectively. The spin wave frequency is the combination of the two stiffness fields $\omega_k = |\gamma| \sqrt{H_{\text{kx}} H_{\text{ky}}}$, so for the isotropic sample ω_k is the same regardless if the spin waves are propagating in the *x* or the *y* directions. In other words, ω_k is independent of ϕ_k for an isotropic sample.

Now consider the stiffness fields for the anisotropic sample $(H_A \neq 0)$ given in Table 3.2. For this case, a fourth torque field due to the anisotropy field is now present.

For the planar anisotropy ($H_A < 0$) case, the anisotropy field applies a torque such as to oppose a tilt of a dipole moment from the *z* to the *x* direction. This field acts in a very similar fashion as H_{int} but is only present in H_{kx}, and not in H_{ky}. For the uniaxial anisotropy ($H_A > 0$) case, the *x*-axis is the easy-direction, and the anisotropy field now works against H_{ext}, trying to rotate the dipole moments away from the *z*-axis into the *x* direction. Note that for both the planar and uniaxial cases, the product of H_{kx} and H_{ky} is not the same for spin wave propagating in the *x* and *y* directions, i.e., the spin wave frequency is now dependent upon ϕ_k. This dependence will be discussed in more detail shortly. Prior to this, we will first discuss the relationship between the stiffness fields and the ellipticity of spin wave precessing dipole moments.

As with the uniform mode, the ellipticity of the precessing dipole moments are directly related to the stiffness fields. If $H_{kx} = H_{ky}$, then the dipole moments experience the same amount of torque whether they are tilted away from the *z*-axis to the *x* or *y* directions. Therefore, $m_{kx} = m_{ky}$ and the precessional cones are circular. If $H_{kx} > H_{ky}$, then the dipole moments experiences more torque when they are tilted into the *x*-direction than when they are tilted into the *y* direction, $m_{kx} < m_{ky}$, and the elliptical precessional cones are elliptical.

Figure 3.8 summarizes the ellipticity of the spin wave dipole precessional cones for several propagation directions in an isotropic and an anisotropic sample. Diagram (a) in the figure illustrates the orientation of the precessional cones. The cones are viewed from the positive *z*-axis, and rotate in the counter-clockwise Larmor direction. The lower diagrams in the figure show the relative magnitude and phase of the precessing dipole moments for spin waves traveling in the *x* and *y* directions for both (b) isotropic and (c) planar anisotropic samples. See Table 3.2 for the explicit H_{kx} and H_{ky} equations for the above cases.

First consider the isotropic case shown in Fig. 3.8(b). As is seen in Table 3.2, a spin wave traveling along the *x*-axis $(\theta_k, \phi_k = \pi/2, 0)$ has $H_{kx} > H_{ky}$ and therefore $m_{kx} < m_{ky}$,

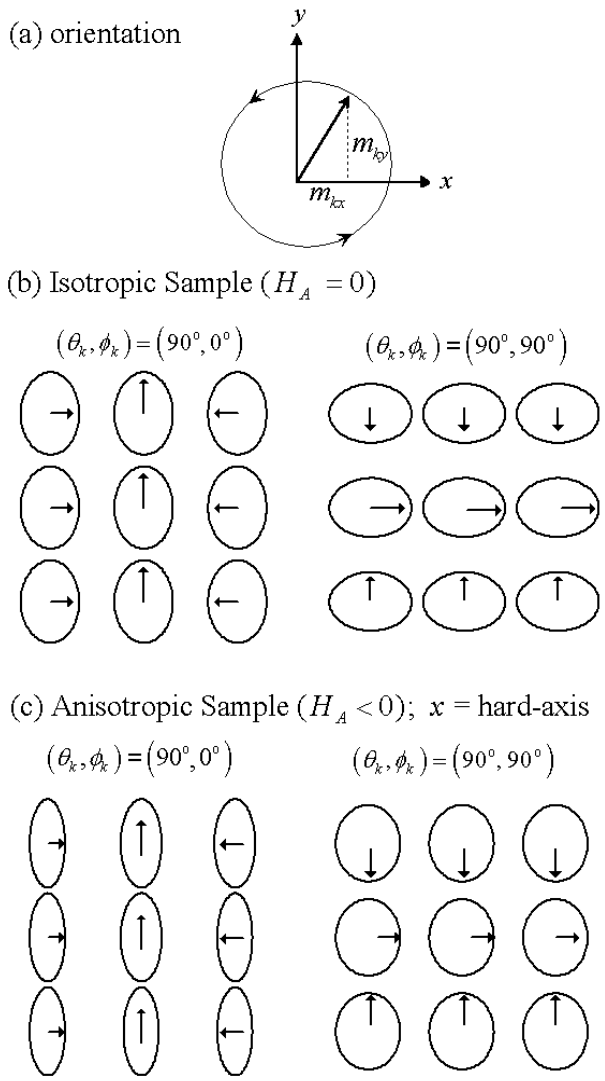

Figure. 3.8. Top view of the precessing dipole moments that comprise spin waves propagating in the x $(\theta_k, \phi_k = \pi/2, 0)$ and y $(\theta_k, \phi_k = \pi/2, \pi/2)$ directions, for the sample and field geometry shown in Fig. 3.5(c). The self dipole-dipole fields act to minimize the dynamic component of the magnetization that is parallel to the propagation direction, and the anisotropy field acts to minimize the dynamic component that is aligned in the hard-direction.

whereas a spin wave traveling along the y-axis $(\theta_k, \phi_k = \pi/2, \pi/2)$ has $m_{kx} > m_{ky}$. For both propagation directions, the precession cones are elliptical, with the minor axis aligned in the propagation direction. For spin waves traveling in the z-axis direction $(\theta_k = 0)$, $H_{kx} = H_{ky}$ and precessional cones are circular (not shown in the figure).

Now consider the precessional cones for the planar anisotropy case shown in Fig. 3.8 (c). As can be seen in Table 3.2, if $|H_A| > 4\pi M_s$ then $H_{kx} > H_{ky}$ for spin waves traveling in the *x*, *y*, and *z* directions. For spin waves traveling in the *x* direction, the effect of the anisotropy reinforces the dipole-dipole induced preference for alignment along the *y*-axis and therefore $m_{kx} << m_{ky}$. For spin waves traveling along the *y* direction, the torque field from the anisotropy field counteracts the effect of the dipole-dipole interactions, and $m_{kx} < m_{ky}$. Finally consider the precessional cones for spin waves traveling in the *z*-axis for the anisotropic sample (case not shown in Fig. 3.8). For this case, there is no longer any dipole field present to increase or decrease the effect of $|H_A|$, so an elliptical precession is obtained which has a relative ellipticity that is between the two cases shown in Fig. 3.8(c).

The above discussions regarding the spin wave frequency, stiffness fields, and ellipticity have been limited to spin waves propagating only along the principle *x*, *y*, or *z* coordinate axis. Attention will now given to a general spin wave dispersion relation for spin wave propagating in an arbitrary direction. This relation is obtained by substituting the A_k and B_k expressions given in Eq. (3.65) into Eq. (3.64) and may be written as

$$\frac{\omega_k^2}{|\gamma|^2} = \left(H_{int} + Dk^2\right)\left(H_{int} + Dk^2 + 4\pi M_s \sin(\theta_k)^2 - H_A\right) - H_A 4\pi M_s \sin(\theta_k)^2 \sin(\phi_k)^2 . \quad (3.71)$$

In the limit of zero anisotropy, Eq. (3.71) reduces to the well-known isotropic bulk spin wave dispersion relation first developed by Kittel [1947] and Herring and Kittel [1951]. Upon inspection of Eq. (3.71), one can see that anisotropy has the following two main effects on the spin wave manifold: (1) it acts as an added internal field which either boosts or opposes the applied external magnetic field depending on whether the anisotropy is planar (negative sign) or uniaxial (positive sign), respectively, and (2) it introduces a dependence upon the azimuthal angle ϕ_k.

Figure 3.9 shows a three-dimensional sketch of the spin wave dispersion relationship. The plot is for an anisotropic sample with planar anisotropy in the *y*-*z* plane (orientation shown in Fig. 3.5(c)). The spin wave band, which is commonly referred to as the spin wave manifold, consists of the region between the lower and upper planes. The upper and lower bounding planes correspond to spin wave polar propagation angles $\theta_k = \pi/2$ and $\theta_k = 0,$ respectively.

As was discussed in Chapter 2, the spin wave manifold can be understood physically via energy considerations. The Zeeman energy from the static field causes the whole manifold to move up with increasing external magnetic field strength. The exchange

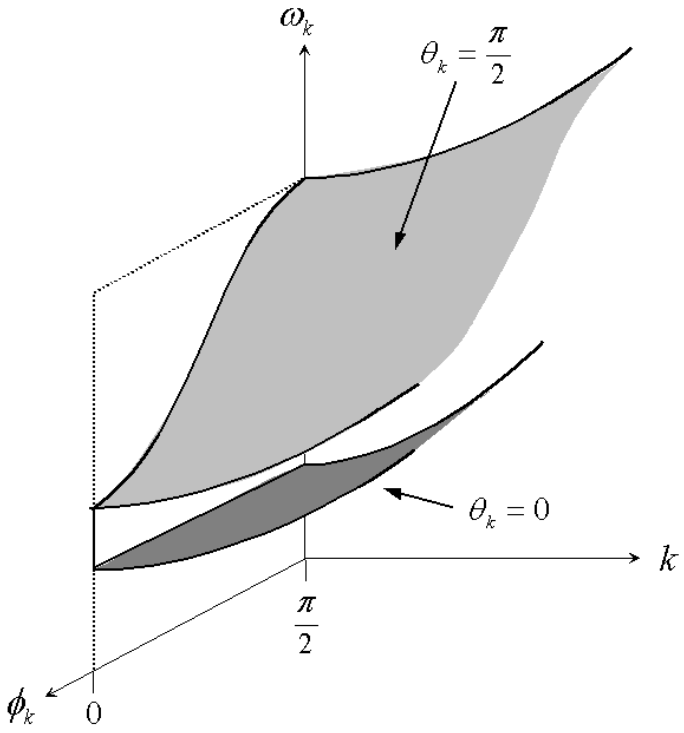

Figure 3.9. Three-dimensional sketch of the spin wave dispersion manifold for an easy-plane anisotropic sample with static field and anisotropy orientation shown in Fig. 3.5(c). The upper and lower shaded surfaces in the sketch correspond to spin wave propagation directions normal and parallel to the z-axis, respectively. The orientation of the *k* axis was chosen such as to provide the best perspective of the manifold, after Hurben [1996].

energy is the source of the k^2 dependence, and the self dipole-dipole energy is the source of the θ_k dependence. The magneto crystalline anisotropy leads to the ϕ_k dependence, and it is also the cause of the warping of the manifold along the ϕ_k axis shown in the sketch. The reason the spin waves traveling along the *y*-direction have the highest energy is that they have the largest dipole-dipole energy. As can be seen in Fig. 3.8(c), anisotropy acts to reduce the ellipticity of these spin wave as compared to those traveling in the *x*-direction, this in turn results in higher dipole-dipole energy. For a more detailed discussion on the effects of anisotropy on spin wave dispersion and the effects of applying the external static magnetic field off the principle axis, see Hurben [1996].

Figure 3.10 shows a representative set of spin wave dispersion curves for a thin Zn Y-type hexagonal ferrite disk. The graph shows the spin wave frequency as a function of the wave number *k* for the three principal dispersion branches. The solid circle at about 9 GHz on the vertical axis and the dashed line, which crosses the two lower curves, indicate the FMR frequency. As is seen in the figure, anisotropy leads to a warping in

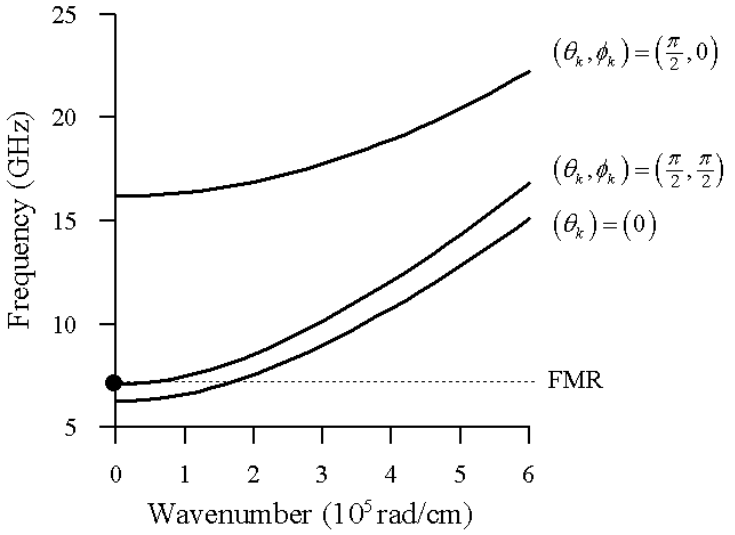

Figure. 3.10. Plot of calculated spin wave frequency versus wave number for the different spin wave propagation directions given in the plot. The curves were calculated using the Zn Y-type hexagonal ferrite sample parameters given in the text, a static field of 500 Oe, and the orientation shown in Fig 3.5(c). The solid circle and the horizontal dashed line indicate the ferromagnetic resonance frequency.

the manifold at about 8 GHz. These numeric results were calculated with standard values associated with the Zn Y-type hexagonal ferrite disc used here, in which $4\pi M_s = 2.85\,\text{kG}$, $N_x = 1$, $N_y = N_z = 0$, $|\gamma| = 2.8\,\text{GHz/kOe}$, $D = 5.4\cdot 10^{-9}\,\text{Oe}/\text{cm}^2$, and $H_A = -9.5\,\text{kOe}$ (negative sign corresponds to planar anisotropy). A static field of 850 Oe and the sample and external field orientation shown in Fig. 3.5(c) were utilized.

3.4.2 Steady State Solutions

The historical approach to obtain the steady state spin wave solutions (eigen vectors) has been to perform a Holstein-Primakoff transformation on Eq. (3.72) using preselected hyperbolic trigonometric functions (Suhl [1957]). This approach is overly cumbersome, involving an unnecessarily large amount of algebraic manipulations, especially when anisotropy is included in the theory. A much simpler approach is to just solve the linear spin wave equation of motion for the eigen vectors with standard linear algebra techniques and then construct the transformation matrix from these vectors (Schloemann *et al*. [1963]). This is the approach utilized here. To do so we can rewrite Eq. (3.63) in matrix form as

$$\frac{\partial}{\partial t}\vec{\mathrm{v}}_{\mathrm{k}} = i\overleftrightarrow{A}\,\vec{\mathrm{v}}_{\mathrm{k}} \tag{3.72}$$

where

$$\vec{\mathrm{v}}_{\mathrm{k}} = \begin{bmatrix} \alpha_k \\ \alpha_{-k}^{\,*} \end{bmatrix}$$

and (3.73)

$$\overleftrightarrow{A} = \begin{bmatrix} A_k & B_k \\ -B_k^{\,*} & -A_k \end{bmatrix}.$$

The eigen values (spin wave frequencies) are obtained by the matrix operation $\left|\vec{A}-\omega_k \vec{I}\right|=0$, where $\vec{I}$ is the identity matrix, and the eigen vectors are obtained by requiring $\left(\vec{A}\text{-}\omega_k \vec{\mathrm{I}}\right)\vec{\mathrm{v}}=0$. Upon doing this, one finds that the eigen vectors are

$$\mathbf{v}_+ = \begin{bmatrix} 1 \\ \Gamma^* \end{bmatrix} \quad \text{and} \quad \mathbf{v}_- = \begin{bmatrix} \Gamma \\ 1 \end{bmatrix} \tag{3.74}$$

where

$$\Gamma = \left(\omega_k - A_k\right) / B_k^{\,*} . \tag{3.75}$$

The inverse transformation matrix is then

$$\vec{\mathrm{T}}^{-1} = \begin{bmatrix} \mathbf{v}_+ & \mathbf{v}_- \end{bmatrix} = \begin{bmatrix} 1 & \Gamma \\ \Gamma^* & 1 \end{bmatrix}. \tag{3.76}$$

The transformation matrix is then determined by requiring that $\vec{\mathrm{T}}\,\vec{\mathrm{T}}^{-1}=1$ and solving for $\vec{\mathrm{T}}$. This results in the following expression

$$\vec{\mathrm{T}} = \frac{1}{1-\left|\Gamma\right|^2}\begin{bmatrix} 1 & -\Gamma \\ -\Gamma^* & 1 \end{bmatrix}. \tag{3.77}$$

When one applies the transformation matrix on the linear spin wave equation given in Eq. (3.72), it diagonalizes the $\vec{A}$ matrix and yields the spin wave dispersion frequency. This is done in the following manner:

$$\frac{\partial}{\partial t}\vec{\mathrm{v}}_{\mathrm{k}} = i\vec{\vec{A}}\,\vec{\vec{\mathrm{I}}}\,\vec{\mathrm{v}}_{\mathrm{k}}$$

$$\vec{\vec{\mathrm{T}}}\left\{\frac{\partial}{\partial t}\vec{\mathrm{v}}_{\mathrm{k}} = i\vec{\vec{A}}\,\vec{\vec{\mathrm{I}}}\,\vec{\mathrm{v}}_{\mathrm{k}}\right\}$$

$$\frac{\partial}{\partial t}\vec{\vec{\mathrm{T}}}\,\vec{\mathrm{v}}_{\mathrm{k}} = i\vec{\vec{\mathrm{T}}}\vec{\vec{A}}\,\vec{\vec{\mathrm{T}}}^{-1}\,\vec{\vec{\mathrm{T}}}\,\vec{\mathrm{v}}_{\mathrm{k}} \tag{3.78}$$

$$\frac{\partial}{\partial t}\vec{\mathrm{b}}_{\mathrm{k}} = i\vec{\vec{\mathrm{B}}}\,\vec{\mathrm{b}}_{\mathrm{k}}$$

$$\frac{\partial}{\partial t}\begin{bmatrix}\beta_k \\ \beta_{-k}{}^{*}\end{bmatrix} = i\begin{bmatrix}\omega_k & 0 \\ 0 & -\omega_k\end{bmatrix}\begin{bmatrix}\beta_k \\ \beta_{-k}{}^{*}\end{bmatrix}.$$

3.5 NONLINEAR SPIN WAVE ANALYSIS

Now that the linear uniform mode and spin wave mode solutions have been obtained, we are now ready to solve the nonlinear spin wave equation of motion given in Eq. (3.25). To do so, we will first transform this equation into a more readily solvable form. This transformed nonlinear spin wave equation is simplified by neglecting the nonrelevant frequency modulation and coupling coefficient terms. Complex frequency damping is then added to the simplified transformed nonlinear spin wave equations, and analytic solutions are obtained. These steady state solutions are then analyzed to determine the microwave threshold field amplitude, termed h_{crit}, required to excite nonlinear spin wave amplitude growth of the critical modes. Thereafter, example resonance saturation butterfly curve plots calculated with the above hcrit expression and typical Zn Y-type hexagonal ferrite sample parameters are provided.

3.5.1 Nonlinear Instability Solutions

The nonlinear spin wave equation of motion, which is obtained from the reduced equation of motion given in Eq. (3.25) by discarding the linear uniform mode and linear microwave field terms, may be written in matrix form as

$$\frac{\partial}{\partial t}\begin{bmatrix} \alpha_k \\ \alpha_{-k}^{*} \end{bmatrix} = i\begin{bmatrix} A_k + c_k(t) & B_k + d_k(t) \\ -B_k^{*} - d_k^{*}(t) & -A_k - c_k^{*}(t) \end{bmatrix}\begin{bmatrix} \alpha_k \\ \alpha_{-k}^{*} \end{bmatrix}. \tag{3.79}$$

Here the A_k and B_k terms are time independent and describe the spin wave frequency via $\omega_k^{\,2} = A_k^{\,2} - |B_k|^2$. The time dependent $c_k(t)$ and $d_k(t)$ depend on the uniform mode $\alpha_o(t)$ and the z-component of the microwave magnetic field $h_{pz}(t)$, and $h_c(t)$. See Eq. (3.30) for the explicit expressions for $c_k(t)$ and $d_k(t)$.

The nonlinear spin wave equation of motion given in Eq. (3.79) can be rewritten in a more readily solvable form via a linear transformation using the matrix $\ddot{\mathrm{T}}$ obtained in the previous section. Upon do so, we obtain the following transformed equation:

$$\frac{\partial}{\partial t}\vec{\mathrm{b}}_{\mathrm{nl}} = i\,\ddot{B}_{\mathrm{nl}}\vec{\mathrm{b}}_{\mathrm{nl}}\,, \tag{3.80}$$

where

$$\vec{\mathrm{b}}_{\mathrm{nl}} = \ddot{\mathrm{T}}\,\vec{\mathrm{v}}_{\mathrm{k}} = \frac{1}{1-|\Gamma|^2}\begin{bmatrix} 1 & -\Gamma \\ -\Gamma^{*} & 1 \end{bmatrix}\begin{bmatrix} \alpha_k(t) \\ \alpha_{-k}^{*}(t) \end{bmatrix}, \tag{3.81}$$

and

$$\ddot{B}_{\mathrm{nl}} = \ddot{\mathrm{T}}\ddot{A}_{\mathrm{nl}}\ddot{\mathrm{T}}^{-1}$$
$$\ddot{B}_{\mathrm{nl}} = \frac{1}{1-|\Gamma|^2}\begin{bmatrix} 1 & -\Gamma \\ -\Gamma^{*} & 1 \end{bmatrix}\begin{bmatrix} A_k + c_k(t) & B_k + d_k(t) \\ -B_k^{*} - d_k^{*}(t) & -A_k - c_k^{*}(t) \end{bmatrix}\begin{bmatrix} 1 & \Gamma \\ \Gamma^{*} & 1 \end{bmatrix}. \tag{3.82}$$

The transformed nonlinear spin wave equation given in Eq. (3.80) can be written in matrix form as

$$\frac{\partial}{\partial t}\begin{bmatrix}\beta_k(t)\\ \beta_{-k}^{*}(t)\end{bmatrix}=i\begin{bmatrix}\omega_k+F_k(t) & G_k(t)\\ -G_k^{*}(t) & -\omega_k-F_k^{*}(t)\end{bmatrix}\begin{bmatrix}\beta_k(t)\\ \beta_{-k}^{*}(t)\end{bmatrix}, \tag{3.83}$$

where

$$G_k(t)=\frac{1}{1-|\Gamma|^2}\left[\Gamma\left(c_k(t)+c_k^{*}(t)\right)+d_k(t)+\Gamma^2 d_k^{*}(t)\right]$$

and (3.84)

$$F_k(t)=\frac{1}{1-|\Gamma|^2}\left[c_k(t)+|\Gamma|^2 c_k^{*}(t)+\Gamma^{*}d_k(t)+\Gamma d_k^{*}(t)\right].$$

In this transformed form, we can readily identify the time dependent nonlinear $G_k(t)$ and $F_k(t)$ terms from the linear spin wave dispersion frequency ω_k.

Equation (3.83) is actually a modified form of the nonlinear Mathieu's Equation. (See Landau and Lifshitz [1984] for details). An exact analytic solution of Eq. (3.83) is not easily, if at all, obtainable. In order to obtain a closed form solution, the following assumption regarding $F_k(t)$ is applied: it is asserted that $F_k(t)$ leads only to a modulation of ω_k and does not play a role in nonlinear spin wave amplitude growth. Therefore, since we are only interested in determining the microwave field strength required to initiate the nonlinear spin wave amplitude growth, and not the modulated frequency of those nonlinearly excited critical modes, $F_k(t)$ can be neglected. See Suhl [1953] and Schloemann [1959] for more detailed discussions.

Thus the transformed nonlinear spin wave equation of motion given in Eq. (3.83) is rewritten in a simplified and analytically solvable form as

$$\frac{\partial}{\partial t}\begin{bmatrix}\beta_k(t)\\ \beta_{-k}^{*}(t)\end{bmatrix}=i\begin{bmatrix}\omega_k & G_k(t)\\ -G_k^{*}(t) & -\omega_k\end{bmatrix}\begin{bmatrix}\beta_k(t)\\ \beta_{-k}^{*}(t)\end{bmatrix}. \tag{3.85}$$

The $G_k(t)$ term in Eq. (3.85) models the effective parametric coupling rate of the microwave field energy into the various spin wave modes. The explicit relationship between $G_k(t)$ and the *z*-component of the microwave field $h_{pz}(t)$ and the uniform mode amplitude $\alpha_o(t)$ is obtained by substituting the $c_k(t)$ and $d_k(t)$ expressions given in Eq. (3.27) into the $G_k(t)$ expression in Eq. (3.84) and may be written as

$$G_k(t) = g_z \left|\gamma\right| h_{pz} + g_{11}\alpha_o + g_{12}\alpha_o^* + g_{21}\alpha_o^{\,2} + g_{22}\alpha_o\alpha_o^* + g_{23}\,\alpha_o^{*\,2} \tag{3.86}$$

where

$$\begin{aligned}
g_z &= \frac{2\Gamma}{1-\Gamma\Gamma^*}, \\
g_{11} &= \frac{\left|\gamma\right|}{1-\Gamma\Gamma^*}\left[\Gamma\left(C_{11}+C_{12}^{\,*}\right)+D_{11}\right], \\
g_{12} &= \frac{\left|\gamma\right|}{1-\Gamma\Gamma^*}\left[\Gamma\left(C_{11}^{\,*}+C_{12}\right)+\Gamma^2 D_{11}^{\,*}\right], \\
g_{21} &= \frac{\left|\gamma\right|}{1-\Gamma\Gamma^*}\left[D_{22}+\frac{1}{2}\Gamma H_2^{\,*}\right], \\
g_{22} &= \frac{\left|\gamma\right|}{1-\Gamma\Gamma^*}\left[\Gamma\left(C_{21}+C_{21}^{\,*}\right)+D_{21}+\Gamma^2 D_{21}^{\,*}\right],
\end{aligned} \tag{3.87}$$

and

$$g_{23} = \frac{\left|\gamma\right|}{1-\Gamma\Gamma^*}\left[\Gamma^2 D_{22}^{\,*}+\frac{1}{2}\Gamma H_2\right].$$

The microwave field and the uniform mode amplitude terms in Eq. (3.86) can be written as

$$h_{pz}(t) = \left(h_{oz}/2\right)\left(e^{i\omega_p t}+e^{-i\omega_p t}\right)$$

and (3.88)

$$\alpha_o(t) = \left(\left|\gamma\right|h_o/2\right)\left(q_L e^{i\omega_p t}+q_{AL}e^{-i\omega_p t}\right),$$

where h_{oz} and h_o are the magnitude of the microwave field components applied parallel and perpendicular to static equilibrium direction of the magnetization vector (z-axis), respectively. From an inspection of the previous three equations, one can see that $G_k(t)$ may be written in terms of the microwave frequency harmonics as

$$G_k(t) = \sum_{n=-2}^{2} G_k^{(n)} e^{in\omega_p t} \ . \tag{3.89}$$

The different harmonic components of $G_k(t)$ correspond to different scattering processes that may lead to nonlinear spin wave amplitude growth.

First consider the constant term $G_k^{(n=0)}$ in Eq. (3.89). Inspection of Eq. (3.83) reveals that this constant term can be taken into account by a linear transformation and does not play a role in the spin wave amplitude growth. It will therefore be ignored here. Next consider the negative ($n<0$) terms in Eq. (3.89). It can be shown that if a spin wave amplitude solution with a positive exponent of the form $\exp(+i\omega_k t)$ is used (the type of solution addressed here), then the scattering terms with the negative exponents $G_k^{(n<0)} \exp(-i|n|\omega_p t)$ in Eq.(3.89) require significantly higher microwave field amplitudes to excite nonlinear spin wave growth than the positive exponential $G_k^{(n>0)} \exp(i|n|\omega_p t)$ terms (see Eq. (3.94) below for details). Therefore, the $n<0$ terms in Eq. (3.89) can also be neglected.

Now consider the positive ($n>0$) terms in Eq. (3.89). As was discussed in Chapter 2, the experimental conditions can be established such that the first and second order nonlinear instability processes are independently excited. The first and second order instability processes correspond to spin waves with frequency harmonics of $\exp(i\omega_p t)$ and $\exp(i2\omega_p t)$, respectively. Therefore, the $n=1$ and $n=2$ $G_k^{(n)}$ terms can be treated independently to model the first and second order nonlinear instability process.

In summary, of all the harmonic terms in Eq.(3.89), we only need to address the $G_k^{(1)}\exp(i\omega_p t)$ and $G_k^{(2)}\exp(i2\omega_p t)$ terms in a separate fashion here. See Suhl [1953] and Schloemann [1959] for more detailed discussions. The explicit $G_k^{(1)}$ and $G_k^{(2)}$ scattering coefficients are obtained by substituting the $h_{pz}(t)$ and $\alpha_o(t)$ expressions given in Eq. (3.88) into Eq. (3.86) and collecting all like $\exp(i\omega_p t)$ and $\exp(2i\omega_p t)$ terms, respectively. These coefficients may be written as

$$G_k^{(1)} = \frac{|\gamma| h_{oz}}{2}\left(g_z\right) + \frac{|\gamma| h_o}{2}\left(g_{11}q_L + g_{12}q_{AL}^{*}\right),$$

and (3.90)

$$G_k^{(2)} = \left(\frac{|\gamma| h_o}{2}\right)^2 \left(g_{21}q_L^{\,2} + g_{22}q_L q_{AL}^{*} + g_{23}q_{AL}^{*2}\right).$$

Prior to solving the simplified transformed nonlinear spin wave equation of motion, given in Eq. (3.85), we first need to include damping. This is done by the complex frequency technique in which the spin wave frequency is replaced with the following complex frequency

$$\omega_k \rightarrow \Omega_k = \omega_k + i\eta_k\,, \tag{3.91}$$

where η_k is the relaxation rate of a specific spin wave mode. Note that the complex frequency damping term in Eq. (3.91) is added to, not subtracted from, the spin wave frequency because we are addressing exponential solutions of the form $\exp(+i\omega_k t)$, not $\exp(-i\omega_k t)$. Substituting $G_k^{(n)}\exp(in\omega_k t)$ for $G_k(t)$ and Ω_k for ω_k into Eq. (3.85) yields the following final form of the simplified transformed nonlinear spin wave equation of motion

$$\frac{\partial}{\partial t}\begin{bmatrix}\beta_k \\ \beta_{-k}^{*}\end{bmatrix} = i\begin{bmatrix}\Omega_k & G_k^{(n)}e^{in\omega_p t} \\ -G_k^{(n)*}e^{-in\omega_p t} & -\Omega_k^{*}\end{bmatrix}\begin{bmatrix}\beta_k \\ \beta_{-k}^{*}\end{bmatrix}. \tag{3.92}$$

These two equations can be readily decoupled into a single second order differential equation, written as

$$\ddot{\beta}_k + \left(2\eta_k - in\omega_p\right)\dot{\beta}_k + \left(-n\omega_p\Omega_k + |\Omega_k|^2 - |G_k^{(n)}|^2\right)\beta_k = 0 \ . \tag{3.93}$$

Note that we now have a second order differential equation with **constant coefficients**, whose solution may be written as

$$\beta_k(t) = b_k^{(n)} \exp\left[\left(i\omega_k + \kappa^{(n)}\right)t\right], \tag{3.94}$$

where

$$\kappa^{(n)} = -\eta_k + \sqrt{\left(|G_k^{(n)}|\right)^2 - \left(\omega_k - n\omega_p/2\right)^2} \ . \tag{3.95}$$

From an examination of the steady state solution to the transformed reduced nonlinear spin wave equation of motion given in Eq.(3.94), it can be easily seen that $\beta_k(t)$ grows exponentially with time when $\kappa^{(n)} > 0$. Therefore, from an inspection of Eq. (3.95), we know that nonlinear spin wave amplitude growth occurs when the magnitude of the coupling coefficient satisfies the following criteria

$$|G_k^{(n)}|^2 > \eta_k^{\,2} + \left(\omega_k - n\omega_p/2\right)^2 \ . \tag{3.96}$$

The spin wave modes that first experience nonlinear amplitude growth, termed critical modes, are the ones that have the minimum $|G_k^{(n)}|$ required to cause $\kappa^{(n)} > 0$. Inspection of Eq. (3.96) reveals that the minimum $|G_k^{(n)}|$ required to cause nonlinear spin wave growth occurs when

$$\omega_k = n\omega_p/2 . \tag{3.97}$$

Therefore, the critical modes for the first order parallel pumping and subsidiary absorption instability processes ($n=1$) must have $\omega_k = \omega_p/2$, and the critical modes for the second order resonance saturation process $(n=2)$ must have $\omega_k = \omega_p$. These critical mode frequency requirements have been verified multiple times via Brillouin Light Scattering (BLS) measurements and are a good indication of the validity of Suhl's and Schloemann's nonlinear spin wave instability theories. See Wilber *et al*. [1984] and Kabos *et al*. [1997] for details on the BLS measurements.

After applying the critical mode frequency requirement given in Eq. (3.97) to Eq. (3.96), the magnitude of the coupling coefficient required for nonlinear spin wave amplitude growth can now be written as

$$\left| G^{(n)}_{k_{crit}} \right| \geq \eta_k . \tag{3.98}$$

The subscript in Eq. (3.98) is written as k_{crit} as a reminder that we are referring to the coupling coefficient associated with the critical spin wave modes, in which $\omega_k = n\omega_p/2$. For ease of comparison with the FMR linewidth it is convenient to express the spin wave relaxation rate η_k in terms in the same units (Oe), and η_k is rewritten as the so-called spin wave linewidth ΔH_k as $\eta_k = |\gamma| \Delta H_k/2$. Therefore, the instability threshold condition $\left|G^{(n)}_{k_{crit}}\right| \geq \eta_k$ discussed above is rewritten in terms of the spin wave linewidth as

$$\left| G^{(n)}_{k_{crit}} \right| \geq \frac{|\gamma| \Delta H_k}{2} . \tag{3.99}$$

3.5.2 Threshold Field Equations

We are now ready to determine the working equations for the first and second order spin wave instability threshold fields (h_{crit}) which are the minimum microwave field

amplitudes required to excite nonlinear spin wave amplitude growth. To do this we substitute the $G_k^{(1)}$ and $G_k^{(2)}$ coefficients given in Eq. (3.90) into Eq. (3.99) and solve for the microwave field amplitude.

Upon performing the above steps, we obtain the following working equations for the parallel pumping (PP), subsidiary absorption (SA), and resonance saturation (RS) critical threshold field amplitudes as

$$h_{\text{crit}}^{(\text{PP})} = \left| \frac{\Delta H_k}{g_k^{(\text{PP})}} \right| \quad \omega_k = \omega_p/2, \mathbf{k} = \mathbf{k}_{\text{crit}},$$

$$h_{\text{crit}}^{(\text{SA})} = \left| \frac{\Delta H_k}{g_k^{(\text{SA})}} \right| \quad \omega_k = \omega_p/2, \mathbf{k} = \mathbf{k}_{\text{crit}}, \text{ and} \tag{3.100}$$

$$h_{\text{crit}}^{(\text{RS})} = \left| \sqrt{\frac{2\Delta H_k}{\gamma g_k^{(\text{RS})}}} \right| \quad \omega_k = \omega_p, \mathbf{k} = \mathbf{k}_{\text{crit}},$$

respectively, where

$$g_k^{(\text{PP})} = g_z,$$

$$g_k^{(\text{SA})} = g_{11} q_L + g_{12} q_{AL}^{*}, \text{ and} \tag{3.101}$$

$$g_k^{(\text{RS})} = g_{21} q_L^{2} + g_{22} q_L q_{AL}^{*} + g_{22} \left(q_{AL}^{*} \right)^2.$$

See Eq. (3.87) for the g_z and g_{ij} terms.

The expressions in Eq. (3.100) are the working threshold field equations which are required in order to perform numeric butterfly curve calculations of h_{crit} versus H_{ext}. These expressions can be used to calculate parallel pumping, subsidiary absorption, and

resonance saturation instability butterfly curves for samples with planar and uniaxial anisotropy, obtained with the field and sample orientation shown in Fig. 3.1. These threshold field expressions contain three extensions over previously published work. They allow for the butterfly curve calculations to be performed in anisotropic samples using: (1) a generalized microwave field expression, (2) static external magnetic fields not only equal to but also away from the FMR resonance field for resonance saturation instability process, and (3) corrected anti-Larmor uniform mode coefficients obtained with a corrected model of the complex damping frequency.

In order to gain confidence in the threshold field expressions given in Eq. (3.100), it will now be shown that they reduce to the same expressions as those originally derived by Suhl [1953] and Schloemann [1959] in the limit of zero anisotropy and specific sample and field geometries. In order to reduce the threshold field equations given in Eq.(3.100) into the well established forms that are found in the literature for certain specific limits, it is helpful to notice that the $1/\left(1-\Gamma\Gamma^{*}\right)$ term, which occurs frequently in Eq. (3.87), can be rewritten in terms of just A_k and ω_k. By applying the following two relationships $\omega_k^{\,2} = A_k^{\,2} - \left|B_k\right|^2$ and $\Gamma = \left(\omega_k - A_k\right)/B_k^{\,*}$, which were originally given in Eq. (3.64) and Eq. (3.75), respectively, the $1/\left(1-\Gamma\Gamma^{*}\right)$ expression can be rewritten as

$$1/\left(1-\Gamma\Gamma^{*}\right) = \left(\omega_k + A_k\right)/2\omega_k \,. \tag{3.102}$$

Now consider the parallel pumping processes. For this case the microwave field and the coupling coefficient can be written as

$$\mathbf{h_p} = h_o \cos(\omega_p t)\,\hat{\mathbf{z}}$$

and (3.103)

$$g_k^{\,(\mathrm{PP})} = g_z = \frac{2\Gamma}{1-\Gamma\Gamma^{*}} = -\frac{B_k}{\omega_k}\,.$$

respectively. Applying the expressions given in Eq. (3.103) into Eq. (3.100) results in the following expression for the threshold field

$$h_{\text{crit}}^{(\text{PP})} = \left. \frac{\omega_p \Delta H_k}{|\gamma| \left| 4\pi M_s \sin^2(\theta_k) e^{2i\phi_k} - H_A \right|} \right|_{\mathbf{k} = \mathbf{k}_{\text{crit}}} . \tag{3.104}$$

In the limit of $H_A = 0$, we obtain the exact solution originally derived by Schloemann [1959]. For the case of planar anisotropy ($H_A < 0$), Eq. (3.104) is also in agreement with Schloemann's later results (Schloemann *et al.* [1963]).

From inspection of the threshold field given in Eq. (3.104), it can be seen that H_A has a very significant effect on the threshold field. Note that depending upon the spin wave linewidth, Eq. (3.104) can yield an extremely small threshold which can lead to very limited power handling capabilities for microwave devices with highly anisotropic materials. The underlying physics for why H_A reduces the threshold field has to do with ellipticity. As was discussed in Chapter 2, for parallel pumping processes, the microwave field couples into the wobble of $m_z(r,t)$. The magnitude of the $m_z(r,t)$ wobble is directly related to the ellipticity of the precessing dipole moments that make up the spin waves. If $H_A < 0$, both the dipole-dipole and the anisotropy fields work together to significantly increase the ellipticity of the precessional cones and, thus, reduce the threshold field required to drive the nonlinear spin wave amplitude growth.

Now consider the subsidiary absorption and resonance saturation threshold fields for an isotropic sphere in which $H_A = 0$, $N_{x,y,z} = 1/3$, and $\mathbf{h_p} = h_o \cos(\omega_p t)\hat{\mathbf{y}}$. This corresponds to the limiting case initially treated by Suhl [1953]. In this case, the subsidiary absorption threshold in Eq. (3.100) reduces to

$$h_{\text{crit}}^{(\text{SA})} = \left. \frac{\omega_p \Delta H_k}{|\gamma| 4\pi M_s \sin(\theta_k)\cos(\theta_k)} \right|_{\mathbf{k} = \mathbf{k}_{\mathbf{crit}}}, \tag{3.105}$$

and the resonance saturation expression for the limiting case in which $H_{ext} = H_{FMR}$ (i.e., $\omega_o = \omega_p$) reduces to

$$h_{\text{crit}}^{(\text{RS})} = \left. \Delta H_{FMR} \sqrt{\frac{\Delta H_k}{4\pi M_s}} \right|_{\mathbf{k} = \mathbf{k}_{\mathbf{crit}}}. \tag{3.106}$$

Equations (3.105) and (3.106) are in exact agreement with the subsidiary absorption equation (Eq. (31)) and the resonance saturation equation (Eq. (37)) of Suhl's original paper (Suhl [1953]).

3.5.3 RS Butterfly Curve Calculations

A full review of all the possible spin wave instability calculations that can be obtained from the instability equations given in Eq. (3.100) is beyond the scope of this work. Chen and Patton [1991] review threshold processes for the subsidiary loss region in isotropic ferrites. Schloemann *et al.* [1963] discuss threshold processes for both the subsidiary loss and FMR regions for easy plane hexagonal ferrites. The theoretical treatment in Schloemann *et al*. [1963] does not consider resonance saturation processes that occur for static magnetic fields unequal to the FMR resonance field. As was mentioned previously, the analysis performed here extends the nonlinear theory to include the field regime *around* the FMR point. To the best of this author's knowledge, off-resonance second order spin wave instability calculations have only been performed once before for isotropic samples (Kabos *et al*. [1997]) but not for anisotropic ones. This section will review how the resonance saturation butterfly curves are calculated and

summarize the key effects that crystalline anisotropy has upon them. All the numerical solutions shown here are obtained with the corrected version (CF-2) of the uniform mode complex damping term, which are given in Table 3.1.

As was stated previously, a butterfly curve plot summarizes the microwave threshold field amplitude (h_{crit}) dependence upon the externally applied static magnetic field (H_{ext}). Typically h_{crit} versus H_{ext} data are first obtained for a specific sample orientation, applied field geometry, and microwave frequency. Then the spin wave linewidth (ΔH_k) is used as a fitting parameter to match the calculated butterfly curve data. The spin wave linewidth that gives the best fit is then assumed to be the intrinsic relaxation rate (expressed in field linewidth units) of the sample. Many different trial ΔH_k functions have been used in the past for parallel pumping and subsidiary absorption calculations. (See Sections 5 and 6 of Chen and Patton [1994] for more details.) In contrast, the limited number of resonance saturation calculations performed to date have primarily utilized the simplest possible form in which $\Delta H_k = A$. The resonance saturation calculations given in this section are performed with the following two forms of the spin wave linewidth: (1) $\Delta H_k = A$ and (2) $\Delta H_k = A + Bk$.

Prior to performing the spin wave instability calculations one must establish: (1) the sample geometry and orientation of the static and microwave magnetic fields, (2) the static and linear dynamic magnetic sample parameters, and (3) the microwave operating frequency and static field ranges. The sample geometry and orientation are usually set by the experimental setup. The required static magnetic sample parameters are the saturation magnetization $(4\pi M_s)$, anisotropy field (H_A), and the demagnetizing constants ($N_{x,y,z}$). The required dynamic sample parameters are the gyromagnetic ratio (γ), the exchange constant (D), and the FMR linewidth (ΔH_{FMR}). All of the above parameters, except for *D*, were determined from FMR and Vibrating Sample Magnetometry (VSM) measurements for the samples studied here. Details are provided in Chapter 5.

(a)

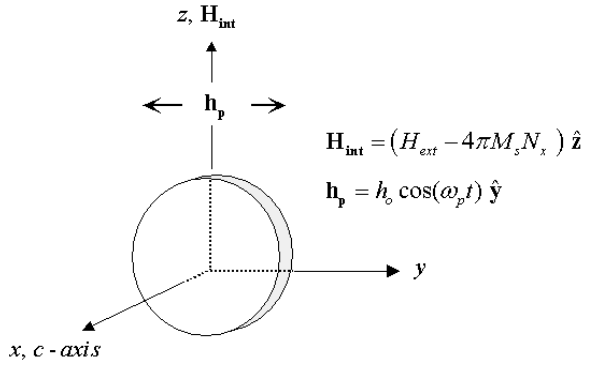

(b)

Parameter Name	Symbol	Value	Units
Saturation Magnetization	$4\pi M_s$	2.85	kG
Gyromagnetic Ratio	$\lvert\gamma\rvert$	2.8	GHz/kOe
Demagnetization Coefficients	N_x, N_y, N_z	1, 0, 0	NA
Exchange Constant	D	$5.4 \cdot 10^{-12}$	kOe/cm^2
FMR Linewidth	ΔH_{FMR}	10	Oe
Anisotropy Value	H_A	0 and -9.5	kOe

Figure. 3.11. (a) Sketch of the sample, field, and coordinate geometry, and (b) table of sample parameters, which are used to perform the spin wave manifold and resonance saturation calculations given in this section. Analysis is performed for isotropic and planar anisotropy.

Figure 3.11 summarizes the sample and field geometry as well as the sample parameters that are utilized in this and the next subsection. As is shown in the figure, the sample is a thin disk-shaped ellipsoid. The static and microwave fields are both applied in the disk plane and are orthogonal to one another. The sample parameters used for the calculations are provided in the table in the figure. Note that calculations are to be performed for two different anisotropy cases: (1) an isotropic case, in which $H_A = 0$, and (2) an easy-plane anisotropy case, in which $H_A = -9.5\,\text{kOe}$ and the easy-plane is aligned in the disk plane. The above parameters are typical for the single crystal Zn Y-type

hexagonal ferrite samples studied here. The operating frequency and static field ranges to be analyzed are as follows. A microwave frequency of 10 GHz is used, and the static field is scanned from ($H_{FMR} - 100$ Oe) to ($H_{FMR} + 100$ Oe) with a static field step size of 5 Oe. The H_{FMR} values for the isotropic and anisotropic cases are 2,420 Oe, and 958 Oe, respectively. At each static field setting, the spin wave modes that are available for excitation are determined by calculating which spin wave modes satisfy $\omega_k(H_{ext}, \theta_k, \phi_k, k) = n\omega_p / 2$. For the calculations performed in this section, n = 2, since we are addressing second order instability resonance saturation process. Once the available spin wave modes are determined, the critical mode is obtained (θ_{crit} , ϕ_{crit} , k_{crit}) as the specific spin wave mode that yields the minimum calculated threshold field. The above procedure is repeated for all the static fields of interest, and the resulting h_{crit} and k_{crit} values are plotted versus H_{ext}.

Figure 3.12 shows two dimensional spin wave dispersion plots which were calculated with the dispersion relationship given in Eq. (3.71), using the sample parameters and geometry shown in Fig. 3.11, and the different static field values noted in Fig. 3.12. Fig. 3.12 shows plots for (a) an isotropic $H_A = 0$ sample and (b) an anisotropic $H_A = -9.5\,\text{kOe}$ sample. For each anisotropy type, three specific spin wave branches which correspond to spin wave modes propagating along the *x*, *y*, and *z* axis are shown. Note that for the isotropic sample, spin waves propagating along the *x* and *y* directions have the same exact spin wave dispersion curve, but for the anisotropic sample they are not degenerate. For more details on these modes, see the previous linear spin wave analysis section of this chapter. The dotted line in the figures corresponds to the 10 GHz frequency of the microwave field, and the solid dot corresponds to the FMR resonance frequency, which was calculated using Eq. (3.33).

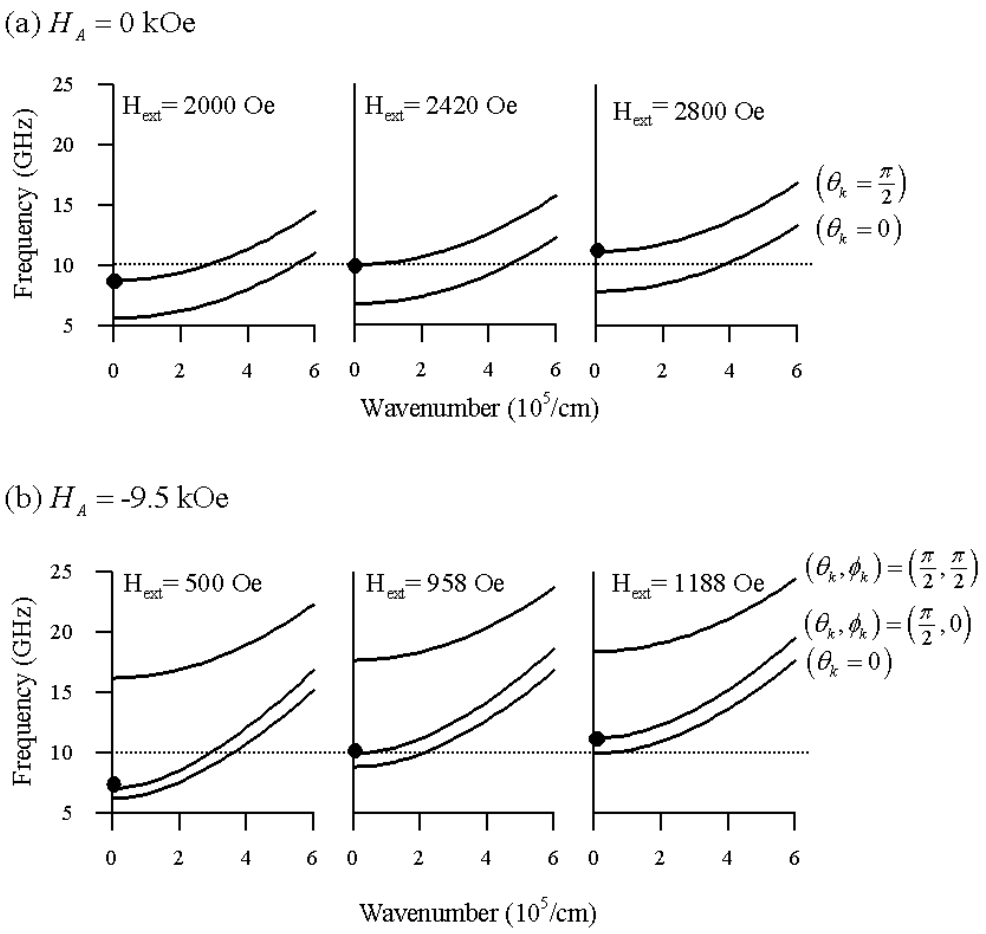

Figure. 3.12. Spin wave manifold plots calculated for (a) isotropic, and (b) anisotropic sample, with the parameters and sample and field geometry given in Fig. 3.11, and different static fields given in the plots. The solid circles and the horizontal dotted line correspond to the FMR resonance and microwave pump frequencies, respectively.

Figure 3.13 shows three-dimensional sketches of the spin wave manifold that are representative of the two dimensional spin wave plots shown in Fig. 3.12(b). These sketches provide insight into how the strength of the static field affects the availability of spin waves for excitation (i.e., ones that satisfy the $\omega_k = \omega_p = 10$ GHz criteria). The wave number contour plots, shown in Fig. 3.13(b), summarize the wave number (k), polar (θ_k) and azimuthal (ϕ_k) angles of the available spin wave modes for the three different field settings. As is seen in the figure, the available spin wave modes change considerably with the different static field settings. As the static field is increased from

500 to 1188 Oe, the maximum allowed wave number decreases from 3.25-to-1.25 (10^5 / cm), and the maximum azimuthal propagation direction decreases from 90 to about 38 degrees.

A Fortran based executable application was developed in order to perform the numeric calculations. The sample parameters, geometry, field ranges, microwave frequency, spin wave linewidth settings, and instability process of interest are specified by a user modifiable configuration file which is read upon the execution of the

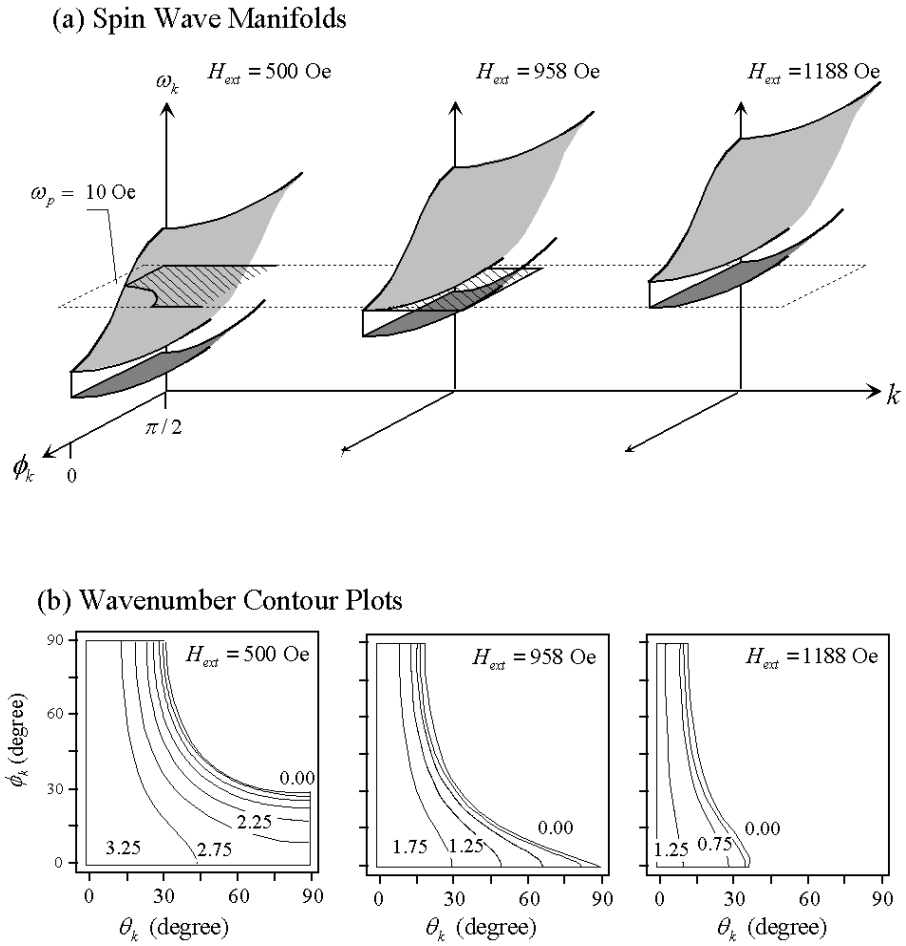

Figure. 3.13. (a) Three dimensional sketches of spin wave manifold plots for different static field values shown. (b) Contour plots of wave number versus θ_k and ϕ_k, obtained for spin waves which satisfy ω_k=ω_p=10 GHz. Calculations performed with sample parameters and geometry shown in Fig. 3.11. Units of contours are 10^5/cm.

application. The program then determines which spin wave modes are available for excitation (similar to what is shown in Figure 3.13(b)) and then searches for the minimum $h_{\text{crit}}(\theta_{crit}, \phi_{crit}, k_{crit})$ from these available states for each static field setting. Two different minimization algorithms are selectable in the configuration file. The first approach is a simple brute force method in which $h_{\text{crit}}(\theta_k, \phi_k, k)$ is found as the minimum threshold field from an array of threshold fields which are calculated over a grid of the available θ_k and ϕ_k, and k values. The θ_k and ϕ_k grid step size is set by the user in the configuration file. The second option is Brent's method of finding a global minimum, which was obtained from the *Numerical Recipes* software library (see Press *et al.* [1992] for details).

The Fortran program determines the $h_{\text{crit}}(\theta_{crit}, \phi_{crit}, k_{crit})$ values for each H_{ext} setting and saves the threshold fields and critical mode information to an output text file. Typically, the above minimization procedure is rerun with different trial forms of the spin wave linewidth until a good agreement is obtained between the calculated and the measured butterfly curve data. However, for the analysis performed here, we will consider just two different spin wave linewidths, without regards to measured data. Real measured data and resulting spin wave linewidths are given in Chapter 5.

Figures 3.14 and 3.15 summarize the resonance saturation butterfly curve threshold field and critical mode calculations performed for an isotropic and a planar anisotropic sample, respectively. The solid circles and the open squares in the plots are the results obtained with a constant spin wave linewidth $\Delta H_k = 10$ Oe and wave number dependent form of $\Delta H_k = 10 \text{ Oe} + (5 \cdot 10^{-5} \text{Oe/cm})\, k$, respectively.

First consider the resonance saturation threshold field results for Figures 3.14 and 3.15. For both the isotropic and anisotropic samples, the resonance saturation h_{crit} versus H_{ext} butterfly curves are approximately "V" shaped with the minimum value centered at the resonance H_{FMR} field. This shape is what one would expect since the applied microwave field couples into the uniform mode most effectively at the resonance

condition and less so as H_{ext} moves away from H_{FMR}. The introduction of the k-dependent spin wave linewidth results in the butterfly curves being asymmetric, such

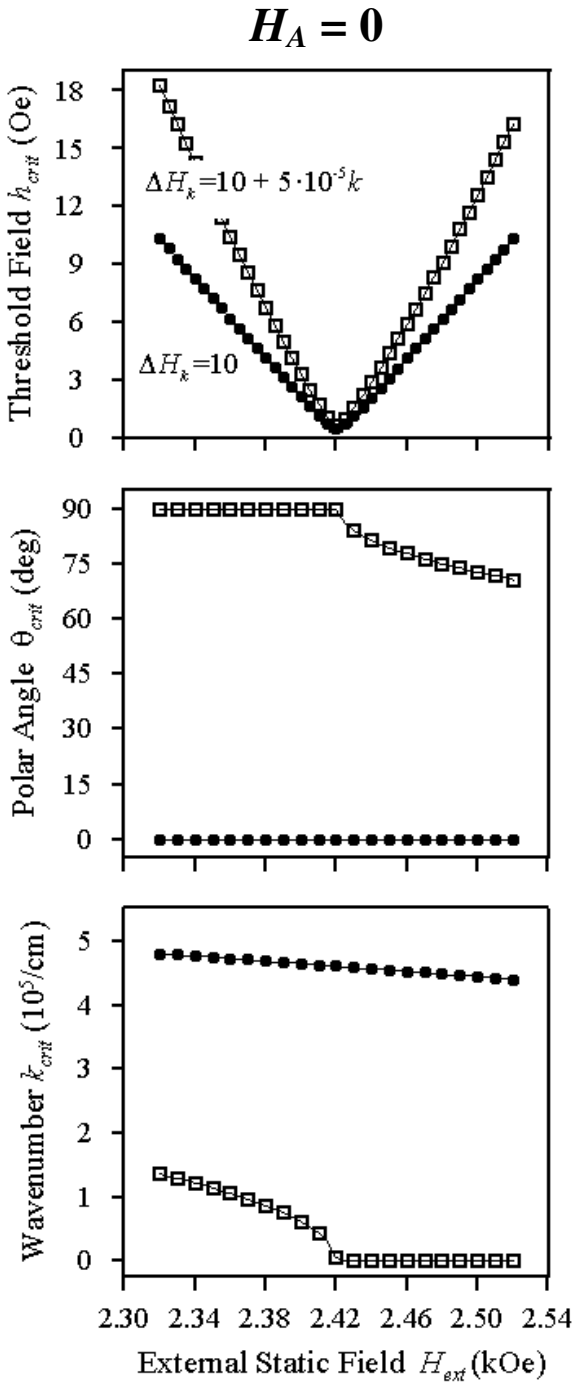

Figure. 3.14. Resonance saturation butterfly curve and associated critical modes, calculated for isotropic ($H_A = 0$) thin film with constant (solid circles) and wave number dependent (open squares) spin wave linewidths, as shown in the plots.

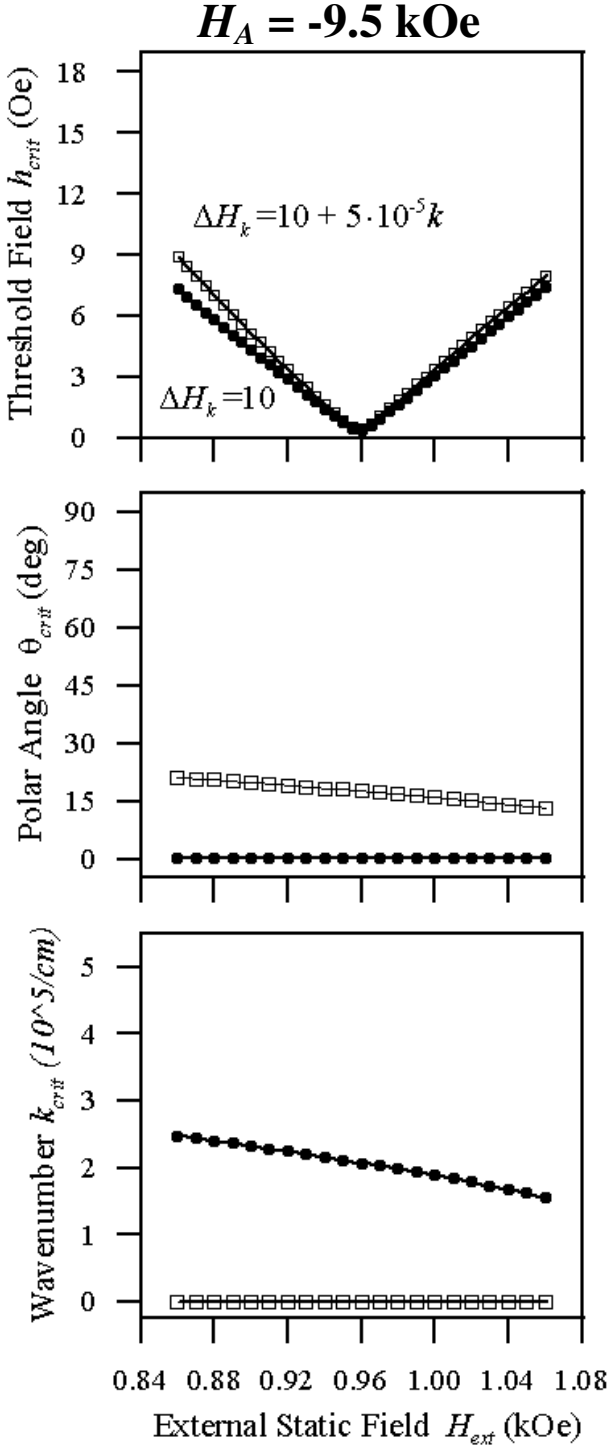

Figure. 3.15. Similar graphs as shown in Fig. 3.14, but for a sample with a planar anisotropy of $H_A = -9500$ Oe . The calculations were performed, with a frequency of 10 GHz, and the sample parameters and orientation given in Fig 3.11.

that h_{crit} increases more rapidly as H_{ext} moves away from H_{FMR} for $H_{ext}<H_{FMR}$ than it does for $H_{ext}>H_{FMR}$. The source of this asymmetric "*V*" shape will be discussed in more detail shortly. Anisotropy affects the RS butterfly curves in two significant ways: (1) it lead to a net decrease in the threshold field of about 65% at the resonance condition and (2) it altered the location of the critical modes within the spin wave manifold.

The reduction in the threshold fields could result in hexagonal ferrite based microwave devices having reduced power-handling capabilities compared to conventional devices. This will be discussed in more detail in Chapter 5. The effect of anisotropy upon the critical modes is the main topic of the remainder of this subsection.

Now consider the resonance saturation critical modes results given in the lower plots of Fig. 3.14 and Fig. 3.15. As can be seen in the plots, when $\Delta H_k = 10$ Oe, the critical modes for both the isotropic and anisotropic samples correspond to the spin wave mode with the minimum available polar angle $\theta_{crit} = 0$. In both these cases, spin waves propagating along the *z*-axis are excited when the threshold field condition is satisfied. The differences in the critical mode wave numbers for isotropic and anisotropic samples are due to the different shapes of the $\omega_k(H_{ext}, \theta_k = 0, k) = \omega_p$ spin wave branch for isotropic versus the anisotropic sample. Now consider the critical modes for the wave number dependent spin wave linewidth. For both anisotropy types, the spin waves with the lowest threshold correspond to the spin wave branch with the lowest possible wave number (*k*=0). For the isotropic sample, this mode corresponds to $\theta_{crit} = 90^o$ when $H_{ext} < H_{FMR}$ and $\theta_{crit} = \max(\theta_k)$ when $H_{ext} > H_{FMR}$. For the anisotropic sample, k =0 spin wave modes are available for all static fields analyzed.

Figure 3.16 provides sketches of the critical mode locations within the spin wave manifold for the different spin wave linewidth and anisotropy cases considered in Fig. 3.14 and Fig. 3.15. Here, the thick solid line represents the critical modes and the solid dot corresponds to the FMR resonance frequency. The sketches show that when ΔH_k shifts from a constant to being *k*-dependent, the critical modes shifts from being the

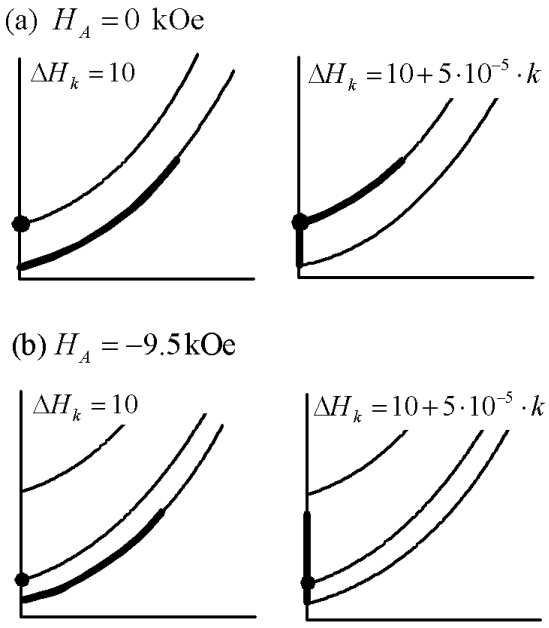

Figure. 3.16. Sketches of the critical mode locations for the RS butterfly curves given in Figs. 3.14 and 3.15. The thick solid lines correspond to the critical mode locations within the manifolds. Note that while these manifolds are shown as stationary, they actually shift up with the external field as is shown in Fig. 3.12.

spin wave modes with the lowest possible θ_k value to being the spin wave modes with the lowest possible k value.

Table 3.3 summarizes the above calculated resonance saturation butterfly curves. The first and second column specify H_A and ΔH_k. The third column, labeled $h_{crit}^{\min}$, corresponds to $h_{crit}(H_{ext}=H_{FMR})$, and the fourth and fifth columns specify the slope of the $h_{crit}(H_{ext})$ curves for $H_{ext}<H_{FMR}$ and $H_{ext}>H_{FMR}$, respectively. The last column summarizes the critical mode position within the spin wave manifold. As can be seen in the table, while H_A leads to a reduction in $h_{crit}^{\min}$ of about 60-70%, it also reduces the impact of the k-dependent spin wave linewidth term upon the slope of the $h_{crit}(H_{ext})$ curves, especially for $H_{ext}<H_{FMR}$. For the isotropic sample, the k-dependent wave linewidth term leads to a 45% increase in the slope of the $h_{crit}(H_{ext})$ response but only about an 11% increase in the anisotropic sample. These differences are directly related to the differing shapes of the $k=0$ spin wave bands for the two sample types.

H_A (kOe)	ΔH_k (Oe)	$h_{crit}^{\min}$ (Oe)	$\Delta h_{crit}/\Delta H_{ext}$ $H_{ext}<H_{FMR}$	$\Delta h_{crit}/\Delta H_{ext}$ $H_{ext}>H_{FMR}$	Critical Modes
0	10	0.52	-0.10	0.10	min θ_k, max k
0	$10+10^{-5}k$	0.70	-0.19	0.16	min k, max θ_k
-9.5	10	0.37	-0.074	0.072	min θ_k
-9.5	$10+10^{-5}k$	0.42	-0.093	0.075	min k, max θ_k

Table 3.3. Summary of the resonance saturation threshold fields and critical modes given in Fig 3.12 and 3.13. The $h_{crit}^{\min}$ term corresponds to $h_{crit}(H_{ext}=H_{FMR})$. The $\Delta h_{crit}/\Delta H_{ext}$ columns specify the slope of the threshold field versus static field response for the two legs of the "V"-shaped butterfly curves.

3.6 IMPACT OF CF SIGN ISSUE ON THRESHOLD FIELDS

It was shown in Section 3.3 of this chapter that uniform mode damping was incorrectly modeled in several past publications when the wrong sign was utilized for the complex damping terms of the anti-Larmor uniform mode coefficient. This section will first show that the sign issue, which was present in the previous publications, had a negligible effect on the calculated first order butterfly curves presented in those papers. Then it will show that the sign issue does play a large role for resonance saturation calculations in anisotropic samples especially at low frequencies. This is one of the cases of interest for this thesis work.

3.6.1 Effect on SA Threshold Fields

Figure 3.17 shows the same subsidiary absorption butterfly curves that are given in Fig. 3 of Patton's paper (Patton [1969]), which corresponded to the first paper in which the complex frequency (CF) method with the sign issue was introduced. The curves of

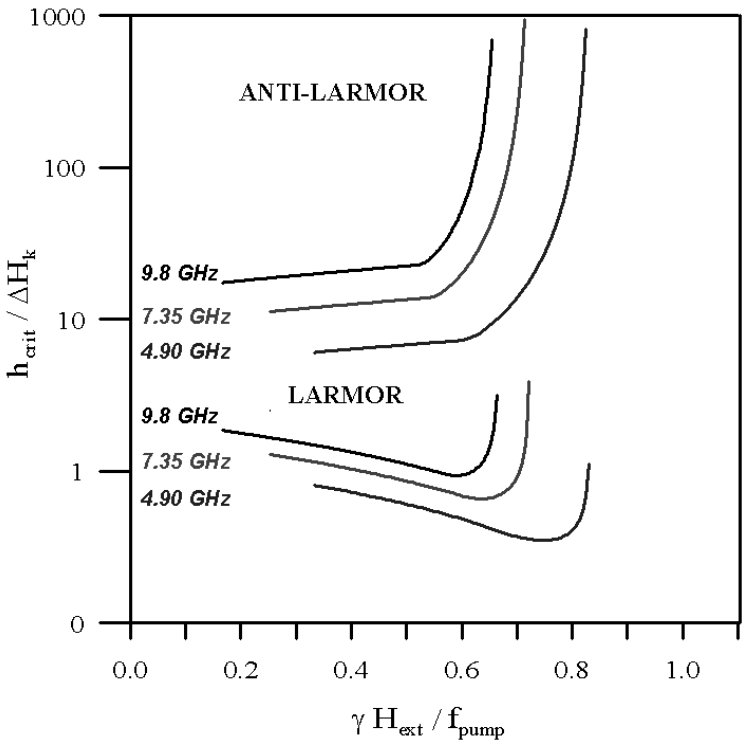

Figure. 3.17. Plots of first order normalized subsidiary absorption threshold field versus normalized external static magnetic field, after Fig. 3 of Patton [1969]. Curves were calculated for an isotropic spherical sample using two different circularly polarized microwave fields, one with Larmor-oriented precession and the other with purely anti-Larmor orientation. Both fields were applied perpendicular to static field direction. Same exact plots were obtained for all four forms of the uniform mode solutions given in Table 3.1.

Fig. 3.17 were recalculated using the linear uniform mode solutions obtained with: (1) the uncorrected uniform mode CF-1 complex frequency solutions, (2) the corrected CF-2 complex frequency solutions, (3) the Landau-Lifshitz uniform mode solutions, and (4) the Bloch-Bloembergen solutions. All of these solutions are given in Table 3.1. The end result is that all four uniform mode solutions yielded the same results which are in exact agreement with Patton's earlier work. The reason the sign issue did not have any effect on the subsidiary absorption butterfly curves is because the subsidiary absorption instability processes are measured with the applied static field far enough below the resonance field such that the sign of the anti-Larmor damping term has a negligible contribution. For this reason, it is likely that all first order instability analyses (not

including coincidence condition) will be unaffected by the sign issue in the anti-Larmor complex frequency damping term.

3.6.2 Effect on RS Threshold Fields

We will now address the effects of the anti-Larmor uniform mode complex damping sign upon the resonance saturation threshold field calculations. Similar resonance saturation threshold field calculations as were originally given in the previous section will be performed, but instead of analyzing the full resonance saturation butterfly curve we will focus only on the static fields which satisfy the FMR resonance condition for varying operating frequencies (i.e., focus on the minimum of threshold field of the butterfly curve). For each operating frequency, the static field is set to the resonance condition such that $H_{ext} = H_{FMR}(\omega_p)$. To the best of the author's knowledge, such curves have never been previously calculated using uniform mode solutions that have the damping sign issue.

Figure 3.18 shows plots of the calculated resonance saturation threshold field versus resonance frequency. The threshold fields were calculated with the RS h_{crit} expression given in Eq. (3.100) using the Zn Y-type hexagonal ferrite sample parameters, geometry, and pumping configuration given in Fig. 3.11. The threshold fields were normalized to the Suhl second order threshold field given in Eq. (3.106). These calculations were performed with two different uniform mode expressions. The solid circles, labeled CF-1 in the figure, correspond to the results obtained with the uniform mode expression that had the anti-Larmor complex damping sign problem, and the open squares, labeled CF-2, correspond to the results obtained with the corrected version. See Table 3.1 for the CF-1 and CF-2 expressions.

As is seen in Fig. 3.18, the sign of the uniform mode complex frequency anti-Larmor damping term has a significant effect on the calculated resonance saturation threshold fields. The difference in the normalized threshold fields obtained with CF-1 versus those obtained with CF-2 is most significant at the lower frequencies because the anti-Larmor

complex term has a more significant role in the total uniform mode response under those conditions. This frequency dependence was discussed in Section 3.3; see Figures 3.5 and 3.6 for details.

The resonance saturation critical modes, which correspond to the threshold fields given in Fig. 3.18, are as follows. For the calculations obtained with the wrong damping sign, the $\theta_{crit} = 0^{o}$ for all frequencies. However, for the calculations obtained with the corrected damping sign, θ_{crit} varies with frequency. For frequencies below 20 GHz, $\theta_{crit} = 0^{o}$ and for frequencies above this $\theta_{crit} = 90^{o}$ and $\phi_{crit} = 0^{o}$. The peak in the normalized threshold versus frequency plot given in Fig. 3.18, which occurs at 20 GHz, corresponds to transition in the critical mode from $\theta_{crit} = 0^{o}$ to $(\theta_{crit}, \phi_{crit}) = (90^{o}, 0^{o})$.

It is worth noting that the resonance saturation calculations shown in Fig. 3.18 were also performed with the Landau-Lifshitz (LL) and the Bloch-Bloembergen (BB) uniform mode expressions given in Table 3.1. The resultant normalized threshold fields obtained from both the LL and BB uniform mode solutions were in excellent agreement with the values determined with the uniform mode solution that had the corrected complex damping sign (CF-2).

In summary, the sign of the uniform mode anti-Larmor complex damping term only plays an important role in the nonlinear threshold field calculations for a few specific conditions. ***The main condition, in which the sign has a significant effect, is second order spin wave instability processes in highly anisotropic materials***. Such instability conditions have not been studied in detail. The majority of the instability work performed to date has focused primarily on first order processes. The little amount of second order stability analyses that have been done has focused mainly on isotropic materials. To the best of the author's knowledge, only one paper has addressed second order processes in hexagonal ferrites. This work, which was published by Schloemann [1963] also contained the sign issue, but was not affected because Schloemann utilized a transformed reference frame such that the uniform mode response was basically circular and the anti-Larmor term was negligible. So while the sign problem with the anti-

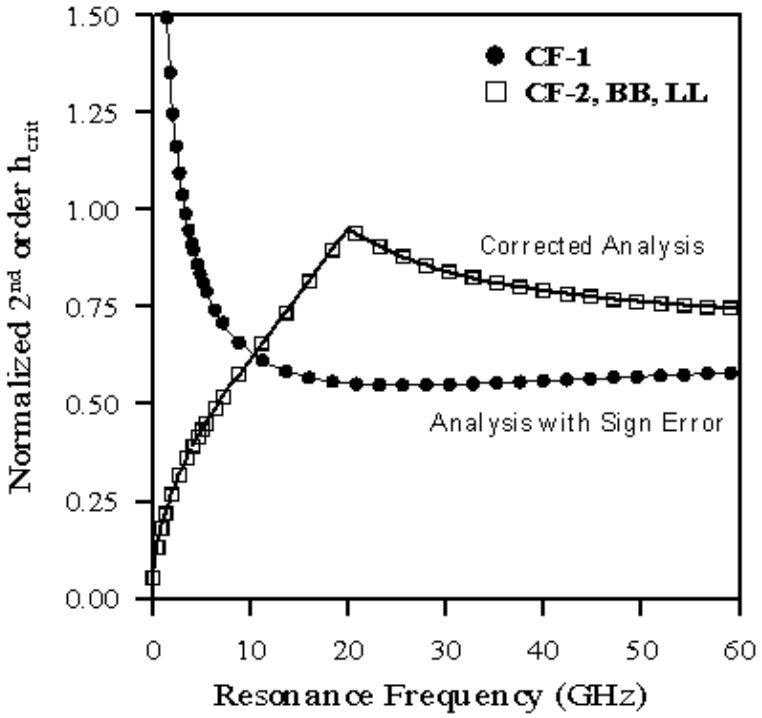

Figure. 3.18. Plots of the normalized resonance saturation threshold field versus FMR resonance frequency. The curves were calculated with uniform mode expressions that had incorrect (solid circles) and corrected (open squares) complex anti-Larmor damping signs; these expressions are given as CF-1 and CF-2, respectively, in Table 3.1. Note that the sign of the anti-Larmor complex frequency damping term has a significant effect on the results.

Larmor uniform mode complex frequency damping term has persisted in the spin wave instability literature for about thirty years, it has not significantly impacted the calculated threshold fields presented in the literature. However, as can be seen in Fig. 3.18, future researchers should be aware of the possible effects of the sign problem with the anti Larmor uniform mode damping term and fully understand the conditions under which it significantly affects the calculated threshold fields.

CHAPTER 4

HIGH-POWER MICROWAVE SPECTROMETER

A state-of-the-art high-power microwave spectrometer was designed, built, and automated as part of this study. The key components of the system were obtained with funds provided by the Office of Naval Research and through a generous equipment grant from Raytheon. This chapter provides an overview of the key features of the spectrometer, then discusses system calibration and operation, and provides example data. The chapter concludes with a section on measurement subtleties. Details on the passive waveguide components and automation programs are provided in Appendices A and B, respectively.

This chapter is arranged as follows:

1. The first section gives a general overview of the system.
2. Section two reviews the components used and the methods employed to generate and control the high-power microwave pulses and the static magnetic biasing field.
3. Section three addresses system calibration.
4. Section four reviews the system utilization and provides example high-power threshold field data.
5. The fifth and final section addresses measurement subtleties. Important measurement considerations regarding cavity loading, pulse width, and duty cycles are reviewed.

4.1 SYSTEM OVERVIEW

In order to measure spin wave instability thresholds, one must: (i) generate and control large-amplitude microwave and static magnetic fields, (ii) apply these fields to and set their relative orientation within a given sample, and (iii) measure the power absorbed by the sample as a function of these fields.

Figure 4.1 shows a sketch of the high-power microwave spectrometer that was built to perform the above tasks. The spectrometer can be separated into the following three subsystems based upon functionality: (1) generation and control of high-power microwave pulses, (2) measurement of the microwave power that is incident upon and

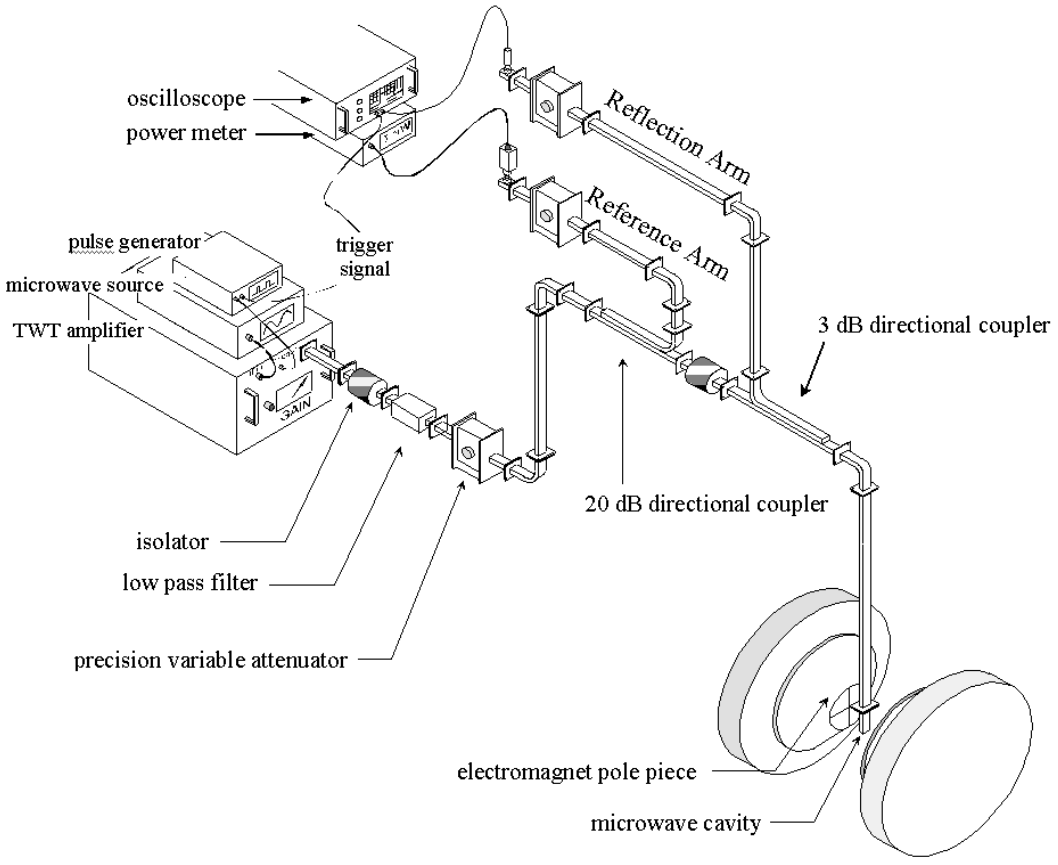

Figure. 4.1. Diagram of the high-power microwave spectrometer, which was designed, built, and automated as part of this thesis work.

reflected by the microwave cavity (reference and reflection waveguide arms), and (3) application and orientation of the microwave and static magnetic fields on the sample. A thorough discussion of these three subsystems will be provided in sections two, three, and four of this chapter. The rest of this section provides a cursory overview of the spectrometer.

The high-power microwave pulses are produced with a voltage pulse generator, synthesized microwave generator, and a traveling wave tube (TWT) amplifier. The high- power pulses are fed into the spectrometer through an isolator, a low-pass filter, and a precision variable attenuator. The isolator protects the high-power source from back reflections caused by down-line load mismatches, the low-pass filter reduces troublesome high-frequency harmonics, and the attenuator is used to set the operating power levels in the spectrometer. A small portion of the power leaving the attenuator is immediately coupled into the reference arm of the spectrometer and the remainder is directed to the reflection type microwave cavity. A significant percentage of the reflected power from the cavity is directed into the reflection arm of the spectrometer.

The reference and reflection arms of the spectrometer are used to monitor the amount of power that is incident upon and reflected by the microwave cavity, respectively. The cavity is used to (i) orient the microwave magnetic field within the sample, (ii) enhance the amplitude of this field, and (iii) increase the sensitivity of the spectrometer. The cavity is located between the pole pieces of an electromagnet. The electromagnet provides the large static magnetic biasing field that saturates and aligns the magnetic moments within the sample in the desired direction.

Table 4.1 summarizes the model number, manufacturer, and primary function of the key components of the spectrometer. Rectangular waveguides are used throughout the spectrometer because of their high-power handling capabilities, low insertion losses, and well-defined TE_{10} modes. These benefits come at a cost, however, both figuratively and literally. The main drawback of rectangular waveguides is their limited bandwidth

Device	Manufacturer	Model	Function (Specification)
Synthesized Sweeper	Hewlett Packard	HP83640A	Microwave generator (0.01- 40 GHz)
TWT	Applied Systems Engineering	174X-Ku	Microwave amplifier (8-18 GHz, 2.2 kW peak power)
Pulse Generator	Wavetek	81	Drive and trigger TWT and digital oscilloscope, respectively.
Power Meter	Hewlett Packard	HP436A	Convert power head output voltage into average microwave power
Power Meter Head	Hewlett Packard	HP8481A	Convert incident microwave signal into output voltage (0.01-18 GHz)
Crystal Detector	Hewlett Packard	HP8474D	Convert input microwave signal into output voltage (0.01-40 GHz)
Digital Oscilloscope	Tektronix	TDS-410A	Display and measure crystal detector output voltages
Magnet Power Supply	Harvey Wells	HS-1050	Current supply for electromagnet (i_{max} = 50Amps, V_{max}=100 Volts)
Electromagnet	Harvey Wells	8-521; 12”	Provide static magnetic field (H_{max} ~ 23 kOe)
Gauss meter	F.W. Bell	9900	Measure magnetic field of electromagnet
Waveguide components	Hewlett Packard, Narda, and Raytheon	———	Filters, isolators, precision variable attenuators, directional couplers, and rectangular waveguides.

Table 4.1. Summary of the manufacturer, model number, and function of the key waveguide components used in the high-power microwave spectrometer. There are four different versions of above components, which operate in the C, X, Ku, and Ka waveguide bands, available for the spectrometer.

which requires that several bands of waveguides be used in order to operate over a wide frequency range. Presently, the high-power microwave spectrometer shown in Fig. 4.1 can be operated in the X and Ku waveguide bands. There is also another magnetron based high-power source (not shown in Fig. 4.1) that is compatible with the system and operates in the C and Ka bands. This means that there are four versions of all the waveguide components (waveguide straights and bends, isolators, precision attenuators, and filters) shown in the figure. The frequency range for each of these bands is given in Table A.1 of Appendix A.

4.2 MAGNETIC FIELD GENERATION

This section focuses on the components used to generate the high-power microwave and the static magnetic fields. The next section focuses on system calibration.

4.2.1 High-Power Microwave Field

Microwave instability measurements are typically performed in a pulsed mode in order to avoid overheating the sample and damaging sensitive subcomponents. Historically, magnetrons have been the source of choice for such measurements (White *et al*. [1992]). The main benefits of magnetrons are their high peak power capability, exceptional durability, and relative affordability. The main drawbacks of such sources are their narrow frequency bandwidths, short pulse widths, poor frequency stability, and incompatibility with computer interfacing. In order to overcome the above shortcomings, a traveling wavetube (TWT) amplifier based high-power source was utilized.

Until recently, traveling wave tube (TWT) amplifiers only operated in continuous wave (CW) mode and at moderate power levels (few Watts). However, TWT amplifiers which operate solely in pulsed mode and with respectable peak power capabilities (few kWatts) are now being manufactured. These amplifiers have large pulse widths (hundreds of μs vs. a few μs for magnetrons), wide bandwidth (tens of GHz vs. a few MHz for magnetrons), high-frequency stability (set by microwave source, typically in the tenths of Hz range versus kHz for magnetrons), but have less peak power capabilities than magnetrons (few kW vs. MW). The main drawbacks of these sources are their limited tube lifetime (5-10 years vs. 20-30 years for magnetrons) and high cost (~$60k vs. $20k for magnetrons). The TWT amplifier purchased for this system has a maximum pulse width, duty-cycle, and peak power of about 100 μs, 4%, and 2.2 kW, respectively, and operates in the 8-18 GHz frequency range.

The high-power microwave pulse generation is accomplished with a Hewlett Packard synthesized sweeper (highly stable and accurate microwave source), a Wavetek voltage pulse generator, and the Applied Systems Engineering TWT amplifier. See Table 4.1 for manufacturer information on these components. The microwave generator provides a low-power 0 dBm (1mW) continuous wave signal that is amplified by the TWT. The pulse generator provides 5 V square pulses which trigger the TWT for the desired pulse widths and duty cycles. It also provides a trigger signal to the oscilloscope in order to set the acquisition timing required to monitor the reflected microwave pulses from the cavity (see Fig. 4.1 for details).

In order to minimize signal noise, the TWT amplifier is operated at maximum gain, and the power of the microwave signals within the spectrometer is set via the high-power precision variable attenuator shown in Fig 4.1. The precision variable attenuator has a maximum attenuation factor of about 50 dB and a frequency range similar to the bandwidth of the waveguide in use. In earlier designs of such spectrometers, the attenuators were controlled manually, whereas the attenuators shown in Fig. 4.1 are computer controlled via the use of stepper motors. The isolator that is located immediately after the high-power source protects the TWT from possible back reflections caused by down-line load mismatches. Typical isolator insertion losses in the forward and reverse directions are about –1 dB and –40 dB, respectively.

One feature of TWT amplifiers, which is often unknown or ignored, is their tendency to amplify subharmonics of the low-power input frequency to relatively large levels. As will be discussed in more detail in the next section, these amplified harmonic signals can lead to significant measurement errors. Therefore, the low-pass filter shown in Fig. 4.1 is placed after the amplifier.

Figure 4.2 shows the TWT output frequency spectrum data obtained at an operational frequency of 9 GHz. The frequency spectrum data were obtained with a spectrum analyzer attached at the crystal detector position of the spectrometer shown in Fig. 4.1.

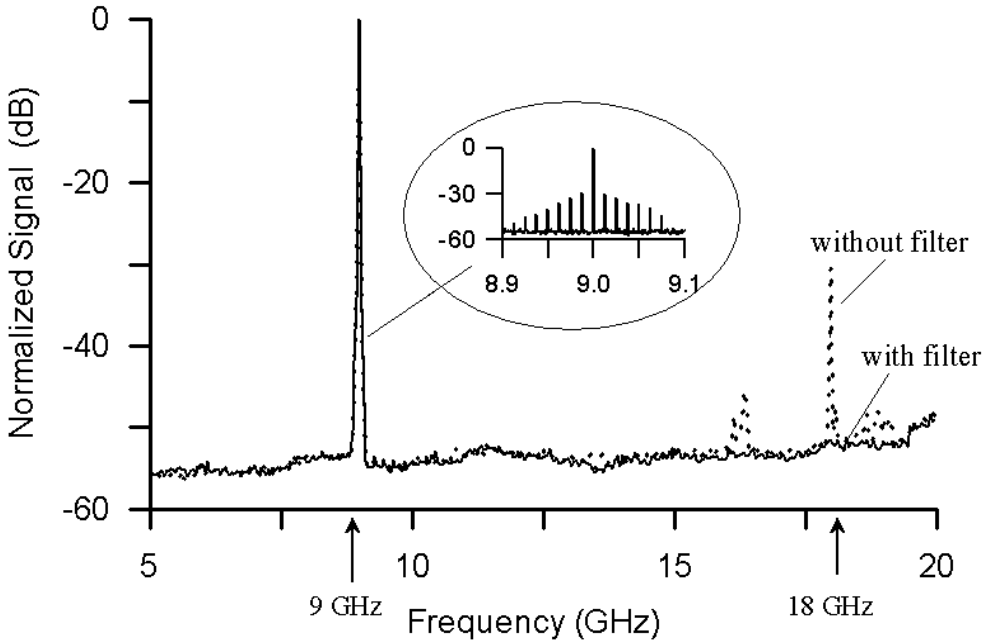

Figure. 4.2. Spectrum analyzer data of the TWT output pulse. The data were obtained with and without the use of a 14 GHz low pass filter. The operating frequency, pulse width, and the repetition rate of the microwave pulses were set to 9 GHz, 10 μs , and 1 kHz, respectively. The TWT amplifier has a maximum pulse width (τ), duty cycle (τ / T), and peak power of 100 μs , 4%, and 2.0 kW, respectively.

The solid and dotted lines correspond to the measurement being performed with and without the low-pass filter, respectively.

4.2.2 Static Magnetic Field

The static magnetic field is generated with a conventional 12-inch Harvey Wells electromagnet. The Harvey Wells power supply provides a maximum DC current of 50 Amps to the two coils of the electromagnet. The two sets of coils are connected in parallel, have a net resistance of 2 Ohms, and are water-cooled. The magnetic field strength is determined not only by the amount of current supplied to the coils but also by the diameter and separation of the electromagnet pole pieces. Several pole pieces, with varying pole face diameters and pole gap separations, are available for the electromagnet. The largest diameter pole pieces have the largest gap separation and

produce the lowest amplitude static magnetic fields with the best uniformity across the gap. The pole pieces with the smallest pole face diameters have the smallest pole gap separation and produce the largest amplitude fields with the least uniformity. A maximum static magnetic field of about 23 kOe is obtained with the pole pieces that have a 2.63-inch pole face diameter and a 1.5-inch pole gap separation.

Figure 4.3 shows magnetic field calibration data for three different pole configurations. The upper graph in the figure shows a plot of the normal component of

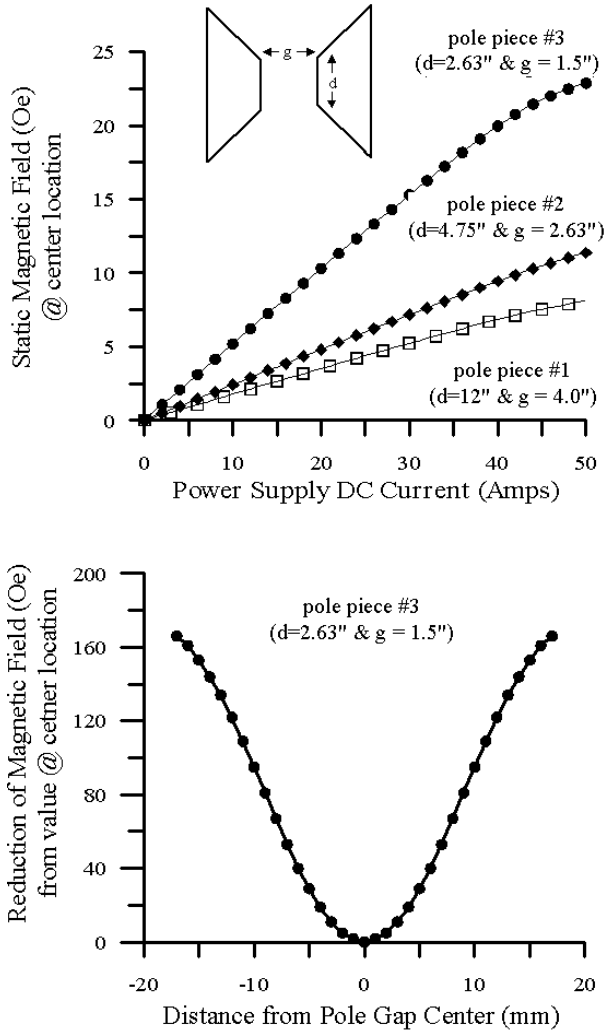

Figure. 4.3. Upper graph is a plot of the electromagnet static magnetic field versus DC operating current obtained for three different pole pieces, as indicated. The lower graph is a plot of the field strength versus the distance between pole pieces, obtained with the smallest available pole pieces and at a maximum DC current of 50 A. This corresponds

the static magnetic field relative to the pole faces versus DC current. The data were obtained with a Bell Gaussmeter Hall probe (described in Table 4.1) located at the center position between the pole pieces. The lower graph shows the uniformity of the field along the central axis for the smallest pole pieces (worst uniformity case). As can be seen in the lower plot, the magnetic field is largest near the pole face and is at a minimum at the center point between the two pole pieces, approximately 160 Oe lower then it is at the pole face. In order to maximize field uniformity, whenever possible the larger diameter pole pieces are used. The large diameter pole pieces also have the added benefit of having large pole gaps that facilitates the insertion and orientation of the microwave cavity.

Once a given pole piece configuration is set, the magnitude of the static magnetic field is controlled either manually or via the computer. The computer control is performed by applying a DC voltage from a D/A card to a BNC connector on the front panel of the electromagnet. A 0-10 volt input signal at the BNC input corresponds to the 0-50 Amp range of the electromagnet power supply. For more details on the computer control software, which was developed as part of this thesis work, see Appendix B.

The relative orientation of the static magnetic field, sample, and microwave field is set by the (1) orientation of the waveguide/cavity within the pole pieces of the electromagnet, (2) location of the sample within waveguide/cavity, and (3) by the rotation of the base of the electromagnet.

Figure 4.4 shows a 3-D side and a 2-D top view of a typical sample and static magnetic field geometry used for this study. As shown in the figure, the sample is placed near the end wall of the microwave cavity which is centered within the electromagnet pole pieces. The vectors indicate the static external magnetic field (H_{ext}) and the microwave pump field (h_p). The angle between H_{ext} and h_p, shown as θ_p in the figure, can be changed from 0^o to 360^o by rotating the electromagnet. This angle was set to 0^o for the parallel pumping measurements, 90^o for the subsidiary absorption

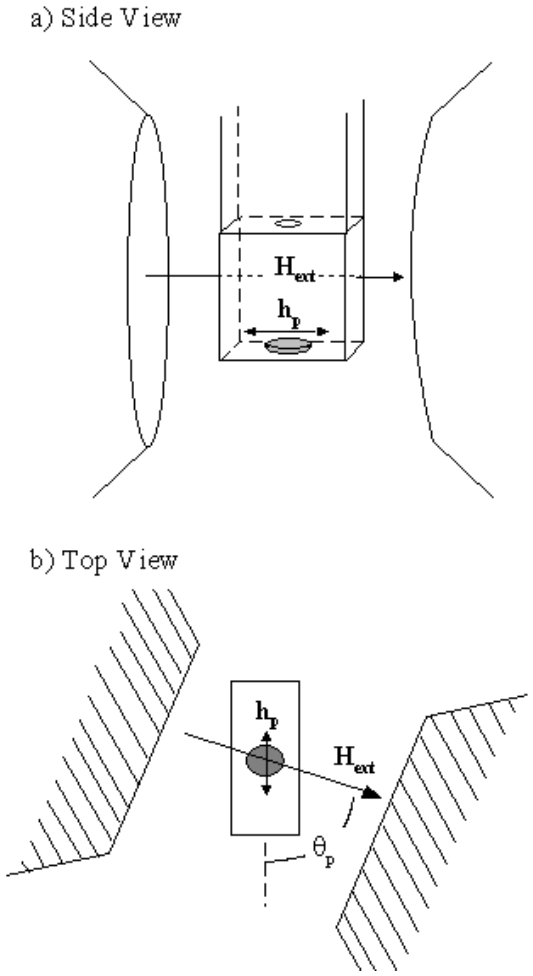

Figure. 4.4. Sketch a) shows 3D drawing of the microwave cavity centered within the electromagnet pole pieces. Sketch b) shows a 2D top view of the orientation of the external static field $\mathbf{H_{ext}}$ and the microwave pump field $\mathbf{h_p}$ at the end wall of the cavity. The angle θ_p is set via a rotation of the base of the electromagnet.

and FMR measurements, and at intermediate values for the resonance absorption measurements. A more detailed description of the angles employed for the resonance saturation measurements are given in Chapter 5.

4.3 SYSTEM CALIBRATION

For most low-power microwave measurements, only the relative change in the microwave power due to sample absorption needs to be measured, and careful calibration of the microwave power throughout the waveguide spectrometer is not required.

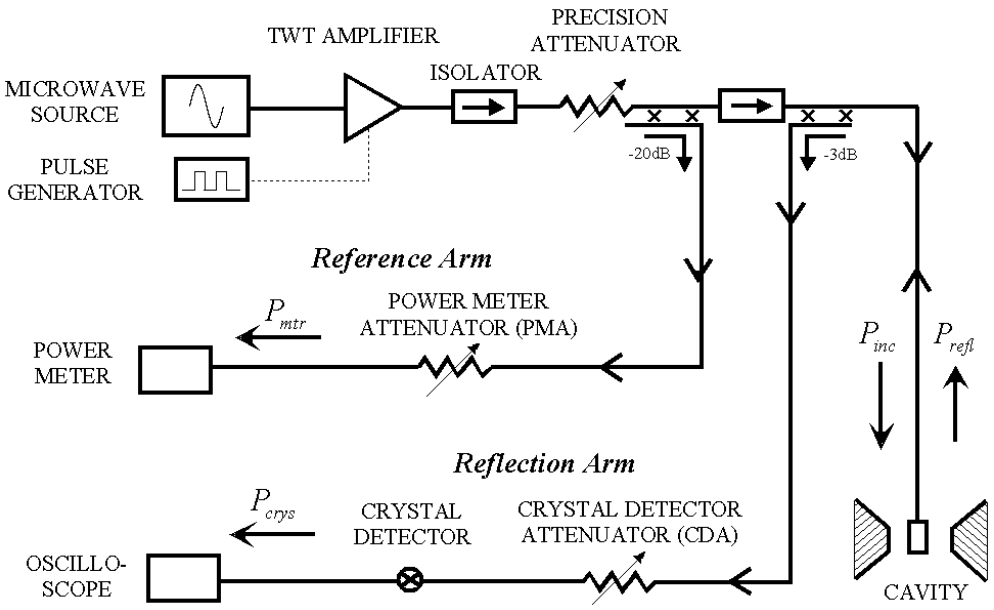

Figure. 4.5. Schematic diagram of the reference and reflection arms of the high-power spectrometer, originally shown in Fig. 4.1.

However, in order to perform high-power nonlinear threshold field measurements one must know the microwave power at the sample location in order to calculate the microwave field amplitude. Also, for most low-power measurements, microwave cavities are not utilized, the microwave frequency is kept at a fixed setting, so frequency dependent waveguide losses can be ignored. However, when performing high-power measurements which involve microwave cavities, the operating frequency often needs to be adjusted in order to match the changes in the cavity resonance frequency caused by sample effects primarily near FMR resonance. This section reviews the methods used to calibrate the microwave losses in the reflection and reference waveguide arms of the high-power microwave spectrometer, and concludes with the calibration equations that are used to calculate the microwave field amplitude at the sample position inside the cavity.

Figure 4.5 shows a schematic diagram of the high-power microwave spectrometer. As is shown in the figure, the reference and reflection arms are coupled to the main line

of the spectrometer by a 20 dB and a 3 dB directional coupler, respectively. The precision variable attenuators, shown as variable resistors in the diagram, are used to protect the sensitive detection components from excessive power levels. The reference and reflection waveguide arms of the spectrometer are used to monitor the peak microwave power that is incident upon and reflected by the microwave cavity, respectively. These arms were assembled in a similar fashion as discussed in Patton and Kohane [1972]; and Green and Kohane [1964], but with two important differences: (1) the incorporation of an isolator located between the two directional couplers and (2) the elimination of the shorting switch prior to the cavity. The inclusion of the isolator minimized troublesome leakage signals, which occur in the directional couplers, and the elimination of the shorting switch reduced the error associated with frequency-dependent standing wave mode patterns. This will be discussed in more detail in Section 4.3.1.

4.3.1 Waveguide Calibration

The relationship between the microwave power that is incident upon (P_{inc}) and reflected from (P_{ref}) the microwave cavity, and the microwave power at the power meter (P_{mtr}) and crystal detector (P_{crys}) locations in the microwave spectrometer may be expressed as

$$P_{inc}(f) = P_{mtr}10^{\left[\frac{PMA+WGC_{mtr}(f)}{10}\right]}, \qquad P_{ref}(f) = P_{crys}10^{\left[\frac{CDA+WGC_{crys}(f)}{10}\right]} \tag{4.1}$$

respectively. Where the PMA and CDA terms are the power meter and the crystal detector variable attenuator settings expressed in dBs, respectively. The $WGC_{mtr}(f)$ and $WGC_{crys}(f)$ terms are the frequency-dependent waveguide calibrated losses between the power meter and the crystal detector locations and the cavity location in the

spectrometer, respectively. The methods used to convert the crystal detector output voltage to power as well as calibrate the waveguide losses in the spectrometer will now be reviewed.

Figure 4.6 shows example crystal detector calibration data. These data were obtained at 9 GHz for the crystal detector with and without a 390 Ω load resistor attached in parallel to the crystal detector. The upper plot in the figure shows output pulse profiles.

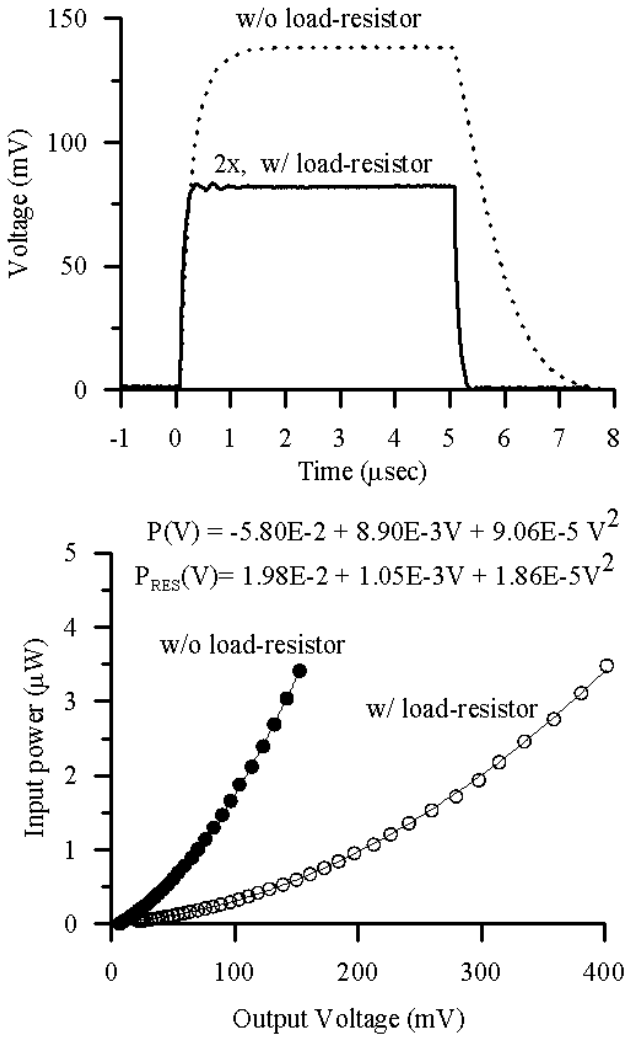

Figure. 4.6. The upper plot shows the crystal detector output obtained with (solid line) and without (dotted line) a 390Ω load resistor. The lower plot shows the output voltage response to the input power. The independent variable (input power) is plotted relative to the dependent variable (voltage) for fitting purposes.

As is seen in the figure, the load resistor increased the rise time and decreased the sensitivity of the crystal detector. All the measurements reported here were performed with the 390 Ω resistor attached to the crystal detector in order to maximize the rise time sensitivity. Rise time and pulse width considerations are discussed in more detail in the last section of this chapter. The lower graph in Fig. 4.6 shows the average input power versus output voltage of the crystal detector with (solid circles) and without (open circles) the 390 Ω load resistor. The solid line is a second order polynomial fit. The fitting parameters are saved in a calibration file and the automation program automatically converts output crystal detector voltage to input power. See Appendix B for a discussion of the automation programs and calibration files.

We will now discuss the waveguide calibration measurements. When calibrating the power differences between different locations in the high-power microwave spectrometer, it is important to realize that the net standing wave pattern is related to the combined mismatches that occur throughout the system. These mismatches occur at bends, flanges, and transitions from waveguides to waveguide components. Therefore, replacing individual components or slightly changing the length of any section in the spectrometer can have a dramatic affect on the standing wave pattern and in turn the waveguide power loss calibration coefficients. Thus, the system must be calibrated as a whole, rather than simply adding up the insertion losses of the individual components.

The waveguide calibration measurements are performed with a highly sensitive Microwave Transition Analyzer (MTA). The MTA controls a synthesized microwave generator and in turn acts as both a source and a detector. It sends out a well-defined continuous wave (CW) signal over a specified frequency range and power level, and then measures the power incident upon its sensor at each frequency step. In order to calibrate the spectrometer, the MTA output signal is inserted into the microwave spectrometer at the TWT output location (the TWT is disconnected from system). The MTA sensor input is connected to specific locations of interest in the spectrometer. The points of

interest for this study correspond to the power meter, microwave cavity, and crystal detector locations.

The waveguide calibration constant for the reference arm, referred to as $WGC_{mtr}(f)$, is determined by first measuring the power versus frequency response at the power meter location and then again at the cavity location. The data at the power meter location are obtained with the input to the MTA placed at the power meter head location ion the system, the power meter attenuator (PMA) set to zero, and a shorting plate located at the cavity iris. The data at the cavity iris location are obtained with the cavity removed from the system. For each connection, the MTA output is swept over the same frequency range, and the calibration constant corresponds to the ratio of the two data sets. The waveguide calibration coefficient for the reflection arm, referred to $WGC_{crys}(f)$, is obtained in a similar fashion.

Figure 4.7 shows plots of $WGC_{mtr}(f)$ and $WGC_{crys}(f)$ calibration data versus frequency, which were obtained from the X-band waveguide version of the microwave spectrometer. The dotted and solid lines in the upper plot are the results for the reference arm calibration measurements performed with and without the isolator located between the two directional couplers in the main line, respectively. As is seen in the graph, the isolator significantly reduced the unwanted reverse traveling leakage signal. This isolator was always used in the system and the reference arm calibration data were therefore considered to be frequency independent.

The lower plot in the figure shows the results for the reflection arm calibration measurements. Note that it was not possible to use an isolator to minimize the leakage into the reflection arm since bi-directional flow is required. Therefore, a "lookup" calibration chart was employed which contained the frequency dependent calibration data for this arm. The lower plot in Fig. 4.7 shows the effect of varying the shorting plate position. Here, one observes how the interference pattern in the reflection arm, which results from the directional coupler leakage and directed signals (See Appendix A

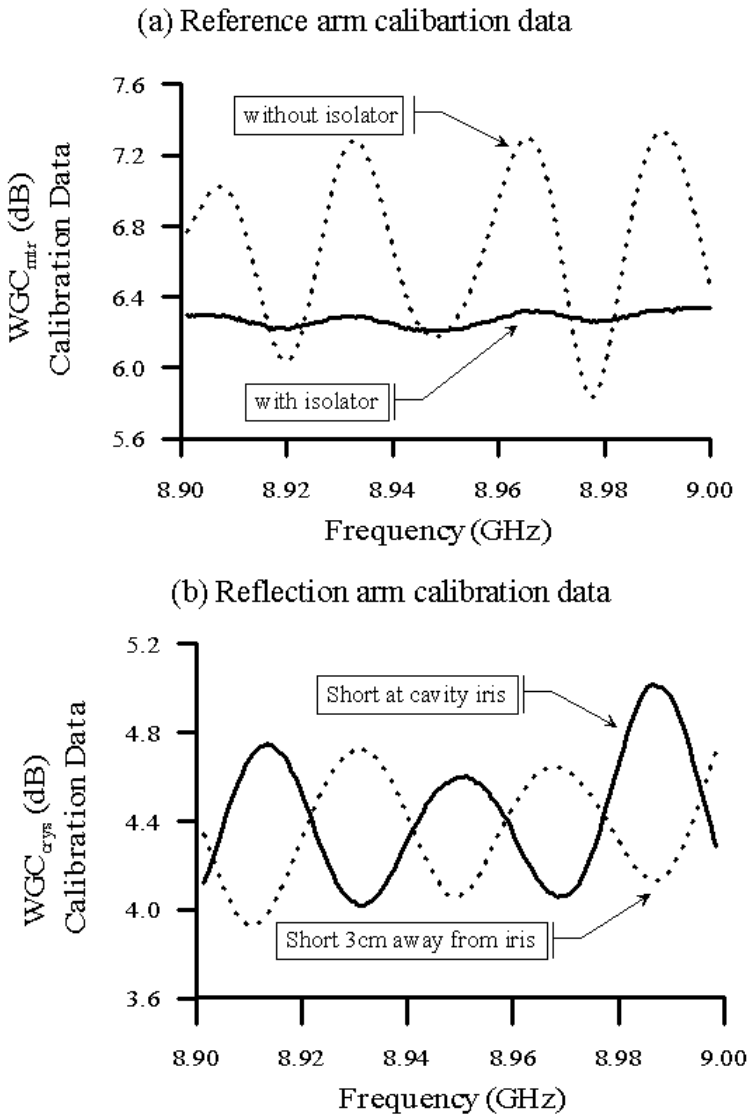

Figure. 4.7. Plots of waveguide loss calibration data versus operating frequency. The upper graph shows the improvements obtained by placing an isolator directly after the reference arm directional coupler. The lower graph shows the effect of varying the shorting plate location.

for more details), differs as the relative phase of the two signals changes. This is the motivation for eliminating the shorting switch used in previous systems. Note that unless the distance between the shorting switch and the cavity location is exactly at an integer multiple of the operational wavelength, using the shorting switch could result in miscalibration.

4.3.2 Cavity Calibration

The final calibration step to be discussed here concerns the microwave magnetic field amplitude inside the reflection type microwave cavity. The method used to calculate this field is based on the following three publications: (Green and Kohane [1964]; Patton and Green [1971]; and Patton and Kohane [1972]). While the procedure is relatively straightforward, following the exact calculations throughout the above referenced papers can be difficult. Difficulties arise because: (i) the Green & Kohane paper inaccurately depict the location in the cavity where h_o is calculated in their paper, (ii) the original publication uses MKS units, whereas the later ones use a mixture of CGS and MKS units, and (iii) different definitions are applied to the same symbols in the above publications. Therefore, in order to clarify the above problems, detailed derivations of the microwave field equations for rectangular and cylindrical cavities are provided in Appendix A. This subsection only provides the final formulae.

Both rectangular and cylindrical shaped reflection type microwave cavities were constructed for the high-power microwave spectrometer. See Figs. A.2 and A.7 in Appendix A for sketches of the magnetic field mode patterns in these two types of cavities. For the under-coupled TE_{101} rectangular cavities used in this study, the samples were located near the center of the cavity end-wall (this location will be referred to here as r_{rect}), and for the TE_{011} cylindrical cavity, the samples were located in the center of the cavity along the central axis of the cylinder (r_{cyl}). The above two locations correspond to regions of maximum microwave magnetic field uniformity and amplitude and zero electric field.

The time averaged microwave magnetic field amplitude at location "*r*" inside an under-coupled reflection type microwave cavity may be is written in terms of measurable cavity parameters and the power incident upon the cavity (P_{inc}) as

$$h_o(r)[\mathrm{Oe}] = \sqrt{\frac{80(1-\rho_{res})\,Q_L}{V_c\,[\mathrm{mm}^3]\,f_{res}[\mathrm{GHz}]\,g_m(r)}\,P_{inc}\,[\mathrm{W}]}\ . \tag{4.2}$$

Here, ρ_{res} is the *voltage* reflection coefficient of the cavity at resonance, Q_L is the loaded Q of the cavity, f_{res} is the cavity resonance frequency, V_c is the cavity volume, and $g_m(r)$ is a dimensionless factor that relates the stored energy in the cavity to the microwave field amplitude at a specific location r within the cavity. All the measurements performed for this work were obtained with the microwave frequency set equal to the cavity resonance frequency.

The voltage reflection coefficient ρ is related to the linear reflection coefficient ($\Gamma = P_{ref}/P_{inc}$) according to $\rho = 10^{\Gamma/20}$. The $g_m(r)$ parameter for locations r_{rect} and r_{cyl} in a TE_{10q} rectangular and TE_{01q} cylindrical cavity may be written as

$$g_m(r = r_{rect}) = \frac{1}{4}\left[1+\left(\frac{d}{qa}\right)^2\right], \tag{4.3}$$

and

$$g_m(r = r_{cyl}) = \frac{1}{2}\left\{J_o(\dot{\rho}_{o1})\right\}^2\left[1+\left(\frac{q\pi R}{d\,\dot{\rho}_{o1}}\right)^2\right] \tag{4.4}$$

respectively. In Eq. (4.3), the d and a parameters are the length and height of the rectangular type cavity, respectively. See Appendix A for more details. The $J_o(r)$ function in Eq. (4.4) is the zeroth order Bessel function and the $\dot{\rho}_{o1}$ term is the first root of $\dot{J}_o(r)$, such that $\dot{J}_o(\dot{\rho}_{o1}) = 0$, and equals 3.832 (Spiegel [1994]).

The loaded cavity Q (Q_L), resonance frequency (f_{res}), and resonance reflection coefficient (Γ_{res}) are determined from the analysis of reflected power versus frequency

sweep data. The data are obtained from the cavity with and without a short placed at the cavity iris hole location. The exact procedure is explained in detail by McKinstry and Patton [1989].

Based on the above equations the microwave magnetic field calibration ratios $h_o^2(\mathbf{r})/P_{\text{inc}}$ of the empty X-band TE_{101} rectangular and the TE_{011} cylindrical cavities, which were built as part of this study, are as follows. The rectangular cavity which has $Q_L = 2{,}100$, $\Gamma = -17\,\text{dB}$, and $f_{\text{res}} = 8.93\,\text{GHz}$ has a calibration ratio $h_o^2(r = r_{rect})/P_{\text{inc}} = 5.1\ \text{Oe}^2/\text{W}$. The cylindrical TE_{011}, which has $Q_L = 12{,}400$, $\Gamma = -20\,\text{dB}$, and $f_{\text{res}} = 8.99\,\text{GHz}$, has a ratio $h_o^2(r = r_{cyl})/P_{\text{inc}} = 14.1\ \text{Oe}^2/\text{W}$. Therefore, one obtains about three times as large of a microwave field for the same power in the cylindrical cavity than in the rectangular cavity. See Appendix A for a detailed discussion on cavity resonance modes, coupling factors, Q choice, construction methods, and calculation details.

4.4 SYSTEM UTILIZATION

The microwave pulse width, duty-cycle, frequency, and amplitude as well as the static magnetic field settings of the microwave spectrometer are all computer-controlled. Therefore, the spectrometer can be used to perform "stand-alone" low and high-power microwave loss measurements with minimal user input. This section will briefly review the hardware and software employed to automate the system, provide recommendations on system utilization, and conclude with example data.

4.4.1 Automation

Three different controller cards are used to interface a personal computer (PC) to the high-power microwave spectrometer. These include: (1) a general-purpose interface bus (GPIB) card, (2) a SMC800 stepper motor controller (SMC) card, and (3) a digital-to-analog converter (DAC) card. The GPIB card is inserted in the 16-bit PCI expansion slot

on the PC's motherboard, and allows for direct two-way communication between the computer and the GPIB compatible instruments used in the spectrometer. The SMC card connects to the PC's serial printer port and allows the computer to control the stepper motors attached to the variable attenuators. Thus, the computer utilizes the SMC card to directly control the attenuation setting of all the attenuators and in turn the power levels throughout the spectrometer. The DAC card is inserted into the 16-bit ISA slot on the PC's motherboard, and is used to apply a 0-10V DC signal to the front panel of the electromagnet power supply, and in turn control the static magnetic field amplitude between the electromagnet pole pieces.

Figure 4.8 summarizes the computer interface techniques used for the system. Note that the square box labeled "High-Power Microwave Source" in the figure actually consists of the Wavetek pulse generator, the HP synthesized sweeper, and the Applied Systems Engineering TWT amplifier. All three of these devices are GPIB compatible. National Instruments LabVIEW software was used to automate the high-power microwave spectrometer. LabVIEW is a graphical programming language in which stand-alone subprograms can be built, independently tested, and combined in a seamless fashion to form a complex computer control software package. Numerous LabVIEW programs were developed in the course of this study. See Appendix B for a review of the key calibration and measurement control programs that were written as part of this thesis work.

4.4.2 Butterfly Curve Data Collection

This section shows how the above system is used to obtain butterfly curve data. Here details are given on how (1) the $\mathbf{h_p}$ and $\mathbf{H_{ext}}$ vector fields are oriented, (2) the h_p and H_{ext} field ranges are chosen, and (3) the instability data are analyzed. The data shown in this section were obtained on a thick YIG film. The film was grown using standard flux techniques by Litton Corporation. The sample was rectangular in shape

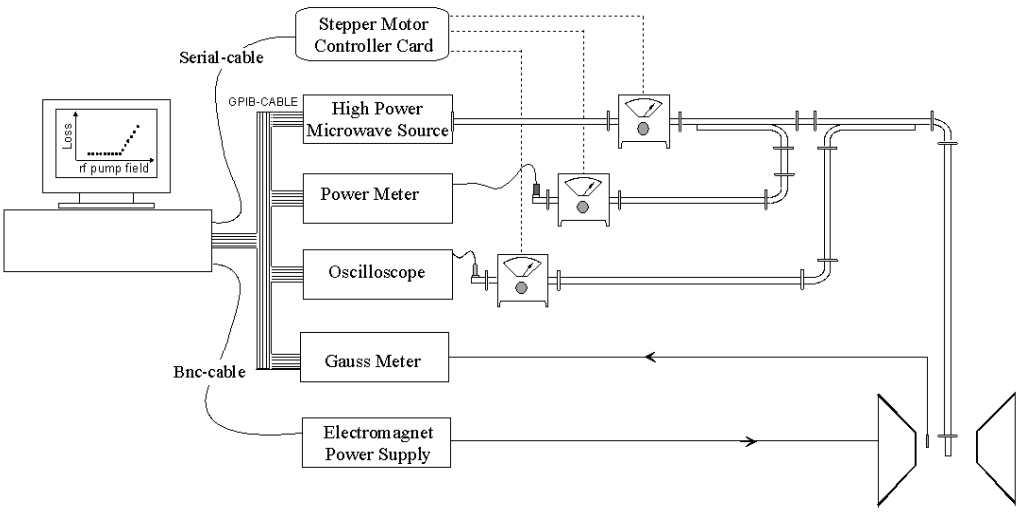

Device	Interface	Purpose of Communication
Synthesized Sweeper	GPIB	Control→ microwave frequency
Pulse Generator	GPIB	Control→ pulse width & duty cycle
TWT Amplifier	GPIB	Control→ microwave field on/off
Variable Attenuators	Stepper Card	Control→ microwave power levels
Magnet Power Supply	DAQ Card	Control→ static magnetic field
Power Meter	GPIB	Read→ average power
Gaussmeter	GPIB	Read→ magnetic field
Oscilloscope	GPIB	Read→ crystal detector voltage

Figure. 4.8. Schematic diagram of the three different methods used to interface the computer to the high-power microwave spectrometer, and a summary table that summarizes the interface method used for the various devices in the spectrometer.

(1x3 mm), approximately 20 μm thick, and had an FMR linewidth of about 5 Oe at 8.9 GHz. Note that all the measurements to be discussed in this section were performed with a reflection-type rectangular microwave cavity which had a resonance frequency of about 9 GHz.

In order to align the microwave and static magnetic fields within the sample to the orientation of interest, the following steps are taken. First, the microwave cavity and the

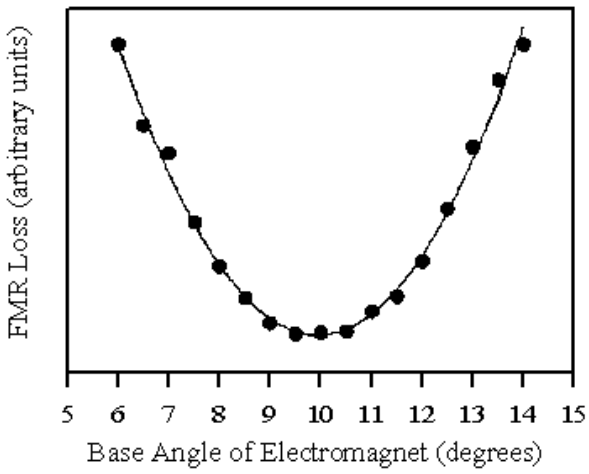

Figure. 4.9. Plot of FMR loss versus electromagnet base angle. The minimum loss, which occurs at a base angle of about 10 degrees, corresponds to the microwave and static magnetic fields being aligned parallel.

electromagnet pole pieces are arranged such that the microwave and static magnetic fields are coplanar with the cavity end-wall (See Fig. 4.4 for details). The angle θ_p between the two fields is then set by rotating the base of the electromagnet. This angle is calibrated using the following procedure. First, the FMR resonance response is measured. Then the magnitude of the static magnetic field is set to the FMR resonance field, and the peak FMR absorption is measured for various electromagnet angles. The angle that yields the minimum amount of FMR absorption corresponds to $\theta_p = 0^o$.

Figure 4.9 shows FMR peak losses versus electromagnet base angle. As is seen in the figure, the peak FMR loss has a clear parabolic dependence on the base angle. The minimum loss, which occurs at about a 10-degree base angle, corresponds to a parallel alignment of $\mathbf{h_p}$ and $\mathbf{H_{ext}}$. Typically, the above method of alignment is accurate to within 0.05 degrees. Once this angle is determined, the electromagnet is then rotated to the proper setting according to the type of instability process of interest. In this example a base angle of 10^o and 100^o would be used for the parallel ($\theta_p = 0^o$) and the perpendicular pumping ($\theta_p = 90^o$) configurations, respectively.

Once the angle between the $\mathbf{h}_p$ and $\mathbf{H}_{ext}$ fields is set, the relative magnitudes of these fields, which are required to obtain the butterfly curve data are determined. This is accomplished by measuring the sample loss versus static field at various h_p settings for a fixed microwave frequency ω_p.

Figure 4.10 shows example static field scan data obtained on the YIG thick film with the parallel pumping field alignment at four different microwave power levels and a

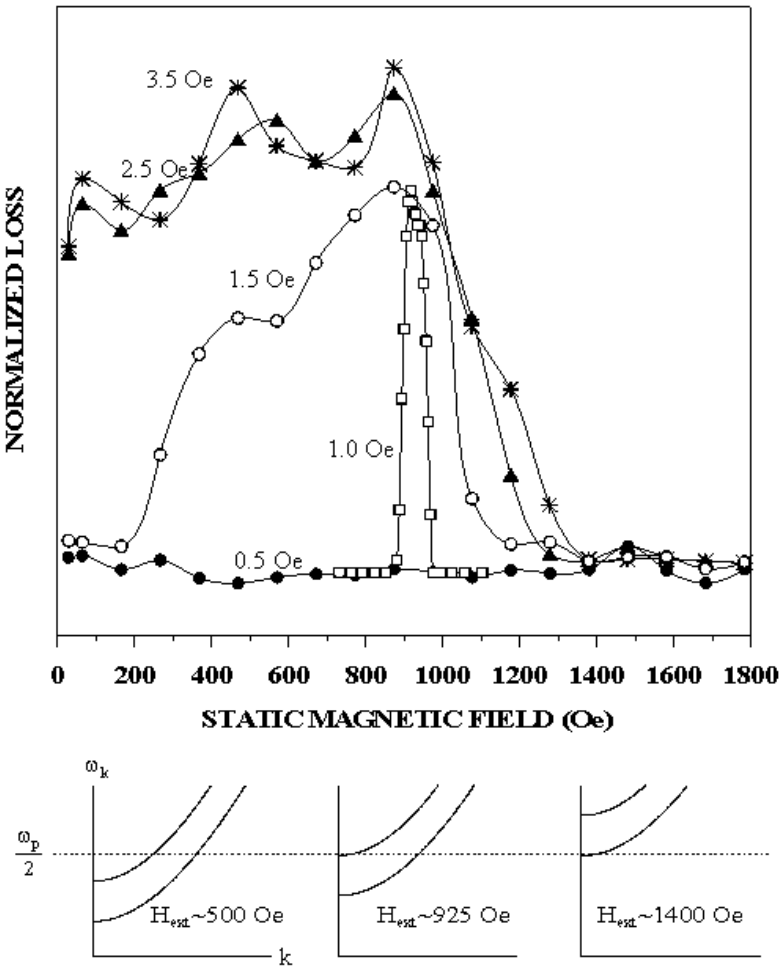

Figure. 4.10. Plot of normalized loss versus static magnetic field for various microwave field amplitudes as indicated in the figure. The data were obtained on a thick YIG film at 8.9 GHz with the parallel pumping configuration. The first notable sign of a nonlinear response occurs for microwave field amplitude of 1.0 Oe. The lower spin wave dispersion sketches show the relative positions of the upper and lower manifold branches for three different static field values

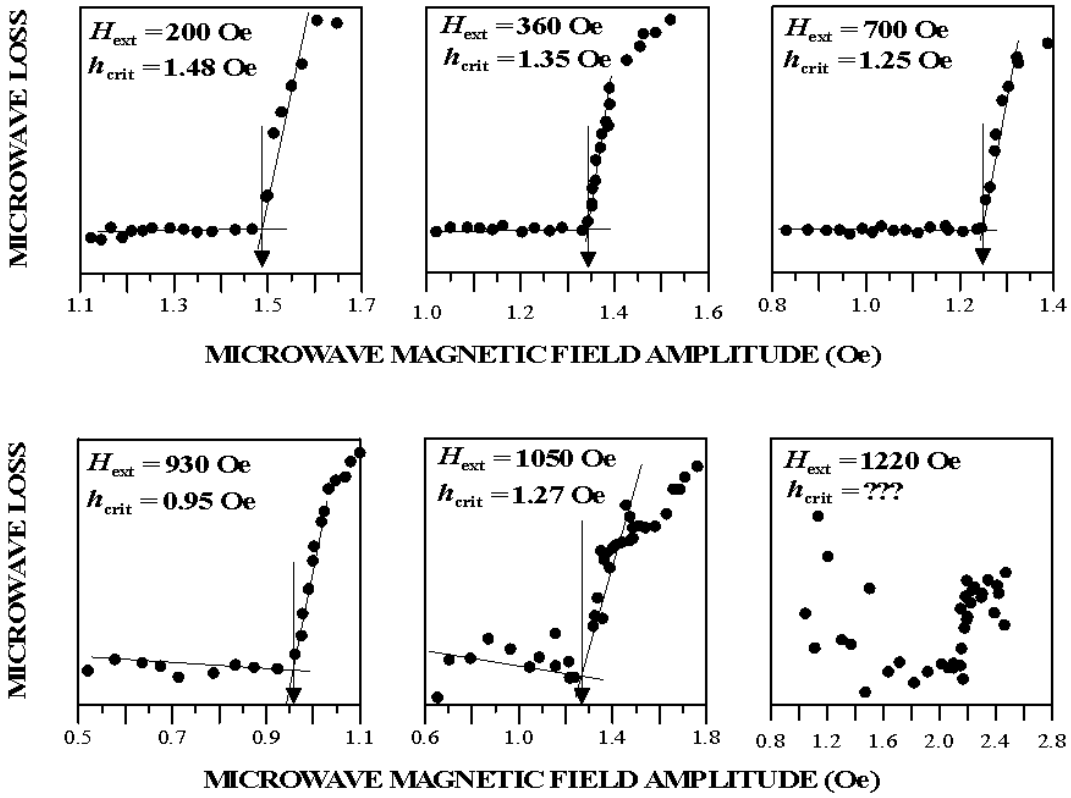

Figure. 4.11. Parallel pumping normalized microwave loss versus pump field amplitude, obtained on a thick YIG film at 8.9 GHz, for several different static magnetic fields (H_{ext}). The threshold field (h_{crit}) required to excite the nonlinear effects is given in each plot and indicated with the solid arrow. For $H_{ext} > 1100$ Oe, the threshold response becomes undetectable, so another method shown in Fig. 4.12 is employed.

frequency of 9 GHz. From these four scans, one learns a considerable amount of information regarding the required h_p and H_{ext} settings needed to excite the parallel pump spin wave instability response. One determines (1) at what H_{ext} the minimum threshold of the butterfly curve occurs, (2) the appropriate H_{ext} and h_p field ranges to scan in order to excite the nonlinear effects, and (3) the maximum H_{ext} for which spin waves are available for excitation.

Analysis of the data shown in Fig 4.10 reveals that: (1) the minimum of the butterfly curve occurs at $H_{ext} \approx 900$ Oe for a microwave field amplitude between 0.5 and 1.0 Oe, (2) for $200 < H_{ext} < 900$ Oe that $1 < h_{crit} < 1.5$ Oe, while for $H_{ext} > 900$ Oe that

$1.5 < h_{crit} < 3$ Oe, and (3) the maximum H_{ext} field at which spin waves are available for excitation is about 1400 Oe as no significant changes in the absorption profiles occur for $H_{ext} > 1400$ Oe when the microwave field amplitude is increased from 2.5-to-3.5 Oe.

The required static field ranges for exciting the nonlinear butterfly curve data can also be obtained from the analysis of the spin wave manifold. The lower plots in Fig. 4.10 show the spin wave manifold calculation results for three different static field settings. The calculations were performed with saturation magnetization $4\pi M_s = 1750$ Gauss and static fields of 500, 925, and 1400 Oe. The dotted line corresponds to $\omega_p / 2(2\pi) = 4.5$ GHz, which corresponds to the frequency of the excited spin wave modes. It is known that minimum of the butterfly curve occurs for the static field setting at which $\omega_p / 2 = \omega_k(\theta_k = 90^o, k = 0),$ and the maximum static field for which spin wave modes are available for excitation occurs for the static at which $\omega_p / 2 = \omega_k(\theta_k = 0^o, k = 0)$. From an inspection of field values given in the lower manifold plots in Fig. 4.10, one can see that these field values are in reasonable agreement with the values obtained from the upper plots in Fig 4.10.

4.4.3 Example Threshold Field Data

Once the approximate static and microwave field ranges required to obtain the butterfly curve data are determined, the h_{crit} threshold data can then be obtained either by keeping H_{ext} fixed and measuring the sample absorption versus h_p, or by keeping h_p fixed and measuring sample absorption versus H_{ext}.

Figure 4.11 shows plots of sample absorption versus microwave field amplitude h_p data obtained at six different fixed static field settings. The data were obtained on the same YIG sample as discussed in Fig. 4.10. For most of the plots in Fig. 4.11 there is an abrupt and sharp increase in the sample losses, which corresponds to a transition from the linear to nonlinear sample response at a specific microwave field, h_{crit}. From an inspection of the plots in Fig. 4.11 one can see that h_{crit} depends upon the H_{ext} setting.

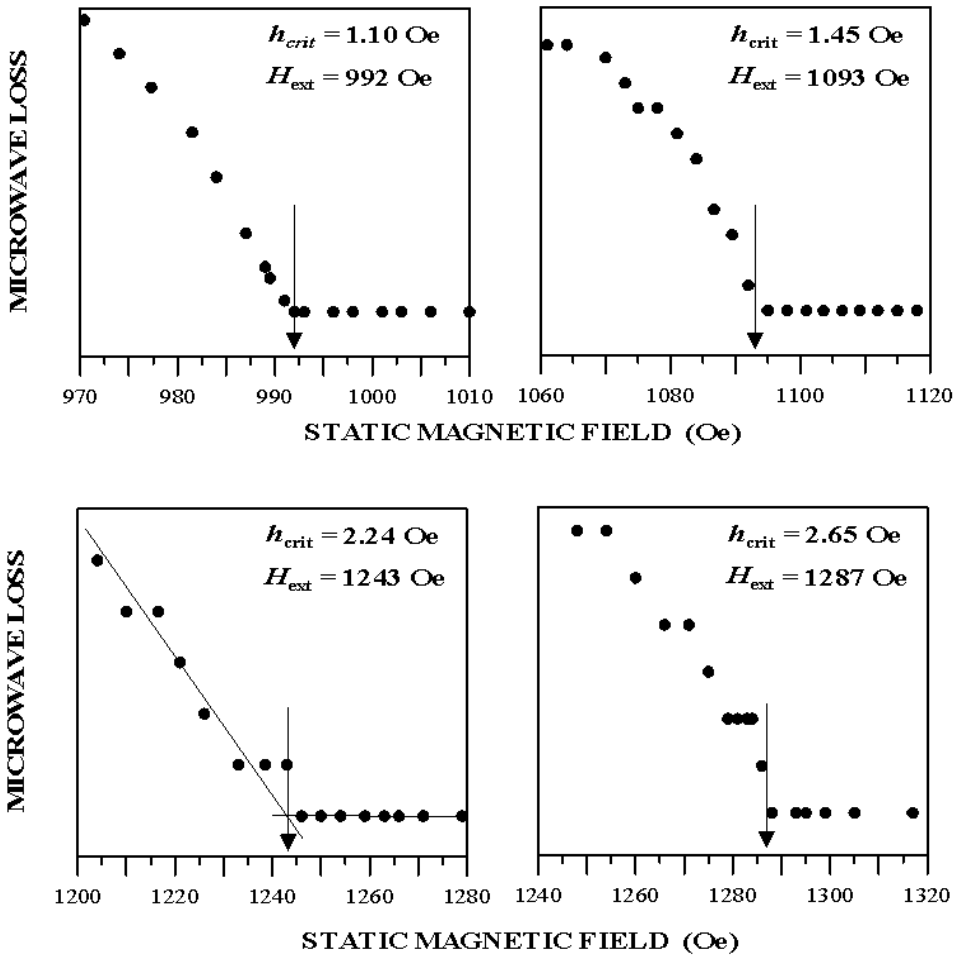

Figure. 4.12. Parallel pumping microwave loss versus static magnetic field plots obtained on thick YIG film at 8.9 GHz. The plots were obtained with microwave field values as shown. The static field is scanned from high-to-low (linear to nonlinear region) in the above plots.

Furthermore, the abruptness of the linear to nonlinear transition, and therefore the accuracy of the threshold field determination, also depends on H_{ext}. For static fields higher than the minimum threshold response (i.e., $H_{ext} > 900$ as in Fig. 4.10) the sharpness of the transition from the linear to the nonlinear reduces as H_{ext} increases. In order to overcome this, a second sweep method shown in Fig. 4.12 is used.

Figure 4.12 shows normalized sample loss versus static field data obtained at several fixed microwave field amplitude values. The data were obtained using the sample and

parallel pumping orientation as used in Figs. 4.10 and 4.11. The static field sweeps were scanned from the high-to-low H_{ext} values, which yields a more abrupt change in normalized loss response than if one scans from the low-to-high field ranges.

Inspection of the data shown in Fig. 4.12 shows that there is a clear correlation between the static field at which spin waves suddenly become excited and the value of the microwave field amplitude used. The higher the microwave field amplitude, the larger the static field at which one observes the transition. This method of determining the threshold field was utilized extensively for the parallel pumping measurements obtained on the Zn Y-type hexagonal ferrites samples studied here. The results of these measurements are discussed in Chapter 5.

Once all the microwave and static field scans are complete, and the h_{crit} threshold fields are determined at each static field setting, one can plot the butterfly curve h_{crit} versus H_{ext} sample response. See Figure 2.12 in Chapter 2 for a plot of the resultant butterfly curve, which summarizes threshold field data shown here. As was mentioned in Chapters 2 and 3, these plots provide a direct summary of the transition regime from linear to nonlinear response versus static magnetic field, and, therefore, a direct feedback on the material's high-power handling capabilities. They also provide a means for determining the relaxation rates of the spin wave modes excited at the threshold field.

During the course of the above measurements, the linear magnetic susceptibility of the sample changes with the external static magnetic field, and in turn can alter the cavity resonance frequency. The size of the frequency change depends on the relative sample-to-cavity volume, and is strongest for the perpendicular pumping processes near FMR resonance. If the effect is large enough, then the operating frequency must be tuned to the altered cavity resonance frequency for each static field setting. This is done automatically with the LabVIEW program developed for this study.

4.5 MEASUREMENT SUBTLETIES

This section provides guidance on how to obtain spin wave instability butterfly curve data in a reliable manner. Some of the pitfalls discussed here are quite obvious and are included for completeness while others are more subtle and have led to errors in past publications (McKinstry and Patton [1989]). The pitfalls discussed here are grouped into two categories: (i) those that lead to errors in the calculation of the microwave magnetic field amplitude and (ii) those that lead to a misinterpretation of the threshold response.

4.5.1 Microwave Field Calculation Errors

This subsection addresses three concerns regarding the calculation of the cavity magnetic field amplitude (h_o): (1) proper shorting techniques, (2) correct use of the TWT amplifier, and (3) the importance of avoiding cavity overloading.

The first source of h_p error, which was discussed earlier, is caused by improper shorting procedures. Often a shorting switch, which is located relatively far from the cavity location, is used to monitor sample absorption and to calibrate the cavity (Patton and Kohane [1972]; Cox *et al*. [2001]). As was discussed previously, locating the short in this manner can lead to errors in the waveguide calibration factor ($WGC_{crys}(f)$) and the cavity parameters (Q_L and ρ_{res}). As was shown in Fig. 4.7, varying the shorting position can effect the net shorted reflected signal at the crystal detector by as much as 2dB (20% effect on measured reflected power). Therefore, care must be taken to locate the short at the cavity iris position in the waveguide system.

A second source of h_p calculation error is related to the improper use of TWT amplifiers. The first issue involves TWT amplifiers that operate only in pulse mode, and the second issue is in regards to continuous wave (CW) TWT amplifiers. As was discussed in Section 4.2, pulse-mode TWTs amplify the higher harmonics of the input frequency to relatively high levels (see Fig. 4.2 for details). These higher harmonics are

transmitted through the waveguide system to the power meter. The power meter used for the microwave spectrometer reports the average of all the microwave signals that are present over its full operational frequency band. Therefore, the higher TWT harmonics can lead to higher measured power than what is actually incident on the sample at the cavity resonance frequency, and can in turn, result in miscalculated h_p values. To avoid this, the low-pass filter shown in Figures 4.1 and 4.2 was utilized to eliminate these higher harmonic signals.

The second possible h_p calculation error, which is related to improper TWT usage, has to do with continuous wave (CW) TWT amplifiers. While such amplifiers were not used in this study, it is worth pointing out a possible problem concerning their use. If a CW TWT amplifier is used to amplify microwave pulses, then care must be taken to avoid false power readings. The problem arises because all TWT amplifiers have a certain amount of positive feedback and, therefore, generate a small but non-negligible signal over their entire bandwidth. For a CW TWT amplifier, this small background signal can have a significant contribution to the net measured power if (1) small duty cycles/pulse widths are used and if (2) the power meter reports the average reading of all the input signals over its entire bandwidth as is the case with the power meter used in this study. As was mentioned previously, only signals at the cavity resonance frequency excite the nonlinear sample, so the meter will be yielding a higher than actual power at sample position and one will report larger than actual threshold fields. One method way to eliminate this error is to insert a narrow band pass filter centered on the cavity operating frequency prior to the reference arm. A preferred method is to locate a microwave switch after the *CW* TWT to eliminate the background CW signal when the pulse signal is not present.

The third and final source of h_p calibration error to be discussed is related to cavity overloading. A key assumption in the formulation (See Appendix A for details) is that the sample has a negligible effect upon the empty cavity response. Therefore, care must

be taken to avoid excessive sample power absorption in the cavity. The actual amount of sample absorption that is tolerable depends upon the value of the empty cavity Q. The larger the Q, the smaller the amount of sample absorption that can be allowed. For all the measurements performed in this study, the loaded Q was never allowed to decrease to less than 90% of the empty cavity Q value.

Cavity overloading is typically not a concern for the first order subsidiary absorption and parallel pumping instability measurements because large amounts of sample absorption are only observed for microwave magnetic field amplitudes above the threshold field. However, cavity loading is a significant issue for resonance saturation measurements in which FMR absorption is usually quite large at low-power levels. In previously performed resonance saturation measurements, cavity-loading issues were minimized by using very small samples and low-Q cavities. However, for the measurements performed here, the thresholds were measured not only at resonance but also for static magnetic fields away from the resonance field. If the above methods of reducing cavity loading do not provide the sensitivity needed for these off-resonance measurements, and therefore a different method was used.

For the resonance saturation measurements performed in this study, cavity overloading was avoided by varying the angle θ_p between the microwave field and static magnetic field; see Fig. 4.4 for sketch of this angle. In a resonance saturation experiment, only the transverse microwave field component to the static field drives the losses, such that the losses are proportional to $(h_o \sin\theta_p)^2$. Therefore, the total cavity Q may be written as

$$Q = \frac{2\pi \langle U_{\text{stored}} \rangle}{\langle U_{\text{lost}} \rangle} \approx \frac{h_o^{\,2}}{\mathrm{P}_{\text{empty-cav-loss}} + (h_o \sin\theta_p)^2}. \tag{4.5}$$

As is observed in the above relation, when θ_p is decreased, the effect of sample loss upon the cavity Q is lessened. Therefore, θ_p was set to a minimum value when the static

field was equal to the FMR resonance field and θ_p was increased as the static field was set at values away from the resonance field. This was done in such a manner that the loaded Q of the cavity was never allowed to decrease to more than 10% of its empty cavity Q value (Cox *et al*. [2001]).

4.5.2 Misinterpretation of Threshold Data

Mischaracterization of the true onset of the nonlinear instability point can occur due sample heating and not properly accounting for the nonlinear response time. When a ferrite sample is heated, its net saturation magnetization decreases and in turn yields an absorption response that can be easily mistaken for an instability threshold. These heating related effects have led to the threshold fields being misreported as smaller than they actually are (McKinstry and Patton [1989]). Such overheating related threshold field errors can be avoided by decreasing the duty cycle of the microwave pulses while maintaining a fixed pulse width. This method works well for the parallel pumping and subsidiary absorption measurements where small amounts of sample absorption occur for microwave fields below the threshold value. However, for the resonance saturation measurements, in which large sample absorption occurs at even low-power levels, the pulse width as well as the duty cycle is important. Here it is essential not only to maintain small duty cycles but also short pulse widths. For the resonance saturation measurements reported here, a duty cycle of 0.1% and a pulse width of 10 μs were adequate to avoid overheating the samples.

Mischaracterization of the threshold field can also occur if the microwave pulse width is so short that the time required to excite the nonlinear response of the spin wave system is not properly accounted for. The delay time required for the nonlinear instability response to occur depends upon the relaxation rate of the critical modes and the relative amount of microwave power that is required to excite the instability process. A classical analogy is water overflowing from a bathtub: the rate of incoming water from

the faucet corresponds to the rate of microwave energy being coupled into a given spin wave mode, and the tub drain corresponds to the relaxation rate of the spin wave modes. The initial level of the water in the tub, prior to turning on the faucet, corresponds to the preexisting thermal energy in the spin wave modes. Once the water is turned on, if the rate of flow into the tub is less than the drain flow rate, then the tub does not over-flow. This corresponds to the linear spin wave excitation regime. If the flow rate from the faucet exceeds the drain rate, then once the water is turned on it fills up the tub, and eventually overflows (i.e., nonlinear spin wave amplitude growth). The delay time between the faucet turn on time and water overflow corresponds to the time required to excite nonlinear spin wave growth. A failure to account for this delay time, and thereby using too short of a microwave pulse width, will lead to the threshold fields being reported as larger than they actually are.

Figure 4.13 shows data that exhibit the delay time requirements for the nonlinear transition response which highlight the necessity for using wide enough microwave pulse widths to obtain accurate threshold field data. The plot shown in Fig. 4.13 shows crystal detector output voltage pulses versus time, obtained at four different microwave power levels (see Fig. 4.1 for location of crystal detector within microwave spectrometer). The data were obtained on the YIG sample discussed above using the parallel pumping configuration. Each output pulse shown in the figure was obtained at a fixed microwave power level. For the lowest microwave amplitude, $h_p = h_1$ the amount of reflected power is constant over the pulse width of 10 microseconds. Then for the next highest amplitude, $h_p = h_2$, there is a stair-step in the voltage pulse which occurs at about $6\mu\text{sec}$. For the time $\text{T} < 6\mu\text{sec}$ the difference in the pulse heights for the pulses obtained at $h_p = h_1$ and $h_p = h_2$ corresponds to a linear increase in sample absorption associated with the increased microwave field amplitude. The increased losses, which occur for $\text{T} > 6\mu\text{sec}$ on the pulse $h_p = h_2$, correspond to the nonlinear response of the spin system.

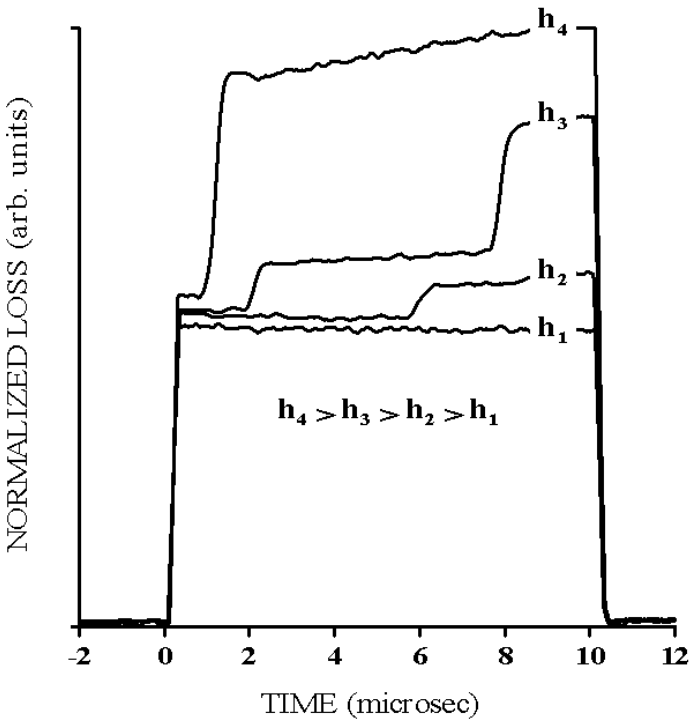

Figure 4.13. Plots of microwave loss versus time. The data were obtained on a thick YIG film at 8.9 GHz, for parallel pumping orientation, at single H_{ext} value, and four different microwave fields. The stair step jump in the h_2 response data, which occurs at about 6 microsec, corresponds to the onset in the nonlinear amplitude growth of the critical mode. The two different steps observed in the $h = h_3$ and h_4 plots, correspond to the nonlinear excitation of two different spin wave modes.

For the pulse at $h_p = h_3$ shown in Fig. 4.13, one observes two stair-step rise in the amplitude of the pulse. This corresponds to the nonlinear excitation of two different spin wave modes. The first step corresponds to the excitation of the critical mode which has either a lower damping rate and/or better coupling to the microwave driving field than the secondary mode excited at the later time. If the microwave power is increased even further, these two nonlinearly excited spin wave modes interact and will eventually display a chaotic response (period doubling, tripling, etc.). There is a rich area of nonlinear dynamics that are studied using parallel pumping in YIG (Wigen [1994]). Such nonlinear responses are not the focus of this work; rather the work addresses the transition point from the linear to the nonlinear regime.

From an inspection of Fig. 4.13, it is clear that if one were to measure the sample loss versus h_p with a pulse width of 1 μsec, one would think that $h_{crit} > h_3$. If a microwave pulse width of 5 μsec was used, then the sample loss versus h_p analysis would lead one to think that $h_2 < h_{crit} > h_3$, whereas if a pulse width of 9 μsec was used, one would know that the nonlinear transition occurred for $h_1 < h_{crit} < h_2$.

In summary, if a microwave pulse width that is too long is used, sample heating will occur and the reported threshold field will be smaller than the actual threshold field; if a pulse width that is too short is used, the spin system will not have adequate time to respond and the reported threshold field will be larger than the actual threshold field. Therefore, when acquiring instability data on a given sample for the first time, the threshold data should be acquired for several pulse widths and duty cycles to ensure that the measured threshold is independent of variations in pulse width (allowing for nonlinear response time) and duty cycle (not overheating the sample). For the resonance saturation data reported here, a duty cycle of 0.1% and a pulse width of 10 μs were utilized. Larger duty cycles or longer pulses resulted in observable heating effects. For the subsidiary absorption and parallel pumping measurements, pulse widths of approximately 50 μs and duty cycles of about 0.1% were used. Shorter pulse widths resulted in larger than actual threshold field measurements.

CHAPTER 5

MEASUREMENT RESULTS AND ANALYSIS

This chapter discusses the spin wave instability measurements and analyses that were performed on single crystal easy-plane Mn substituted Zn Y-type hexagonal ferrite disks as part of this thesis work. It should be noted that the resonance saturation, subsidiary absorption, and parallel pumping spin wave instability threshold measurements and analyses presented here constitute the first extensive work on butterfly curves for planar hexagonal ferrites for all three pumping configurations.

The presentation of the high-power data and analyses shown here is organized as follows:

1. The first section addresses the sample details.
2. Section two discusses the resonance saturation butterfly curve measurements and analyses.
3. Sections three and four present the subsidiary absorption and parallel pumping measurements and analyses.
4. Section five summarizes the measured threshold fields and calculated spin wave linewidths.
5. The last section reviews follow-up measurements performed by Alex Nazarov, which address questions raised by the parallel pumping data and analyses presented here.

5.1 OVERVIEW

The three main measurement and analysis objectives of this thesis work were: (1) to obtain spin wave instability threshold data for a range of static magnetic fields and microwave pump field configurations; (2) to use these data to construct resonance saturation, subsidiary absorption, and parallel pump butterfly curves; and (3) to analyze the butterfly curves in order to determine which spin wave modes are excited at the instability threshold and the spin wave linewidths of these critical modes. Prior to discussing the results of these objectives, a review of the composition, static magnetic, and linear microwave magnetic properties of the single crystal Mn doped Zn Y-type hexagonal ferrite samples that were used in this study will be given.

5.2 HEXAGONAL FERRITE SAMPLE DETAILS

The single crystal samples were grown at Purdue University using a standard 2BaO-B_2O_3 flux technique (Savage and Tauber [1964]; Tauber *et al*. [1964]; Savage *et al*. [1965]). A commercial composition analysis of the material gave an Mn concentration of 2.6% by weight. This corresponds to a nominal formula unit of $Ba_2Zn_{2-x}Fe_{12-y}Mn_{x+y}O_{22}$, subject to the condition $x + y = 0.7$. The manganese substitution compensated for any residual Fe^{2+} that may have been present in order to maintain a high resistivity material and thereby eliminate the eddy current complications in the microwave response that are observed in the nonsubstituted materials (Truedson *et al*. [1994]).

The particular samples used for the study were obtained from three as grown c-plane platelets of the Zn Y-type hexagonal material. The hexagonal crystal structure of the material causes it to be readily cleaved into platelets with the hexagonal crystallographic c-axis normal to the platelet plane. Therefore, the anisotropic easy plane of the Zn Y-type hexagonal ferrite samples corresponded to the plane of the platelets. The edges of

the platelets were ground with silicon carbide 600 grit paper and polished with 1 μm alumina powder. The extremely smooth flat surfaces of the platelets were left untouched. The final disks were nearly circular and nominally 1 mm in diameter with nominal thicknesses of 90 μm, 100 μm, and 200 μm. These disks, in order of increasing thickness, are denoted here as samples S1, S2, and S3. The thinnest sample, S1, most closely resembled a cylindrical disk. The edges of the other two samples were somewhat beveled.

The sample parameters that are needed to perform threshold calculations are the saturation magnetization ($4\pi M_s$), anisotropy field (H_A), gyromagnetic ratio (γ), and the demagnetizing factors ($N_{x,y,z}$). The measured FMR linewidth ΔH_{FMR} also enters into the formulae for resonance saturation processes. The demagnetizing factors for a disc shaped ellipsoid sample with disc plane in *y*-*z* coordinate plane can be rewritten as $N_y = N_z = \left(1 - N_x\right)/2$. Therefore, there are four sample unknowns $4\pi M_s$, H_A, γ, and N_x. These four unknowns are determined from four different equations and associated measurements which describe the applied static magnetic fields required to (1) saturate the magnetization within the disk plane, (2) saturate the magnetization normal to the disk plane, (3) achieve the high field cut off point for the parallel pumping butterfly curve, and (4) obtain the low-power FMR peak position.

The applied static magnetic fields required to saturate the magnetization within and normal to the disk plane were measured with a vibrating sample magnetometer (VSM). Figure 5.1 shows typical VSM hysteresis plots of magnetization versus static magnetic field obtained on sample S3. The solid circles and open squares correspond to measurements performed with the static magnetic field applied within and orthogonal to the plane of the disk, respectively. The large difference in the static magnetic fields required to saturate the sample in the two directions is due to the large effective planar anisotropy and demagnetizing fields. The theoretical in-plane and out-of-plane saturation fields may be written as

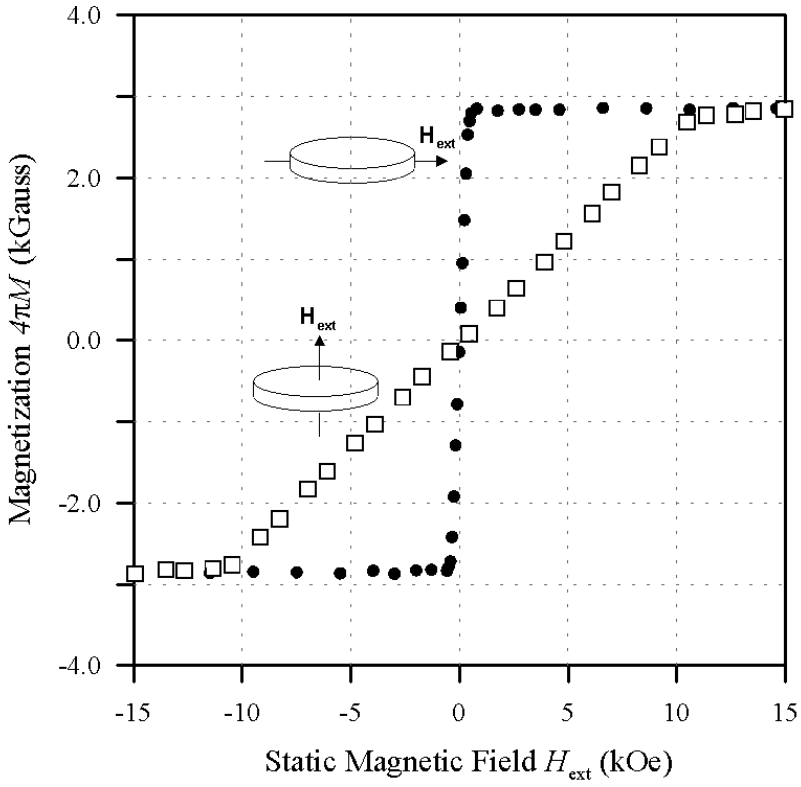

Figure 5.1. Magnetization hysteresis data obtained on hexagonal ferrite sample S3. The sample's easy anisotropy plane was coplanar to the disk plane. The solid circles and the open squares correspond to the data obtained with the external magnetic field applied in and out of the disk plane, respectively.

$$H_{\text{sat-in}} = 4\pi M_s N_y \tag{5.1}$$

and

$$H_{\text{sat-out}} = \left|H_A\right| + 4\pi M_s N_x \,. \tag{5.2}$$

The parallel pumping butterfly curve cut off field (H_{cut}) corresponds to the static field at which the spin wave mode with the lowest frequency is excited. The equation for H_{cut} is obtained from the spin wave dispersion, given in Eq. (3.68), by setting ω_k to $\omega_p / 2$, and k and θ_k to zero. Upon doing so, one gets the following expression

$$\left(\omega_p/2\right)^2 = \gamma^2\left(H_{cut} - 4\pi M_s N_z\right)\left(H_{cut} - 4\pi M_s N_z + \left|H_A\right|\right). \tag{5.3}$$

Note that the cutoff field is readily measured as a part of the parallel pumping instability butterfly curve measurements. For examples of this, see the vertical dotted lines in Fig. 5.6. As seen in the figure, sample S3 has H_{cut} field of about 650 Oe.

The fourth and final equation and associated measured parameter used to calculate the sample parameters is the FMR resonance field. The expression for the FMR resonance field (H_{FMR}) for a hexagonal ferrite disk-shaped sample magnetized in-plane can be obtained from Eq. (3.33) with ω_o set equal to ω_p. This results in the following expression

$$\left(\omega_p/\gamma\right)^2 = \left[H_{\text{FMR}}\right]\left[H_{\text{FMR}} + 4\pi M_s\left(1-3N_z\right) + \left|H_A\right|\right]. \tag{5.4}$$

Table 5.1 summarizes the four measured fields and calculated parameters for each sample. Sample S1 was damaged before the VSM data were acquired. Therefore for

Sample	Thickness (mm)	$H_{\text{sat-in}}$ (Oe)	$H_{\text{sat-out}}$ (kOe)	H_{cut} (Oe)	H_{FMR} (Oe)	ΔH_{FMR} (Oe)	$4\pi M_s$ (kG)	H_A (kOe)	$\lvert\gamma\rvert/2\pi$ (GHz/kOe)	N_z
S1	0.090	---	---	413	775	16	2.957	-9.500	2.840	0.054
S2	0.113	230	12.20	502	845	10	2.992	-9.668	2.715	0.077
S3	0.205	380	11.50	650	900	14	2.855	-9.335	2.720	0.130

Table 5.1. Sample parameters for the three Mn substituted Zn Y-type hexagonal ferrite disc shaped samples studied here. The symbolic headers give the static magnetic fields required to saturate the sample in the disk plane, $H_{\text{sat-in}}$, and out of the disk plane, $H_{\text{sat-out}}$, the parallel pumping butterfly curve cut off field H_{cut}, the ferromagnetic resonance (FMR) field H_{FMR}, and the FMR half-power linewidth ΔH_{FMR}. From the first four measured field parameters, the saturation magnetization $4\pi M_s$, the anisotropy field H_A, the in-plane demagnetizing factor N_z, and the electron gyromagnetic ratio $\left|\gamma\right|$ were calculated.

this sample, the demagnetizing factors were estimated from the Osborn analysis, H_A was set to the average value obtained for S2 and S3, and $4\pi M_s$ and $|\gamma|$ were obtained from the FMR field and the butterfly curve cut-off field. The parameters listed in Table 5.1 are consistent with literature values (Smit and Wijn [1959]; Savage and Tauber [1964]). Note that H_{cut} and H_{FMR} become larger as one moves from sample S1 to sample S3. This is due to the increase in N_z with disk thickness.

The measured FMR half power linewidths for samples S1, S2, and S3 were 16 Oe, 10 Oe, and 14 Oe, respectively. These values are reasonably small for single crystal Zn Y-type hexagonal ferrites. Typical FMR linewidths from the literature are in the 8-30 Oe range at 10 GHz. Savage *et al*. [1965] reported one sample with a 3.8 Oe linewidth at 9 GHz, but this appears to be an exception.

5.3 BUTTERFLY CURVES

Figure 5.2 shows the general sample and magnetic field orientation that was used to obtain all the microwave measurements, at low as well as at high power levels, as a part

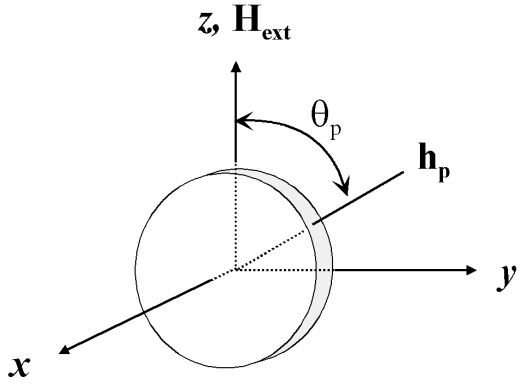

Figure. 5.2. Orientation of the sample, static field ($\mathbf{H}_{\text{ext}}$), and microwave field ($\mathbf{h}_{\text{p}}$) used to obtain the data given in this chapter. The hexagonal easy-plane corresponded to the disk-plane. The angle (θ_p) between $\mathbf{H}_{\text{ext}}$ and $\mathbf{h}_{\text{p}}$ was varied for the resonance saturation measurements depending on static field setting in order to minimize cavity overloading. For the subsidiary absorption and parallel pumping measurements, θ_p was fixed to 90^{o} and 0^{o}, respectively.

of this thesis work. As is shown in the figure, both the static field and microwave magnetic fields were applied in the disk plane which coincided to the crystallographic easy anisotropy plane of the Zn Y-type hexagonal ferrite samples. The angle θ_p between the in-plane static and microwave fields varied depending upon the measurement of interest. Typically, for resonance saturation measurements this angle is set to 90 degrees. However, in order to reduce cavity loading, small θ_p values were used for measurements at and near H_{FMR}. This angle was then increased in order to achieve the higher sensitivities required for the resonance saturation h_{crit} measurements obtained at static field settings further away from the FMR field. For the subsidiary absorption and parallel pumping measurements, θ_p remained fixed at 90 and 0 degrees, respectively.

Figure 5.3 shows several spin wave dispersion curves. The curves were calculated using Eq. (3.68), with sample S2 parameters given in Table 5.1, and static fields as shown in the figure. The solid circle corresponds to the FMR resonance frequency, and the dotted line is the frequency of the parametrically excited spin waves. The top three curves show the orientation of the dispersion manifold for the parallel pumping butterfly curve measurements at three different static field settings. The three static fields used in calculating the lower three dispersion curves were chosen to show the location of the excitation frequency ($\omega_p / 2$) within the manifold for (1) the minimum static field used to obtain parallel pumping butterfly curve data, and (2) the static field at which the $\omega_k(\theta_k = 90^\circ, \phi_k = 0^\circ, k = 0) = \omega_p / 2$ condition is satisfied, and (3) the static field at which $\omega_p / 2$ matches the minimum frequency of the spin wave manifold. For more details on spin wave dispersion relation see Section 3 of Chapter 3.

The lower three dispersion curves shown in Fig 5.3 show the shape and orientation of the dispersion manifold for the resonance saturation butterfly curve measurements. The three static fields used to calculate these curves were chosen to show the location of the excitation frequency (ω_p) within the manifold for the maximum and minimum static

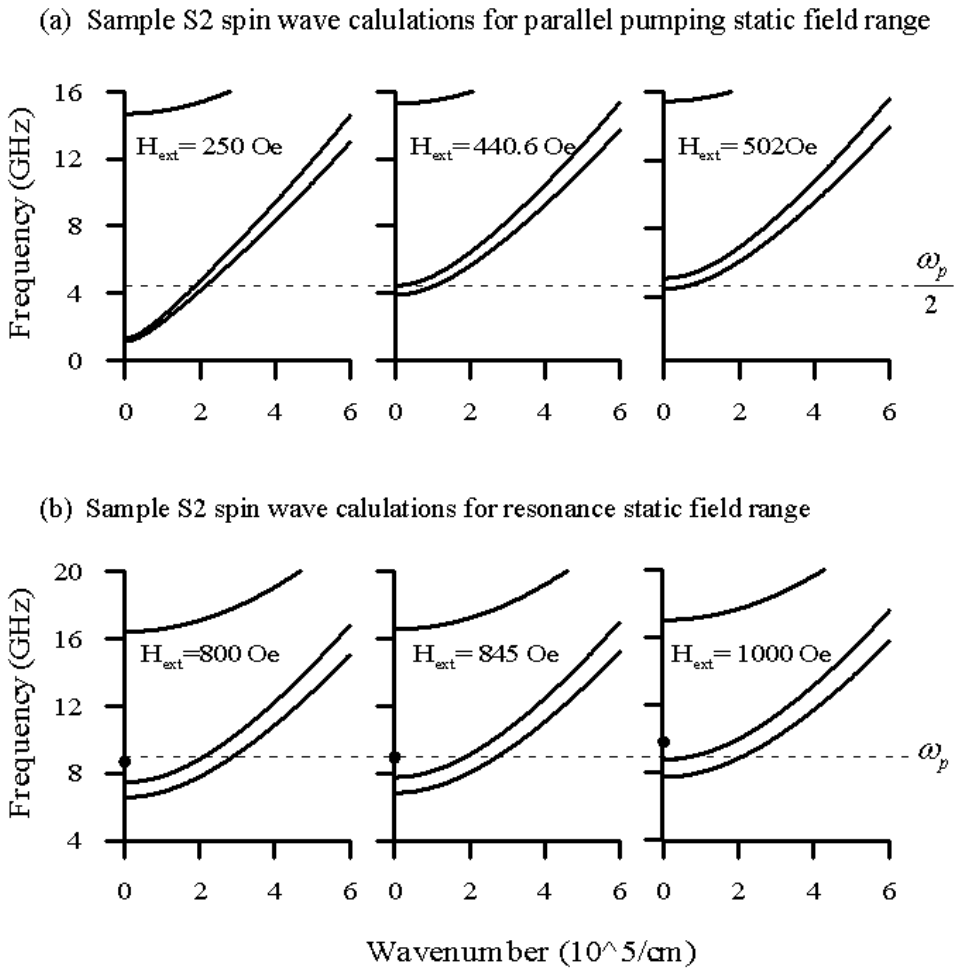

Figure 5.3. Spin wave dispersion curves calculated with the sample S2 parameters, given in Table 5.1, for several static fields as indicated. The upper and lower plots were calculated using the static fields for the parallel pumping and resonance saturations field ranges.

magnetic fields that were used to obtain resonance saturation thresholds and for when the FMR resonance condition is satisfied.

Having discussed the sample preparation techniques and the low-power parameters of interest, the high-power instability data obtained on these samples will now be discussed.

5.3.1 RS Butterfly Curves

Figure 5.4 shows low-power FMR absorption curves along with resonance saturation butterfly curves. The data were obtained on the Zn Y-type hexagonal c-plane disk samples at a nominal operating frequency of 8.93 GHz. In graph (b) of Fig. 5.4, the high-power data for samples S1 and S2 are shown as the solid circles and open squares,

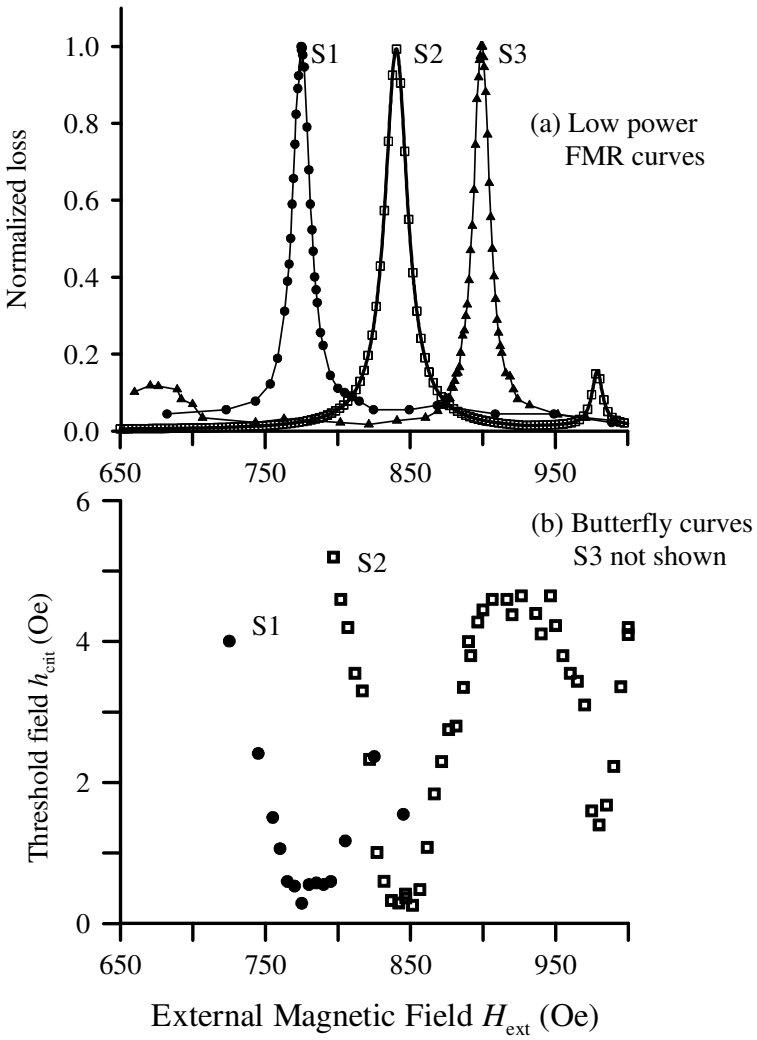

Figure 5.4. Graph (a) shows low-power ferromagnetic resonance absorption curves of loss versus static external magnetic field for the three Zn Y-type hexagonal ferrite c-plane disk samples S1, S2, and S3 as indicated. Graph (b) shows resonance saturation butterfly curves of the spin wave instability threshold microwave field amplitude h_{crit} versus H_{ext} for samples S1 and S2. The operating frequency was 8.93 GHz.

respectively. The butterfly curve for sample S3 is not shown because S3 was damaged before the resonance saturation measurements were obtained. For the data shown in graph (a), the angle θ between the in-plane static and microwave fields was set at $8°$. For the data in (b), this angle was also set at $8°$ for the h_{crit} measurements at the FMR point. For h_{crit} measurements away from the FMR field, this angle was increased as needed to achieve higher sensitivity, and the angle was set to a maximum of approximately $60°$ for the extreme end point data in the figure.

The low-power FMR curves in Fig. 5.4(a) are typical for Zn Y-type c-plane hexagonal ferrites. The difference in the FMR peak positions for the three disks is mainly due to the different thicknesses and the corresponding difference in the demagnetizing factors. In addition to the prominent primary FMR absorption peaks, the absorption curves also show secondary peaks at higher fields. These peaks are associated with magnetostatic mode (MSM) resonances. The MSM peak is clearly visible in the S2 data and is less pronounced for the S1 data. The graph does not extend far enough to show the MSM peak for S3 that is centered at $H_{ext} \approx 1070$ Oe.

The butterfly curves in Fig. 5.4(b) demonstrate the correlation between the low-power FMR response and the h_{crit} threshold field behavior. The minimum thresholds for both samples occur at $H_{ext} = H_{FMR}$. Within about one linewidth of either side of the main FMR peak position, there is little change in h_{crit}. However, as H_{ext} is set further away from the peak, the thresholds increase rapidly. It is important to note the effect of the MSM resonances on the h_{crit} response. The MSM peak in graph (a) for sample S2 is centered at about 980 Oe. At this same point in field, there is a second minimum in the h_{crit} data shown in graph (b). The apparent drop in h_{crit} for fields above about 825 Oe for sample S1 may also be due to an MSM effect. This drop occurs at about the same external magnetic field for which the low-power absorption curve turns upward. The MSM peak for sample S1 is much weaker and the high-power data extend only to 850 Oe.

The data in Fig. 5.4(b) represent the first actual measured butterfly curves for resonance saturation on hexagonal ferrites to be reported in the literature. As has been mentioned before, all previously reported resonance saturation h_{crit} measurements have been limited to the thresholds at $H_{\text{ext}} = H_{\text{FMR}}$ only. As will be discussed below, such data give new information on the threshold response and on the spin wave loss processes that are not apparent from measurements at the FMR point only. To the author's knowledge, only one previous study on YIG has examined the field dependence of the h_{crit} threshold and provided actual butterfly curve profiles for this dependence (Kabos *et al*. [1996]).

Qualitatively, the results are as one would expect. The reduced amplitude for the uniform mode response away from resonance results in a decrease in the $g_k^{(RS)}$ factor given in Eq. (3.98) and a corresponding increase in the h_{crit} threshold. In quantitative terms, however, there are two new results from Fig. 5.4(b). First, there is a rather rounded h_{crit} response for fields near resonance. Second, for fields outside the rounded region there is a sharper "V" shaped response with a small but distinct asymmetry in the butterfly curve. Both effects are unexpected. First consider the rounded h_{crit} response. One would expect the increase in h_{crit} as one moves away from the FMR peak position in field to mirror the drop in the FMR response. The data in Fig. 5.4 show that this is not the case. The data show that the threshold seems to respond rather weakly to the drop in the FMR amplitude until the static field is off from the FMR field by a linewidth or so. Then, and only then, does the threshold increase. Now consider the asymmetry. The low-power FMR absorption line is essentially symmetric, whereas the threshold field data show that this symmetry is not transferred to the resonance saturation butterfly curve profile. Rather, the data show that as the static field is set out of the rounded response region, the rate of increase for h_{crit} is greater for fields below resonance than for fields above the FMR point.

Figure 5.5 shows the resonance saturation butterfly curve data from Fig. 5.4 for sample S2 along with computed h_{crit} versus H_{ext} curves and the corresponding critical mode k values as a function of field, based on the theory. In the upper graph of Fig. 5.5, the solid circles are the same S2 data as shown before and the dashed and solid lines show the calculation results. The solid curve corresponds to a fixed k-independent ΔH_k

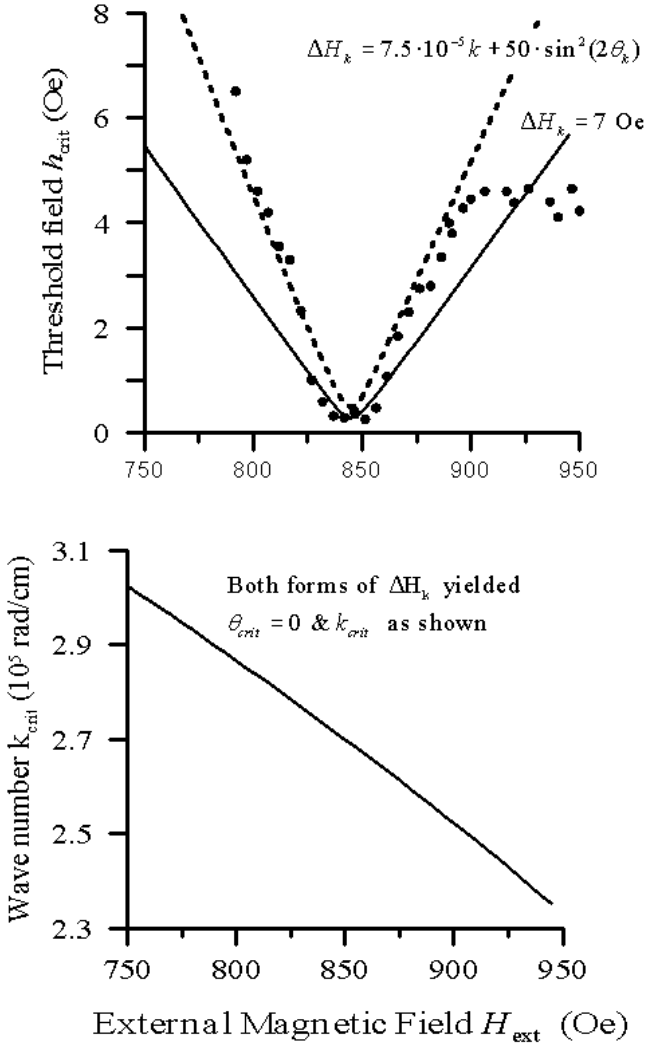

Figure 5.5. Resonance saturation butterfly curve measurements and calculation results for sample S2. The solid circles are the same data as in Fig. 5.4(b). The solid and dashed lines are the computed results for spin wave linewidth ΔH_k as shown. The same wave number k_{crit} versus static field results shown in the lower plot were obtained for both forms of ΔH_k .

value of 7.0 Oe. The dashed curve in Figure 5.5 was calculated for a *k* dependent spin wave linewidth of the form $\Delta H_k = A + B\,k + C\sin^2(2\theta_k)$, with *A* equal to zero, *B* equal to $7.5\cdot 10^{-5}\,\mathrm{Oe}\cdot\mathrm{cm}$, and *C* = 50 Oe. The second order $h_{\mathrm{crit}}^{(\mathrm{RS})}$ equation, given in Eq. (3.97), was minimized over all allowed values of θ_k and ϕ_k, and the minimum threshold always occurred for $\theta_k = 0$ regardless of the static field setting for both forms of the spin wave linewidth. This $\theta_k = 0$ condition is the same as expected from the Suhl theory for isotropic materials (Suhl [1957]). The lower graph in Fig. 5.5 shows the calculated wave number of the critical mode excited at various static field settings.

The computed butterfly curves in Fig. 5.5 provide an indication of some of the effects that control the h_{crit} response. It is to be noted that the $\Delta H_k = A$ form of the spin wave linewidth replicates the rounded butterfly curve near FMR response quite well, while the dashed curve for $\Delta H_k = A + B\,k + C\sin^2(2\theta_k)$ models the data away from the central FMR region reasonably well. This may be taken as an indication that there is a fundamental change in the form of $\Delta H_k(\mathbf{k})$ as one moves from the FMR peak region out to the tails of the FMR response. In the absence of a quantitative theory and the inability to actually measure the critical mode with Brilloun Light Scattering (BLS) measurement techniques, no effort was made to examine a wider range of $\Delta H_k(\mathbf{k})$ functions.

While it is not clear how or why there is a change in $\Delta H_k(\mathbf{k})$ for resonance saturation, it is to be noted that similar effects occur for oblique pumping in single crystal YIG. In the case of second order Suhl processes in the vicinity of FMR, this transition may be related to some sort of saturation process. One might speculate that for H_{ext} close to the FMR resonance condition, the large uniform mode amplitude drives the spin waves to very high amplitudes and that this leads to a washing out of the *k*-dependence for ΔH_k. Further work, both experimental and theoretical, is needed to clarify these effects.

5.3.2 PP Butterfly Curves

Figure 5.6 shows parallel pumping butterfly curve results for the three samples as indicated. The symbols and the solid lines show the data and the theoretical fits, respectively. The first order $h_{\text{crit}}^{(\text{PP})}$ expression given in Eq. (3.97) was minimized over all allowed values of θ_k and ϕ_k, and the minimum threshold always occurred for the spin wave mode with the largest ellipticity. The critical modes will be discussed in more detail shortly. The vertical dashed lines indicate the cutoff point for each of the theoretical curves at $H_{\text{ext}} = H_{\text{cut}}$. The three graphs all show the same two general features: (1) the h_{crit} values for a relatively wide range of static fields are all between 4.5-to-7.5 Oe and (2) there is a cutoff static field at which h_{crit} diverges rapidly. As will be discussed in more detail below, the constant threshold at low field indicates a **k**

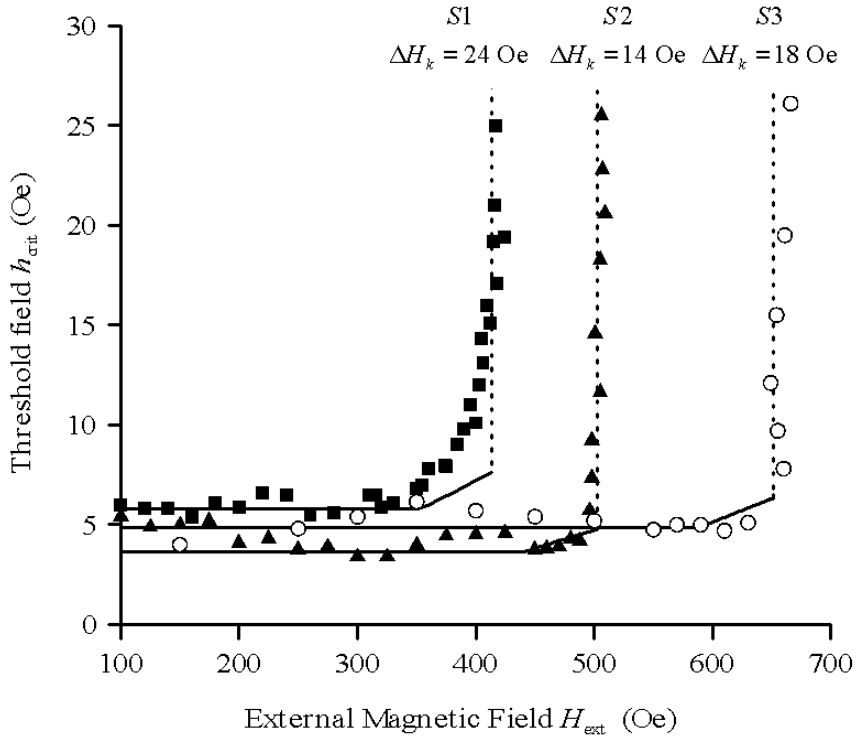

Figure 5.6. Parallel pump butterfly curves for samples S1, S2, and S3, as indicated. The data and calculated results are shown by the points and solid lines, respectively. The vertical dashed lines show the cutoff point for first order processes at $H_{ext} = H_{cut}$.

independent spin wave linewidth for parallel pumping. The cutoff fields correspond to the H_{cut} values in Table 5.1. The gradual shift in H_{cut} to higher fields as one moves from S1 to S2 to S3 is due to the increase in disk thickness and corresponding in-plane demagnetizing factor. Similar shaped parallel pump butterfly curves obtained on hexagonal ferrites have been published in the literature (Green and Healy [1963]).

The computed butterfly curves in Fig. 5.6 were obtained with the parameters listed in Table 5.1 and the $h_{\text{crit}}^{(\text{PP})}$ expression given in Eq. (3.97). A fixed value of the spin wave linewidth parameter was used in each case in order to obtain the best match with the fixed h_{crit} values at low static fields. These fitted ΔH_k values for samples S1, S2, and S3 were 24 Oe, 14 Oe, and 18 Oe, respectively. The relatively wide range of the low field h_{crit} and the corresponding ΔH_k values for similar samples match the findings in the work cited by Tauber *et al*. ([1964]). Note the small but distinct corner in all of the computed butterfly curves close to the high field cut off point. This effect is clearly evident from the solid curve for samples S1 and S2, but less apparent for sample S3. These corners are due to a combination of effects: (1) a critical mode ϕ_k value of 0° over the entire range of static fields for the parallel pumping response, (2) the extreme warp in the $\theta_k = 90°$ dispersion surface, and (3) the extremely narrow width for the spin wave band at $k = 0$ and $\phi_k = 0°$ which results from this warp.

The corner response in the butterfly curves given in Fig. 5.6 and 5.7 contain a second effect which is unique to anisotropic samples. This effect consists of a *finite* value of h_{crit} for the high field corner point at $H_{\text{ext}} = H_{\text{cut}}$. For isotropic ferrites, the spin wave precession is strictly circular at this butterfly curve cutoff point. This leads to a h_{crit} which increases rapidly as H_{ext} approaches H_{cut} and diverges to infinity at $H_{\text{ext}} = H_{\text{cut}}$. For planar ferrites magnetized in the easy plane, the critical mode has elliptical polarization even in the $H_{\text{ext}} = H_{\text{cut}}$ limit, and this keeps the threshold field finite at cutoff. The theoretical curves in Fig. 5.6 show this finite threshold at cutoff by the truncated solid lines at $H_{\text{ext}} = H_{\text{cut}}$ and the vertical dashed lines which extend vertically

from this point. The S2 and S3 data in Fig. 5.6 show these effects to varying degrees. In both cases, the experimental butterfly curves exhibit a very rapid divergence at $H_{\text{ext}} = H_{\text{cut}}$ (see Fig. 2.12 for an example). While there may be an experimental corner effect for these two samples, the resolution in h_{crit} is not sufficient to establish the effect unambiguously. The S2 data show a rapid increase in h_{crit} as one approaches $H_{\text{ext}} = H_{\text{cut}}$, but there is no evidence of either the corner effect or the finite threshold at the cutoff point.

Figure 5.7 shows the parallel pump butterfly curve data and fit for sample S3 from Fig. 5.6 on an expanded scale and an additional graph with details on the critical mode behavior as a function of H_{ext}. The left and right vertical axes in the bottom graph show the critical mode k and θ_k values, respectively. The critical mode azimuthal angle ϕ_k remains at 0° for the entire range of fields for the butterfly curve. The critical mode behavior can be divided into two parts, depending upon whether H_{ext} is below or above 590 Oe. For external fields below about 590 Oe, the critical mode polar propagation angle θ_k is constant at 90°, and there is a smooth and continuous decrease in the critical mode k value from about 3×10^5 1/cm to zero as H_{ext} is increased from 100 to about 590 Oe. As discussed above, spin wave ellipticity considerations give the strongest coupling for $\theta_k = 90°$ and $\phi_k = 0$. For external fields above $590\,\text{Oe}$, $\theta_k = 90°$ is no longer allowed and the critical mode corresponds to the available mode with the maximum θ_k and both ϕ_k and k equal to zero, this results in the smooth drop in θ_k from 90° to zero as H_{ext} is increased. This second region is the origin of the characteristic butterfly curve corner close to the high field cut off point in the upper graph of Fig. 5.7 and, as already noted, in all three of the theoretical butterfly curves of Fig. 5.6.

The results raise a number of questions. One question concerns the characteristic corner shapes for the theoretical butterfly curves in Figs. 5.6 and 5.7. Here the question is, "Why are these characteristic corners not consistently resolved in the experiment?" From Fig. 5.6, one sees a variety of experimental results. For sample S1, the increase in

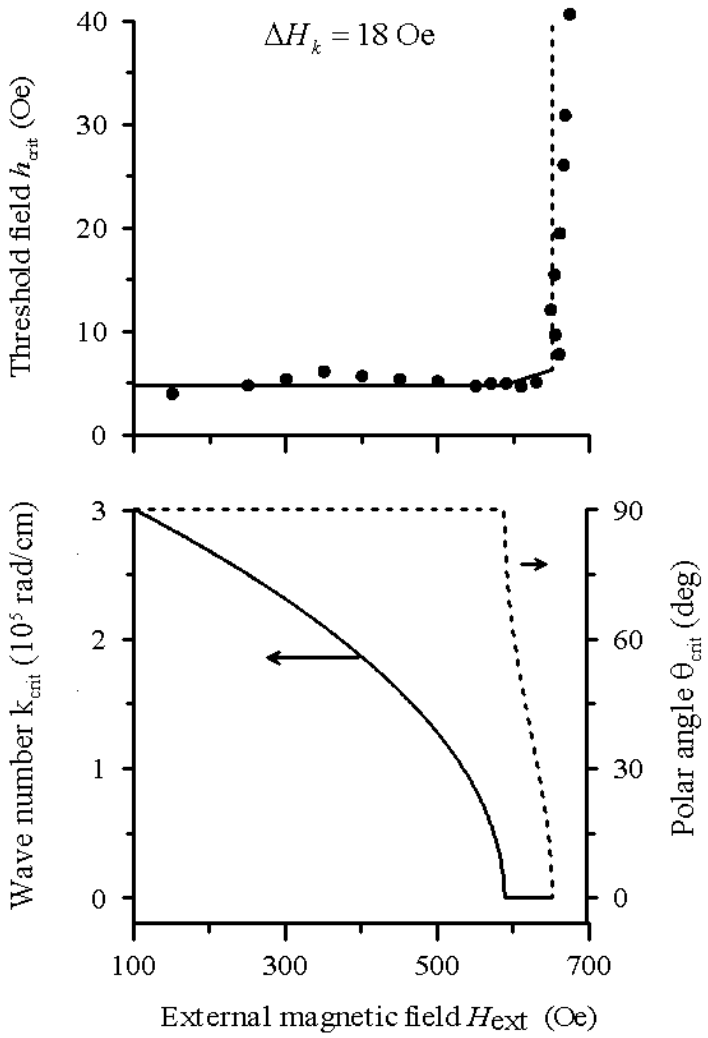

Figure 5.7. Parallel pump butterfly curve and critical mode results for sample S3. The upper graph shows the threshold versus field data and the computed butterfly fit from Fig. 5.6. The lower graph shows the critical mode wave number k_{crit} and polar angle θ_{crit} versus H_{ext}.

h_{crit} as the static field approaches H_{cut} is gradual and the h_{crit} values fall well above the theoretical corner shaped response. For samples S2 and S3, the increases in h_{crit} at the band edge are much sharper, but there is still no clearly resolved corner effect from the data. It may be that the actual critical modes for the range of fields near the corner are different than those predicted from bulk instability theory. It is important to keep in mind that the bulk theory gives $k = 0$ for these critical modes. In this limit, it is

necessary to take the sample surface boundary conditions into account, which makes the spin wave instability analysis much more complicated, even for isotropic materials, and introduces magnetostatic mode considerations into the analysis. This problem is still unresolved. A second question is, "Why are the parallel pumping spin wave linewidths so large?" This question will be discussed in detail in the final two sections of this chapter.

5.3.3 SA Butterfly Curves

Figures 5.8 and 5.9 show subsidiary absorption (SA) measurement and calculation results. The figure formats follow those in Figs. 5.6 and 5.7. Only results for sample S3 are shown. As reference points for the discussion below, the parallel pumping butterfly curve data from Fig. 5.6 and the FMR data from Fig. 5.4 are also shown. The vertical dashed line in Fig. 5.8 indicates the static field required for magnetic saturation, $H_{\text{sat-in}}$, from Table 5.1. As before, all results are for a nominal operating frequency of 8.93 GHz. The subsidiary absorption data were obtained with the angle between the static and microwave fields set at 90°. For the low-power FMR loss profile, this angle was set at 8°. Note that the subsidiary absorption h_{crit} data in both Fig. 5.8 and 5.9 extend to field values that are somewhat above the subsidiary loss and first order process cut off point at $H_{\text{ext}} = H_{\text{cut}} = 650$ Oe.

Figure 5.8 shows that the overall SA response for h_{crit} as a function of H_{ext} is very different from the parallel pump butterfly curve response. Three specific points of comparison may be noted. First, the SA h_{crit} response and the PP response show small maxima at about the same field. This field is slightly below the static field necessary for saturating the domains in the sample $H_{\text{in}} = 380$ Oe.

The second point to note is that the SA h_{crit} values are much lower than the parallel pumping h_{crit} values in the region between $H_{\text{ext}} = H_{\text{sat-in}}$ and $H_{\text{ext}} = H_{\text{cut}}$. The reduction in threshold relative to the PP h_{crit} values for these Zn Y-type hexagonal materials may

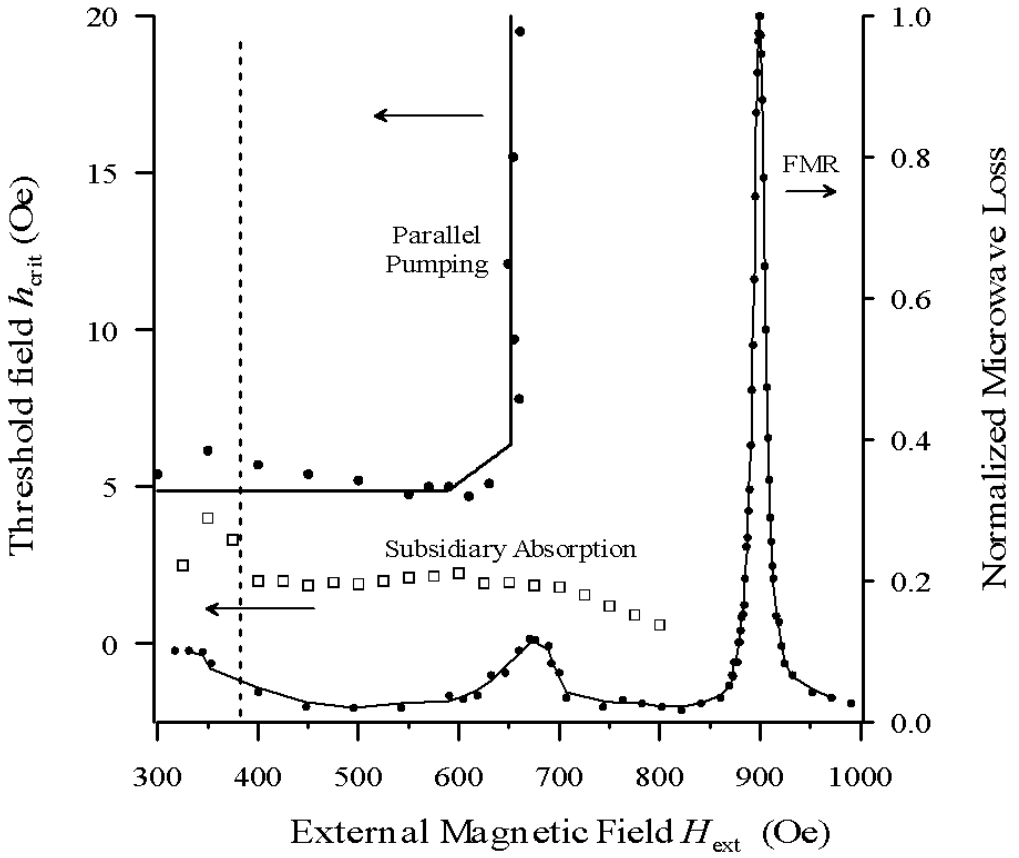

Figure 5.8. Subsidiary absorption (SA) and parallel pump (PP) threshold field amplitude versus static external magnetic field butterfly curve data, and low-power normalized ferromagnetic resonance (FMR) loss profile for Zn Y-type hexagonal ferrite sample S3. The vertical long dashed line at H_{ext} = 380 Oe corresponds to the field required for magnetic saturation, given in Table 5.1. The angle between the static magnetic field and the microwave field was set to 90°, 0°, and 8° for the SA, PP, and FMR measurements, respectively. The PP data are the same as shown in Fig. 5.7.

be significant. For YIG materials, one always finds that the SA threshold at low field is above the PP threshold. Here, the order appears to be reversed. Fits of the theory to the data and the spin wave linewidth implications are considered below.

The third point to note is that the SA h_{crit} versus H_{ext} response does not follow the usual result for conventional low anisotropy polycrystalline ferrite materials. For such samples, one usually finds a threshold which (i) first decreases with increasing field for a range of low fields and then (ii) diverges as the external field approaches $H_{ext} = H_{cut}$.

Neither of these standard subsidiary absorption responses are observed here. The data in Fig. 5.8 show a range of fields from about 400 to 700 Oe for which the threshold is more or less constant. There is certainly no divergence in h_{crit} at $H_{ext} = H_{cut} = 650$ Oe. Then, for fields above 700 Oe, h_{crit} decreases. Except for the initial match with the parallel pump threshold at the lowest fields and the initial drop in h_{crit} as the field is increased, these data look nothing like the usual subsidiary absorption butterfly curves.

The different character for the subsidiary absorption response found for the Zn Y-type hexagonal ferrite disks is related to two anisotropy effects. First, there is the spin wave band shift. The planar anisotropy shifts the spin wave band *up* by a significant amount. Second, there is the FMR shift. The anisotropy shifts the FMR and magnetostatic mode resonance fields *down* so that these resonances are close to or even coincide with the subsidiary absorption regime. These shifts have a major effect on the h_{crit} response.

The shape of the subsidiary absorption h_{crit} vs. H_{ext} response between 400 and 600 Oe is then due to a combination of factors. First, there is the θ_k dependence of the critical mode coupling factor $g_k^{(SA)}$ for the zero k or close to zero k, critical modes. Second, there is the field dependence of the uniform mode and magnetostatic mode responses. As one moves up in field and down in θ_k for modes at $\omega_k = \omega_p / 2$ and $k = 0$, the coupling factor decreases. At the same time, one is moving up the tail of the magnetostatic and uniform mode response curve and this increases the net coupling to the SA modes. For samples S1 and S2, the FMR peak and the magnetostatic mode resonances occurred at such low static fields that the thresholds could not be uniquely associated with the usual subsidiary absorption. Even for sample S3, the proximity of these resonances to H_{cut} was sufficient to suppress the usual SA threshold divergence at $H_{ext} = H_{cut}$. For fields above $H_{ext} = H_{cut}$, it appears that the onset of second order processes cause the h_{crit} response to go smoothly from the constant threshold found for first order processes to the rapid drop in threshold associated with the resonance

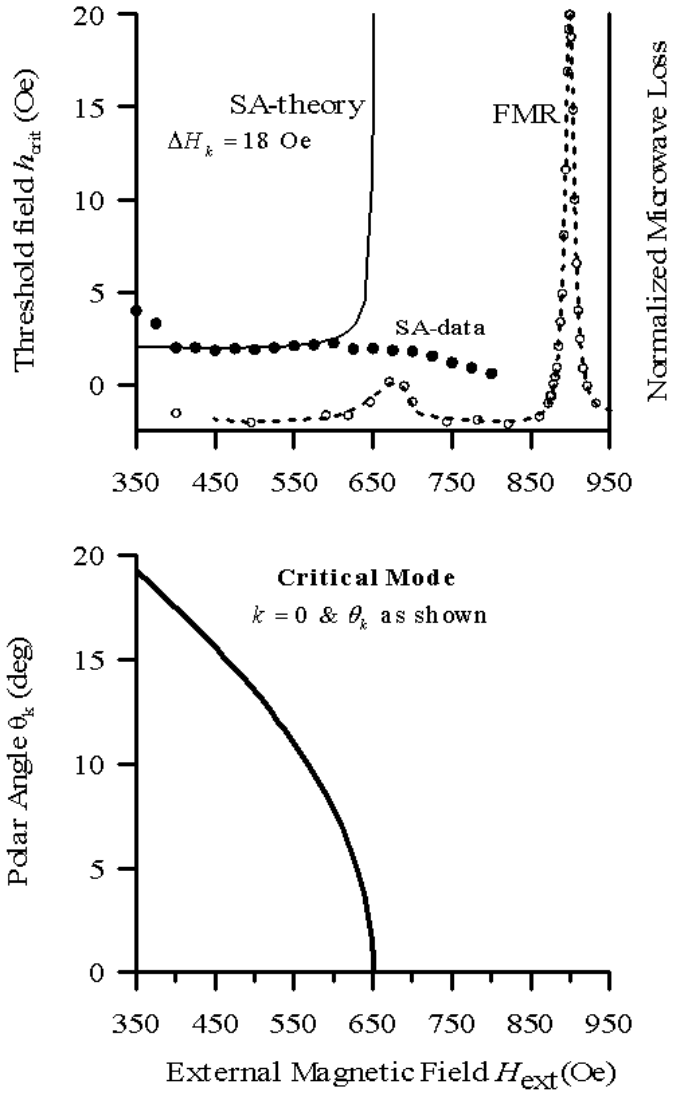

Figure 5.9. Subsidiary absorption (SA) butterfly curve and critical mode results for sample S3. The upper graph shows the SA butterfly curve data (solid circles) and fit (solid line). The dotted line is the low-power FMR response. The lower graph shows the critical mode polar angle versus static field.

saturation butterfly curve response discussed above. Note that the approach to FMR causes the measured *second order* h_{crit} to drop to values as low as a few tenths Oe. The SA data for fields above H_{cut} show this same trend. The drop in h_{crit} is not as sharp as one might extrapolate from the RS results in Figs. 5.4 and 5.5. This is probably due to

the additional cavity loading effects which come in as one approaches the FMR field with the pump angle θ set at 90°.

Figure 5.9 shows the h_{crit} vs. H_{ext} data from Fig. 5.8 along with a computed subsidiary absorption butterfly curve and details on the critical mode θ_k versus field response associated with the computed thresholds. The critical mode k and ϕ_k values were zero and 90^0, respectively, over the entire subsidiary absorption region. The calculated butterfly curve and critical modes were obtained for the sample parameters indicated above and with a constant spin wave linewidth value of 18 Oe. The low-power FMR response profile is shown, again as a point of reference. The flat portion of the theoretical butterfly curve response matches the data for fields between 400 Oe and 600 Oe.

5.4 ANALYSIS SUMMARY

Table 5.2 summarizes the measured FMR linewidths, threshold field values, and calculated spin wave linewidths for the three samples. The butterfly curve minimum values are also given. As was mentioned previously, to the best of the author's knowledge, these data represent the first time the resonance saturation (RS), parallel

Sample	**FMR** $\omega_o = 8.93$ GHz	**Resonance Saturation** $\omega_k = 8.93$ GHz		**Parallel Pumping** $\omega_k = 4.465$ GHz		**Subsidiary Absorption** $\omega_k = 4.465$ GHz	
	ΔH_{FMR}	h_{crit_min}	ΔH_k	h_{crit_min}	ΔH_k	h_{crit_min}	ΔH_k
S1	16	0.28	7.0	5.8	24	-	-
S2	10	0.28	7.0	3.6	14	-	-
S3	14	-	-	4.8	18	2.0	18

Table 5.2. Summary of the minimum resonance saturation, subsidiary absorption, and parallel pumping threshold fields and corresponding calculated spin wave linewidths for the three Zn Y-type hexagonal samples reviewed in Table 5.1

pumping (PP), and subsidiary absorption (SA) butterfly curve measurements and analyses have been performed on a single-crystal hexagonal ferrite sample.

It is significant that for sample S3 both the parallel pumping and subsidiary absorption thresholds were fit with the same spin wave linewidth value of $\Delta H_k = 18$ Oe. The consistent fits for the PP and SA h_{crit} values, which differ by a factor of two, indicate that the data and analyses are valid and consistent. There is, however, a clear problem between the PP and SA versus the RS spin wave linewidths. In the RS case, the nominal value of ΔH_k needed to fit the data is about 7 Oe for the critical modes at the pump frequency. For the PP and SA cases, the critical modes are at half the pump frequency, and the fitted spin wave linewidths are a factor of 2-3 larger than the resonance saturation values. Usually the spin wave linewidth scales with frequency so one would expect values of about half of those for the resonance saturation, not double. **The main question is, "Why are these first order spin wave linewidths so large?"** These samples were made from single crystal platelets with low conductivity. The parallel pump process is expected to yield an intrinsic spin wave linewidth value that is independent of inhomogeneous broadening effects, such as two magnon scattering processes, and other non-intrinsic processes. Yet, the measured ΔH_k values range from 14 to 24 Oe. After the publication of the above results (Cox *et al*. [2001]), further research was performed to address the above question. The next section discusses the new findings.

5.5 FOLLOW-UP PARALLEL PUMPING WORK

In order to understand the above spin wave linewidth inconsistencies, more extensive parallel pumping instability measurements were performed by Alex Nazarov (Nazarov *et al*. [2002a]). These measurements revealed that the large first order spin wave linewidths described above are related to sample size effects. This section briefly summarizes the additional work.

Nazarov's parallel pump instability measurements were performed on Zn Y-type hexagonal ferrite samples that were obtained from the same "batch" as the three samples studied in this thesis. The data were obtained with the high-power system, which was developed as part of this work, on thin circular and rectangular shaped samples at both 9.0 and 16.7 GHz. Note that the sample numbering given in the figures, table, and text of this section are the same as provided in Nazarov's paper, and care must be taken to not confuse with the sample numbering in the previous sections. See (Nazarov, *et al*. [2002a]) for more details on the samples.

Figure 5.10 shows parallel pump butterfly curves measured by Nazarov *et al*. for three different configurations at a pumping frequency of 9 GHz. The S5 slab was magnetized along the short and long sides. The solid arrow indicates the direction of the

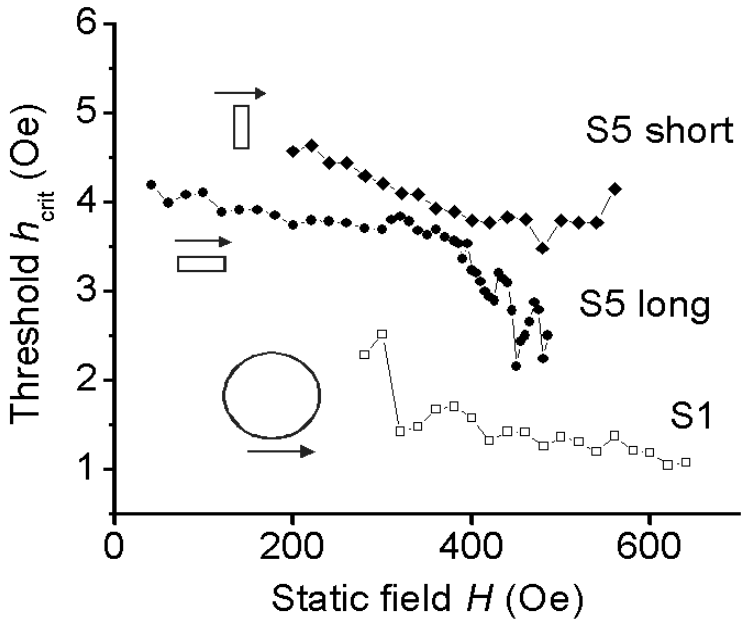

Figure 5.10. Parallel pumping threshold h_{crit} as a function of the external field H obtained by Alex Nazarov *et al.* at 9 GHz on two different Zn Y-type hexagonal ferrite samples obtained from the same batch processes as samples used in this study. Note that the sample labeled "S1" in this figure does not correspond to sample S1 that was studied as part of this thesis work. The data show a clear dependence on sample orientation, which is not observed at 17 GHz (Nazarov *et al*. 2002a]).

Sample	Shape	Thick (mm)	In-plane Dia. (mm)	Min. h_{crit} 16.7 GHz (Oe)	Min ΔH_k 8.35 GHz (Oe)	ΔH_0 17.5 GHz (Oe)	Min. h_{crit} 9 GHz (Oe)	Min. ΔH_k 4.5 GHz (Oe)	ΔH_0 9.5 GHz (Oe)
S1	disk	0.34	2.39	6.1	12.0	18	1.0	3.0	11
S2	disk	0.19	2.32	6.5	12.8	20	0.9	2.7	13
S3	disk	0.14	1.52	6.6	13.0	20	1.8	5.3	13
S4	disk	0.09	2.32	6.4	12.6	-	1.2	3.5	13
S5	slab	0.09							
	long		1.62	6.6	13.0	-	2.2	6.4	10
	short		0.72	6.6	13.0	-	3.5	10.2	-
S6	slab	0.05							
	long		1.44	-	-	15	3.0	8.8	12
	short		0.64	-	-	-	3.5	10.2	-

Table 5.3. Minimum parallel pump threshold fields and corresponding calculated spin wave linewidths obtained by Nazarov *et al.* for different sample orientations and frequencies (Nazarov *et al*. [2002a]).

applied static magnetic field. The H_{ext} regions where spin wave instability occurs are different for the three curves because the samples have different demagnetizing fields. In the case of Nazarov's disk S1, the curve was terminated on the right side when the proximity of the FMR position loaded the cavity so much that measurements ceased to be reliable. Note that the h_{crit} response differs significantly for the two orientations of the S5 sample, especially for low *k* values at larger H_{ext} values.

Table 5.3 summarizes the minimum parallel pumping threshold fields and the corresponding calculated spin wave linewidths obtained by Nazarov *et al*. The analysis shows that the lateral size has a significant effect on the 9 GHz ΔH_k values, while it has almost no effect on the 16.7 GHz values. Larger lateral sizes generally corresponded to smaller spin wave linewidths. The smaller lateral sizes yielded ΔH_k values that were more than half the FMR linewidths. At 16.7 GHz there were no significant size effects, the ΔH_k values were about half the 16.7 GHz FMR linewidths, and they were close to the ΔH_{FMR} values at 9 GHz. As can be seen, the data show that the 9 GHz first order linewidth inconsistencies observed as part of this thesis are probably due to sample size effects. Nazarov's results are in reasonable agreement with the resonance saturation

measurements discussed in the previous section. Therefore, the second order resonance saturation linewidths, which were obtained on spin waves excited at about 9 GHz, were probably not affected by the sample size effects.

One possible explanation for the sample size dependence for the parallel pumping h_{crit} response at 9 GHz is transit time effects. Such effects have often been used to explain the dependence of h_{crit} on grain size in polycrystalline ferrites (Vrehen *et al*. [1970]). The basic idea is that some dimension d in combination with the group velocity of the mode determines the transit time of the mode. If the transit time is less than the intrinsic relaxation time then the dimension d not the intrinsic relaxation time, limit the lifetime of the mode. For more details on the transit time calculations see Nazarov *et al.* [2002]. As is mentioned in the above reference, it may be possible to utilize the size effect to control the high power capability of hexagonal ferrite devices.

CHAPTER 6

SUMMARY AND CONCLUSIONS

This chapter summarizes the work that was performed as part of this thesis, discusses its implications, and gives suggestions for further work.

6.1 RESULTS

In order to measure the high-power handling capabilities of hexagonal ferrites and determine whether the large low-power microwave losses exhibited by these materials are due to extrinsic or intrinsic relaxation processes, spin wave instability processes were characterized in thin film disc shaped samples of Zn Y-type hexagonal ferrites. To accomplish this: (1) a state-of-the-art high-power microwave spectrometer was designed, built, and automated, (2) the classical spin wave instability theory, originally developed by Suhl and Schloemann, was extended and a sign problem in the anti-Larmor damping term discovered in later theoretical treatments was corrected, and (3) parallel pumping, subsidiary absorption, and resonance saturation instability butterfly curve measurements and analyses were performed on Mn doped Zn Y-type hexagonal ferrites. The results presented here constitute the first time such extensive butterfly curve analyses have been performed on hexagonal ferrites. Furthermore, for the first time, the second order resonance saturation measurements were performed in hexagonal ferrites for static magnetic fields not only equal to but also in the vicinity of the FMR resonance field.

The resonance saturation data were as one would expect, and the analysis showed that a spin wave linewidth of about 7 Oe could fit the butterfly curve minimum. The shape of the parallel pumping butterfly curves were in good agreement with previous measurements on Zn Y-type hexagonal ferrites, and the analysis showed good fit to the data when a constant spin wave linewidth of about 18 Oe was used. This spin wave linewidth also yielded a good match to the subsidiary absorption butterfly curve. However, the parallel pumping and subsidiary absorption spin wave linewidth values were significantly higher than one would expect. Further work performed by Nazarov *et al*. showed that the source of these inflated first order spin wave linewidths were due to sample size effects. Because of this and due the large low-power losses exhibited by these materials, the microwave power required to excite the nonlinear effects was about the same as what is observed in good quality polycrystalline YIG samples. Therefore, the high-power handling capabilities of hexagonal ferrites should not be a major factor in device usage.

6.2 CONCLUSIONS

Setting aside the parallel pumping spin wave linewidth results, which were inflated by the sample shape, it should be noted that other data that were not affected by size effects also show significantly larger losses than one would expect for high quality single crystal materials. These data include: (1) the resonance saturation spin wave linewidth shown here, (2) the follow-up parallel pumping spin wave linewidth measurements performed at 9 and 17 GHz by Nazarov *et al.* [2002a], (3) previous parallel pumping analysis done on hexagonal materials by Green and Healy [1963], and (4) high field effective linewidth measurements obtained by McKinstry [1991]. All of the above measurements have yielded values that are notably higher than what is seen even in polycrystalline YIG samples, where the losses are dominated by extrinsic mechanisms.

These measurement results indicate that the large damping that is observed in hexagonal ferrites is probably an intrinsic property of the material. One possible intrinsic mechanism for this damping is spin-orbit coupling. It is likely that the strong spin-orbit coupling, which leads to the large anisotropy fields that make hexagonal ferrites so attractive for high frequency applications, is the source for the materials large losses, which limits its wide utilization.

In the following section, several follow-up experiments, which may provide further insight into the root cause of the large damping, are proposed.

6.3 FUTURE WORK

At this time, two pieces of additional follow-up work have been completed: (1) the source of the large parallel pumping and subsidiary absorption spin wave linewidths observed in this work was determined to be due to lateral sample size effects (Nazarov *et al*. [2002a]), and (2) the nonlinear spin wave instability theory was further extended to include an arbitrary orientation of the static magnetic field (Nazarov *et al*. [2002b]).

In this section, four additional areas of further work are suggested, which pertain to: (1) Brillion Light Scattering (BLS) measurements, (2) parallel pumping instability measurements versus temperature, (3) resonance saturation instability measurements versus frequency, (4) and the full characterization of samples with varying strengths of crystalline anisotropy.

6.3.1 BLS Measurements

The Brillion Light Scattering (BLS) measurement technique can be used to directly measure the wave vector of the critical spin wave modes. Previous work performed on isotropic samples has confirmed the theoretically predicted propagation directions of the critical modes for parallel pumping and subsidiary absorption nonlinear processes (Wilber *et al*. [1984]). However, such measurements have yet to be performed on

hexagonal ferrites. Two attempts at acquiring BLS data on the critical modes excited by parallel pumping in Zn Y-type hexagonal ferrites, first by Pavel Kabos and then by Christoph Mathieu and the author were unsuccessful. In both cases, the researchers were not able to detect spin waves at the half pump frequency. One possible explanation could be that the spin-orbit coupling is providing a direct relaxation path that is so efficient that the half pump frequency spin waves are not detectable. More work in this area is needed. It is recommended that focus be placed on detection of both phonons and magnons.

6.3.2 Temperature Dependent PP

The anisotropy of the Zn Y-type hexagonal ferrites is strongly temperature dependent and falls off quickly with increasing temperatures (von Aulock [1965]). Therefore, performing parallel pumping instability measurements as a function of increasing external temperature may provide evidence for the root mechanism of the large losses. Specifically, if the spin wave linewidth decreases with increasing temperature, one could argue that the spin-orbit coupling is the mechanism.

6.3.3 Frequency Dependent RS

The normalized resonance saturation threshold field versus microwave frequency plots in Figure 3.18, which were obtained with Zn Y-type hexagonal ferrite parameters for both the incorrect and corrected sign of the uniform mode anti-Larmor complex damping term, showed that the sign of the damping term had a significant effect on the calculations. The curve obtained with the corrected damping sign has a clear peak in the normalized threshold response at about 20 GHz, which is not present for the curve obtained with the damping error. The peak is associated with a switch in the critical mode polar angle from 0 to 90 degrees. To the best of this author's knowledge, an experimental study of the above response has never been previously performed. Such a

study could be readily performed with the high-power microwave spectrometer developed as part of this thesis work. These measurements would provide a direct test of the theory, and they could also provide insight into whether the damping in hexagonal ferrites is frequency dependent as predicted by the Landau-Lifshitz phenomenological damping term or frequency independent as predicted by Bloch-Bloembergen phenomenological damping.

6.3.4 Variable Anisotropy Fields

The system that was developed as part of this thesis work is highly versatile and could be utilized to perform a variety of detailed measurements of the linear and nonlinear microwave properties on a variety of materials. This could include, low-power frequency and angle dependent FMR linewidth measurements, low and high-power microwave dielectric constant measurements, low and high-power high field effective linewidth measurements, and detailed butterfly curve measurements. To the best of the author's knowledge, high-power dielectric and high-power effective linewidth measurements have never been performed before on ferrite materials, nor have such detailed measurements been performed on a single sample. These measurements could be performed on samples with a range of anisotropy fields, and thereby validate or refute the author's proposal regarding spin-orbit coupling being the source of the large losses. The measurements would also provide needed comparisons between the various experimental techniques.

APPENDIX A

PASSIVE WAVEGUIDE COMPONENTS

This appendix reviews the passive waveguide components that are utilized in the high power microwave spectrometer that was discussed in Chapter 4. Here the basics of rectangular waveguides, directional couplers, and microwave cavities are addressed. Derivations of the microwave magnetic field expression inside rectangular and cylindrical reflection type microwave cavities are also provided.

This appendix is divided into the following four sections:

1. Section 1 reviews the bandwidths and TE01 mode pattern of rectangular microwave waveguides.
2. Section 2 addresses directional couplers. The section addresses the importance of choosing the appropriate directional coupler as well as minimizing troublesome leakage signals that occur in them.
3. Section 3 focuses on microwave cavities. Here the cavity Q, coupling coefficients, mode patterns, and design equations are reviewed.
4. In the last section the microwave field expressions, which describe the magnetic field amplitudes inside rectangular and cylindrical reflection type microwave cavities, are derived.

A.1 RECTANGULAR WAVEGUIDES

As was mentioned in Chapter 4, rectangular waveguides are used in the high power microwave spectrometer because of their high-power handling capabilities, low insertion losses, and well-defined TE_{10} modes. The main drawback of rectangular waveguides is their limited bandwidth which requires that several waveguide bands be used in order to operate over a wide frequency range. This section discusses the reasons behind the limited bandwidths, gives the recommended operating frequency range of the most commonly used waveguide bands, and concludes with a discussion of the mode patterns in these guides.

The operating frequency range of a rectangular waveguide is bound by the cutoff frequency at the low-frequency end and the onset of multimode propagation at the high-frequency end. The low-end cutoff frequency occurs because there is only a single conductor present in rectangular waveguides. The single conductor only allows for TE (transverse electric) and TM (transverse magnetic) wave propagation, not TEM propagation as supported by transmission lines with more than one conductor such as coaxial cables (Pozar [1998]). The TE and TM waves propagate at oblique angles relative to the central axis of the waveguide, and as the frequency of the waves decreases, the propagation angle relative to the central axis of the guide increases. At the low-frequency cutoff point, the propagation angle equals 90^o and no energy is transmitted down the line (Pozar [1998]).

The high-frequency limit is imposed on a waveguide band in order to avoid multimode propagation. The upper recommended limit of a waveguide band corresponds roughly to the cutoff frequency of the next highest frequency mode (TE_{11}) supported by the guide. Therefore, as long as frequencies below the maximum specified operating frequency range for a given band, are used, one can be assured of single TE_{10}

Band	Recommended Frequency Range (GHz)	TE_{10} Cutoff Frequency (GHz)	Inside Dimensions {a x b} (cm)
S	2.6-4.0	2.1	7.21x3.40
H	4.0-5.9	3.2	4.76x2.22
C	**5.9-8.2**	**4.3**	**3.49x1.58**
X	**8.2-12.4**	**6.6**	**2.29x1.02**
Ku	**12.4-18.0**	**9.5**	**1.58x0.790**
K	18.0-26.5	14.1	1.07x0.430
Ka	**26.5-40.0**	**21.1**	**0.711x0.356**
Q	33.0-50.5	26.3	0.570x0.280
U	40.0-60.0	31.4	0.480x0.240
V	50.0-75.0	39.9	0.380x0.190
E	60.0-90.0	48.4	0.310x0.015

Table A.1. Table of standard microwave rectangular waveguide data Pozar [1998]. The bold items correspond to the bands presently available for the high power microwave spectrometer shown in Fig. 4.1 of Chapter 4.

mode propagation. The electric and magnetic field patterns of this mode will be discussed shortly.

Table A.1 summarizes the frequency range, cutoff frequency, and the dimensions of various rectangular waveguide bands. The bolded bands (C, X, Ku, and Ka) correspond to the waveguide bands that are utilized by the microwave spectrometer.

Figure A.1 shows a plot of the normalized transmission loss versus frequency data obtained on the X-band version of the high-power spectrometer. The data were obtained with a microwave transition analyzer (MTA). The MTA microwave source, and detector were located at the Traveling Wave Tube (TWT) amplifier and cavity positions, respectively, of the microwave spectrometer shown in Fig. 4.1. The plot clearly shows a lower cutoff frequency at which none of the input power is transmitted to the cavity position; and shows an upper frequency limit at which the transmission characteristics

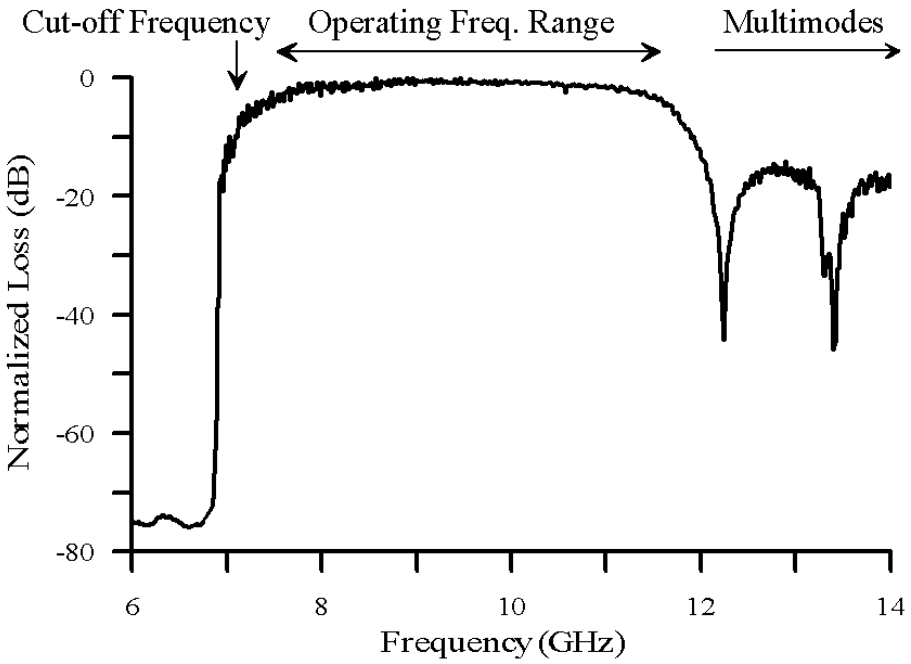

Figure A.1. Plot of normalized waveguide transmission loss versus frequency. The data were obtained on the X-band version of the spectrometer and are in reasonable agreement with the recommended X-band operating frequency range given in Table A.1.

deteriorate due to multi-mode propagation. The measured low-end cutoff frequency agrees well with the specified value shown in the table, whereas the measured upper-end frequency at which multimode propagation occurs is slightly lower than the value given in the table. This decrease in the upper frequency limit of about 0.4 GHz compared to the value shown in Table A.1 was caused by the reduced bandwidth capabilities of the two isolators present in the system.

Figure A.2 provides a sketch of the electric and magnetic field distributions of the main waveguide mode (TE_{10}). The upper sketch shows a three-dimensional view and the lower one shows a top-down two-dimensional view of this mode pattern. The coordinate systems of the sketches were chosen such that the *x*, *y*, and *z*-axes are aligned along the width, height, and length of the waveguide, respectively. Therefore, the net propagation direction is along the *z*-axis. As is seen in the figure, the electric field (**e**) is distributed

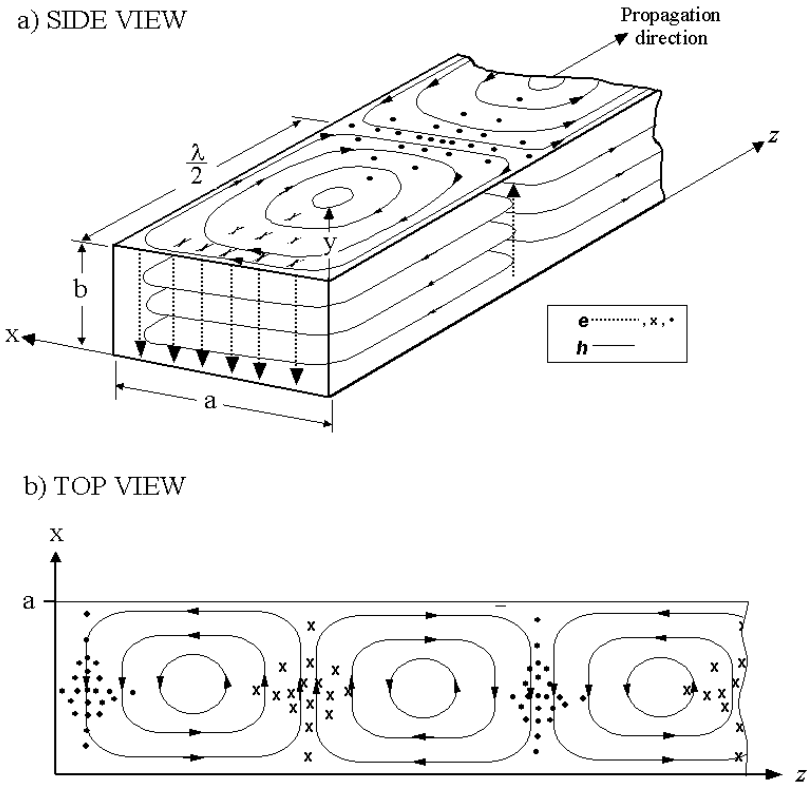

Figure A.2. Three and two-dimensional sketches of the electric (***e***) and magnetic (***h***) field profiles of the TE_{10} traveling wave mode in a rectangular waveguide. Note that for a shorted waveguide (not shown), the relative maxima of the fields are shifted by a quarter of a wavelength, such that maximum ***h*** occurs in region where ***e*** = 0.

perpendicular to the propagation direction in the *x*-*y* plane. The magnetic field (**h**) forms an oval-like pattern in the *x*-*z* plane of the waveguide. For the traveling wave case shown in the figure, the maxima of the **e** and **h** fields occur at the same point along the *z*-axis of the waveguide. However, if the waveguide is shorted, a standing wave pattern will develop in which the maxima of the **e** and **h** fields are a quarter of a wavelength apart. Typically the shorted waveguide geometry is used for low-power FMR measurements and the sample is placed either near the side or end wall of the waveguide in the region of uniform **h** and zero **e** field. For microwave cavities, the cavity iris is usually located at the end wall of the shorted waveguide section. This location will be discussed in more detail shortly.

A.2 DIRECTIONAL COUPLERS

Directional couplers are used to couple a percentage of the power flowing in a primary waveguide line to a secondary one. The amount of power coupled from the main line to the secondary line is referred to as the coupling value of the directional coupler. The main benefits of couplers are that they are highly linear over a wide power range and are readily available with differing coupling values. The main drawback of directional couplers is that a small portion of a wave traveling in the reverse direction relative to the main line of the coupler can be leaked into the secondary line (Pozar [1998]). If the leakage power is of significant magnitude compared to the forward coupled signal, then significant difficulties in calibrating the microwave power flow in the main line can arise because the interference of the coupled and leaked signal will be strongly dependent upon sample absorption and the operating frequency (see Fig. 4.7(a) for details). The amount of unwanted leakage is characterized by the directivity of the coupler and will be discussed in more detail shortly.

Figure A.3 shows two and three-dimensional diagrams of a directional coupler (Poole [1967]). As is seen in the figure, a directional coupler is made up of four ports. Two ports are for the primary line, a third port is for power flow into a secondary line, and the forth port is terminated with a matched load. Holes in the primary line provide the means in which the electric field of the traveling TE_{10} mode (shown in Fig. A.2) is coupled from the primary to the secondary line. The amount of power that is coupled from the main line is the same regardless of which direction the microwaves are traveling in the primary line. What occurs to this coupled power depends on the flow direction of the microwave signal. If the flow is in the forward direction (middle diagram of Fig. A.3), the power is coupled into the secondary waveguide arm. However, if the flow is in the reverse direction (lower diagram), the power is coupled into the matched load. How well the load impedance is matched to the impedance of the primary

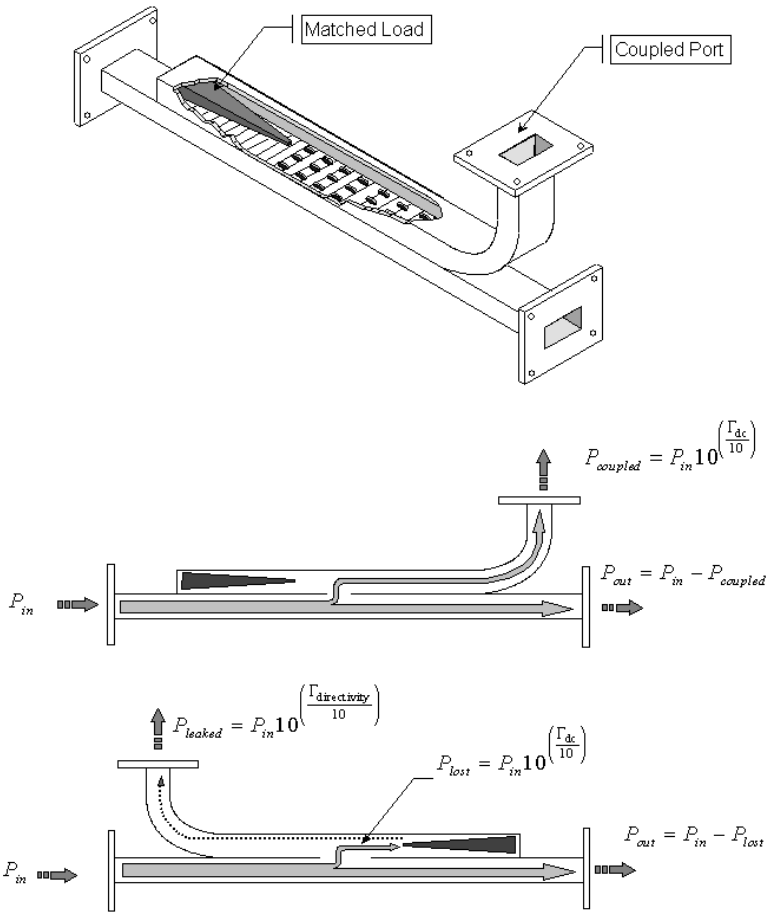

Figure. A.3. Upper diagram shows a three-dimensional view of a directional coupler. The middle and lower diagrams show the response of a directional coupler to microwave signals that are traveling in the forward and the reverse directions relative to the coupler, respectively.

and secondary lines has a significant effect upon the performance of the device and will be discussed in more detail shortly. The amount of input power P_{in} that is coupled from the main line into the secondary line $P_{coupled}$ may be expressed as

$$\mathrm{P_{coupled}} = 10^{(\Gamma_{dc}/10)}\mathrm{P_{in}}\ , \qquad \text{(A.1)}$$

where Γ_{dc}, which is referred to as the coupling value, is a negative quantity given in dBs. Note that Eq. (A.1) is valid regardless of the direction of flow in the primary line.

Commercially available directional couplers typically have coupler values of -3, -10, -20, or -30 dB. For the -30 dB couplers, approximately 0.1% of the forward/reverse traveling input power is coupled into the secondary-line/absorber-load and the remaining 99.9% of the power remains in the primary line. The -3 dB couplers have about 50% of the power in the primary line coupled to the secondary-line/absorber-load.

The criteria used to determine what coupling value to use for the two directional couplers in the high-power microwave spectrometer, which was shown in Figure 4.1, are as follows. For the reference arm coupler, the criterion is relatively simple. Here it is preferable to couple as little power from the main line as possible in order to maximize the power incident upon the cavity. The minimum power requirement is set by the sensitivity of the power meter. For the power meter used in this work, the minimum *average* power needed for accurate measurements is approximately 1μW. The high-power microwave spectrometer is typically operated at small duty-cycles of about 0.01%, so while the peak power in the main line can be a few kWatts, this corresponds to an average power of only a few mW. Therefore, at the highest operating power levels, at least 0.1% of this average power must be coupled to the reference arm. The system is currently optimized for measuring thresholds on samples that have moderate threshold power levels, so about 1% of the power is needed to be coupled into the reference arm. Therefore, the -20dB coupler value shown in Fig. 4.1 is used. If a sample, which requires notably smaller or larger amounts of power to exhibit nonlinear spin wave growth is studied, then this coupler is replaced with a -3dB or -30dB directional coupler, respectively.

When choosing the coupling value for the reflection arm directional coupler the following two competing requirements must be taken into account: (1) the need to minimize the amount of forward flowing power (traveling from the TWT towards the microwave cavity) that is coupled from the main line to the matched load and just "thrown away", versus (2) the need to maximize the amount of reverse flowing power

(microwave signal traveling from cavity towards the TWT) that is coupled to the reflection arm of the spectrometer in order to provide the maximum signal strength to the crystal detector. The crystal detector has a minimum operating power of about 0.25 μW. To best handle these two competing needs, different directional coupler values are used depending upon the operating power levels. When samples with nonlinear instability thresholds in the low to medium spectrometer operational power levels are studied, a -3dB directional coupler is utilized. This corresponds to 50% of the TWT output power being "thrown away" and 50% of the reflected signal from the cavity being coupled into the reflection arm of the spectrometer. When samples that have very large threshold power requirements are studied a -10 dB directional coupler is used, and only 10% of the incident and reflected signals are coupled to the matched load and crystal detector, respectively. Note that the above issue of wasted power could be avoided by replacing the reflection arm directional coupler with a circulator that has high-power handling capabilities. Such a device was not on hand for the power levels used in this study.

It is not possible to perfectly match the impedance of all four ports of a directional coupler. Therefore, some unwanted "leakage" occurs from one port to the other. See Fig. 4.7 for a plot that shows the detrimental effects of this leakage signal. The leakage into the absorber port of a directional coupler has no detrimental effects and may be ignored. The leakage of signal from the matched load to the secondary line causes considerable problems and must not be ignored. The parameter that quantifies the amount of unwanted leakage is referred to as the directivity, $\Gamma_{directivity}$, of the coupler (Pozar [1998]). The larger the directivity, the smaller the amount of leakage that occurs. The exact relationship between the input power (P_{in}), the directivity ($\Gamma_{directivity}$), and the amount of power leaked (P_{leak}) can be written as,

$$P_{leak} = 10^{\frac{-|\Gamma_{directivity}|}{10}} P_{in} . \qquad (A.2)$$

Standard directional couplers have a directivity of approximately -35 dB. However, special high directivity couplers are available with directivities of about -50 dB. Such high directivity directional couplers are used in the high-power spectrometer discussed here. But, even so, there are still leakage signals present that must be eliminated or otherwise accounted for in order to avoid miscalculation of the microwave field power at the sample location and in turn misreporting the microwave threshold field amplitude. See the discussion regarding system calibration in Section 4.3 for more details.

A.3 MICROWAVE CAVITIES

Microwave cavities play an essential role in the high-power microwave spectrometer: they (1) enhance the amplitude of the microwave magnetic field, (2) provide a means of supplying a uniform linearly polarized magnetic field to the sample, and (3) increase the sensitivity of the spectrometer to small amounts of sample absorption. Because of the important role microwave cavities play in the spectrometer, this section will discuss them in detail. First, the key differences between the reflection and transmission type microwave cavities are reviewed. Next, the importance of choosing the correct cavity Q based upon the amount of sample losses is reviewed. This is followed by a discussion of the microwave-coupling iris and the methods that were used to design and construct the rectangular and cylindrical microwave cavities used in this study. This appendix concludes with a derivation of the formulas used to calculate the microwave magnetic field amplitude at various locations in rectangular and cylindrical cavities.

A.3.1 Reflection and Transmission Cavities

Figure A.4 shows sketches of the frequency dependent response of transmission and reflection type microwave cavities. As is seen in the figure, at cavity resonance the maximum amount of power is transmitted through the transmission cavity, and the

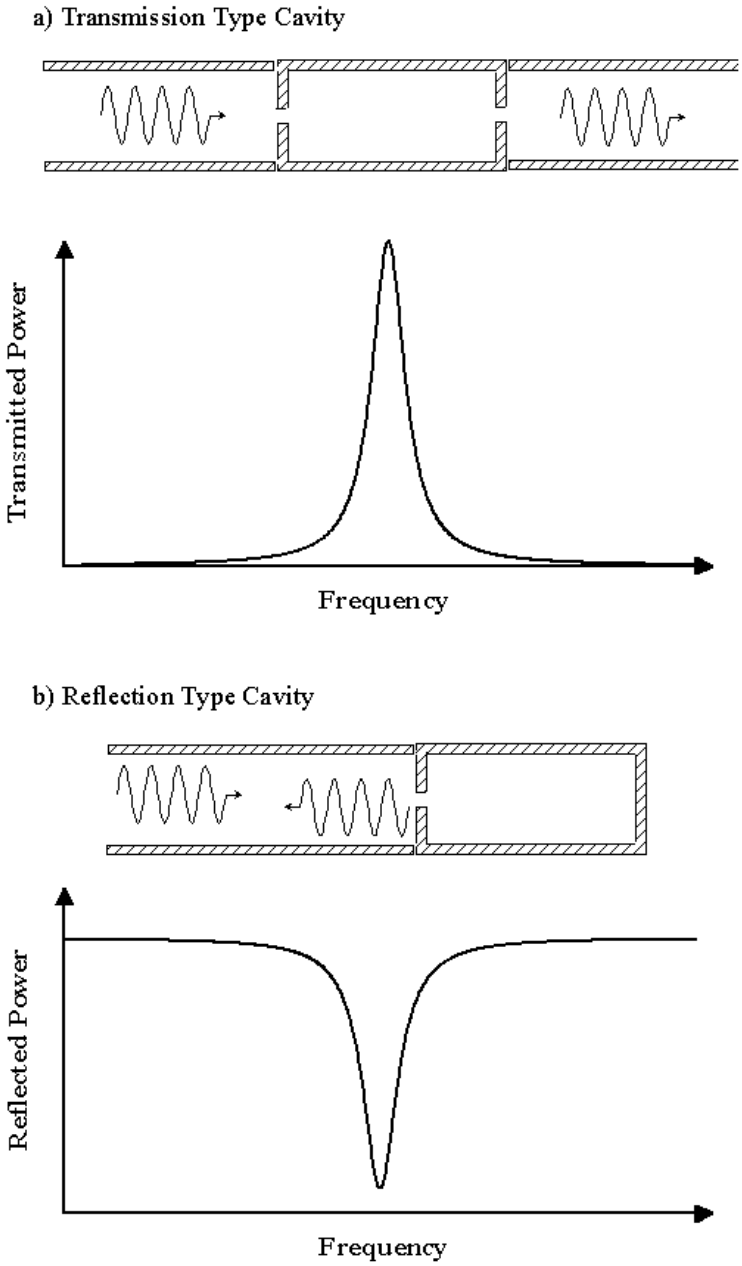

Figure A.4. The top and bottom sketches show the frequency response of transmission and reflection type cavities, respectively.

minimum amount is reflected from the reflection cavity. Therefore, for low-power measurements in which the incident power levels are far below the maximum power handling capabilities of sensitive detection equipment, transmission cavities are used.

However, for high-power measurements in which the operating powers usually far exceed the maximum limits of the detection equipment, reflection type cavities are used. The remainder of this section will focus on reflection type cavities.

A.3.2 Cavity Q

The relative increase in system sensitivity and amplification of the microwave field amplitude attained by a microwave cavity can be quantified by the so-called quality factor, or Q value of the cavity.

The Q parameter may be expressed as

$$Q = \frac{2\pi \langle U_{\text{stored}} \rangle}{\langle U_{\text{lost}} \rangle}, \tag{A.3}$$

where $\langle U_{\text{stored}} \rangle$ and $\langle U_{\text{lost}} \rangle$ are the average amounts of energy stored and lost in the cavity per cycle, respectively (Green and Kohane [1964]). If the frequency dependent response of a cavity is lorentzian shaped, then the above relationship may also be expressed as

$$Q = \frac{f_{\text{res}}}{\Delta f}, \tag{A.4}$$

where f_{res} is the resonance frequency and Δf is the width of the resonance profile at half its maximum height. Therefore, based on the above relationships, the larger the cavity losses, the smaller its Q and the wider its resonance width Δf.

Eddy current ohmic losses in the cavity's inner walls are the main source of loss in an *empty* cavity. These ohmic losses depend upon the conductivity and geometry of the cavity. This dependence on cavity geometry arises because the current densities in the inner walls are directly related to the smoothness of the walls. For instance, much larger

densities occur at the sharp corners of rectangular shaped cavities than in the rounded walls of cylindrical cavities. This results in rectangular cavities having Q values of about ten to one hundred times smaller than those of cylindrical cavities.

It is important to note that large Q values are not always beneficial. The optimal cavity Q is directly related to the amount of sample absorption that is present. When small amounts of sample absorption occur, cavities with large Q's are required. However, when large sample absorption occurs, cavities with smaller Q values should be used in order to avoid saturating the cavity response. Therefore, when high field effective linewidth measurements are performed in which sample losses are extremely small cylindrical cavities with Q's of about 25,000 are used, whereas for FMR experiments where sample losses are at a maximum, rectangular cavities with Q values of about 1000 are used (Truedson *et al*. [1994]); (McKinstry [1991]). The importance of balancing cavity Q and sample loss, is the reason for building both cylindrical and rectangular cavities for the high-power microwave spectrometer.

A.3.3 Coupling Iris

The microwave signal in the waveguide is coupled into the microwave cavity via a coupling iris. The location and size of the iris determines (1) whether the coupling occurs via the electric, magnetic, or both field components of the microwave signal, (2) the value of the cavity Q, and (3) the method in which the power reflected from the cavity responds to sample absorption. For the cavities built in this study, the iris is located to promote the maximum coupling of the magnetic field component of the TE_{10} rectangular waveguide mode to the cavity resonant mode of interest. For the rectangular type cavities, the iris is located at the center of the end-wall of the cavity, while for the cylindrical cavities it is located at the center of the sidewall. For both cavity types, the iris is located in the center of the end-wall of the rectangular waveguide. These locations

and the magnetic field patterns of the cavity modes will be discussed in more detail shortly.

The reflected power versus sample absorption response of reflection type microwave cavities is strongly dependent upon the coupling iris size. To understand this, one needs to realize that the net reflected signal from the cavity is the linear superposition of two out-of-phase reflected signals; one is reflected from the iris plate and the other is reflected from the cavity end-wall. At resonance, the phase difference between these two signals is at 180 degrees because (1) the cavity length is equal to an integer multiple of half the wavelength of the operating signal, and (2) the different boundary conditions experienced at the iris plate (open) and the end wall (short).

Figure A.5 shows a sketch of the two reflected signals and a plot of the reflected power versus sample loss. The relative amplitude of the two reflected signals depends upon both the size of the iris hole and the amount of sample absorption present. First consider the empty cavity case. For small irises, the reflected signal from the iris plate has the larger amplitude and the cavity is referred to as being *under-coupled*. Then as the iris is enlarged, a certain "medium" iris hole size is obtained, the two signals have equal amplitude, and zero net power is reflected from the cavity. The cavity is then referred to as being *critically-coupled*. If the iris hole is larger than this, the reflected signal from the cavity end wall is dominant and the cavity is then referred to as being *over-coupled* (Poole [1967]).

The effect of sample losses on the net reflected power from a reflection type microwave cavity depends on whether the cavity is under, critically, or over coupled. The lower drawing in Figure A.5 is a sketch of the reflected power dependence on sample absorption for the three coupling types. The solid, dotted, and dashed lines correspond to the under-coupled, critically-coupled, and over-coupled cases, respectively. As is seen in the graph, the reflected signal from an under-coupled cavity starts at a non-zero value and increases with sample absorption. The critically-coupled

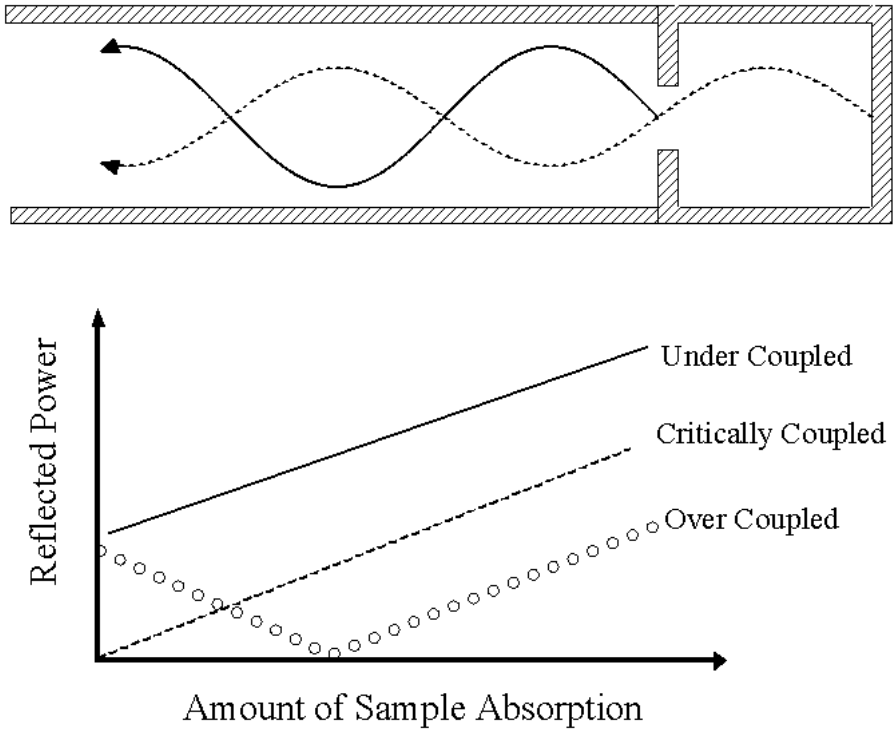

Figure A.5. Upper sketch shows the two component signals that combine to make up the total reflected microwave signal from a reflection type microwave cavity. The solid and dotted lines correspond to the microwave signals that are reflected from the coupling iris plate and then end-wall, respectively. The size of the coupling iris determines whether the cavity is under, critically or over coupled. The lower sketch shows the net reflected power versus sample loss for an under-coupled, critically-coupled, and over-coupled cavity. Under-coupled cavities were used for this study.

cavity has a similar dependence except it starts with a zero value. The over-coupled cavity response is the most complicated. For this coupling type, the reflected power starts at a non-zero value, and it initially decreases with increasing sample absorption until the net reflected signal equals zero. Then with further sample losses, the reflected power increases. While upon first impression, these responses may appear to be counterintuitive, they can actually be easily understood when one realizes that (1) the net reflected signal is actually comprised of two reflected signals (one from the iris plate and the other from the cavity end-wall) and (2) the sample losses, to first order, only affect the reflected signal from the cavity end-wall.

Of the three reflection cavity types described above, the under-coupled cavity is preferred. The over-coupled is not desired because of the complicated response to sample absorption, and the critically-coupled cavity does not reflect enough power back to meet the minimum power specification of the crystal detector. The exact size of the iris hole used for each cavity was determined experimentally using an iterative technique which will be discussed in the next section.

A.3.4 Cavity Fabrication

This subsection briefly reviews how the under-coupled reflection-type microwave cavities used for this study were designed and built. The design equations were obtained from Pozar [1998] and Jackson [1975]. The techniques employed were based on the excellent description of microwave cavities provided by Poole (Poole [1967]) and systematic trial-and-error. Each cavity was designed for a specific resonance mode and a particular resonance frequency.

The two main criteria used in choosing the cavity resonant mode were: (1) it had to have a large uniform magnetic field region and (2) the resonance frequency of the main mode needed to be separated from its adjacent resonant mode by a relatively large amount. For the rectangular cavities, the TE_{101} and TE_{102} modes were selected, while the TE_{011} mode was utilized for the cylindrical cavities.

A microwave cavity is operated at a single frequency corresponding to the particular resonant mode of interest. Therefore, four different rectangular cavities with resonance frequencies of about 9, 12, 15, and 18 GHz were built for the high-power microwave spectrometer. Only one cylindrical cavity, which had a resonance frequency of about 10 GHz, was constructed. The remainder of this subsection will describe the design equations and fabrication methods used to construct the cavities.

The resonance frequency for a rectangular microwave cavity may be written as:

$$f_{\text{rct-cav}} = \frac{c}{2\pi\sqrt{\mu\varepsilon}}\sqrt{\left(\frac{m\pi}{\text{a}}\right)^2 + \left(\frac{n\pi}{\text{b}}\right)^2 + \left(\frac{q\pi}{\text{d}}\right)^2}\,, \tag{A.5}$$

where c is the speed of light in a vacuum, and μ and ε are the relative permeability and permittivity, respectively, of the material filling the cavity. Here, MKS units are employed, and values of 1 are used for μ and ε. The m, n, and q terms are the number of integer multiplies of half wavelengths that subtend the three-principle axes of the rectangular cavity. The a, b, and d parameters in Eq. (A.5) are the dimensions of the rectangular cavity along those three axes.

The rectangular cavities were made from preexisting rectangular waveguides. Therefore, the a and b terms were set by the dimensions of the particular waveguide band used. See Table A.1 for these dimensions in the several different waveguide bands. The length of the cavity, d, was then determined for a particular resonant mode (m, n, q) and frequency using Eq. (A.5). Rewriting Eq.(A.5) for the TE_{10q} mode in terms of d yields the following relationship for length of the cavity:

$$\text{d} = \frac{q\pi}{\sqrt{\left(\frac{2\pi f_{\text{rct-cav}}}{c}\right)^2 - \left(\frac{\pi}{\text{a}}\right)^2}}\,. \tag{A.6}$$

This equation was used to determine the exact length of all the rectangular cavities built for this study. For example, a rectangular cavity made from X-band waveguide (a = 2.29cm) with a TE_{102} resonance mode frequency of 10 GHz has an approximate length of d = 3.9 cm.

The cylindrical cavities were made from hollow cylindrical tubing, the end caps were machined from copper stock, and then rectangular waveguides were soldered in place. The dimensions of the cylindrical cavity required to obtain the desired resonance

frequency and mode pattern were determined as follows. The resonance frequency for a cylindrical microwave cavity may be written as:

$$f_{\text{cyl-cav}} = \frac{c}{2\pi\sqrt{\mu\varepsilon}}\sqrt{\left(\frac{\dot{\rho}_{nm}}{\text{R}}\right)^2 + \left(\frac{q\pi}{\text{d}}\right)^2}\ . \tag{A.7}$$

Here the $\dot{\rho}_{nm}$ term is the m$^{\text{th}}$ root of $\dot{\text{J}}_{\text{n}}(r)$, where $\dot{\text{J}}_{\text{n}}(r)$ is the first derivative of the n$^{\text{th}}$ order Bessel function $\text{J}_{\text{n}}(r)$ (Poole [1967]); (Pozar [1998]). The R term in the equation is the radius of the cylinder. The TE_{011} cylindrical resonant mode was chosen, and the length of the cavity (d) and radius (R) were determined such as to avoid proximity to other possible cavity modes. A graphical method, which is described in detail by Poole [1967] and Pozar [1998], was used to select d and R. For a cylindrical radius of 2.5 cm and a TE_{011} resonance mode frequency of 10 GHz, $\dot{\rho}_{nm} = \dot{\rho}_{01} = 3.832$, and an approximate cylinder length of 2.20 cm is calculated from Eq. (A.7).

Figure A.6 shows sketches of which summarize how the cavities were assembled. Once the cavities were built, the iris was then enlarged to the appropriate size. The goal is to approach the critical coupled point, yet remain under-coupled. This was accomplished by using an iterative process in which the diameter was increase slightly and the cavity response was measured. This process was continued until only about 1% of the power was reflected at resonance while taking care to keep the cavity under-coupled.

A.4 MAGNETIC FIELD EXPRESSIONS

The derivation of the formulas used to calculate the magnetic field amplitude in a reflection type microwave cavity is based upon the work in the following three publications: Green and Kohane [1964]; Patton and Green [1971]; and Patton and Kohane [1972]. These references will be referred to as R-1, R-2, and R-3 (according to

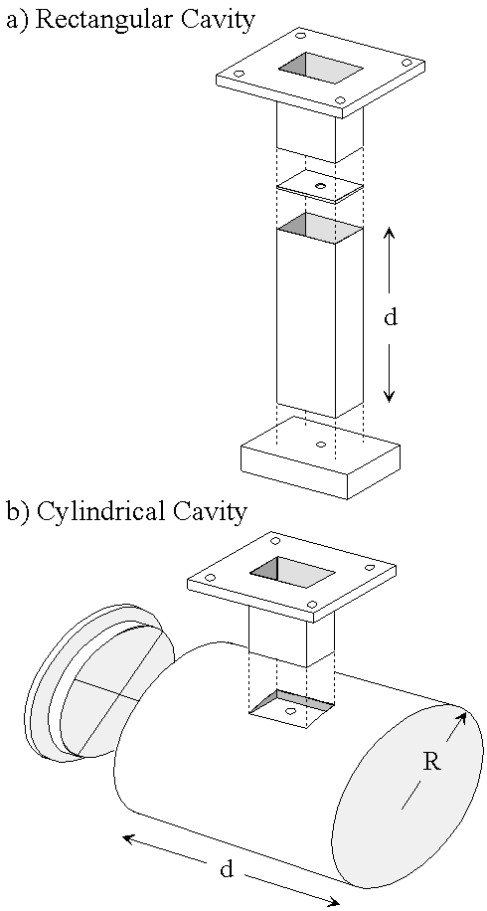

Figure A.6. Sketches of rectangular and the cylindrical cavities assymblies. The "bodies" of the rectangular and cylindrical cavities were made from rectangular waveguides and a tube of oxygen free copper (OFC), respectively.

publication date), respectively, throughout the following text. While the procedure is relatively straightforward, trying to follow the exact calculations throughout the above referenced papers can be difficult. Difficulties arise because: (1) the first publication R-1 inaccurately depicts the position in the cavity where h_o is calculated, (2) the R-1 publication uses MKS units, whereas R-2 and R-3 use a mixture of CGS and MKS units, and (3) while the same symbols are used in the three papers, different definitions are applied to these symbols in R-1 compared to R-2 and R-3. Therefore, in order to clarify the procedure, this section provides the analysis in detail. MKS units are used throughout the calculations.

The analysis procedure is based upon the work provided R-1. First, two different expressions are obtained for the time-averaged microwave energy stored in a microwave cavity. The first expression is written in terms of the microwave magnetic field amplitude and the second in terms of measurable cavity Q parameters. Then, these two equations are equated and an explicit relationship for the magnetic field amplitude is obtained. The above formalism is done for the empty cavity case, and it is then assumed that the sample losses are small enough that this expression is valid for the sample-loaded cavity.

A.4.1 Energy

The time averaged energy, $\langle \mathrm{U} \rangle$, stored in the electric $\mathbf{e}(\mathbf{r},t)$, and magnetic $\mathbf{h}(\mathbf{r},t)$ field expressions of an electromagnetic wave may be written as

$$\langle \mathrm{U} \rangle = \tfrac{1}{4} \iiint d^3 r \left(\varepsilon \left| \mathbf{e}(\mathbf{r},t) \right|^2 + \mu \left| \mathbf{h}(\mathbf{r},t) \right|^2 \right), \tag{A.8}$$

where the triple integral is performed over a volume of space that has a permeability and permittivity of μ and ε, respectively. For the problem of interest, the integral is performed over the volume ($\mathrm{V_c}$) of an empty cavity, and the same amount of average energy is assumed to be stored in $\mathbf{e}(\mathbf{r},t)$ and $\mathbf{h}(\mathbf{r},t)$. Therefore, Eq. (A.8) is rewritten as

$$\langle \mathrm{U} \rangle = \tfrac{1}{2} \mu_{\mathrm{o}} \iiint_{\mathrm{V_c}} d^3 r \left(\left| \mathbf{h}(\mathbf{r},t) \right|^2 \right). \tag{A.9}$$

The magnetic field is calculated for a specific location ($\mathbf{r_o}$) inside the cavity. This field amplitude at location $\mathbf{r_o}$ will be written as $h(\mathbf{r_o})$ here. The general complex expression for the magnetic field at all points in the cavity can be written as

$$\mathbf{h}(\mathbf{r},t) = h(\mathbf{r}_\mathbf{o})\tilde{\mathbf{h}}(\mathbf{r})\exp(\mathrm{i}\omega_p t)\,, \tag{A.10}$$

where ω_p is the angular frequency of the microwave field. Using this form of the magnetic field, Eq. (A.9) can be rewritten as

$$\langle \mathrm{U} \rangle = \tfrac{1}{2}\mu_\mathrm{o} V_\mathrm{c}\, g_m h^2(\mathbf{r}_\mathbf{o})\,. \tag{A.11}$$

Here g_m is a unitless constant that relates the stored energy to a particular mode pattern and the geometry of the cavity, and is given as

$$g_m = \frac{1}{V_\mathrm{c}} \iiint d^3 r \left(\left| \tilde{\mathbf{h}}(\mathbf{r}) \right|^2 \right). \tag{A.12}$$

Note that these expressions for $\langle \mathrm{U} \rangle$ and g_m are the same as in R-1. Whereas, in R-2 and R-3 the factor of 1/2 in Eq. (A.11) is not present in the $\langle \mathrm{U} \rangle$ expression, instead it is contained in the g_m expression. This becomes apparent only after the expressions in R-2 and R-3 are converted from CGS to MKS units.

A.4.2 Cavity Q

A second expression for $\langle \mathrm{U} \rangle$ may be written in terms of measurable cavity *Q* parameters as

$$\langle \mathrm{U} \rangle = \tilde{Q}\, \mathrm{P}_\mathrm{inc}\,, \tag{A.13}$$

where P_inc is the incident microwave power upon the cavity and $\tilde{Q}$ is the conversion parameter that relates this incident power to the amount of energy stored within the

cavity (Slater [1950]). Different forms of this term are used in R-1 and R-3. In R-1, it is written as

$$\tilde{Q} = \frac{4Q_{\mathrm{L}}^{2}}{\omega_{\mathrm{res}} Q_{\mathrm{iris}}}, \tag{A.14}$$

while in R-3, it is written as

$$\tilde{Q} = \frac{2(1-\rho_{\mathrm{res}})Q_{\mathrm{L}}}{\omega_{\mathrm{res}}}. \tag{A.15}$$

The Q_{L} and Q_{iris} terms in the above expressions are the Q values associated with the total loaded cavity and the iris plate, respectively. The ω_{res} and ρ_{res} parameters are the cavity angular frequency and voltage reflection coefficient, respectively. The voltage reflection coefficient is given as $\sqrt{\Gamma}$, where Γ is the cavity reflection coefficient and equals the ratio of the reflected power to the incident power. The relationship between the above Q parameters and the voltage reflection coefficient may be written as

$$Q_{\mathrm{L}} = \frac{1}{2}(1-\rho_{\mathrm{res}})Q_{\mathrm{iris}}. \tag{A.16}$$

Equating equations (A.11) and (A.13) results in the following relationship for the microwave field amplitude at a specific point (r) within the cavity

$$h(r) = \sqrt{\frac{2\tilde{Q}}{\mu_{\mathrm{o}} V_{\mathrm{c}} g_{m}} \mathrm{P}_{\mathrm{inc}}}. \tag{A.17}$$

All of the terms in Eq.(A.17) except g_m can be determined experimentally from cavity reflected power versus frequency data (see McKinstry and Patton [1989] for details).

The specific g_m calculations for the TE_{10q} and TE_{01q} modes in a rectangular and a cylindrical cavity, respectively, will now be addressed.

A.4.3 Calculation of g_m

Based upon Eq. (A.12), the g_m expressions for a rectangular and cylindrical cavity may be written as

$$g_m\{\mathrm{rec}\} = \frac{1}{(\mathrm{abd})}\int_o^a \mathrm{d}x\int_o^b \mathrm{d}y\int_o^d \mathrm{d}z\left\{\tilde{h}_x(x,y,z)^2 + \tilde{h}_y(x,y,z)^2 + \tilde{h}_z(x,y,z)^2\right\} \qquad \text{(A.18)}$$

and

$$g_m\{\mathrm{cyl}\} = \frac{1}{(\pi R^2 \mathrm{d})}\int_o^d \mathrm{d}z\int_o^{2\pi} \mathrm{d}\phi\int_o^R r\,\mathrm{d}r\left\{\tilde{h}_r(r,\phi,z)^2 + \tilde{h}_\phi(r,\phi,z)^2 + \tilde{h}_z(r,\phi,z)^2\right\}, \qquad \text{(A.19)}$$

respectively. Here, a and b are the width and height of the rectangular cavity, respectively, R is the radius of the cylindrical cavity, and d is the length of both cavities. The magnetic fields are written in terms of their amplitude at the location where the sample is to be placed in the cavity. For the TE_{10q} resonate modes in the rectangular cavity the samples are typically placed near the center of the end wall of the cavity at location $r_{rec} = (x,y,z) = (a/2, b/2, 0)$. Whereas for the TE_{01q} mode in the cylindrical cavity, the sample is placed in the very center of the cavity and $r_z = d/2$.

Explicit expressions for the magnetic fields inside the rectangular and cylindrical cavities are determined with Maxwell's equations and by applying boundary conditions (metal walls are assumed to have infinite conductivity). See Jackson [1975] and Pozar [1998] for more details. The magnetic fields for the TE_{10q} mode in a rectangular cavity and TE_{01q} in a cylindrical cavity may be written as,

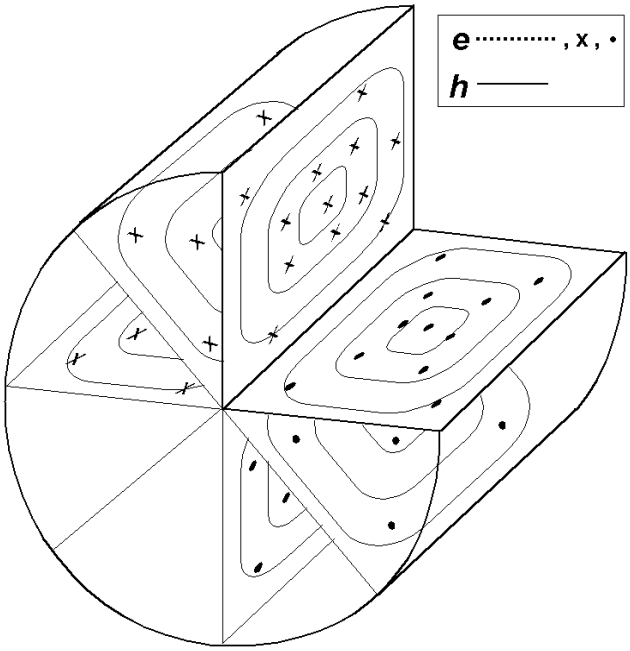

Figure A.7. Three-dimensional sketch of the electric and magnetic fields that comprise the TE011 cylindrical cavity resonance mode. The high power instability measurements are obtained with the sample is placed along the central axis of the cavity in the region of uniform magnetic field.

$$\mathbf{h}_{\mathbf{10q}}^{\mathbf{rect}}(\mathbf{r}) = h_{10q}^{\text{rect}}(r_{rct})\left\{\sin\left(\frac{\pi}{a}x\right)\cos\left(\frac{q\pi}{d}z\right)\hat{\mathbf{x}} - \frac{d}{qa}\cos\left(\frac{\pi}{a}x\right)\sin\left(\frac{q\pi}{d}z\right)\hat{\mathbf{z}}\right\} \tag{A.20}$$

and

$$\mathbf{h}_{\mathbf{01q}}^{\mathbf{cyl}}(\mathbf{r}) = h_{01q}^{\text{cyl}}(r_{cyl})\left\{\frac{q\pi a}{\dot{\rho}_{01}d}\dot{J}_o\left(\frac{\dot{\rho}_{01}}{R}r\right)\cos\left(\frac{q\pi}{d}z\right)\hat{\mathbf{r}} + J_o\left(\frac{\dot{\rho}_{01}}{R}r\right)\sin\left(\frac{q\pi}{d}z\right)\hat{\mathbf{z}}\right\}, \tag{A.21}$$

respectively. Here, $J_o(r)$ is the zeroth order Bessel function and $\dot{J}_o(r)$ is the first derivative of this function. As was mentioned previously the $\dot{\rho}_{o1}$ term is the first root of $\dot{J}_o(r)$, such that $\dot{J}_o(\dot{\rho}_{o1}) = 0,$ where $\dot{\rho}_{01} = 3.832.$ The magnetic fields given by Eq. (A.21) for the TE_{01q} cylindrical cavity are sketched in Figure A.7. The field pattern for a rectangular cavity is similar to what is shown in Fig. A.2.

The g_m expressions for the rectangular and cylindrical cavity are obtained by substituting the expressions given in Eqs. (A.20) and (A.21) into Eqs. (A.18) and (A.19), respectively, and solving the integrals. The resulting solutions for the rectangular and cylindrical cavities may be written as

$$g_m\left\{\mathrm{TE}_{10q}^{\mathrm{rect}}\right\}=\frac{1}{4}\left[1+\left(\frac{\mathrm{d}}{q\mathrm{a}}\right)^2\right] \tag{A.22}$$

and

$$g_m\left\{\mathrm{TE}_{01q}^{\mathrm{cyl}}\right\}=\frac{1}{2}\left\{\mathrm{J_o}(\dot{\rho}_{o1})\right\}^2\left[1+\left(\frac{q\pi\mathrm{R}}{\mathrm{d}\,\dot{\rho}_{o1}}\right)^2\right], \tag{A.23}$$

respectively.

A.4.4 Summary and Comparisons

In summary, the microwave magnetic field amplitude $h(\mathrm{r_o})$ at a specific location $\mathrm{r_o}$ in a microwave cavity may be written in terms of unitless $\tilde{\mathrm{Q}}$ and g_m parameters. These $\tilde{\mathrm{Q}}$ and g_m terms relate the stored energy in the cavity to measurable cavity parameters and calculable cavity mode functions, respectively. The expressions given here for these terms will now be compared with those in references R-1, R-2, and R-3.

In publication R-1, an explicit equation for $h(\mathrm{r_o})$ at the endplate of a TE_{10q} rectangular cavity is given. In order to compare the results presented here with the R-1 results, the $\tilde{Q}$ expression given in Eq. (A.14) and the $g_m\left\{\mathrm{TE}_{10q}^{\mathrm{rect}}\right\}$ term given in Eq. (A.22) are substituted into Eq. (A.17). This yields the following expression for the microwave field amplitude at the center of the cavity endplate

$$h(\tfrac{\mathrm{a}}{2},y,0)=\sqrt{\frac{32Q_{\mathrm{L}}{}^2\mathrm{P_{inc}}}{\mu_o\mathrm{V_c}\omega_{\mathrm{res}}Q_{\mathrm{iris}}\left[1+\left(\frac{\mathrm{d}}{q\mathrm{a}}\right)^2\right]}}\ . \tag{A.24}$$

Upon comparison of Eq. (A.24) with the corresponding equation in R-1, one observes differences in the denominators; specifically the squared term in the denominator of Eq. (A.24) is inverted in the corresponding R-1 equation. It was determined after careful analysis that this discrepancy is due to an error in R-1. While it is stated that the microwave field amplitude equation given in R-1 corresponds to the magnetic field amplitude at the cavity endplate, it actually corresponds to the amplitude at the *sidewall* of the cavity. As is seen in Eq. (A.20), the ratio of the sidewall and end-wall cavity field amplitudes equals $\mathrm{d}/q\mathrm{a}$. Therefore, if the result in R-1 is multiplied by $\left(q\mathrm{a}/\mathrm{d}\right)^2$, it agrees exactly with Eq. (A.24).

We will now turn our focus on comparing the results obtained here with those given in publications R-2 and R-3, which contain terms expressed in both MKS and CGS units. In order to compare the results presented here with those in R-2 and R-3, the $\tilde{Q}$ expression given in Eq. (A.15) is substituted into Eq. (A.17) and the following unit conversions are performed: $\mu_o = 4\pi\cdot 10^{-7}\ \mathrm{N/A^2}$, $\mathrm{A/m} = 4\pi\cdot 10^{-3}\mathrm{Oe}$, $\omega_{\mathrm{res}} = 2\pi f_{\mathrm{res}}$, where f_{res} is expressed in GHz, and $\mathrm{V_c}$ is expressed in $\mathrm{mm^3}$. Upon doing this, one obtains the following expression

$$h(r)[\mathrm{Oe}] = \sqrt{\frac{80\left(1-\rho_{\mathrm{res}}\right)Q_{\mathrm{L}}}{V_{\mathrm{c}}[\mathrm{mm^3}]\,f_{\mathrm{res}}[\mathrm{GHz}]\,g_m(r)}\,\mathrm{P_{inc}}[\mathrm{W}]}\ . \qquad \text{(A.25)}$$

While the field expression given in reference R-2 has a factor of 40 in the numerator instead of value of 80 given in the above expression, the two expressions are actually in agreement. Upon comparing the g_m terms for the rectangular and cylindrical cavities given here with the results in R-2 and R-3, one finds that the R-2 and R-3 values are in exact agreement to within a factor of ½. This ½ factor is due to the different definitions used for $\langle \mathrm{U} \rangle$ and g_m in R-2 and R-3 than the definitions used here and in R-1. Therefore, taking this difference into account, one sees that the results presented here are in exact agreement with those in R-2 and R-3.

APPENDIX B

AUTOMATION PROGRAMS

This appendix reviews the software programs that were developed to operate the high-power microwave spectrometer discussed in Chapter 4 in an automated fashion. This appendix will first review the calibration programs and then address the measurement programs. The goal is to provide a quick overview of the key programs that are available for use with the high power microwave spectrometer. For more details see the user manual that was written as part of this thesis work entitled "*User Manual for the High Power Microwave Spectrometer.*"

B.1 CALIBRATION PROGRAMS

Table B.1 summarizes the LabVIEW calibration programs that were developed to calibrate the (1) the crystal detector, (2) the waveguide losses, (3) the cavity parameters, and (4) the control voltage to the electromagnet power supply. The LabVIEW program entitled *CrystalDetCalib.vi* was developed to calibrate the crystal detector. The program obtains crystal detector output voltage versus microwave power data, which are then fit to a third order polynomial. The fitting parameters are stored in *ConvertVcrystoPcrys.vi*.

Two different LabVIEW programs were developed to perform waveguide calibration measurements. The first one, entitled *PwrmtrWgdCalib.vi* is used to calibrate the frequency dependent power differences between the power meter and cavity locations in the high-power spectrometer. The second program, termed *CrysdtcrWgdCalib.vi* is used

LabVIEW Program	Calibration Type	Required Analysis	Calibration Files
CrystalDetCalib.vi	Calibrates crystal detector output voltage versus input power	User must fit data to the following polynomial: $P_{in}(\mathrm{v}) = a_o + a_1\mathrm{v} + a_2\mathrm{v}^2 + a_3\mathrm{v}^3$	Calibration constants stored in: *ConvertVcrystoPcrys.vi*
PwrmtrWgdCalib.vi	Calibrates waveguide losses between power meter & cavity iris.	NA	Data stored in *PmtrCavWgdLoss.dat*
CrysdtcrWgdCalib.vi	Calibrates waveguide losses between cavity & crystal detector	NA	Data stored in text file: *CavCrysWgdLoss.dat*
MTAMain.vi	Calibrate cavity Q, resonance frequency & reflection coefficient	User must analyze data with the MathCAD program "*ReflCavityCalib.mcd*"	Calibration constant $h_o = \sqrt{C_{cav} P_{inc}}$ entered when prompted
HvsVltCalib.vi	Calibrate electromagnet control voltage.	User must fit data to the following polynomial $P_{in}(\mathrm{v}) = a_o + a_1\mathrm{v} + a_2\mathrm{v}^2 + a_3\mathrm{v}^3$	Calibration constants stored in *CalcVout(Hext).vi*

Table B.1: Summary of the LabVIEW calibration programs and the corresponding analysis that must be performed in order to calibrate the high power microwave spectrometer.

to measure the relative power differences between the cavity and the crystal detector locations. The data are stored in calibration files, titled *PmtrCavWgdLoss.dat* and *CavCrysWgdLoss.dat.* The measurement programs then use these calibration files to convert the measured power at the power meter and crystal detector locations into the power incident upon and reflected by the cavity, respectively.

The LabVIEW program titled *MTA_Main.vi*. was developed to calibrate the microwave cavity. The program acquires reflection coefficient versus frequency data with and without a short placed in front of the cavity position in the high-power microwave spectrometer. A MathCAD program, called *ReflCavityCalib.mcd* can then be used to analyze the raw data. The analysis yields the cavity resonance frequency, resonance reflection coefficient, and loaded Q_{L}. These values are then used in

combination with Eqs. (A.22) and to calculate the cavity calibration constant C_{cav}, where $h_o = \sqrt{C_{cav} P_{inc}}$.

The LabVIEW program titled *HvsVltCalib.vi* was developed to measure the electromagnet magnetic DC field versus power supply control voltage (0-to-10V). The data are fit to a third order polynomial, and the fitting constants are entered into the LabVIEW program titled, *CalcVout(Hext).vi*. These fitting parameters vary with pole piece geometry, and care must be taken to make sure that the correct calibration constants match the particular pole pieces used for a given experiment. The intercept point of the calibration data (field value obtained 0 Volts) and the resulting fitting constants depend upon the remnant magnetization of the pole pieces and the temperature

LabVIEW Program	Summary of Key Features
FMRShrtdWvguideLowPower.vi	Acquires FMR reflection coefficient versus H_{ext} data on a sample mounted in a shorted waveguide.
FMRCavityLowPower.vi	Similar program as above, but has the added feature of cavity resonance tuning. The microwave frequency is reset to the cavity resonance value for each static field value. Acquires all the data at single fixed power level.
FMRCavityHighPower.vi	Similar as above, but data obtained at different microwave power levels. The user enters the desired microwave scan ranges, and FMR data are obtained at various power levels.
Vreflcoeff_vs_ho(single rf-scan).vi	Used to obtain cavity reflection coefficient versus rf at a single static magnetic field value. The user must properly set the protection attenuators at the appropriate values for the given scan range of the main attenuator.
ButterflyCurve.vi	Performs similar measurement as *Vreflcoeff_vs_ho(single rf-scan).vi*, but for various static magnetic field values, and will full automation of the three attenuators.

Table B.2. Summary of the LabVIEW measurement programs developed to perform FMR and butterfly curve instability measurements.

of the coil windings. Therefore, to set the static magnetic main biasing field to a high degree of accuracy, a feedback correction method is used when necessary. This method will be discussed briefly below.

B.2 MEASUREMENT PROGRAMS

Table B.2 summarizes some of the key measurement programs that were developed to perform low and high power microwave measurements in a automated fashion. This section will focus on the program entitled *ButterflyCurve.vi* which was developed to obtain spin wave instability butterfly curve data.

Figure B.1 shows a flow chart of the *ButterflyCurve.vi* measurement program. The objective of this program is to obtain sample loss versus microwave field amplitude (h_o) data at various static magnetic field (H_{ext}) values. As is seen in Fig. B.1 this done in three main phases. The details of each phase are discussed below

B.2.1 Phase-1 of *ButterflyCurve.vi*

In the first phase of the *ButterflyCurve.vi* a series of screens are displayed in which: (1) an overview of the program is provided to the user (2) the user is prompted to perform the necessary manual settings, and (3) required input parameters are obtained from the user.

Figure B.2 shows the first introductory screen that appears upon execution of the program. The screen reminds the user of the general initial spectrometer settings that must be set prior to running the program. As is seen in Fig. B.2, the user must manually: (1) set $\mathbf{h_o}$ and $\mathbf{H_{ext}}$ to the proper alignment, (2) powered on and allowed for the required warm up time of all the devices, (3) set the attenuators to the proper default settings, and (4) have the microwave operating frequency near the microwave cavity resonance frequency. The procedures used to align $\mathbf{h_o}$ and $\mathbf{H_{ext}}$ are discussed in Chapter 4. The required default attenuator settings correspond to a general “safe” starting point in which

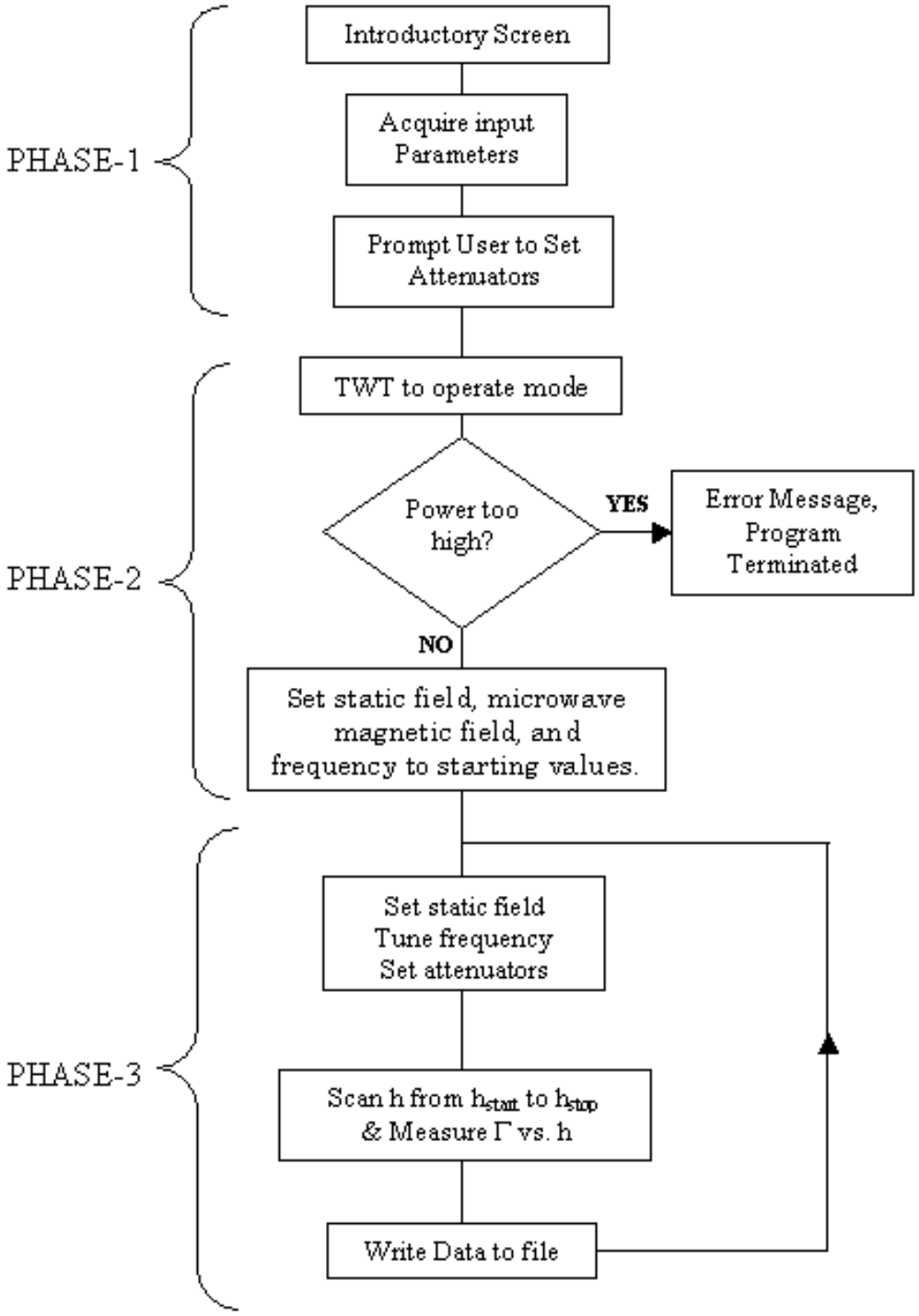

Figure B.1. Flow chart for the LabVIEW program titled *ButterflyCurve.vi*. This program was developed to perform spin wave instability measurements in a stand-alone

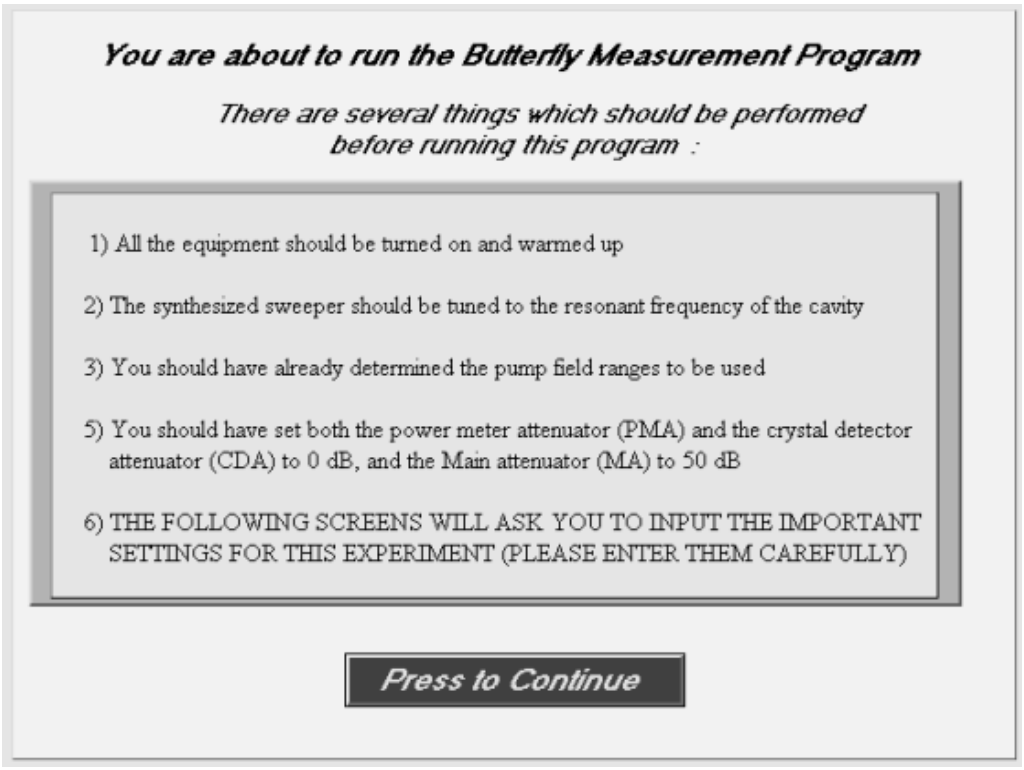

Figure B.2. First prompt screen of the *ButterflyCurve.vi* LabVIEW program. This introductory screen prompts the user to insure that the required initial system settings are established prior to continuing the program.

the main attenuator (MA), the crystal detector attenuator (CDA), and the power meter attenuator (PMA) are set to 50 dB, 0 dB, and 0 dB, respectively. See Fig. 4.1 in Chapter 4 for a sketch of the location of these attenuators within the high-power spectrometer.

After the user verifies that the above initial starting criteria are met, the program then acquires the necessary measurement parameters from the user.

Figure B.3 shows the first of three LabVIEW prompt screens that obtain these parameters. As is seen in the figure, the user must enter the output data filename, the static magnetic scan field range and step size, the number of static magnetic field scan ranges, the microwave pulse-width and duty-cycle, and the cavity calibration constant. The scan range option allows the user to employ different microwave magnetic field amplitude start, step, and stop values for different static magnetic field ranges. As is

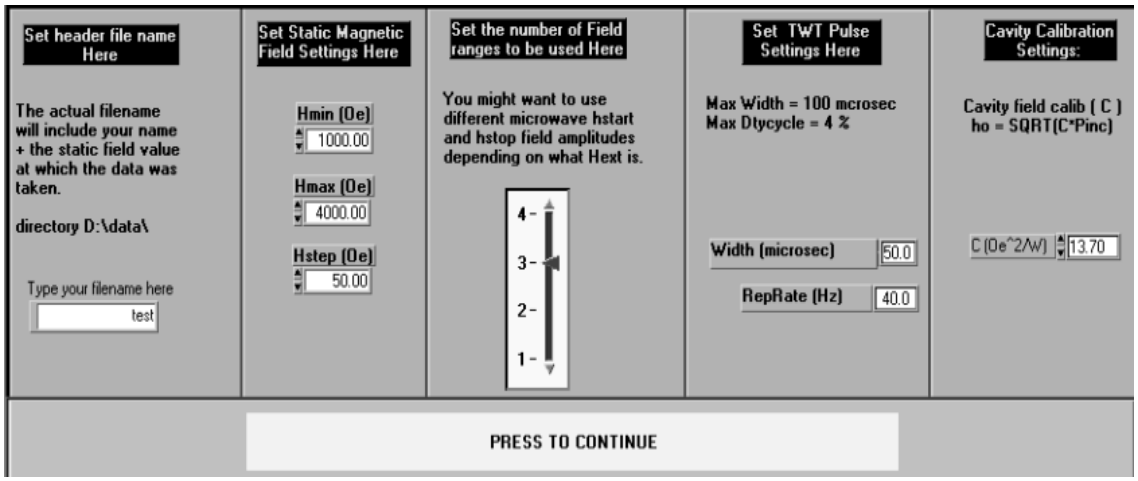

Figure B.3. Second prompt screen of the *ButterflyCurve.vi* program, which acquires the filename, static field scan range, microwave pulse width and frequency, and cavity calibration setting from the user.

seen in the figure, the user is able to select up to four different H_{ext} ranges. After entering the above scan range selections, another prompt window appears in order to obtain the required microwave field amplitude scan settings from the user. The format of this screen depends on the number of H_{ext} ranges selected by the user.

Figure B.4 shows two different possible prompt windows. The left image in Figure B.4 is displayed if the user requested two H_{ext} scan ranges, and the one on the right appears if the user asked for three H_{ext} scan ranges. The corresponding prompt screens for user inputs of one and four scan ranges are not shown.

After the above inputs are obtained, the program determines a rough estimate of the variable attenuator settings required to set $h_o = h_{start}$, and prompts the user to manually set the attenuators to these starting values. After the user informs the program that the attenuators have been set to the above-specified values, the program checks to see that the power levels are within acceptable limit. If the power levels at the crystal detector and power meter are within acceptable limits, the program proceeds to phase-II, if not the program immediately shuts the system down and displays a warning message.

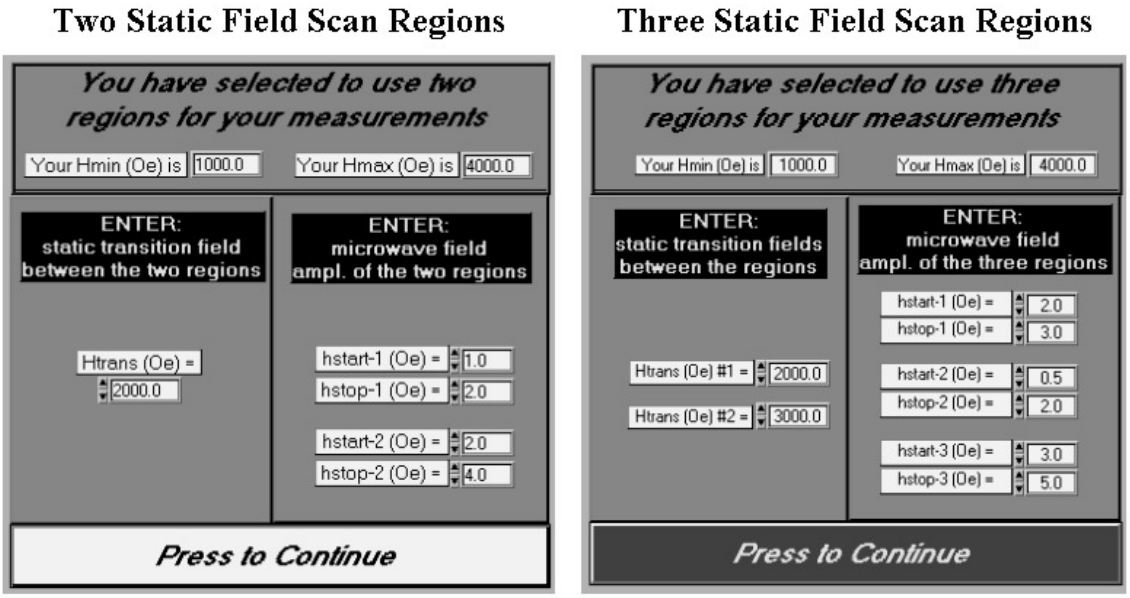

Figure B.4. Third prompt screen of the *ButterflyCurve.vi* LabVIEW program, which obtains the microwave field amplitude scan range settings. The images on the left and right correspond to what is shown if the user selected a static field scan range setting of two or three, respectively, from the prompt window shown in Fig. B.3.

B.2.2 Phase-2 of *ButterflyCurve.vi*

In Phase-II of *ButterflyCurve.vi* the static magnetic field, microwave frequency, and microwave magnetic field amplitude are set to the appropriate starting values. The three subprograms that perform these initializations will now be discussed.

The subprogram that sets the H_{ext} to its initial value, termed *HextSetLoop.vi* proceeds in the following manner. First the DC control voltage required by the electromagnet to set $H_{ext} = H_{start}$ value is calculated. This calculation is performed by the *CalcVout(Hext).vi*. As was stated previously, prior to running the *ButterflyCurve.vi* the user must insure that the correct calibration constants are being applied for the given pole piece configuration in use. The control voltage is applied to the electromagnet power supply via the DAQ card discussed in Section 4.4 of Chapter 4, and the static field is allowed to stabilize and then compared to the desired setting. If necessary, a

correction voltage is applied to the electromagnet power supply. The above technique typically results in an H_{ext} setting that is within 1 Oe of H_{start}.

The microwave measurements are performed with the operating frequency set to the cavity resonance frequency $f_{\text{cav-res}}$. This frequency can depend on H_{ext}, so each time H_{ext} is changed the operating frequency is retuned to $f_{\text{cav-res}}$. The LabVIEW subprogram called *FindCvtResFreq.vi* is utilized to perform this task. The basic procedure is as follows. First a narrow frequency scan is performed about the user supplied operating frequency obtained in Phase-1 of *Butterfly Curve.vi* . Then the *Find cvty res freq.vi* program analyzes the reflected power versus frequency data, checks to make sure it is parabolic, and resets the operating frequency to the minimum of the response curve. If the acquired data does not contain a clearly defined symmetric response about a minimum, the data are reacquired over a wider frequency range. This is continued until an absolute minimum is obtained. For most parallel pumping and subsidiary absorption butterfly curve measurements the cavity resonance frequency is typically determined in one frequency scan. However, it can take up to three scans for resonance saturation which are obtained in the vicinity of FMR resonance.

The scan widths and number of data points obtained per scan depend upon the cavity of interest. Cavities with a large Q require smaller scan widths than cavities with small Q values. The scan widths and number of scan points should be set prior to the running the *ButterflyCurve.vi* program. These settings are stored in the LabVIEW subprogram entitled *CavityScanSettings.vi*. Once these values are set for a given cavity, they should only be changed when another cavity with a significantly different Q value is utilized.

Once the static magnetic field and the microwave frequency are set, the variable attenuators are then automatically adjusted to their appropriate starting values. As was discussed in Chapter 4, the stepper motors, which are attached the variable attenuators, are used to set the attenuators. The stepper motor controller card provides the necessary drive voltages to turn the stepper motors. The computer communicates with the

controller card via DOS executable C++ compiled programs. These programs are called and run from LabVIEW to set the attenuation of variable attenuators as needed.

The LabVIEW subprogram, titled "*Set_MA,CDA,& PMAtoStartPos.vi*" sets the attenuators into their starting positions. The procedure is as follows. The main attenuator is gradually decreased (increases operating power in the system), while the microwave power levels at the power meter and the crystal detector is monitored. If the power at the power meter or the crystal detector approaches their maximum operating limits, then their attenuators are increased until the power is lowered to acceptable values. Then the main attenuator is decreased further until the desired starting microwave magnetic field amplitude inside the cavity is obtained.

After h_o is set to h_{start}, final adjustments are made to the crystal detector and power meter attenuators. The attenuators are set such that the minimum power levels needed for accurate measurements are incident upon the detectors. This provides the maximum power range for a given scan, and most often the protection attenuators do not have to be readjusted during the scans performed in Phase-3 of *ButterflyCurve.vi*. Note that the operating power ranges of the power meter and crystal detector are set in the *PMA_AllowedRanges.vi* and the *CDA_AllowedRanges.vi* subprograms, respectively.

B.2.3 Phase-3 of *ButterflyCurve.vi*

In the third and final phase of *ButterflyCurve.vi,* the microwave field scans are performed at various static magnetic fields. During the h_o scans, the power levels at the power meter and the crystal detector are constantly monitored and the attenuators are automatically adjusted as necessary. After each microwave field scan, the reflection coefficient versus h_o data are stored to a new data file. The data filename is comprised of the user supplied filename entered in Phase-I and the static field at which the scan was performed. The data files are stored in the "D:\buttefly-curve-data" directory of the PC.

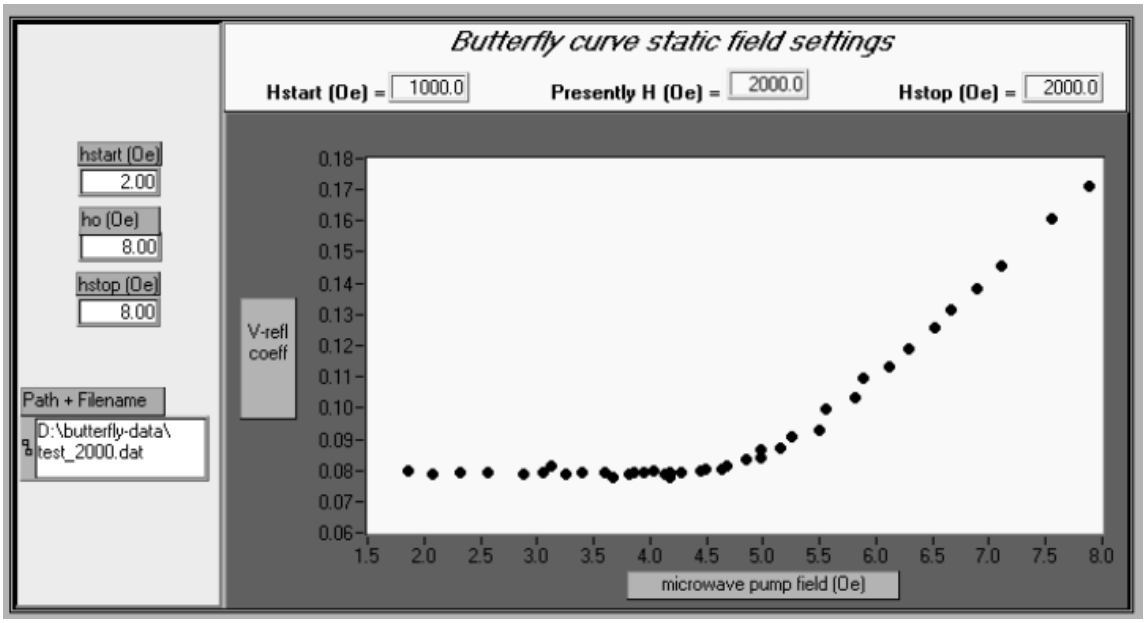

Figure B.5. Results of microwave field scan obtained during stage-3 of the *ButterflyCurve.vi* program. The plot of cavity reflection coefficient (proportional to sample loss) versus microwave field shows a clear transition from no sample loss (linear region) to notable sample losses.

After the scans are performed the attenuators are reset to their initial general settings and the instruments are placed into "standby mode.

Figure B.5 shows example microwave field scan data that were obtained during Phase-3 of the *ButterflyCurve.vi* program. Note that in this case the user-entered filename was "*test*", the microwave field was scanned from 2 to 8 Oe. The h_o scans were done at H_{ext} values of 1000 Oe, 1100 Oe, 1200 Oe, ... , and 2000 Oe. The data shown in the figure corresponds to sample loss versus microwave magnetic field amplitude for the last static magnetic field setting of 2000 Oe. Therefore, the data file was named "*test_2000.dat"*.

Note that the LabVIEW program titled "*FMR_cavity-High-power.vi"* works in a similar fashion as *ButterflyCurve.vi*. But, H_{ext} is scanned for fixed h_o values rather than h_o scanned for fixed H_{ext}. The usefulness of scanning one field versus the other is discussed in the operation section of Chapter 4.

BIBLIOGRAPHY

[Bloch, 1946] F. Bloch, Phys. Rev. 100, 1788 (1946).

[Bloembergen and Wang, 1954] N. Bloembergen and S. Wang, Phys. Rev. 93, 72 (1954).

[Bloembergen, 1956] N. Bloembergen, Proc. I.R.E. 44, 1250 (1956).

[Chartaryzhskii et al., 1976] D. N. Chartaryzhskii, B. A. Kalinikos, and O. G. Vendik, Solid State Communications. 20, 985 (1976).

[Chikazumi, 1994] S. Chikazumi, Physics of Ferromagnetism, 2nd edition. (Oxford University Press, New York, 1997).

[Chen and Patton, 1991] M. Chen and C. E. Patton, J. Appl. Phys. 69, 5724 (1991).

[Chen and Patton, 1994] M. Chen and C. E. Patton, Nonlinear Phenomena and Chaos in Magnetic Materials, edited by P. E. Wigen (World Scientific, Singapore, 1994) Chapter 3.

[Cox et al., 2001] R. G. Cox, C. E. Patton, M. A. Wittenauer, P. Kabos, L. Chen, J. Appl. Phys. 89, 4454 (2001).

[Cullity, 1972] B. D, Cullity, Introduction to Magnetic Materials, (Addison-Wesley, California, 1972).

[Damon, 1951] R. W. Damon, Revs. Mod. Phys. 25, 239 (1951).

[Damon and Eshbach, 1961] R. W. Damon and J. R. Eshbach, J. Phys Chem. Solids 19, 308 (1961).

[Green and Healy, 1963] J. J. Green and B. J. Healy, J. Appl. Phys. 34, 1285 (1963).

[Green and Kohane, 1964] J. J. Green and T. Kohane, Semicond. Prod. 7, 46 (1964).

[Griffiths, 1946] J.H.E. Griffiths, Nature 158 (1946) 670.

[Gurevich et al., 1999] A. G. Gurevich, A. V. Nazarov, and O. A. Chivileva, Phys. Solid State. 41, 1513 (1999).

[Heisenberg, 1928] W. Heisenberg, Z. Physik, 49 (1928), 619.

[Helszajn and McStay, 1970] J. Helszajn and J. McStay, IEEE Trans. Microwave Theory Tech. MTT-18, 518 (1970).

[Herring and Kittel, 1951] C. Herring and C. Kittel, Phys. Rev. 81, 869 (1951).

[Hurben and Patton, 1988] M. J. Hurben and C. E. Patton, J. Appl. Phys. 83, 4344 (1988).

[Hurben and Patton, 1996] M. J. Hurben and C. E. Patton, J. Magn. Magn. Mater. 162, 39 (1996).

[Hurben, 1996] M. J. Hurben, Ph.D. dissertation, Two Magnon Scattering and Relaxation in Thin Ferrite Films, Colorado State University, Fort Collins, Colorado (1996).

[Hurben et al., 1997] M. J. Hurben, D. R. Franklin, and C. E. Patton, J. Appl. Phys. 81, 7458 (1997).

[Jackson, 1975] J. D. Jackson, Classical Electrodynamics 2nd edition (John Wiley and Sons, New York) 1975.

[Kabos et al., 1996] P. Kabos, C. E. Patton, G. Wiese, A. D. Sullins, E. S. Wright, and L. Chen, J. Appl. Phys. 80, 3962 (1996).

[Kabos et al., 1997] P. Kabos, M. Mendik, G. Wiese, and C. E. Patton, Phys. Rev. B, 55, 11 457 (1997).

[Kalinikos, 1980] B. A. Kalinikos, IEE Proc. (London) 127 (H1) 4 (1971).

[Karim et al., 1993] R. Karim, S. D. Ball, J. R. Truedson, and C. E. Patton, J. Appl. Phys. 73, 4512 (1993).

[Kittel, 1947] C. Kittel, Phys. Rev. 71, 270 (1947).

[Kasuya and LeCraw, 1961] T. Kasuya and R. C. LeCraw, Phys. Rev. Lett., 6, 223 (1961).

[Kohane and Schlomann, 1968] T. Kohane and E. Schlomann, J. Appl. Phys. 39, 720 (1968).

[Landau and Lifshitz, 1935] L. Landau and E. Lifshitz, Phys. Z. Sowjet Union. 8, 153 (1935).

[Landau and Lifshitz, 1984] L. D. Landau and E. M. Lifshitz, Mechanics, 3rd edition. (Pergamon Press, New York, 1984).

[Lax and Button, 1962] B. Lax and K. J. Button, Microwave Ferrites and Ferrimagnetics (McGraw-Hill, New York) 1962.

[LeCraw et al., 1958] R. C. LeCraw, E. G. Spencer, and C. S. Proter, Phys. Rev. 110, 1311 (1958).

[Liu and Patton, 1981] Y. H. Liu and C. E. Patton, J. Appl. Phys. 53, 5116 (1981).

[McKinstry et al., 1985] K. D. McKinstry, C. E. Patton, and M. Kogekar, J. Appl. Phys. 58, 925 (1985).

[McKinstry and Patton, 1989] K. D. McKinstry and C. E. Patton, Rev. Sci. Instrum. 60, 439 (1989).

[McKinstry, 1991] K. D. McKinstry, Ph.D. dissertation, Off Resonance Losses In Hexagonal Ferrites, Colorado State University, Fort Collins, Colorado (1991).

[Milano and Schloemann, 1961] U. Milano and E. Schloemann, Inst. Elect. Eng. No. 3598, 59 (1961).

[Mita and Shinizu, 1973] M. Mita and H. Shinizu, J. Phys. Soc. Japan 35, 414 (1973).

[Motizuki et al., 1965] K. Motizuki, M. Sparks, and P. E. Seiden, Phys Rev. 140, A972 (1965).

[Nazarov et al., 2002a] A. V. Nazarov, R. G. Cox, & C. E. Patton, J. Appl. Phys. 92, 3890 (2002).

[Nazarov et al., 2002b] A. V. Nazarov, C. E. Patton, R. G. Cox, L. Chen, P. Kabos, JMMM. 248, 164 (2002).

[Osborn, 1945] J. A. Osborn, Phys. Rev. 67, 351 (1945).

[Patton, 1969] C. E. Patton, J. Appl. Phys. 40, 2837 (1969).

[Patton, 1970a] C. E. Patton, J. Appl. Phys. 41, 1637 (1970).

[Patton, 1970b] C. E. Patton, Proc. Intern. Conf. Ferrites, July, Kyoto. Japan, 524 (1970).

[Patton, 1972] C. E. Patton, IEEE Trans. on Magn. MAG-8, 433 (1972).

[Patton, 1975] C. E. Patton, Microwave Resonance and Relaxation edited by D.J. Craik (John Wiley, London, 1975) Chap. 10.

[Patton, 1976] C. E. Patton, Czech. J. Phys B 26, 925 (1976).

[Patton, 1979] C. E. Patton, Phys. Stat. Sol. (b) 92, 211 (1979).

[Patton, 1980] C. E. Patton, Ferrites – Proc. of the Int. Conf., Univ. of Tokyo Press, Tokyo Japan, 807 (1980).

[Patton, 1988] C. E. Patton, Microwave Excitations in Solids, Physical Reports 103, No. 5 (1984).

[Patton, 1988] C. E. Patton, IEEE Trans. Magn. 24, 2024 (1988).

[Patton and Green, 1971] C. E. Patton and J. J. Green, Rev. Sci. Instruments 42, 193 (1971).

[Patton and Kohane, 1972] C. E. Patton and T. Kohane, Rev. Sci. Instruments 43, 76 (1972).

[Poole, 1967] C. P. Poole, Electron Spin Resonance. (John Wiley & Sons, New York, 1967).

[Pozar, 1998] D. M. Pozar, Microwave Engineering 2nd ed. (John Wiley & Sons, New York, 1998).

[Press, Flannery, Teukolsky, and Vetterling, 1992] Numerical Recipes, The Art of Scientific Computing Fortran (Cambridge University Press, New York, 1992).

[Pucel, 1959] R. A. Pucel, Technical Report No. R-20, Oscillators and Amplifiers Using Time-Varing Parameters, Raytheon Company, 1959, (unpublished).

[Robinson, 1992] T. M. Robinson, J. Appl. Phys. 72, 607 (1992).

[Rodrigue, 1963] G. P. Rodrigue, IEEE Trans. Microwave Theory Tech. MTT-11, 351 (1963).

[Rodrigue, 1985] G. P. Rodrigue, Adv. Ceramics 21, 37 (1985).

[Sandercock and Wettling, 1979] J. R. Sandercock and W. Wettling, J. Appl. Phys. 50, 7784 (1979).

[Savage and Tauber, 1964] R. O. Savage and A. Tauber, J. Am. Ceram. Soc. 47, 13 (1964).

[Savage et al., 1965] R. O. Savage, S. Dixon, and A. Tauber, J. Appl. Phys. 36, 873 (1965).

[Schloemann, 1959] E. Schloemann, Technical Report No. R-48, Raytheon Company, 1959, (unpublished).

[Schloemann et al., 1960] E. Schloemann, J. J. Green, and U. Milano, J. Appl. Phys. 31, 386S (1960).

[Schloemann et al., 1963] E. Schlömann, R. I . Joseph, and I. Bady, J. Appl. Phys. 34, 672 (1963).

[Silber and Patton, 1982] L. M. Silber and C. E. Patton, IEEE Trans. on Magn. MAG-18, 1630 (1982).

[Slater, 1950] J. .C. Slater, Techniques of Microwave Measurements (McGraw-Hill, New York) 1950.

[Smit and Wijn, 1959] J. Smit and H. P. J. Wijn, Ferrites (John Wiley & Sons, New York) 1959.

[Sparks, 1964] M. Sparks, Ferromagnetic Relaxation Theory (McGraw-Hill, New Jersey) 1964.

[Spiegel, 1994] M. R. Spiegel, Mathematical Handbook of Formulas and Tables (McGraw-Hill, New York) 1994.

[Spencer et al., 1958] E. G. Spencer, R. C. LeCraw, C. S. Porter, J. Appl. Phys. 29, 429 (1958).

[Suhl, 1957] H. Suhl, J. Phys. Chem. Solids 1, 209 (1957)

[Stancil, 1993] D. D. Stancil, Theory of Magnetostatic Waves (Springer-Verlag, New York) 1993.

[Tauber] Tauber private communication with C. E. Patton.

[Tauber et al., 1964] A. Tauber, S. Dixon, and R. O. Savage, J. Appl. Phys. 35, 1008 (1964).

[Thompson and Rodrigue, 1985] S. B. Thompson and G. P. Rodrigue, IEEE Trans. Microwave Theory Tech. MTT-33, 1204 (1985).

[Truedson et al., 1994] J. R. Truedson, P. Kabos, K. D. McKinstry, and C. E. Patton, J. Appl. Phys. 76, 432 (1994).

[Vittoria, 1980] C. Vittoria, J. Magn. Magn. Materials 21, 109 (1980).

[von Aulock, 1965] W. H. von Aulock, Handbook of Microwave Ferrite Materials (Academic Press, New York) 1965.

[Vrehen et al., 1970] Q. H. F Vrehen, A. Brose van Groenou, and J. G. M. deLau, Phys. Rev., B1, 2332 (1970).

[Wiese et al., 1995] G. Wiese, P. Kabos, and C. E. Patton, Phys. Rev. B51, 15085-15102 (1995).

[White and Patton, 1978] G. O. White and C. E. Patton, JMMM, 9, 299 (1978).

[White et al., 1992] G. O. White, L. Chen, C. E. Patton, and R. L. Tinkoff, Rev. Sci. Instrum. 63, 3156 (1992).

[Wigen 1994] P. E. Wigen, Nonlinear Phenomena and Chaos in Magnetic Materials (World Scientific Publishing Company, Singapore) 1994.

[Wilber et al., 1984] W.D. Wilber, W. Wettling, P. Kabos, C. E. Patton, and W. Jantz, J. Appl. Phys. 55, 2533 (1994).

[Wittenauer et al., 1993] M. A. Wittenauer, J. A. Nyenhuis, A. I. Schindler, H. Sato, F. J. Friedlaender, J. Truedson, R. Karim, and C. E. Patton, J. Crys. Growth 130, 533 (1993).

[Wittenauer 2005] private conversation with Mike Wittenauer. Research Associate at Physics Department of Colorado State University.

[Yiu and Patton, 1982] Y. H. Yiu and C. E. Patton, J. Appl. Phys. 53, 5116 (1982).

[Zhang et al., 1987] Y. T. Zhang, C. E. Patton, G. Srinivasan, G. O. White, C. J. Brower, and C. A. Edmondson, Rev. Sci. Instrum. 58, 620 (1987).